R-11-23

The Greenland Analogue Project

Yearly Report 2010

Harper J[1], Hubbard A[2], Ruskeeniemi T[3], Claesson Liljedahl L[4], Lehtinen A[5], Booth A[6], Brinkerhoff D[1], Drake H[7], Dow C[6], Doyle S[2], Engström J[3], Fitzpatrick A[2], Frape S[8], Henkemans E[8], Humphrey N[9], Johnson J[1], Jones G[6], Joughin I[10], Klint KE[11], Kukkonen I[3], Kulessa B[6], Landowski C[9], Lindbäck K[12], Makahnouk M[8], Meierbachtol T[1], Pere T[5], Pedersen K[13], Pettersson R[12], Pimentel S[2], Quincey D[2], Tullborg E-L[14], van As D[11]

1 University of Montana
2 Aberystwyth University
3 Geological Survey of Finland
4 Svensk Kärnbränslehantering AB
5 Posiva Oy
6 Swansea University
7 Linnéuniversitetet
8 University of Waterloo
9 University of Wyoming
10 University of Washington
11 GEUS
12 Uppsala University
13 Micans AB
14 Terralogica

December 2011

Svensk Kärnbränslehantering AB
Swedish Nuclear Fuel
and Waste Management Co

Box 250, SE-101 24 Stockholm
Phone +46 8 459 84 00

ISSN 1402-3091
SKB R-11-23
ID 1334696

The Greenland Analogue Project

Yearly Report 2010

Harper J[1], Hubbard A[2], Ruskeeniemi T[3], Claesson Liljedahl L[4], Lehtinen A[5], Booth A[6], Brinkerhoff D[1], Drake H[7], Dow C[6], Doyle S[2], Engström J[3], Fitzpatrick A[2], Frape S[8], Henkemans E[8], Humphrey N[9], Johnson J[1], Jones G[6], Joughin I[10], Klint KE[11], Kukkonen I[3], Kulessa B[6], Landowski C[9], Lindbäck K[12], Makahnouk M[8], Meierbachtol T[1], Pere T[5], Pedersen K[13], Pettersson R[12], Pimentel S[2], Quincey D[2], Tullborg E-L[14], van As D[11]

1 University of Montana
2 Aberystwyth University
3 Geological Survey of Finland
4 Svensk Kärnbränslehantering AB
5 Posiva Oy
6 Swansea University
7 Linnéuniversitetet
8 University of Waterloo
9 University of Wyoming
10 University of Washington
11 GEUS
12 Uppsala University
13 Micans AB
14 Terralogica

December 2011

Contents

1 Introduction

The deep geological repository concept is being considered in a number of countries that are designing and/or incorporating practical solutions for the long-term management and effective isolation of spent nuclear fuel. Long-term management requires that the spent nuclear fuel and associated decay by-products are kept isolated from the biosphere on a time scale of at least hundreds of thousands of years. Within this time frame glacial conditions are expected to occur in cycles in regions that have been glaciated in the past two to ten million years. Climate induced changes, such as the growth of ice sheets and permafrost, will influence and alter the ground surface and subsurface environment, including its hydrology, which may impact repository safety. Glaciationtion impact assessments have, to-date, used simplified models and conservative assumptions, for example in the representation of ice sheet hydrology, that do not reflect the complexity of natural systems and processes. This is largely due to lack of direct observations of such processes from existing ice sheets, which if more readily available could help reduce uncertainties and provide a strong scientific basis for the treatment of glacial impacts in safety assessments. Our current understanding of the hydrological, hydrogeological and hydrogeochemical processes associated with cold climate conditions and glacial cycles, and their impact on the long-term performance of deep geological repositories for spent nuclear fuel, will be significantly improved by studying a modern analogue.

To advance the understanding of processes associated with glaciation and their impact on the long-term performance of a deep geological repository, the Greenland Analogue Project (GAP), a four-year field and modelling study of the Greenland ice sheet and subsurface conditions, has been initiated collaboratively by SKB, Posiva and NWMO. The study site encompasses a land terminus portion of the Greenland ice sheet, east of Kangerlussuaq, and is in many ways considered to be an appropriate analogue of the conditions that are expected to prevail in much of Canada and Fennoscandia during future glacial cycles. The project begin in 2009 and is scheduled for completion in 2012. The GAP will conduct the first *in situ* investigations of some of the parameters and processes needed to achieve a better understanding of how an ice sheet may impact a deep repository, and will provide measurements, observations and data that may significantly improve our safety assessments and risk analyses of glaciation scenarios. The project includes three sub-projects (A-C) with specific individual objectives; these objectives collectively aim at contributing knowledge and input to the overall project goal. Figure 1-1 gives an overview of the different aspects of the three GAP sub-projects. The purpose of subdividing the project is that insights and data obtained from the different sub-projects constitute self-consistent data sets, which will be tested and implemented within the individual sub-projects. The overall idea is that the results of all sub-projects combined will result in large synergistic effects leading to the understanding of hydrological conditions during glacial periods. That is also the reason why all sub-projects are performed within the same geographical area (see Figure 1-2). Finally, the GAP project will contribute to a three-dimensional process understanding of a glaciated environment by obtaining an integrated view of ice sheet hydrology and groundwater flow and chemistry (Figure 1-1).

This report was produced by the GAP team members and presents an overview of the activities within the GAP during the interval January 1 to December 31, 2010, as well as research results obtained during this time frame. Research for the GAP is ongoing, and additional results related to the data presented here may become available in the future and will be presented in subsequent annual reports.

The main field activities in 2010 included: ice radar investigations; operation and maintenance of the GPS and automatic weather station (AWS) network; active and passive seismic studies; ice drilling; tracer and slug tests; subglacial hydrological and hydrogeochemical investigations; groundwater and surface water sampling; borehole monitoring; and, water-rock interaction studies. A number of activities have been carried out in conjunction with the field investigations, which include: design and fabrication of equipment, such as ice drill rig and downhole sensors; remote sensing analysis; numerical ice sheet and groundwater modelling; and, logistical planning of the deep bedrock drilling for 2011.

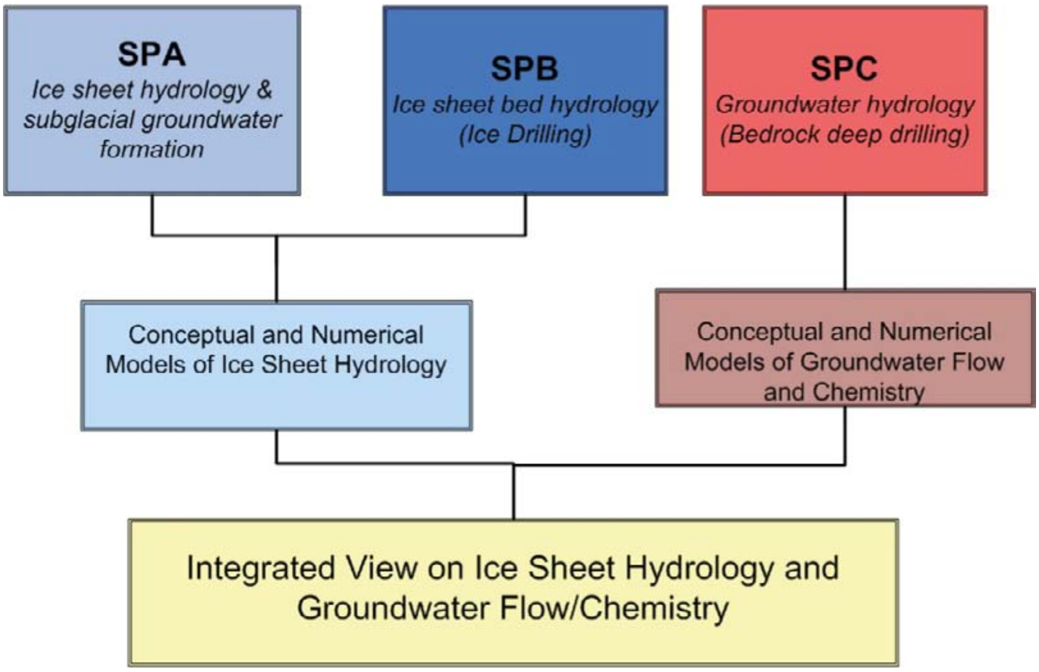

Figure 1-1. *Flow diagram illustrating how the output from the individual GAP sub-projects (SP) will feed into joint modelling work and improve our current understanding of ice sheet hydrology and groundwater flow and chemistry, and how these parameters impact the safety of geological repositories for spent nuclear fuel. The data from each sub-project will be: 1) incorporated into modelling work in the safety assessments carried out by SKB, NWMO and Posiva; and 2) utilized by the researchers involved in the complementary sub-projects.*

1.1 Overview of the GAP sub-projects

Sub-project A (SPA): Ice sheet hydrology and subglacial groundwater formation

Sub-project A aims to improve the understanding of ice sheet hydrology (i.e. to assess how an ice sheet impacts groundwater circulation and chemistry in crystalline bedrock) up to, including, and beyond proposed repository depths. The data collected in SPA will be utilized in numerical ice sheet flow and hydrological modelling. SPA focuses on *indirect* observations of the properties of the basal hydrological system, and on what parts of the ice sheet that contribute water for groundwater infiltration. The latter includes quantification of ice sheet surface water production and how that water is routed from the ice sheet surface to its basal interface. This is achieved through remote-sensing, as well as direct measurements of vertical ice displacement and horizontal velocity fluctuation, and the determination of how these parameters vary in space and time under variable surface meltwater production and routing. Main activities within SPA involve 1) the installation and monitoring of GPS receivers and automatic weather stations on the ice sheet, and 2) air borne/ and ground-based radar studies.

SPA contributors: Alun Hubbard (sub-project manager, Aberystwyth University), Dirk van As (GEUS), Adam Booth (Swansea University), Richard Bates (St. Andrews University), Sam Doyle (Aberystwyth University), Christine Dow (Swansea University), Andrew Fitzpatrick (Aberystwyth University), Matt King (Newcastle University), Glenn Jones (Swansea University), Ian Joughin (University of Washington), Henry Patton (Aberystwyth University), Bernd Kulessa (Swansea University), Peter Nienow (Edinburgh University), Duncan Quincey (Aberystwyth University), Rickard Pettersson (Uppsala University), Katrin Lindbäck (Uppsala University), Christian Helanow (Stockholm University), Malin Johansson (Stockholm University), Jemma Wadham (Bristol University).

Sub-project B (SPB): Subglacial ice sheet hydrology

SPB, like SPA, aims at improving the understanding of ice sheet hydrology. SPB aims at collecting *direct* observations and measurements of the characteristics of the hydrological system at the base of the ice sheet. The data collected in SPB will be utilized in numerical ice sheet flow and hydrological modelling. The main activity for SPB is drilling through the ice sheet at a number of locations where the ice sheet has been found to be wet-based from the radar surveys in SPA. The purpose of the drilling and borehole monitoring installations is to observe water pressures at the interface between the ice and bedrock. In addition to the ice drilling, collection of remote sensing data of ice-sheet surface conditions are to be carried out. SPB is the core of the larger ice sheet hydrology and groundwater formation project (i.e. SPA and SPB combined) and will provide pioneering measurements of subglacial water pressures on a full ice sheet scale. This information will provide important input to the conceptualization of hydraulic gradients during glacial conditions for groundwater models applicable in Fennoscandia and Canada, including their spatial and temporal variation. Results from SPA are necessary for the selection of suitable drilling locations.

SPB contributors: Joel Harper (sub-project manager, University of Montana), Neil Humphrey (University of Wyoming), Jesse Johnson (University of Montana), Toby Meierbachtol (University of Montana), Douglas Brinkerhoff (University of Montana), Clair Landowski (University of Wyoming), Chris Cox (University of Wyoming), Luke Maddox (University of Wyoming), Erin Johnson (University of Montana).

Sub-project C (SPC): Bedrock drilling, hydrogeochemistry and hydrogeology

SPC aims at studying the penetration of glacial meltwater into the bedrock, groundwater flow dynamics, and the chemical composition of water when, and if, it reaches repository depth (around 500 m down in the bedrock). Main activities for SPC involve deep bedrock drilling in front of the ice sheet for subsequent down hole surveys and hydrogeological/hydrogeochemical instrumentation, sampling and monitoring. The deep drilling requires a detailed understanding of the geology of the area, including fracture frequencies and composition of rock types and hydrogeochemical information (i.e. chemistry of different water end-members). Before selecting a site for the deep drilling, test drilling of two shallow holes (100-300 meters) were carried out. In addition to providing important information on geology and hydrology, the test drilling has also given useful information on the permafrost extent. In order to study if taliks may act as discharge points for deep groundwater formed under the ice sheet, one of the test holes has been drilled into a presumed talik. Data from SPA, and understanding of the ice sheet hydrology, are necessary for proper selection of the drilling location of the deep borehole. Data on water formation and chemistry at the base of the ice sheet, collected as part of SPB, will be important when analyzing the results of SPC.

SPC contributors: Timo Ruskeeniemi (sub-project manager; Geological Survey of Finland), Jon Engström (Geological Survey of Finland), Emily Henkemans (University of Waterloo), Anne Lehtinen (Posiva), Jari-Jussi Ruskeeniemi (Aalto University), Ismo Aaltonen (Posiva), Lillemor Claesson Liljedahl (SKB), Shaun Frape (University of Waterloo), Dalton Hardisty (University of Indiana), Sarah Hirschorn (NWMO), Jennifer McKelvie (NWMO), Henrik Drake (Linnéuniversitetet), Eva-lena Tullborg (Terralogica), Tuomas Pere (Posiva), Michael Makahnouk (University of Waterloo), Knud Erik Klint (GEUS), Markku Paananen (Posiva), Karsten Pedersen (Micans AB).

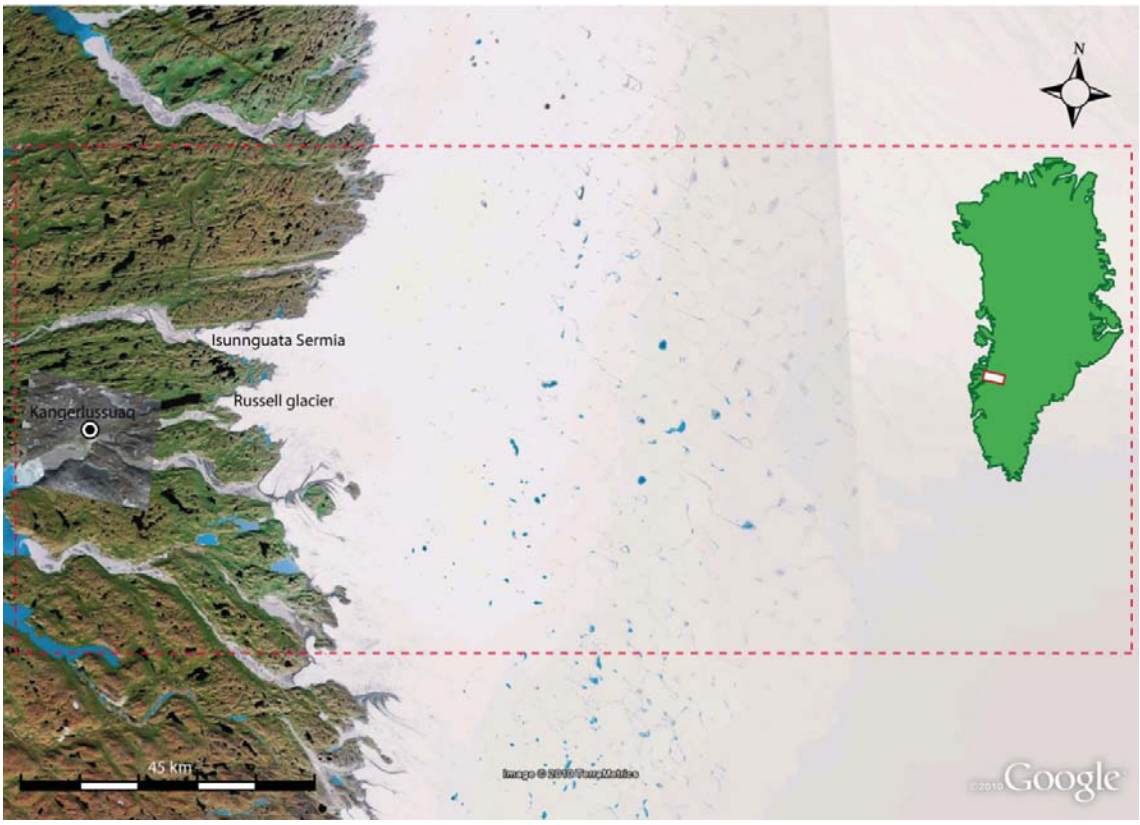

Figure 1-2. *The area within the red dashed rectangle represents the GAP field area, where the three sub-projects carry out field investigations and monitoring work. The green inset map shows Greenland; the location of the GAP is indicated by the white and red rectangle. © Google Earth.*

2 Sub-project A activities 2010

2.1 Introduction and objectives

The overall aim of the GAP project is to obtain an integrated understanding of the interactions between subglacial and bedrock hydrology and bedrock geochemistry under an active ice sheet. The main focus of sub-project A (SPA) are *indirect* observations of 1) the surface and subglacial properties and bed topography, 2) ice speeds and vertical displacement using fixed kinematic-(k)GPS stations, and 3) meltwater production across the ice surface of what we refer to as the wider Russell Glacier Catchment (Figure 2-1). These data sets are critical prerequisites for robust ice dynamics, or subglacial hydrological modelling efforts, and aid in the development of an integrated understanding of the interactions between the ice sheet hydrology, subglacial hydrology and subglacial/groundwater geochemistry.

A field team (Table 2-1) comprising of 4 to 12 persons (at any one time), worked continuously from early May through to August, and for 3 days in September, 2010, to establish and maintain long-term monitoring activities and apply a suite of geophysical techniques. In tandem, a remote-sensing acquisition and processing project was carried out to reveal macro-scale insights into ice sheet behavior.

Table 2-1. List of SPA field personnel during the 2010 campaign.

Person	Institution	Role
Dirk van As	GEUS	Glaciometeorology
Richard Bates	St Andrews University	Moulin access/Video/FA
Adam Booth	Swansea University	Active Seismics
Sam Doyle	Aberystwyth University	k-GPS & Hydrology
Christine Dow	Swansea University	Seismics & Hydrology
Andrew Fitzpatrick	AberystwythUniversity	Remote Sensing
Christian Henlow	Stockholm University	Field Assistant (FA)
Malin Johansson	Stockholm University	Remote Sensing
Matt King	Newcastle University	k-GPS
Glenn Jones	Swansea University	Passive Seismics
Ian Joughin	University of Washington	Remote Sensing
Bernd Kulessa	Swansea University	Seismics
Duncan Quincey	Aberystwyth University	Remote Sensing
Henry Patton	Aberystwyth University	FA/Moulin Access
Rickard Pettersson	Uppsala University	Radar
Jemma Wadham	Bristol University	Water Quality & Tracing

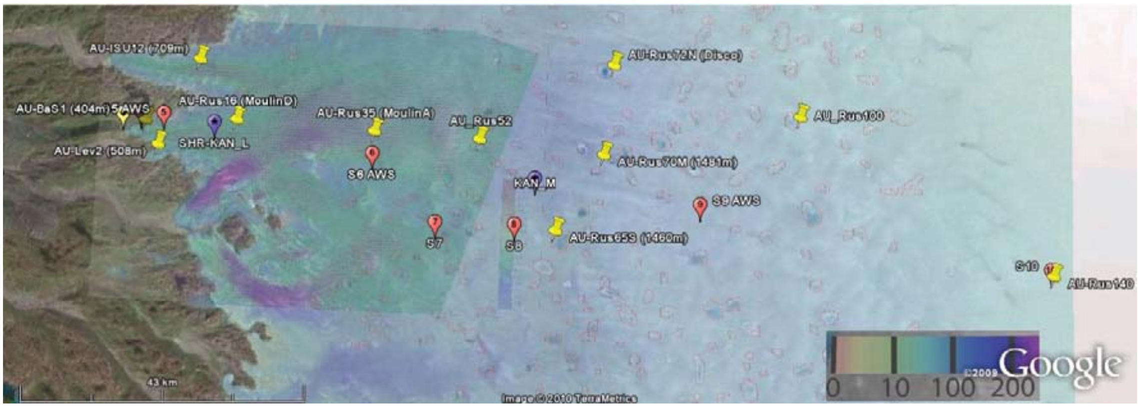

Figure 2-1. Location of stations comprising the Utrecht Univeristy (IMAU) 'K-transect' (red), geodetic-GPS and AWS (yellow) stations across Russell Glacier. Ice camps are located at Kan_M, AU-Rus65S and S9. SHR-KAN_L and KAN_M (purple) are automatic weather stations.

The spring campaign (delayed by ~4 weeks from early April due to flight disruptions resulting from the Icelandic volcanic ash cloud) was primarily concerned with the acquisition of deep-look (2Mhz) impulse radar profiles by snow-mobile, and the maintenance of Automatic Weather Station (AWS) and kGPS stations. The summer campaign focused on using geodetic and seismic (active and passive) techniques to quantify surface to basal coupling processes around 1) two supra-glacial lakes, 2) a presumed subglacial lake and 3) a large draining moulin system. The overall aim of these experiments is to investigate and quantify mechanical feedback(s) between surface and basal hydrodynamic coupling under the potential range of surface draining scenarios (i.e. rapid lake tapping, slow lake drainage via local tapping, and far field drainage via moulins). Three days in September were concerned with downloading AWS & kGPS stations, winterizing equipment, and preparing for 2011 work. SPA also provided scientific support for other major projects in the Russell Catchment region, including: radar; active seismics; and, a geodetic-GPS strain-network around two ESF funded Ice2Sea boreholes, which were drilled to a depth of 600m to the ice bed at SHR/KAN_L. SPA carried out a number of miscellaneous activities as well, including a self-potential study of the near ice/ snow surface, 50MHz ground penetrating radar surveys, and a terrestrial laser-scanning (TLS-LiDAR) survey of the proglacial bedrock zone and glacierer front at Russell.

2.2 Remote sensing

Acquisition of remotely sensed data continued throughout 2010, complimenting the existing data archive. This section briefly outlines additions to the database and some preliminary results, in addition to considering future data applications.

Landsat

Landsat7 carries the Enhanced Thematic Mapper Plus (ETM+) sensor and eight band multispectral scanning radiometer. ETM+ has a spectral range of 0.45-12.5 µm, with a 30 m multispectral resolution, and a 15 m panchromatic resolution captured within a 183 km wide swath. The sun-synchronous orbit of Landsat 7 allows repeat coverage every 16 days, so although it provides very high-resolution data, it is limited by temporal coverage. Scan line correction failure of the ETM+ sensor occurred in May 2003, causing all scenes since then to be missing data in strips across the images. Five scenes acquired in 2010 (31/05/10, 16/06/10, 02/07/10, 18/07/10 and 19/08/10) have been added to the existing archive, which extends back to 1999. The high resolution (15m panchromatic band) of Landsat7 data makes it useful for accurately mapping structural features and surface hydrology, in addition to planning potential locations for fieldwork surveys. The sequence of images from 2010 captured the lifecycle of two lakes (rapidly draining lake 'F', and slowly draining lake 'Z') within the Russell Glacier catchment that were surveyed in the 2010 field campaign (Figure 2-2).

MODIS

The Moderate-resolution Imaging Spectroradiometer (MODIS) on board the Terra satellite has a 2,330 km wide swath and high temporal resolution, providing images of the entire Earth every one to two days. The low and rapid orbit of this satellite yields high temporal resolution data, which allows for change detection monitoring in a variety of environments, and, in this study, is used to record the life cycle of supraglacial lakes within the Russell Glacier catchment. MODIS Level 1B products record calibrated and geolocated radiances in 36 spectral bands ranging in resolution from 250 m to 1 km. Scenes were georeferenced using MODIS Reprojection Tool-Swath, developed by the Land Processes Distributed Active Archive Centre (LP DAAC). A resolution sharpening and classification algorithm was applied to daily images using a remote sensing and GIS software library developed within the Institute of Geography and Earth Sciences at Aberystwyth University. 153 scenes (1st May–30th September) from 2010 were processed and 36% were excluded due to cloud cover. Previous studies have noted high reflectance values from band 3 (Blue), combined with low values of band 1 (Red) reflectance over supraglacial lakes (Box and Ski 2007). Using this information, supraglacial lakes were isolated and classified using a ratio of bands 1 and 3 (0.46-0.67µm) within an empirically determined threshold. Lake classification was carried out on a 7,000 km^2 area of the Greenland Ice Sheet covering the wider Russell Glacier catchment; the results of the classification are shown below (Figure 2-3).

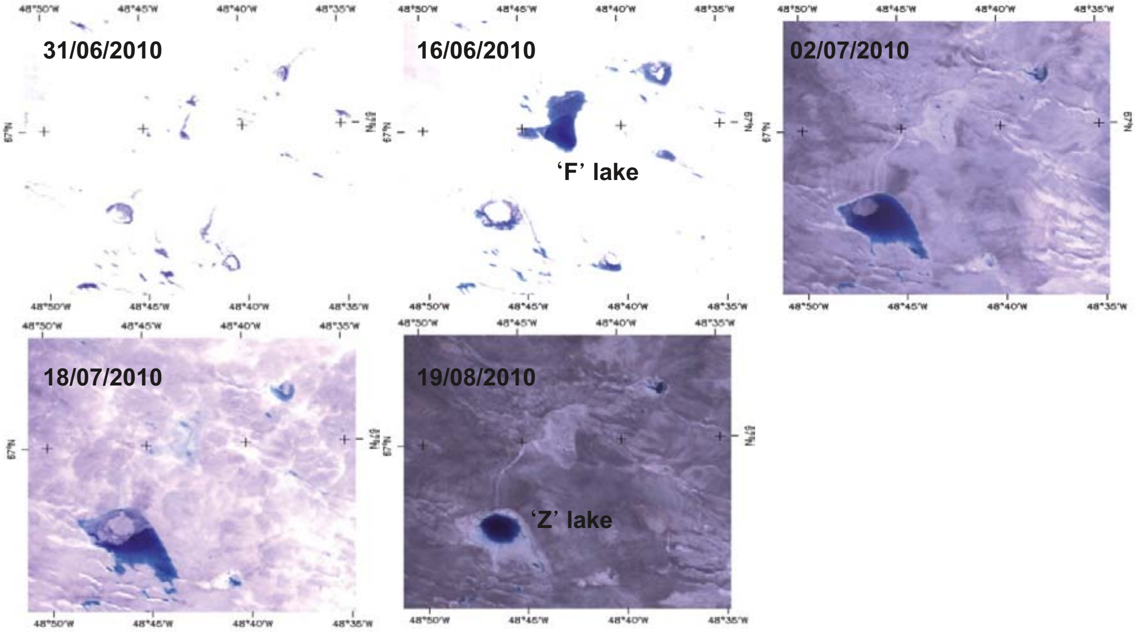

Figure 2-2. Sequence of Landsat images showing the rapid drainage of 'F' lake and the formation of 'Z' lake, followed by its slow drainage.

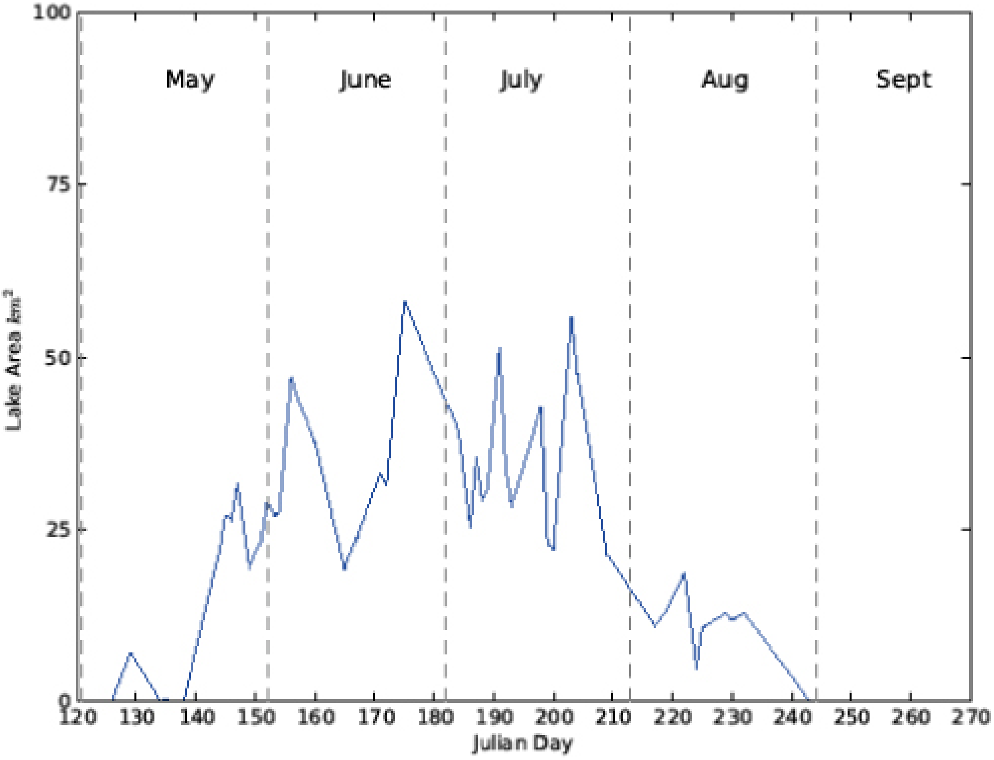

Figure 2-3. Changing supraglacial lake area from May to September within the Russell Glacier catchment.

The high temporal resolution of MODIS images provides a unique view for monitoring the evolution of supraglacial lakes throughout the melt season. Supraglacial lakes form and drain at progressively higher elevations as the melt season unfolds. Peaks in the graph (Figure 2.3) early in the season represent a number small lakes forming and draining rapidly. Peak lake area occurs in July, corresponding to peak melt rates. Large fluctuations in lake area are representative of rapid drainage of supraglacial lakes. Misclassification of pixels with similar spectral signatures to lakes, such as ice containing impurities and thin cloud cover, can result in lake area being overestimated in some scenes; however, this error can be reduced by optimizing the classification on an image-by image basis. Recent studies have shown that due to the sensitivity of visible red and NIR band reflectance to water, lake depth can be extracted from multispectral imagery (Sneed and Hamilton 2007, Box and Ski 2007). Previous studies have shown that lake bathymetry measurements conducted in the field can provide calibration for a lake depth retrieval expression based on surface reflectance. In July 2010, bathymetry measurements were taken following drainage of 'F' lake (Figure 2-4) by using GPS surveys, and from 'Z' lake using a depth sounder mounted on an inflatable boat. MODIS images taken immediately before lake drainage, prior to the GPS survey, provide calibration for a lake reflectance-depth function. Using 'F' and 'Z' lakes as calibration for the expression, future work will allow depth to be determined for individual MODIS pixels (0.0625 km^2). The reflectance-depth relationship will allow for the calculation of lake volume on a catchment-wide scale or on a lake-by-lake basis.

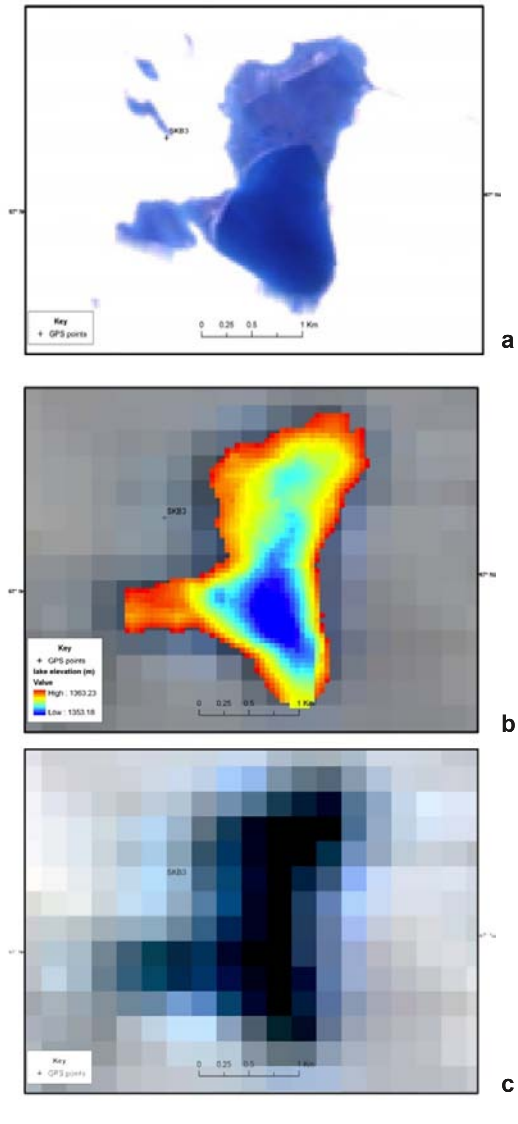

Figure 2-4. *'F' Lake shown in a) Landsat 7 image, b) lake bathymetry and c) 250 m resolution MODIS image.*

TerraSAR-X

Further TerraSAR-X derived velocity data across the wider Russell Glacier catchment has been acquired to complement the existing data set from 2009. Data were acquired in StripMap mode, producing scenes with a 3 m spatial resolution with swaths of 30 km by 50 km. In addition to the five overlapping (11 day repeat pairs) scenes acquired in 2009, 9 more scenes were obtained in 2010 (Table 2-2), with each scene covering an area of 3,047 km^2 (ice extent 2,400 km^2). Velocity data is derived from TerraSAR-X using a combination of conventional interferometry and speckle tracking techniques (Joughin 2002). Error margins for the velocity data was calculated to be 5 m/annum by measuring the average difference from zero of stationary (off-ice) areas in the images.

The velocity data from 2010 has much greater temporal coverage of the study area compared with 2009, which allows for improved analysis regarding the seasonal evolution of ice flow. At present, a number of scenes covering the glacier interior (descending passes) are missing because kGPS data are required for these scenes to provide ground control points. Preliminary results from the 2010 TerraSAR-X data set are shown in Figure 2-5.

The 2010 TerraSAR-X data indicate high surface velocities in the marginal zones at the beginning of the melt season. As the melt season progresses, there is a shift in the area of faster ice flow. Surface velocity decreases in the marginal zones, but increases at higher elevations. Velocity profiles from every month show a sharp increase in ice flow around 20 km (850 m elevation) from the ice margin. Above this, ice flow from the interior is divided between Isunngata Sermia, Russell Glacier, and an unnamed ice-fall to the South. When the full 2010 data set has been processed, comparisons can be made with the 2009 data. The comparison will yield insight into temporal velocity patterns, given the distinct differences in the relative strength of the temperature anomaly and concomitant melt delivery between the two years.

Table 2-2. Attributes of TerraSAR-X scenes acquired in 2010.

Imaging mode	Date	Aquisition Time	Path Direction	Beam ID	Relative orbit	Incidence angle (min)
StripMap (SM)	20/04/2010	20:49:10	Ascending	Strip_013	103	41.691812
StripMap (SM)	01/05/2010	09:57:16	Descending	Strip_009	96	34.007186
StripMap (SM)	01/05/2010	20:49:10	Ascending	Strip_013	103	41.698629
StripMap (SM)	14/06/2010	09:57:18	Descending	Strip_009	96	41.691398
StripMap (SM)	14/06/2010	20:49:12	Ascending	Strip_013	103	41.691812
StripMap (SM)	25/06/2010	09:57:18	Descending	Strip_009	96	34.013151
StripMap (SM)	25/06/2010	20:49:12	Ascending	Strip_013	103	34.011261
StripMap (SM)	06/07/2010	20:49:12	Ascending	Strip_013	103	41.691812
StripMap (SM)	30/08/2010	09:57:22	Descending	Strip_009	96	34.010786
StripMap (SM)	30/08/2010	20:49:16	Ascending	Strip_013	103	41.698629
StripMap (SM)	24/10/2010	09:57:23	Descending	Strip_009	96	34.015387
StripMap (SM)	24/10/2010	20:49:17	Ascending	Strip_013	103	41.691812
StripMap (SM)	04/11/2010	20:49:17	Ascending	Strip_013	103	41.691398
StripMap (SM)	15/11/2010	09:57:23	Descending	Strip_009	96	34.015387
StripMap (SM)	15/11/2010	20:49:16	Ascending	Strip_013	103	41.698629

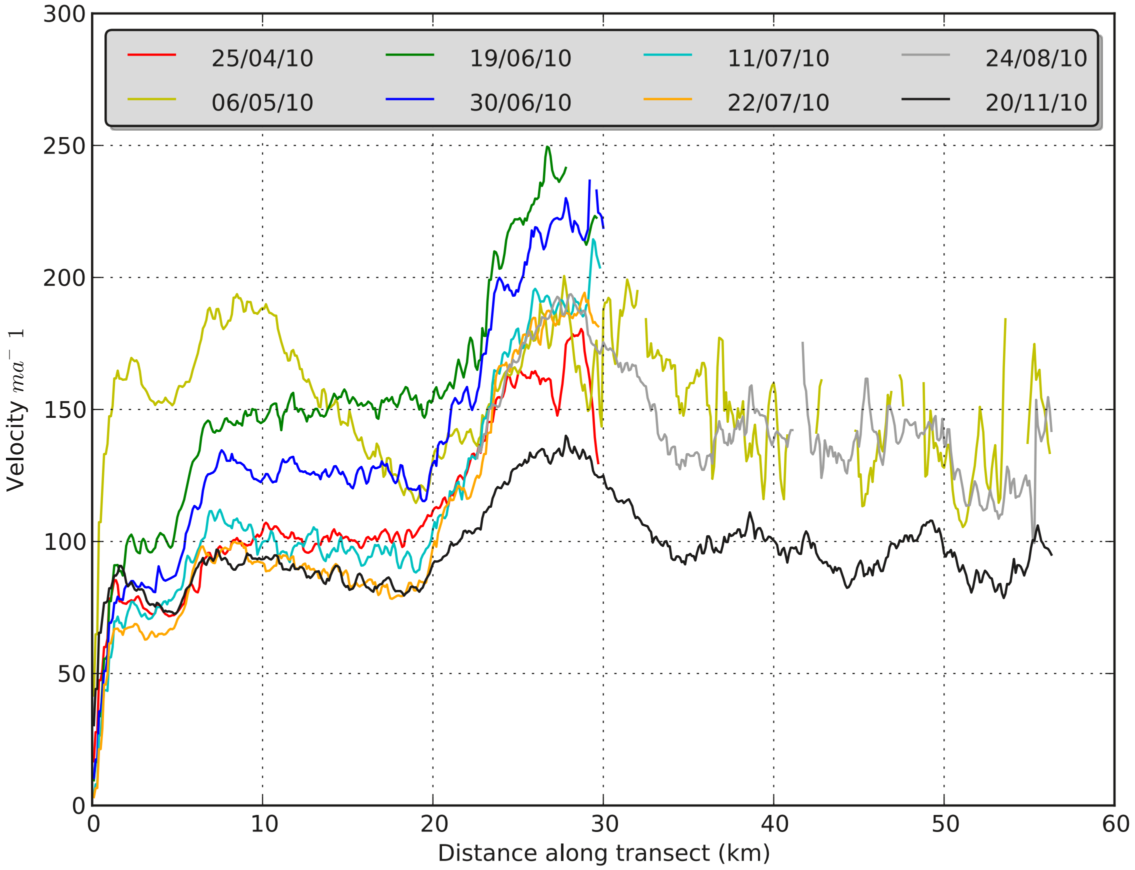

Figure 2-5. *Preliminary 2010 TerraSAR-X results illustrating the change in surface velocity along a transect through Russell Glacier.*

Feature Mapping

Using 2010 Landsat7 scenes as a base map, the predominant surface features within the Russell Glacier catchment were identified and digitized (Figure 2-6). Flowlines and the orientation of foliation correspond well with fast flow zones (summer 2009 TerraSAR-X velocity data). Large transverse crevasses occur 1) at the glacier margins and in zones of slow moving ice, 2) between individual flow units and most notably 3) 25 km from the ice sheet margin, which are thought to be due to the presence of a large bedrock undulation.

Hydrological mapping was conducted based on a 40 m resolution Digital Elevation Model (DEM) derived from SPOT 2008 data. ArcMap's hydrological mapping tool was used to calculate flow direction and accumulation based on surface slope. Dendritic surface drainage patterns were simulated by ArcINFO hydrological catchment tools, which correspond nicely with streams mapped manually based on Landsat, TerraSAR-X and on the ground using roving GPS. The hydrological modelling toolbox also simulates the location of localized sinks (shown as red polygons in Figure 2-6), which represent the location of moulins or lakes on the Ice Sheet surface. These locations correspond well with positions of lakes and moulins mapped in the field and from MODIS/SPOT/Landsat images.

Using hydrological modelling tools in ArcGIS the watersheds of individual catchments on the ice sheet surface can be defined. Knowledge of catchment area, and of supraglacial routing of water feeding individual lakes and moulins, combined with the MODIS database of lake drainage lines and volumes, provides valuable information regarding the input of meltwater into the englacial and subglacial systems. Integration of the localized short-term velocity fluctuations recorded from the kGPS network and the surface flow routing enables the subglacial tracking of meltwater inputs from individual catastrophic lake drainage events.

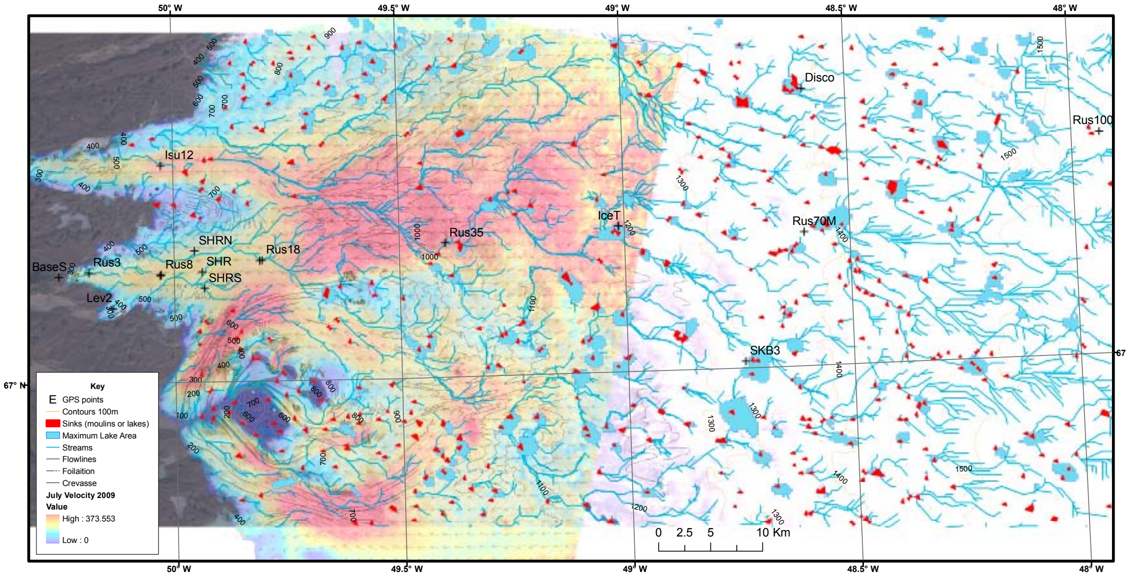

Figure 2-6. *Map of Russell Glacier catchment highlighting the main surface features, surface flow velocities, flow patterns and drainage routes. Also shown are GPS points situated along the K-transect.*

2.3 Meteorology, climate and surface melt / run off

GAP financed three automatic weather stations (AWS) that were installed by Dirk van As at different elevations on the ice sheet in September 2008 and April 2009 (see Table 2-3 for details). The lower station is positioned at 680m asl, near the ice margin in the ablation zone; the middle station is at 1,270 m asl in the upper ablation zone near the equilibrium line altitude; and the upper station is placed well into the accumulation zone at 1,850 m. The AWS measure barometric pressure, air temperature, humidity, wind speed and direction, solar and terrestrial radiation (vertical components), snow accumulation, ablation, subsurface temperatures down to 10m, GPS position, and a number of diagnostic parameters such as battery voltage, station tilt and the current drawn by the ventilator in the radiation shield of the temperature and humidity assembly. Measurements undergo a ten-minute cycle and all data is stored locally. GPS measurements follow the transmission schedule. Hourly averaged data are transmitted by Iridium satellite link between mid-April to end of October (days 100–300 in the calendar year), and daily averages are transmitted during the remaining days of the year when solar power is not sufficient to recharge the batteries.

The surface meltwater production in the Russell Glacier catchment area is calculated using AWS measurements as input for a surface energy balance model. Barometric pressure, temperature, humidity, wind speed, and the incoming radiation components are required to calculate the separate energy fluxes between the atmosphere and ice sheet surface. Any surplus of energy is either used for the heating of the near-surface snow and ice layers, or is consumed by melting. In order to calculate spatially distributed surface melt over Russell Glacier catchment, an interpolation scheme is required to distribute the measured variables. Because surface albedo is highly variable, both spatially and temporally, a dominant parameter for surface meltwater production (satellite (MODIS) derived albedo, calibrated by local AWS measurements) is used. Validation of model calculation is conducted at the AWS sites by comparing modelled and measured ablation. Finally, the computed run-off is compared to the discharge measured at the bridge over the proglacial Watson River in Kangerlussuaq.

Table 2-3. AWS metadata. KAN_L is the lower station, KAN_M denotes middle station and KAN_U the uppermost station.

Station name	Latitude (ºN)	Longitude (ºW)	Elevation a.s.l. (m)	Placement date	Date last maintenance visit
KAN_L	67.097	49.933	680	1/9/2008	16/5/2010
KAN_M	67.066	48.818	1,270	2/9/2008	15/5/2010
KAN_U	67.000	47.017	1,850	4/4/2009	16/5/2010

Fieldwork

A spring fieldwork campaign, involving maintenance and data readout, was carried out in May 2010. The field camp was erected next to KAN_M on 10 May (Figure 2-7), facilitating thorough maintenance and side-projects, such as determining snow density from a snow pit and taking time-lapse imagery over a multi-day period. The lower station maintenance was performed over two days, 15 and 16 May, and also involved the installation of the time-lapse camera (to be removed in 2011). The upper station was also serviced on 16 May. Both KAN_L and KAN_U were visited by helicopter due to the crevassed terrain, and large distance between camp and station, respectively. All three stations have been worked according to specification since installation. An inclinometer had broken and was replaced on the upper station, but for the other two the work consisted of standard minimal maintenance. The sonic ranger membranes, hygroclips and flash cards were exchanged, stakes were re-drilled, new thermistor strings were drilled in, desiccant packs in logger enclosure and battery box were replaced, new logger software was uploaded, and a general systems check-up took place.

AWS Observations

Data coverage of primary variables is 100% since the installation of all three AWS. Figures 2-8 to 2-14 indicate the daily-mean values of those variables. Transmitted data was added to the data series to cover the summer of 2010 also. Figure 2-8 shows air pressure. Correlation between the three measurement series is high since air pressure varies more temporally than spatially. Air pressure is in general higher in summer, but because it is more variable in winter the highest value was measured in winter, on 3 January 2010.

The amplitude of the annual cycle in temperature is about 20ºC (Figure 2-9). Temperature decreases with elevation with a relatively constant lapse rate (e.g. –5.3°C/km in summer). As with air pressure, the largest variability occurs in winter. In summer, temperatures are a few degrees above freezing. The presence of the melting surface prohibits the near-surface atmosphere to follow free-atmospheric temperatures, which can exceed 20ºC for the continental climate of Kangerlussuaq. The temperature over the ice sheet shows higher values for much of 2010 than for 2009. For instance, the lowest daily-mean temperature occurred at KAN_M in 2009 (–36.7ºC on 4 February), not at the higher placed KAN_U that was erected shortly after. The last decade has been warm in Greenland, and globally, but especially high temperatures were noted in 2010, representing the warmest year on record for most of Greenland. Whereas the mean annual temperature in the town of Kangerlussuaq since 1974

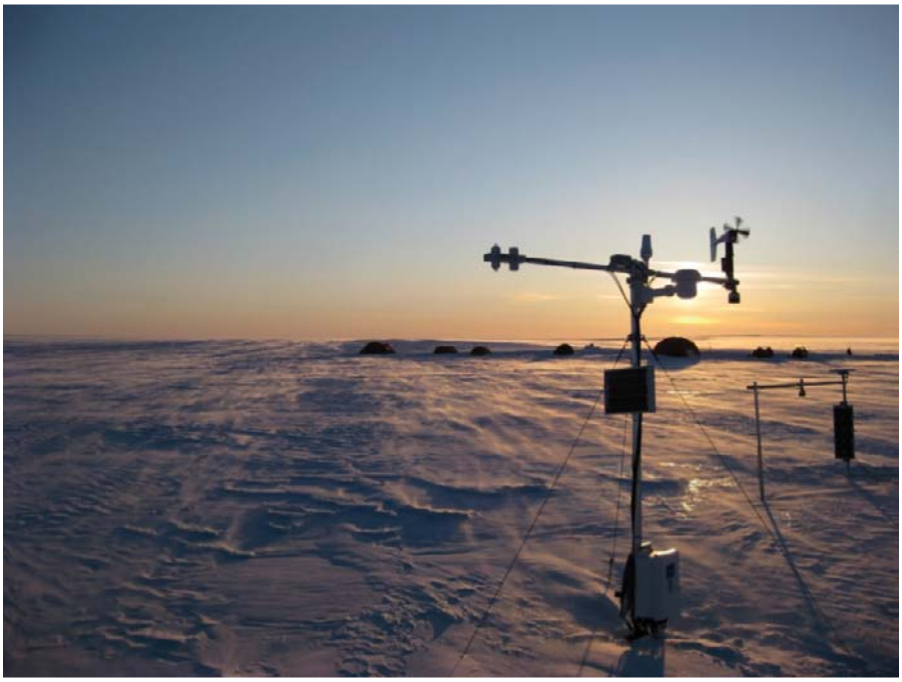

Figure 2-7. *Weather station KAN_M and camp on May 14th, 2010. Photo by Dirk van As.*

has a value of –5.0°C, the 2010 average was –0.1°C, exceeding both the second (2005) and third (2003) warmest years by 2.5°C. Uniquely, all months in 2010 displayed above-average temperatures. January, February, November and December exceeded the monthly average by 7–11°C. The months May, August, and December are the warmest of these particular months in the entire 37-year period of measurements in Kangerlussuaq. Similarly, April, September, and November 2010 are among the warmest three of these months in the whole time series. This is contrasted with 2009 data, in which the annual-mean temperature of –4.7°C was a mere 0.3°C above the 1974–2010 average in Kangerlussuaq. During the months April to August, 2009, mean temperature departed less than 0.8°C from their long-term averages.

Relative humidity (Figure 2-10) typically increases with decreasing temperatures, so humidity is higher in winter than in summer, and increases with elevation. This is because warmer air can hold more water vapour. Nonetheless, relative humidity is generally high due to the presence of a snow or ice surface. Only at KAN_L were values below 50% recorded, partly due to the proximity of the dry tundra. At KAN-L, near-saturation only occurs in winter months. Also wind speed is higher in winter and at higher elevation (Figure 2-11). High wintertime wind speeds are due to the more frequent occurrence of low-pressure systems passing. Also, the radiative cooling of the surface in winter produces a deeper atmospheric inversion layer, producing stronger gravity-driven katabatic winds. The ever-present katabatic forcing can be recognized in the year-round non-zero wind speed. The strongest winds during the measurement period were recorded on 14 December 2009, when the daily-mean speed at KAN_U reached 25.7 m/s.

Russell Glacier, positioned just north of the polar circle, experiences a short period of midnight sun in summer and polar night in winter (Figure 2-12). Daily-mean radiative fluxes of incoming solar radiation in summer exceed 400 W/m^2. Observed values are similar at the three AWS. Incoming solar radiation is commonly lowest at KAN_U, mostly due to the more frequent presence of clouds. Clouds can also be recognized from the down-welling longwave radiation record (Figure 2-13), because cloudy skies have a higher emissivity than clear skies, and clouds over ice sheets often cause higher temperatures (i.e. the radiation paradox). The distinct annual cycle in Figure 2-13 is a consequence of the atmospheric temperature cycle, because a colder/warmer atmosphere emits smaller/larger amounts of longwave radiation. Measurements of accumulation and ablation in Figure 2-14show that the surface mass budget in 2010 was lower than in 2009 due to the higher temperatures. At KAN_L, nearly 4 m of ice ablated in the summer of 2009, while more than 5 m ablated in 2010. Whereas the mass budget at KAN_M was in near-balance in 2009, about 2 m ablated in 2010. Even at KAN_U, far into the accumulation zone, the surface lowered in 2010 due to melt exceeding the wintertime precipitation. However, this should not be interpreted as net ablation because the meltwater will have refrozen in the snow pack. Finally, note that very little or no snow accumulates in the lower regions of Russell Glacier in winter.

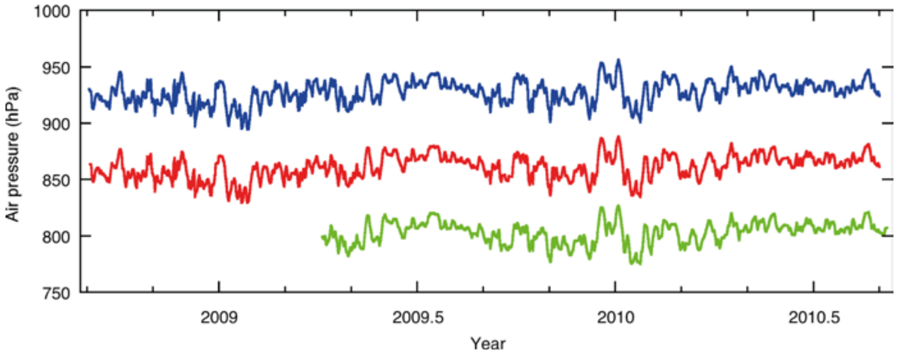

Figure 2-8. *Daily mean values of air pressure at KAN_L (blue), KAN_M (red), and KAN_U (green).*

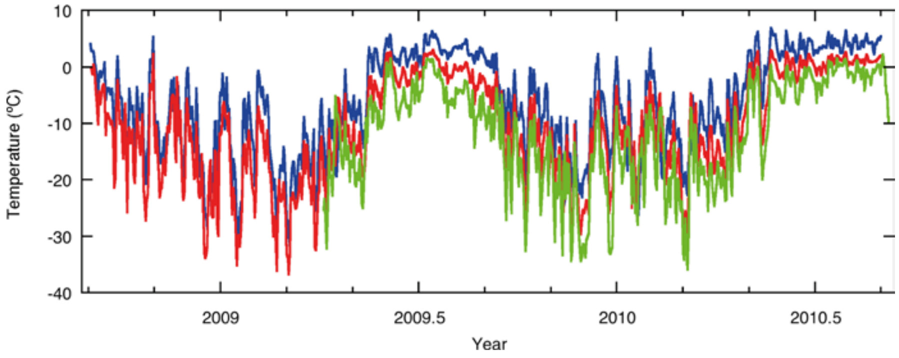

Figure 2-9. Daily mean values of air temperature at KAN_L (blue), KAN_M (red), and KAN_U (green).

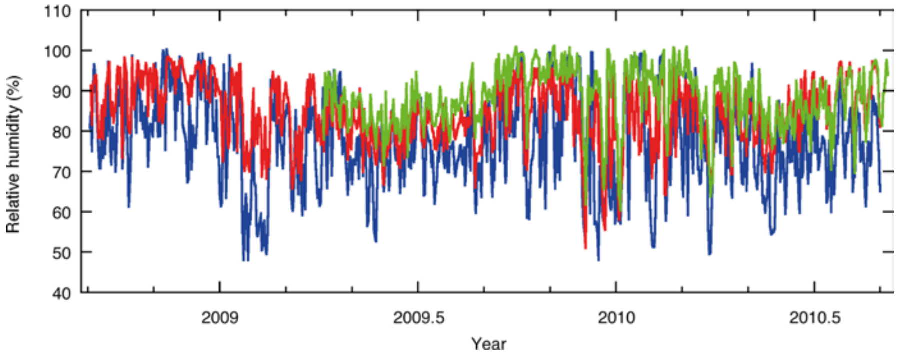

Figure 2-10. Daily mean values of relative humidity at KAN_L (blue), KAN_M (red), and KAN_U (green).

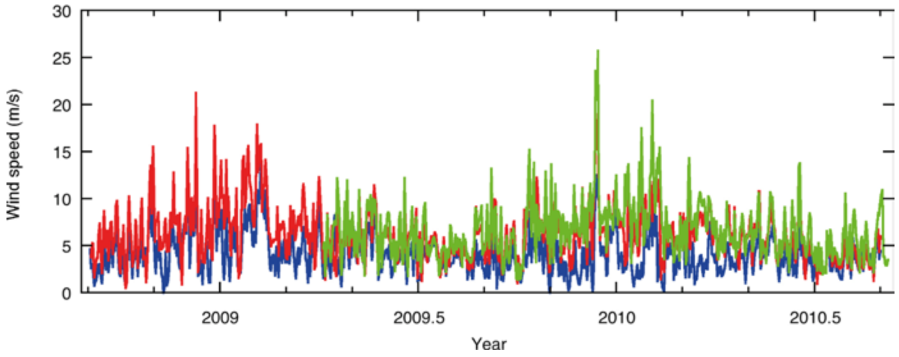

Figure 2-11. Daily mean values of wind speed at KAN_L (blue), KAN_M (red), and KAN_U (green).

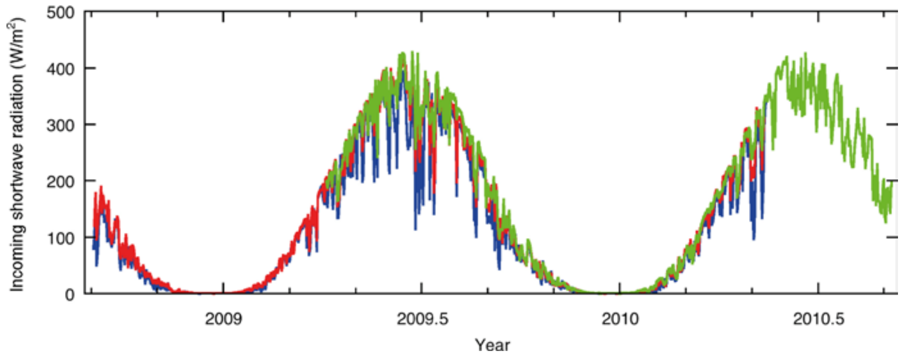

Figure 2-12. Daily mean values of incoming shortwave radiation at KAN_L (blue), KAN_M (red), and KAN_U (green).

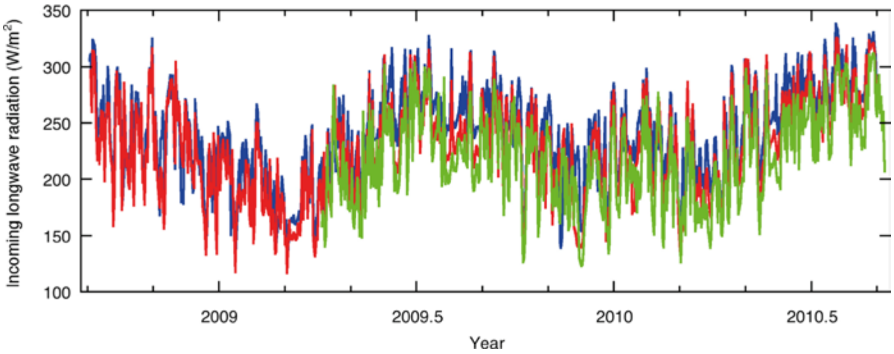

Figure 2-13. *Daily mean values of incoming longwave radiation at KAN_L (blue), KAN_M (red), and KAN_U (green).*

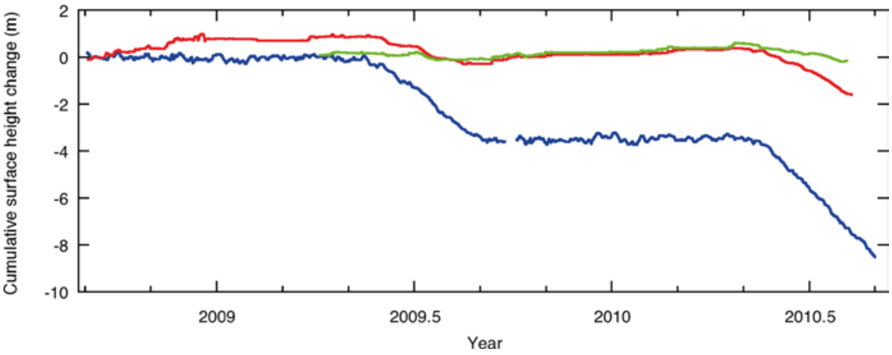

Figure 2-14. *Cumulative surface height change due to accumulation and ablation at KAN_L (blue), KAN_M (red), and KAN_U (green).*

Melt Modelling

The results of interpolating the above-mentioned measurements over the entire catchment area, and running a surface energy balance model for 100m elevation bins, are shown in Figure 2-15 for 2009 and 2010. The black lines give summer temperatures. Note that also over the ice sheet temperatures were considerably higher in 2010 than in 'normal year' 2009. Near the ice sheet margin, 2010 summer temperature exceed the average value from the previous year by 2°C, but at the top of the transect the difference is 4°C. In the lower regions, where summer melting occurs frequently and where near-surface temperature is bound by the 0°C boundary condition of the ice surface, the temperature cannot follow the atmospheric temperature freely. In higher regions, where sub-freezing temperatures are common, there is more freedom for near-surface temperatures to increase. The higher temperatures in 2010 are reflected in the calculated surface mass balance in Figure 2-15. At the lowest elevations of the glacier (which have only a small surface area), the net ablation is 6 m of ice in both years. With increasing elevation the difference between the years increases, and especially the relative difference is large for the upper ablation zone (1,000-1,500 m). Averaged over all elevations, surface ablation in 2010 was 70% larger than in the previous year. However, because the ice sheet surface becomes less steep with elevation, the relative contribution of the upper ablation zone to the 2010 melt excess is large. The total freshwater volume that ran off the ice sheet was 170% larger in 2009 than that recorded in 2010.

Freshwater run-off equals surface melt minus the water retained/refrozen in the snow pack above the snow line. The result of multiplying the calculated run-off with the surface area of the elevation bins is shown in Figure 2-16 for 2009 and 2010. The run-off is compared to the discharge measured at the proglacial river in Kangerlussuaq (by Bent Hasholt and Andreas B. Mikkelsen of Copenhagen University). There is an excellent quantitative agreement between the calculated and measured values, giving confidence in the model output. It should be noted that the surface run-off is more variable as atmospheric conditions differ from day to day; the discharge measurements indicate that the internal drainage system of the ice sheet removes the peaks because it cannot accommodate the

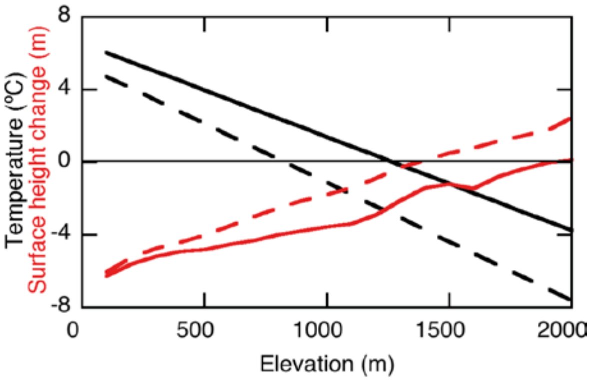

Figure 2-15. *Mean annual temperature (black) and surface height change due to ablation/accumulation (red) versus elevation over the Russell Glacier catchment. Dashed lines are for 2009, solid lines for 2010.*

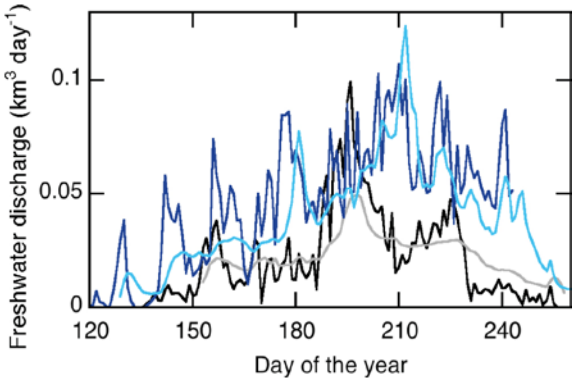

Figure 2-16. *Meltwater runoff from the Russell Glacier catchment (including the three glaciers directly south of Russell) from model calculations (dark blue) and measurements at the bridge over the Watson River in Kangerlussuaq (light blue) for 2009 (black and grey) and 2010 (blue).*

large amounts of meltwater. In the beginning of the melt season, when the drainage channels within and underneath the ice are still being developed by the increasing water pressure, the transit time of water from the ice sheet surface to the melt river is up to a few days. Near the end of the melt season, when the channels are larger than is needed to drain the surface meltwater, the peaks in meltwater run-off at opposite ends of the glacier's drainage system are more closely timed. These results are supported by AWS data from the Institute for Marine and Atmospheric Research in Utrecht (IMAU), the Netherlands, who have been active in the study region since the early 1990s (van den Broeke et al. 2011).

2.4 Ice dynamics and kinematic-GPS

Fieldwork

Table 2-4 presents the GPS data statistics for 2010. All existing kinematic (k) GPS stations were visited in May 2010. S10 (s10a), SKB1 (skb1), SKB3 (skb3) and Disco (disc) were serviced (SKB1 and SKB3 had stopped due to start-up issues, see section: Practical issues of continuous GPS operation).

Table 2-4. Summary of kGPS data collected in 2010.

	2010											
	J	F	M	A	M	J	J	A	S	O	N	D
base	🟩	🟩	🟩	🟩	🟩	🟩	🟩	🟩				
kely	🟩	🟩	🟩	🟩	🟩	🟩	🟩	🟩	🟩	🟩	🟩	🟩
skb3		🟦	🟦	🟦	🟦	🟦	🟦	🟦				
disc	🟦	🟦	🟦	🟦	🟦	Removed by third party						
sudd							🟦	🟦				
nord							🟦	🟦				
east							🟦	🟦				
isum	Installed 31st May 2010: Not serviced											
skb1	Serviced 18th May 2010: Not serviced											
s4aa	Installed/repaired 31st May 2010				Not serviced							
s10a		🟦	🟦	🟦	🟦	🟦						
skb4	Serviced 31st May 2010: Not serviced											
shrr				🟦	🟦	🟦	🟦	🟦				
shrn							🟦					
shrs							🟦					
shre				🟦	🟦	🟦	🟦	🟦				
shrw				🟦	🟦	🟦	🟦	🟦				
blow	Installed 26th July 2010											
moul	Installed May 2010											
zlak	Installed 28th July 2010											

The kGPS and Hobo-AWS at L8D (l8dd) was removed and a kGPS was installed at Isunngata Sermia (isum). kGPS at S4 (s4aa) and SKB4 (skb4) were repaired. Five kGPS were installed in a strain diamond at SHR (shrr, shrn, shre, shrw, shrs). Ice-T kGPS (icet) was reinstated upglacier of a large supraglacial lake and where gf15 was sited in 2009. A GPS was installed at a moulin west of Lake Ice-T (moul) that formerly drained the lake together with the short-term deployment of a passive seismometer. The base station installed on bedrock overlooking Russell Glacier front was serviced, downloaded and the Trimble R7 receiver was replaced with a Trimble NetRS, which is more flexible for programming and better suited to long term base-station monitoring. In June 2010, three additional kGPS were installed around the lake adjacent to SKB3 in a strain diamond array to monitor the expected rapid drainage of the supra-glacial lake that was identified in 2009 (sudd, nord, east). Additionally, passive seismic, and lake level monitoring equipment was deployed. A kGPS station was also installed at Z-Lake (zlak), and at the large moulin (blow) that drains Z-Lake, to complement the active and passive seismic experiment investigating diurnal changes in subglacial hydrology.

Practical Issues of Continuous kGPS Operation

Over winter it is expected that the kGPS receivers will turn off for a short-period when there is insufficient sunlight reaching the solar panels to charge the batteries. To prevent this, vertical wind generators were installed on over-wintering GPS, but due to long periods of relative calm, windvane icing, and other cold issues, there often is insufficient power to maintain operation of the receivers for the entire winter. All kGPS receivers have a start up feature where they automatically turn on and log data when a critical voltage is attained. Unfortunately, the startup and shutdown voltages vary between receivers and even between the same models of receiver. Some receivers have suitable startup voltages (Table 2-5). Trimble 5700 Continuous Operating Reference Station (CORS), for example, startup at 12.0 V and shutdown at 11 V and Trimble Net-RS receivers have user- programmable startup/shutdown voltages. Other receivers do not have suitable startup/shutdown voltages (e.g. Trimble R7/5700 non-CORS startup at 15 V and shutdown at 11 V). To ensure continuous operation on the ice, each receiver was bench-tested at the AU cold-lab to determine what voltage was required for the receiver to start-up. The Leica 1200 has been used infrequently, and only during the summer months, and as of yet has not been bench-tested.

Table 2-5. Receiver models and power characteristics.

Receiver model	Start-up (V)	Shutdown (V)	Power (W)
Trimble 5700 (CORS)	12.0	11.0	2.5*1
Trimble 5700 (non-CORS)	15.0	11.0	3.3
Trimble NetRS (User-programmable)	11.5*2	10.5*2	4.0*1
Leica System 500 (Mains Power Option)	12.0	< 5.0	5.6
Leica System 500 (Battery Power Option)	14.0	10.2	5.6
Leica 1200	n.d	n.d	3.2*1

*1 This is the stated power consumption – values for other receivers are tested. *2 The startup and shutdown voltages for the Trimble NetRS.

A circuit has been designed and built to power Trimble 5700 (non-CORS) and Leica System 500 receivers, by providing a regulated 15.6V DC output. To protect the batteries from deep discharge, the circuit is designed with a low disconnect voltage of 10.5 V and a startup voltage of 11.5 V. The power circuit was tested with a non-CORS Trimble 5700 in the AU Cold Laboratory. The receiver started up after 20 hours at –17° C without issue. The circuits will be installed in all permanent kGPS stations over Russell Glacier catchment in 2011.

Results

The margin of the Greenland Ice Sheet experiences strong (50–100%) diurnal variation in ice velocity, which is directly coupled to surface melt (Shepherd et al. 2009). The extent to which this melt-forcing of ice velocity extends inland is currently unknown. The velocity of S4 GPS located 2.5 km from the terminus of Russell Glacier shows good correlation with the temperature record from the GPS base station located 2.7 km away (Figure 2-17 and Figure 2-18).

Figure 2-18 indicates an average lag time of 4 hours between peak temperature at the GPS base station at 15:00 UTC and peak S4 GPS surface velocity at 19:00 UTC in June 2010. This short-period diurnal melt forcing of glacier velocity results in longer-period intra- and inter-annular variations in ice velocity (Figure 2-19 to Figure 2-23; Zwally et al. 2002, Joughin et al. 2008). Initial analysis of GPS data sets suggests that long period variations in ice velocity propagate somewhere between 70 km and 150 km inland. SKB3 kGPS located 70 km inland shows a summer-time increase (+ 10 m/yr) in velocity. S10 GPS, located at KAN-U AWS 150 km inland, shows negligible intra and interannular variability, and potentially represents a dynamic control. Superimposed on these periods of variation are transient accelerations resulting from the rapid drainage of supraglacial lakes, evident in the GPS records from SKB3 (Figure 2-22) and also multiple drainage events recorded at Ice-T (Figure 2-23). Summer velocities at Ice-T are relatively high at ~150 m/yr. Inter annular variations should be interpreted with care as the dates used to calculate the velocity vary due to the availability of data. The timing of the melt season also varies year by year. SKB3 shows a seasonal variability in speed from stable winter velocities of 83 m/yr and a summer time acceleration of 10–20 m/yr. The speeds for Summer 2009 and Summer 2010 were calculated from intervals that ended 3 days after the lake at SKB3 drained rapidly.

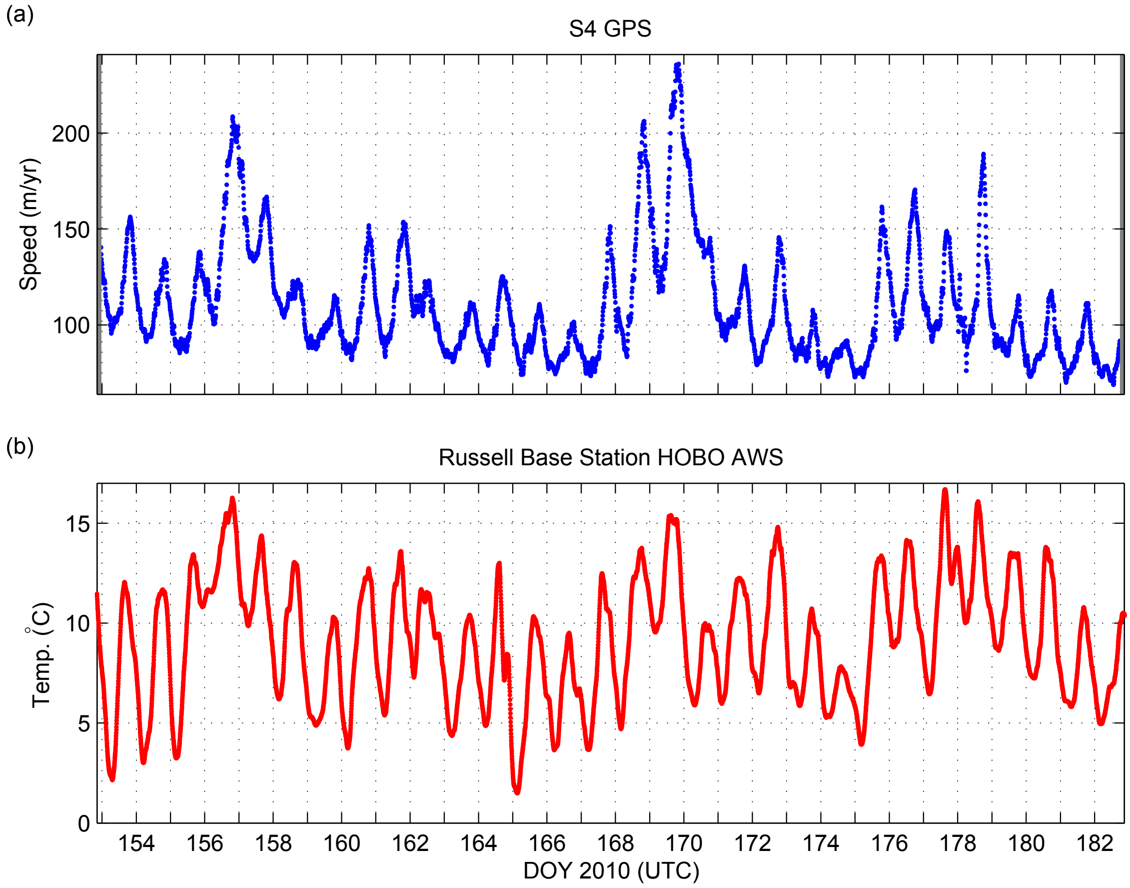

Figure 2-17. *Time series of a) ice surface speed at S4 GPS with a 3-hour moving average, and b) air temperature recorded at Russell Base Station for the month of June, 2010.*

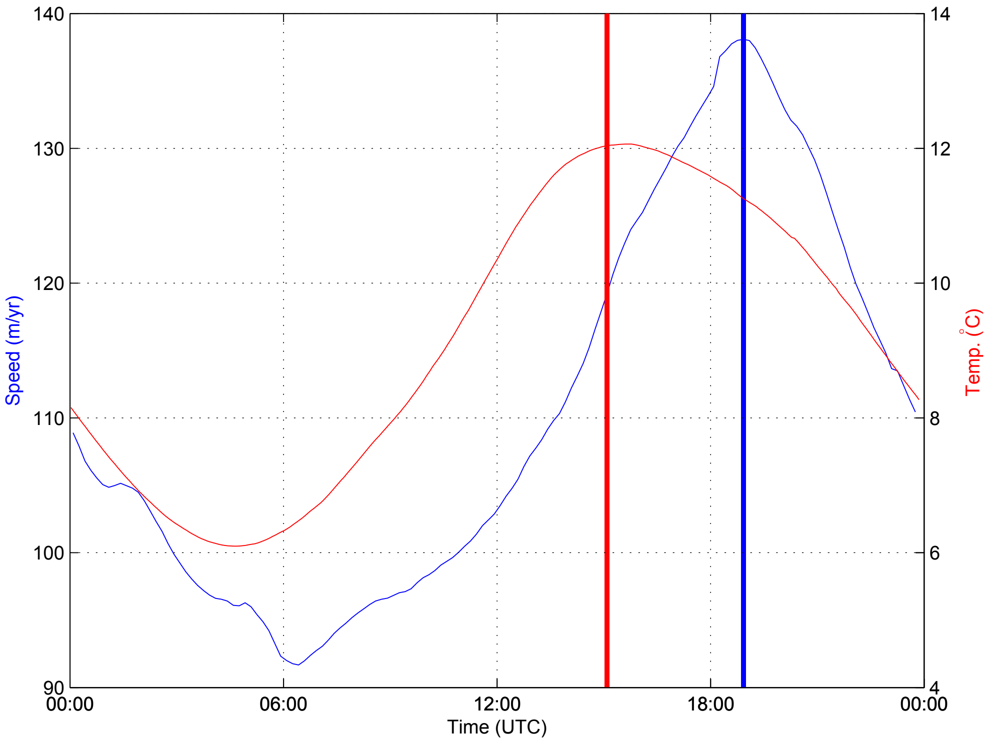

Figure 2-18. *Mean daily surface speed (m/yr) and air temperature at SHR in June, 2010. Red and blue bars indicate timing of peak air temperature and ice speed, respectively, indicating a ca. 4 hour phase lag between them.*

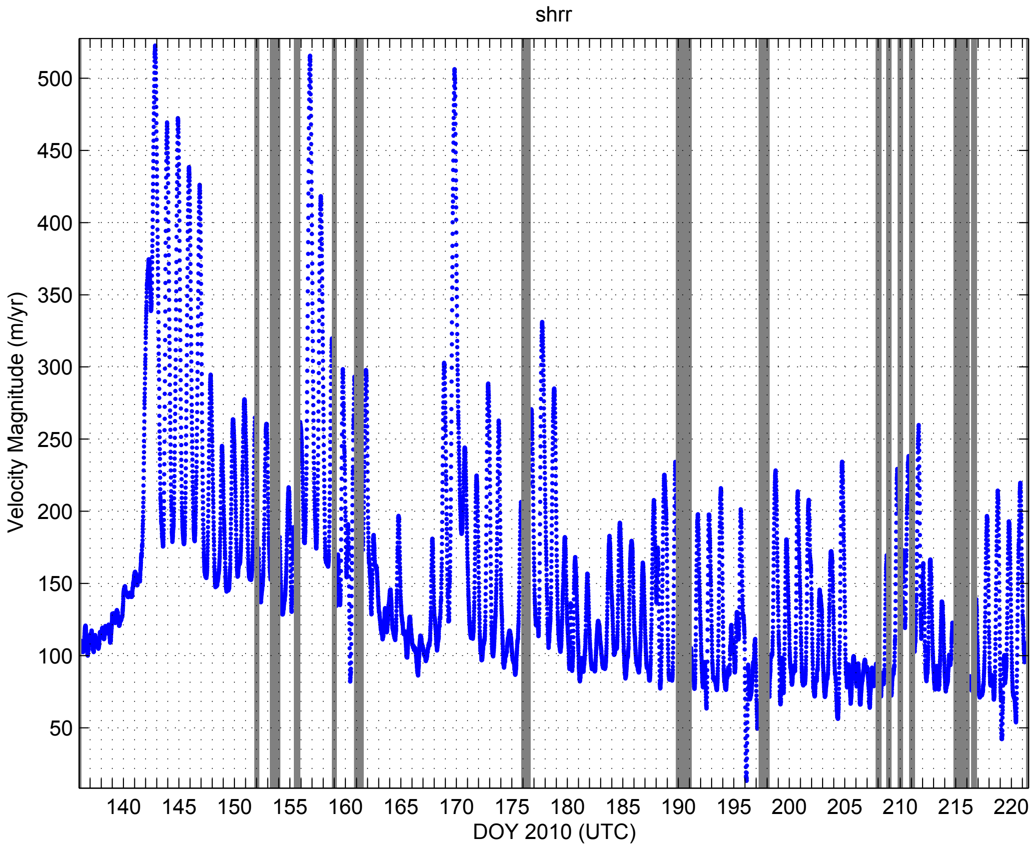

Figure 2-19. *The diurnal and seasonal evolution of ice surface speed at SHRR between 16May, 2010 (DOY 136) and the 9 August, 2010 (DOY 221), filtered with a 3-hour moving average. Shaded grey bars represent gaps in the processed data.*

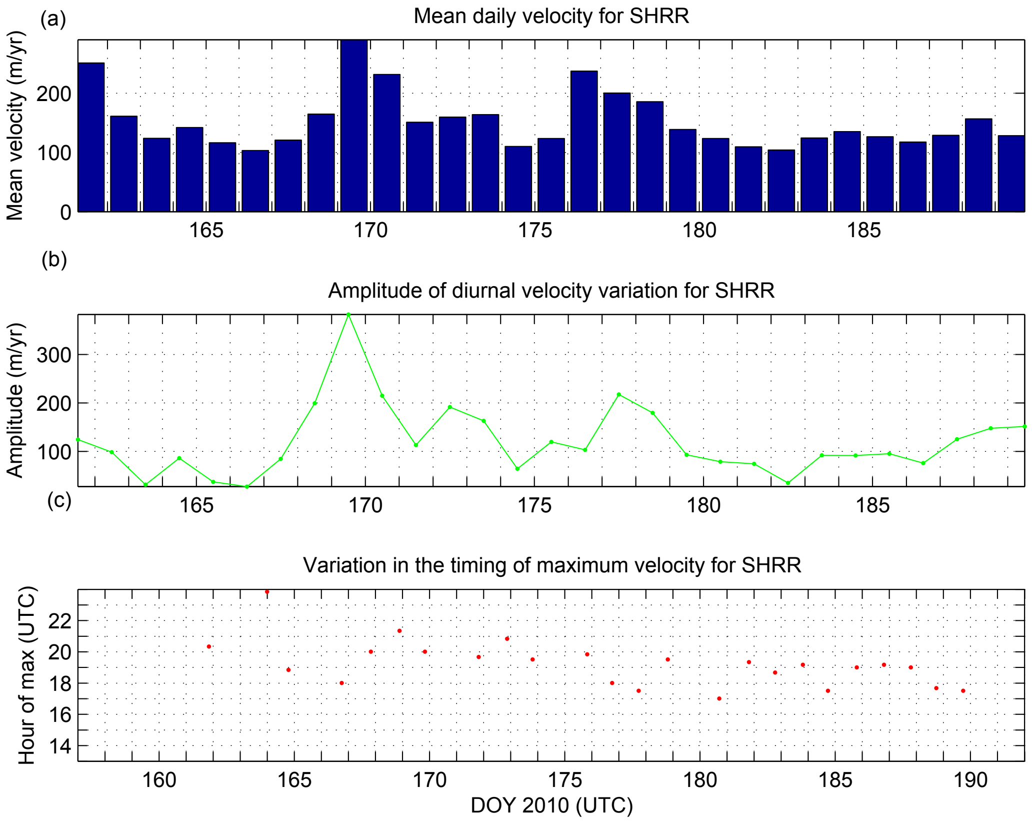

Figure 2-20. *Time series of mean daily ice surface velocity, the amplitude (difference between min and max) of the diurnal variability, and the timing of peak speed at SHR (UTC).*

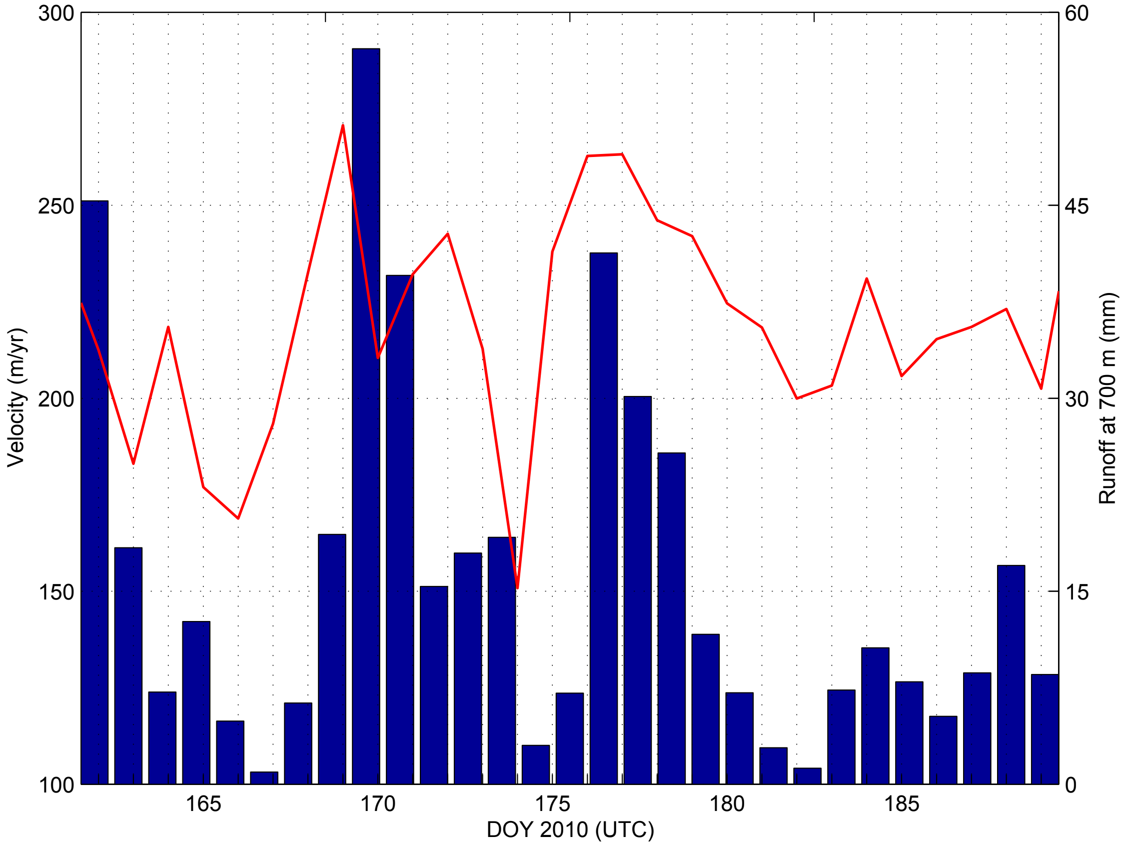

Figure 2-21. *Mean daily velocity (blue) at SHR GPS plotted together with mean daily runoff (red). Runoff calculated from the GEUS model.*

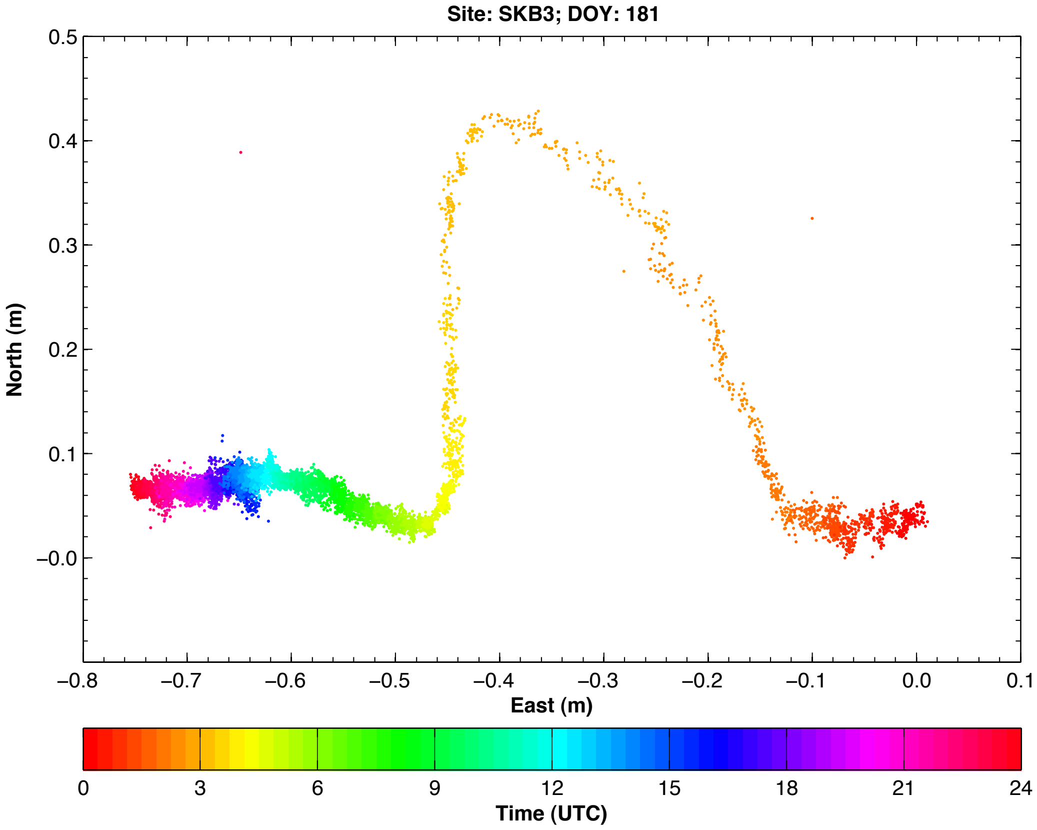

Figure 2-22. *Horizontal displacement of SKB3 kGPS over a 24-hour period of DOY181 (30 June, 2010), coincident with rapid drainage of the associated supra-glacial lake.*

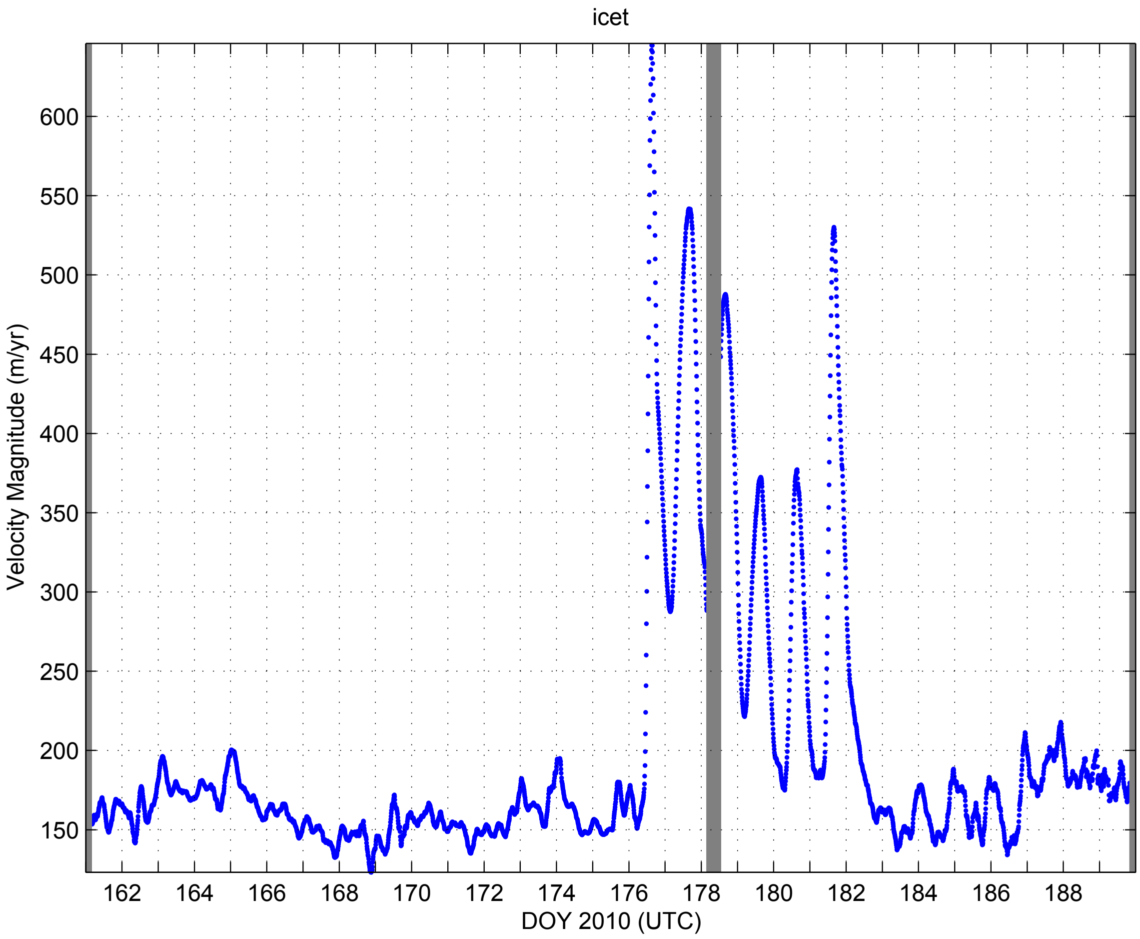

Figure 2-23. *Velocity at Ice-T between 11 June, 2010 (DOY 161) and 8 July, 2010 (DOY 189). Shaded grey bars represent gaps in the processed data. Note the maximum, minimum and therefore the amplitude of the velocity variation decreases with time between DOY's 177 and 180. SKB3 lake drained on DOY 181 at 01:05 UTC.*

SHR kGPS Results

Data from SHR (12 km inland; 646 m elevation) show the evolution of the diurnal velocity cycle through the melt season of 2010. During the winter, when surface melt is negligible, it is likely that the ice sheet flows mainly by internal deformation with relatively little sliding at the base of the glacier. As a result, winter velocities are low and constant (~100 m/yr at SHR). The background winter velocity is perhaps just visible on Figure 2-23 between day of year (DOY) 136–137. The onset of melt in early to mid–May 2010 brings with it a spring event and the highest observed velocity at SHR of 525 m/yr. Spring events are well documented from alpine glaciers (e.g. Iken et al.1983). Following the spring event, velocity follows a diurnal cycle in melt and runoff, suggesting the ice-bed interface is lubricated by pressurised meltwater entering the glacier through moulins and crevasses. During cold periods with low melt, velocities are low and steady with no significant diurnal variation. With prolonged periods of melt, several studies (e.g. Gordon 1998, Barthalomew et al. 2010, Schoof 2010, Sundal et al. 2011) suggest that the subglacial hydrological system becomes more efficient, leading to lower subglacial water pressures and lower glacier velocities. This is evident and observed from the records at SHR. Following the spring event, mean daily velocities decrease, the time of occurrence of maximum velocity decreases, and the amplitude of the diurnal variation in velocity decreases (Figure 2-19). Short periods of cold weather 'reset' the subglacial hydrological system (i.e. channels that formed during high water flow collapse due to ice creep at low flow) allowing subsequent days of high meltwater supply to cause higher velocity responses than if there were neighboring days of high melt. These data strongly support the view of Schoof (2010) that it is the variability in meltwater supply, not the magnitude of the seasonal melt, which controls ice discharge. The behavior of the velocity, and its interactions with melt and run-off, provide a great deal of information on the subglacial hydrological system. Figure 2-20 shows the efficiency of the hydrological system improving through the melt season. Daily runoff increases from May through to August, however its influence on ice velocity reduces as velocities decrease following the spring event.

Supraglacial Lake Drainage kGPS Results

The rapid drainage of the 5 km^2 supraglacial lake near SKB3 GPS (70 km inland; 1,391 m elevation) was identified from the 2009 GPS record and from the disappearance of the lake between adjacent MODIS images. This lake was targeted with a combined kGPS, passive seismic and lake monitoring campaign in 2010, and the rapid drainage of the lake was observed in the field and captured by 4 kGPS and six passive seismometers. On DOY 181 (30th June 2010) SKB3 lake began to drain at 01:05 UTC, with the volumetric discharge rate peaking at 02:47 UTC at a magnitude of 3,200 m^3 s^{-1}. Detailed analysis of the position record shows 1 m of uplift in 2010, coincident with horizontal acceleration and anomalous ice motion (Figure 2-22). Ice motion during drainage is described as anomalous because the kGPS was perturbed further south than west; following the transient displacement to the west, ice motion reversed to the east. Dislocations (defined as rapid but transient motion NW and vertically UP) following the drainage event may be hydraulic jacking and subsequent basal sliding initiated by subglacial water pressures exceeding the ice overburden pressure. Analysis of 2010 GPS data, and the addition of passive seismic and lake level monitoring, provide further information on these post-drainage mechanisms. The lake drainage data is comparable to the findings of Das et al. (2008), Sugiyama et al. (2007).

Lake Ice-T GPS Results

A short 30-day period of kGPS data from Ice-T in 2010 (50 km inland) indicates significant speed-up events between DOY 176 and 183 (Figure 2-23). The speed up event of DOY 181 is potentially the result of the rapid drainage of SKB3 lake. Later on day DOY 181 Ice-T began to accelerate at 09:20 UTC, attaining a maximum velocity of 530 m/yr at 15:50 UTC. There is an ~14 hour delay between peak drainage of the lake near SKB3 and peak velocity at Ice-T GPS. Between DOY 176 and 183: 1) velocities are higher than the 'background summer' velocity; 2) there is a strong diurnal variation in velocity; and 3) the amplitude of the variation reduces with time. It is thought unlikely that the input of water causing these accelerations is local. During field study in 2009 and 2010, no moulins were found in the area immediately around Ice-T. The speed up event on DOY 176 could be the result of the drainage of a lake north-east of SKB3 lake, which has been identified from MODIS imagery. An alternative explanation for the Ice-T accelerations is the influence of the drainage of Ice-T through the large moulin located 4 km down-glacier. In 2011, a combined GPS and passive seismic campaign aims to characterize and map the initiation of this moulin and its influence on the ice dynamics of the RGC.

Further work

Work is under way to obtain GIPSY-OASIS (the point positioning software behind APPS), which will enable processing of GPS data without a base station. These data will provide high quality relative position to allow for kinematic data analysis, which will complement current absolute results from TRACK (Chen, 1998). Work is also ongoing to de-trend final position and velocity datasets to investigate, for example, bed separation as opposed to vertical position. Scripts are being developed to extract inline position velocity (see Gudmundsson 2007, Nettles et al. 2008). Optimization of TRACK processing and filter parameters is an ongoing process.

2.5 Ice radar

The objective of the radar work within the SPA is to establish high spatial resolution coverage of subglacial topography and thermal conditions at the base of the ice sheet that will be used for constraining ice dynamics, groundwater modelling, and other analyses within the project. The scientific goals are to obtain an increased understanding of the spatial distribution of subglacial hydrology and its coupling to ice dynamics. Here, the activities performed during 2010 and the current status of available ground penetrating radar and radio-echo sounding are summarized.

Instrumentation and fieldwork

During spring 2010, two radio-echo sounding system plans within the GAP project were finalized. The systems consist of a 16-bit receiver, with 200 MHz bandwidth, able to acquire 6,000 traces/second. The receiver is connected with a ruggedized industrial computer for control, visualization and storage of collected data. The receiver is connected to a Trimble R7 kGPS receiver for positioning and time-signal control. The receiver and GPS are built into a custom made enclosure. The transmitter consists of an ~35 W impulse generator, with a pulse repetition frequency of up to 5 KHz. Several sets of resistively loaded dipole antennas were constructed with center frequencies of 3, 5 and 10 MHz.

In May 2010 a field campaign was conducted, which unfortunately was delayed and considerably shortened due to problems related to the eruption of Eyjafjallajokull volcano on Iceland in April 2010. The eruption and resulting ash cloud stopped air-traffic and delayed transport of equipment and personnel to Greenland, as well as interrupted helicopter support for field activities on the ice. After relocating camp to a position further inland, due to rapidly melting/saturated snow-pack, a total of 4 days of radar work (8 total days on the ice) was achieved compared to the planned 14 days. Approximately 500 km of radar data was collected (see discussion below).

Current data sets

Currently, three different data sets of subglacial topography are available within the GAP project, which include data collected by Danish Technical University (DTU) and GEUS, NASA through the project ICEBridge, and Uppsala University (within the GAP project). Limited data acquired by Kansas University (CReSIS) are also available for the study area. However, the spatial coverage of Kansas data is sparse (only two profiles have been repeated several times following flight routes in and out of Kangerlussuaq air field).

ICEBridge

The NASA owned P3 aircraft flew a grid of profiles over the GAP study area in May 2010 while operating a deep sounding radar system (Figure 2-24). They profiled approximately 1,750 km, of which ~900 km is over glaciated areas. This data set is maintained and processed by University of Kansas, USA, and is available for the GAP project through the National Snow and Ice Data Center (NSIDC). However, the quality of the collected data is poor due to problems caused by interference and calibration issues with the radar system. The amount of data with clear bed return appears to be limited (<50 km of profile), and thus is does not currently contribute a significant addition to the bed topography in the Russell Glacier catchment area. The ICEBridge mission will repeat the flight lines in April 2011, and it is hoped that these initial problems will be addressed. Echo strength profiles will be included also in the data release. It may be difficult to extract information about the thermal state of the bed due to variable flight height above the ice surface, which affects ground coupling and consequently the amount of the power that reaches the bed. These variables can be modelled and compensated for, but the effects are not entirely removed, which limits the use of the echo strength data for characterization of subglacial hydrological conditions.

DTU/GEUS

DTU/GEUS collected approximately 2,000 km of airborne data over the GAP study area in 2005 (Figure 2-24). The data was processed and the GAP project has access to the ice thickness data along the flight lines (Figure 2-25). The data have variable quality over the area. The data are very sporadic in the 10–20 km closest to the terminus. The data set contains the position of the collected profiles and the interpreted ice thickness along those profiles. Amplitude information of the bed return is not currently available and thus cannot provide any information of the thermal state at the bed.

GAP

Approximately 500 km of ground based radio-echo sounding was collected during May 2010 (Figure 2-24). The data have good quality and clear bed return along all profiles. The data have been processed following the processing scheme in Figure 2-26, but problems with positioning of the profiles due to kGPS base-station issues has slightly delayed processing. The travel time of the bed reflections for ice thickness are currently picked and the bed return power has been extracted as proxy data for the basal thermal regime, following correction of attenuation within the ice of the radar signal.

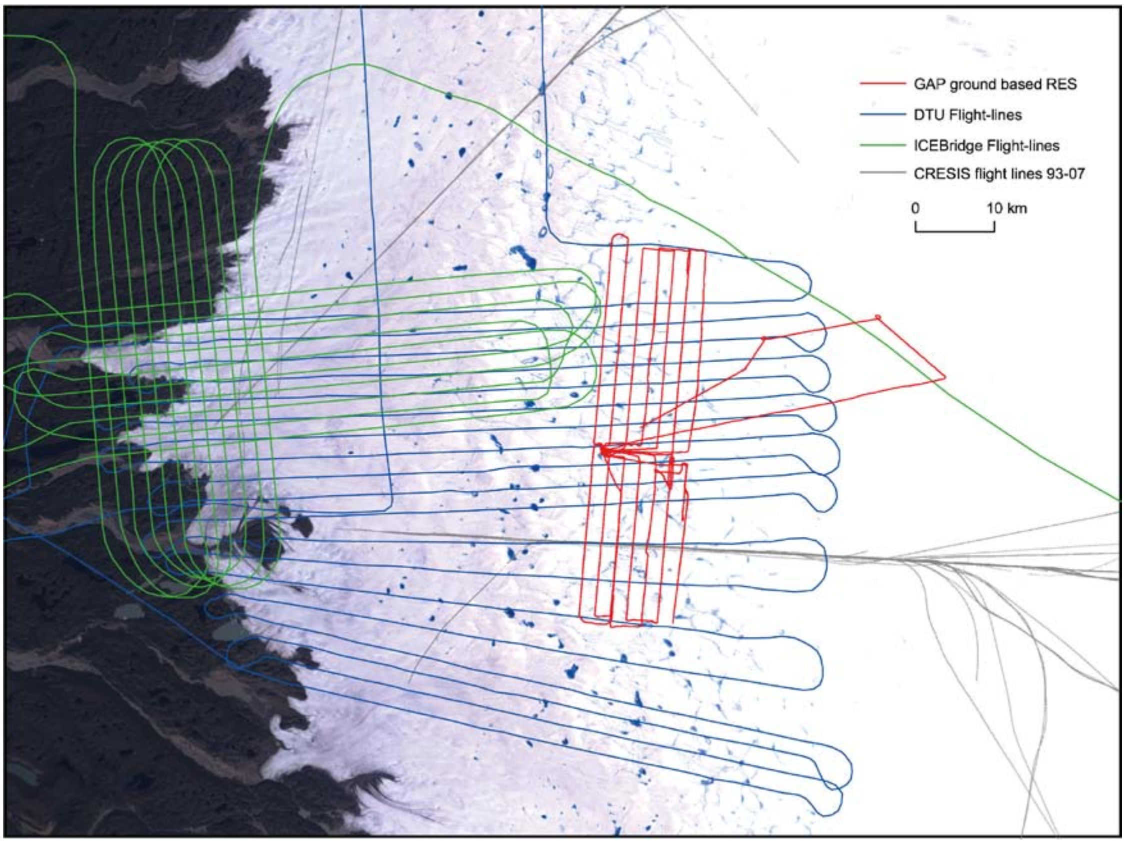

Figure 2-24. *Available radar data for the GAP study area.*

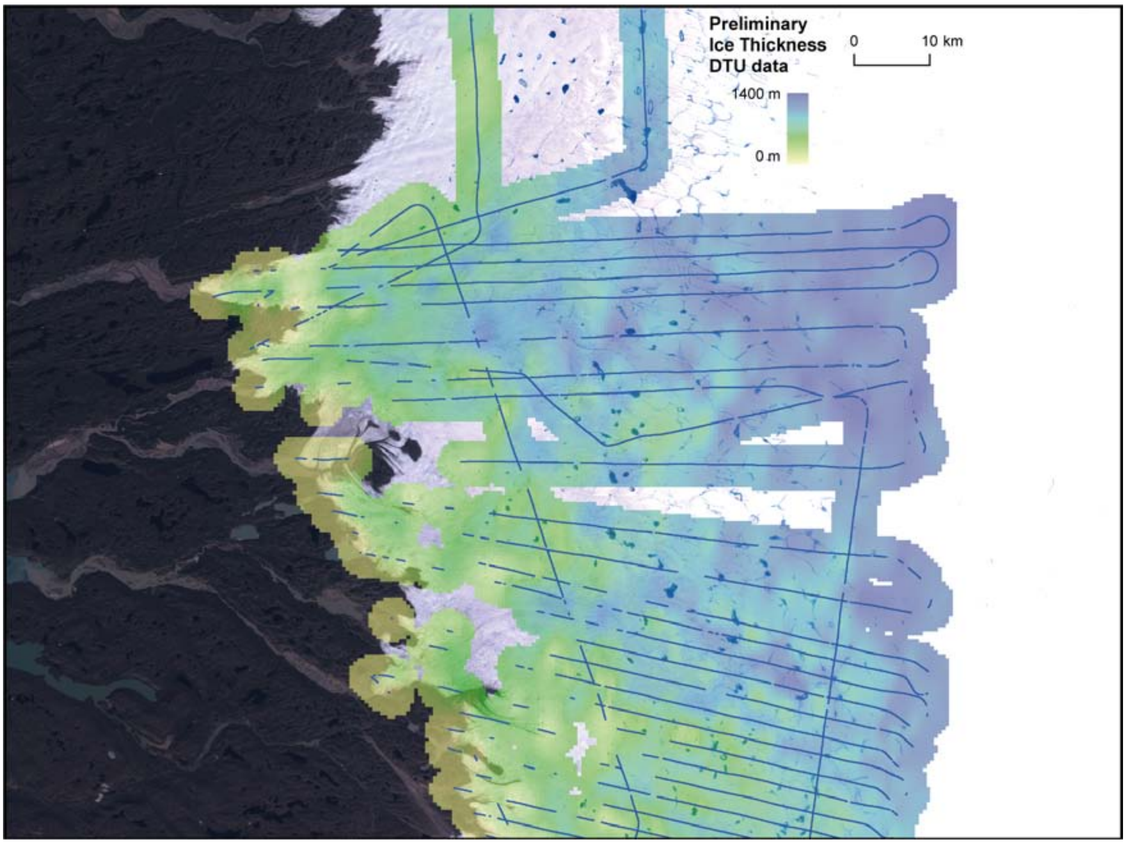

Figure 2-25. *Preliminary bed topography from only DTU/GEUS data.*

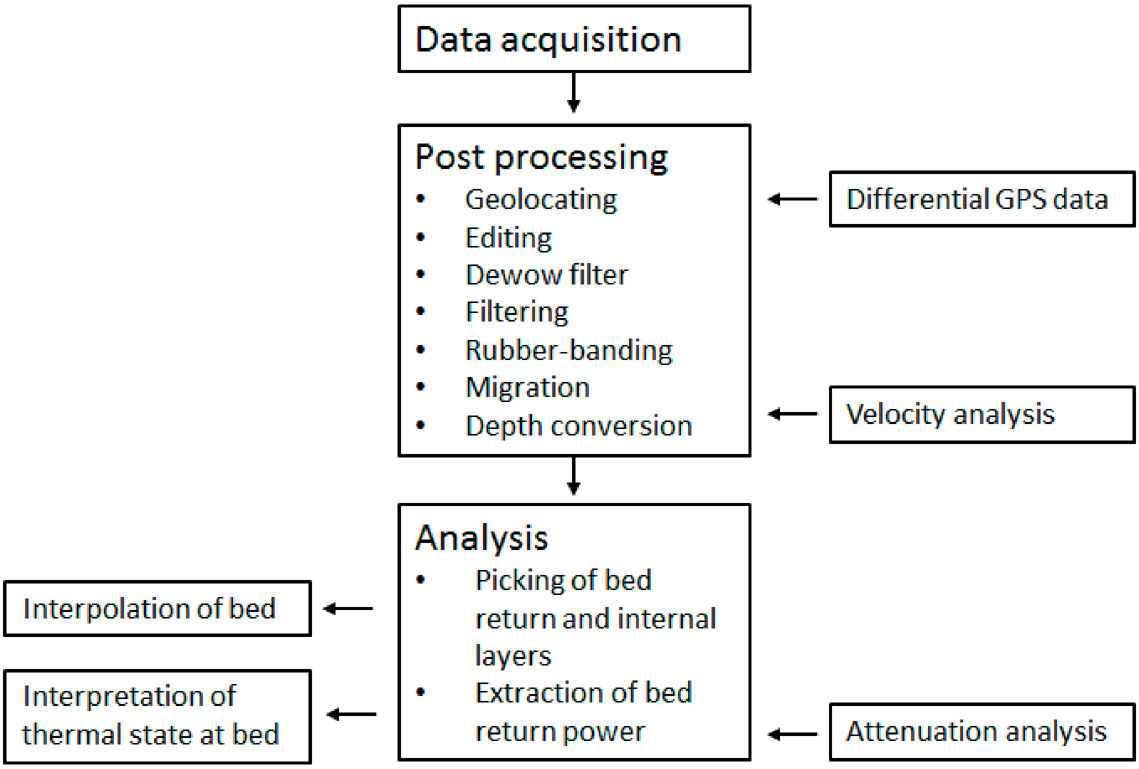

***Figure 2-26.** Simplified processing scheme for radio-echo sounding data.*

Preliminary results from the GAP data sets show a highly variable subglacial topography, with an ice thickness ranging from 200 to 1,600 m. Figure 2-27 shows an example profile that cuts across the ice flow direction. Several interesting features can be observed. The strong hyperbolic reflections (for example at ~0.5, 4, 13.5, 16 km along the profile) are ringing effects from supraglacial lakes at the surface, and possibly englacial drainage features such as moulins. All supraglacial lakes that the profiles cross, as identified in satellite images, cause these ringing effects. It is possible that the ringing appears when the lake has not drained before freezing at the end of the previous melt season, causing different characteristics of the ice (frozen lake water) or even the presence of liquid water.

A remarkably flat bed is seen ~18–19 km along the profile in Figure 2-27. The appearance of the bed reflector is very similar to features seen in radar data from Antarctica and has been interpreted as subglacial lakes. Additional profiles were conducted in this area to investigate the consistency and extent of the flat area (Figure 2-28). In studies on subglacial lakes in Antarctica several properties of the radar reflection can be used to determine and confirm (within reason) the presence of subglacial lakes. These include the reflection strength over the assumed lake, the specularity of the reflection, and its hydraulic character, gradient and setting. The reflectivity should be high because an ice-water interface will cause a substantial stronger bed return than an ice-substratum interface. The specularity is a measure of variation in bed reflectivity over the lake, and should be low because the ice-water interface should be smooth on the scale of the wavelength of the radar signal. A hydraulic gradient close to zero indicates ice near to floatation. Preliminary analysis of bed reflectivity, specularity and hydraulic slope over the flat area (Figure 2-29) show a high reflectivity and low variability in reflectivity (indicating high specularity) and suggest that it may be a subglacial lake, which would be the first observed in Greenland. However, the hydraulic gradient across the candidate subglacial lake shows considerable variation, but this could be expected for a small target due to the significant support from the surrounding bedrock areas that relax the floatation condition.

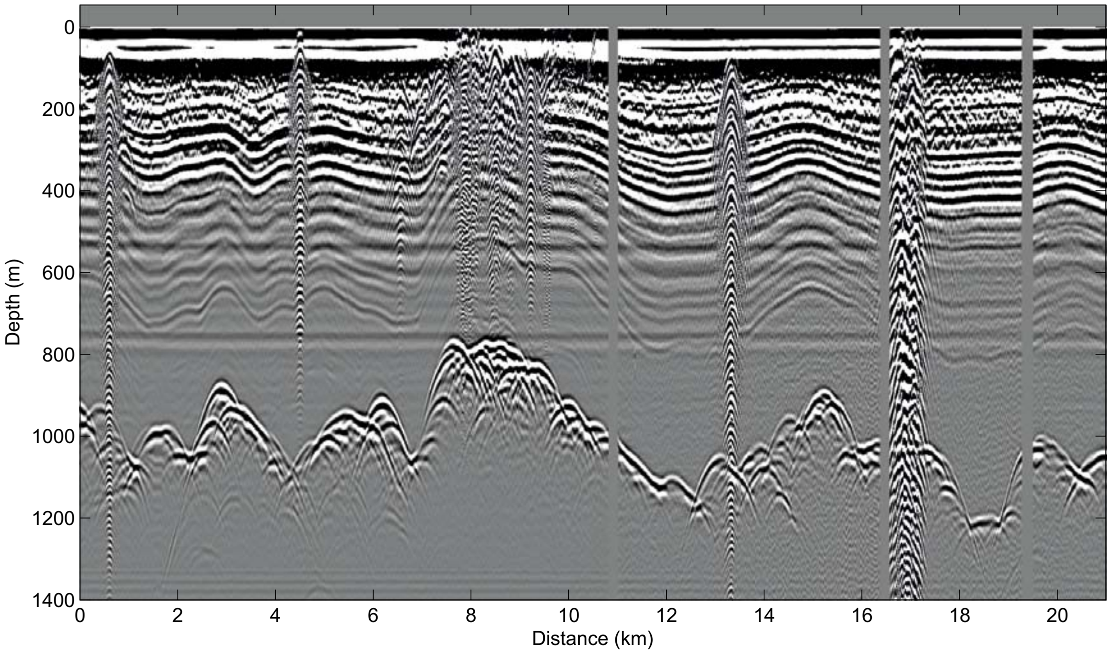

Figure 2-27. *Example of a ground based radio-echo sounding profile collected in perpendicular direction to ice flow. The data has been low-pass filtered and Normal-moveout corrected, but not migrated.*

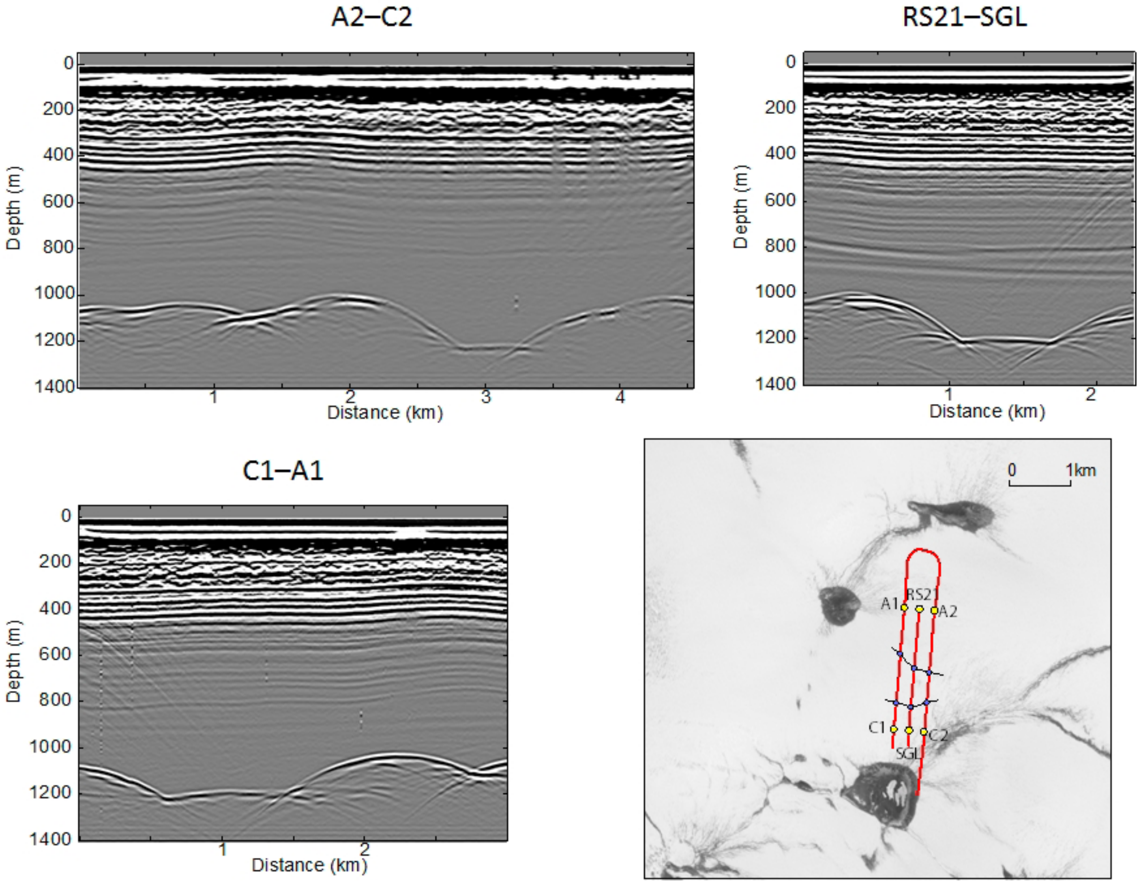

Figure 2-28. *Radar profiles collected in 2010 and extent of the subglacial lake candidate.*

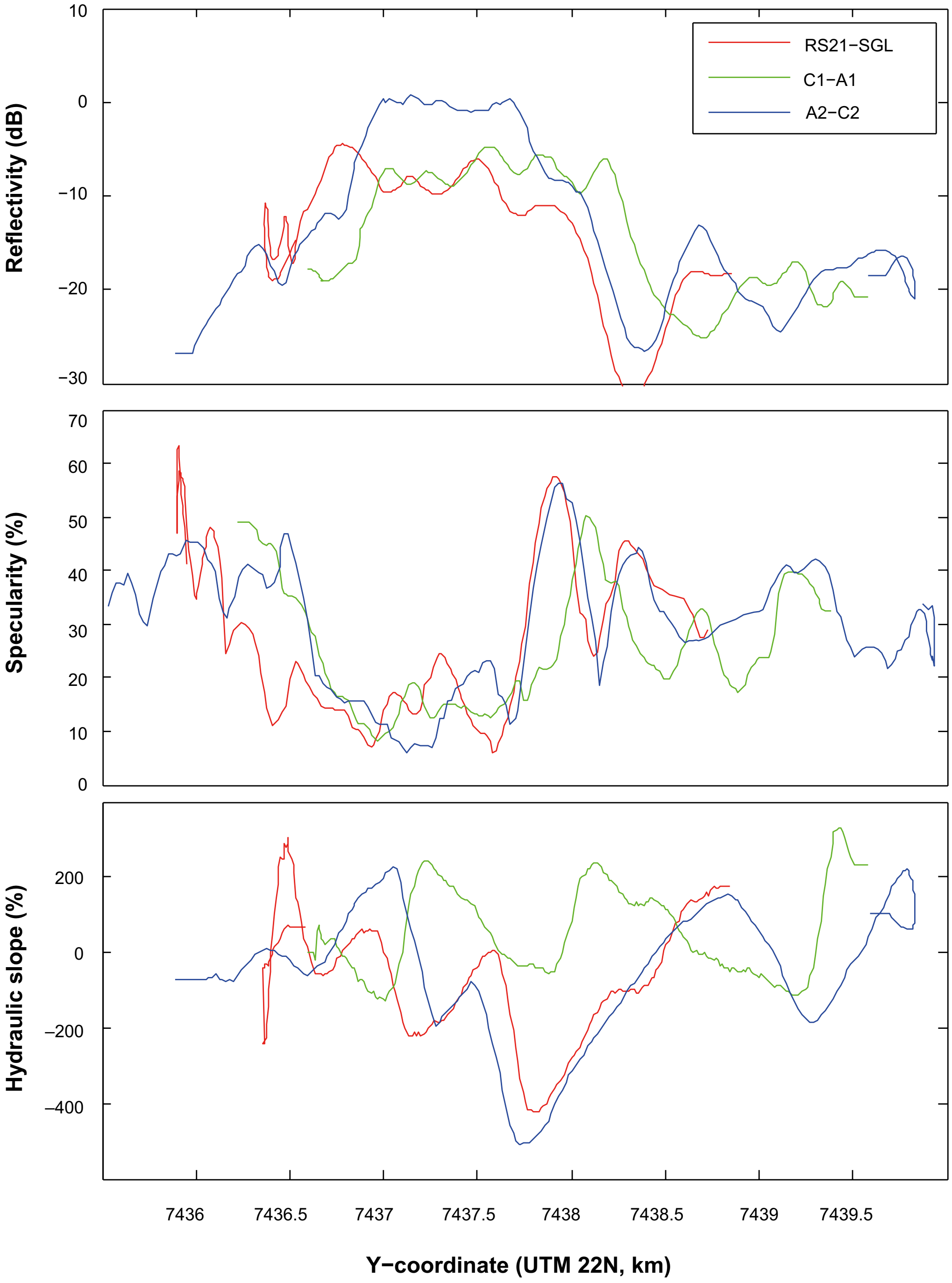

Figure 2-29. *Reflectivity, specularity, and hydraulic gradient along the three profiles across the subglacial lake candidate that is shown in Figure 2-27.*

2.6 Active seismics

A series of seismic reflection experiments were conducted through the summer melt season in 2010 to provide information on internal structure of the ice sheet and the characteristics of the ice-bed interface. Changes in wave phase and velocity between layers can be analyzed to ascertain the type and hydraulic character of underlying substrate. Amplitude versus offset (AVO) analysis provides further information on the substrate characteristics, such as sediment porosity, sediment density and changes in water content, through the examination of reflection angles from subsurface layers relative to individual shot gathers.

The goals of the 2010 active seismic campaign were to:

1) Identify englacial reflectors.
2) Establish the subglacial substrate and the characteristics of this material (i.e. sediment thickness, porosity etc.) in the regions of hydrological interest.
3) Identify diurnal variations in sediment water content immediately down-glacier of a large moulin input site using temporal AVO over a 30 hour period.

Fieldwork

During the 2010 summer field expedition, six active seismic lines were gathered at four locations (Figure 2-30). At each site, 48 vertical component geophones, with a mean spacing of 10m, were set into concrete slabs (of dimensions 15×15×5cm) and were buried within the ice surface to reduce surface noise (only one exception existed at site 4, where 24 geophones were used). Shot holes were drilled to ~3 m depth, at a spacing of 80 m. At each site, the large thickness of ice (determined from the spring radar campaign) required that explosive sources were used to reflect energy off the bed. Each shot hole was loaded with one detonator, and one or two charges of Pentex, supplemented by an additional charge of dynamite where required. Most charges were left to freeze overnight in order to yield improved coupling so that all available energy from the explosions travels into the ice rather than upward; the occasional blow-out did occur. Shotboxes were provided by Dr. S. Anandakrishnan,

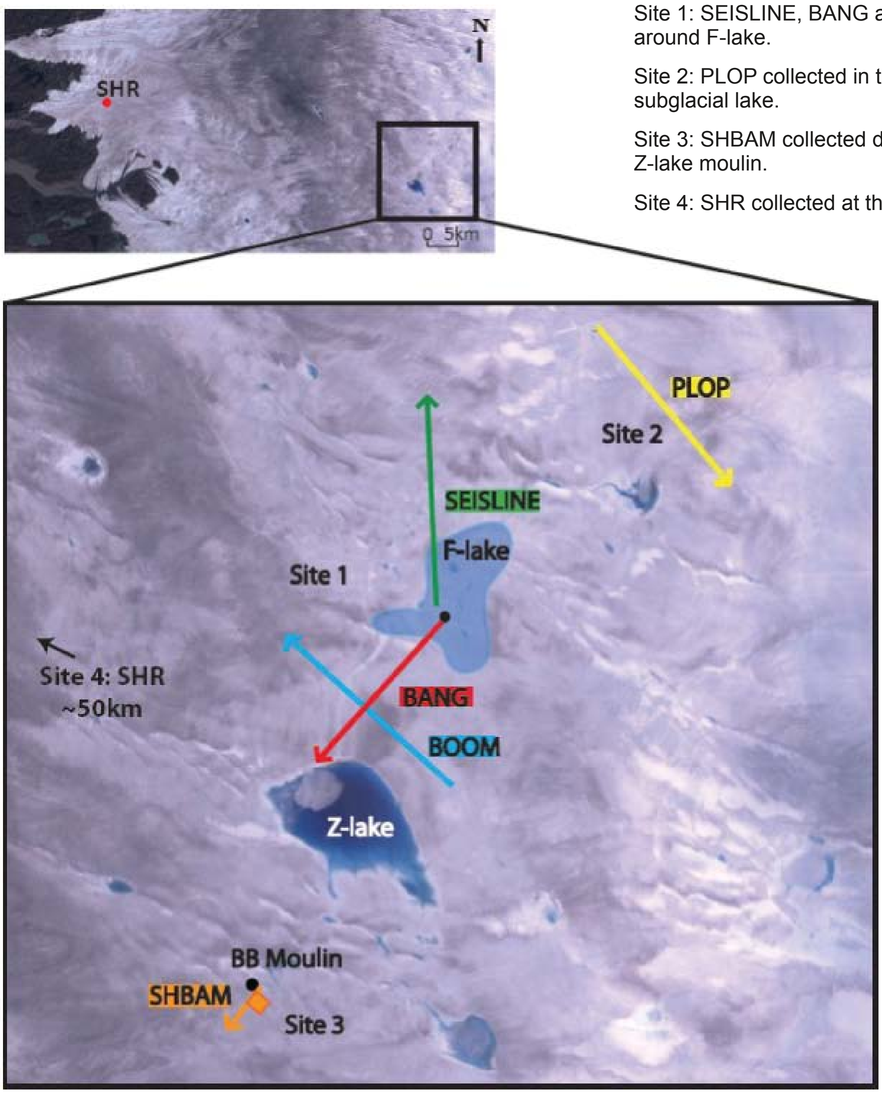

Site 1: SEISLINE, BANG and BOOM collected around F-lake.

Site 2: PLOP collected in the region of a potential subglacial lake.

Site 3: SHBAM collected downstream from the Z-lake moulin.

Site 4: SHR collected at the Ice2Sea borehole site.

Figure 2-30. *Landsat image from July 18th, 2010 with the active seismic sites labeled; the arrows represent the direction of acquisition. F-lake is marked at the maximum extent prior to drainage.*

Penn State University, and SeisUK, NERC Geophysical Equipment Facility. Accurate dGPS locations of the shot holes (using a Leica SR520/Trimble 5700/ProXH receiver, processed against the Russell base-station to an accuracy of 10 cm in the horizontal/vertical direction) were collected to establish both the exact location of the shots and the elevation change along the line. Table 2-6 gives information about the main line characteristics.

SEISLINE

SEISLINE was the first active seismic line to be deployed. Unfortunately, there was insufficient time at the field site to run a seismic survey prior to lake drainage; as a result, SEISLINE was located upstream of F-lake (as shown in Figure 2-30) as a proxy for an area not likely affected by lake drainage. The presence or absence of basal sediment in this region will be compared with areas where lake water likely has drained.

The line ran approximately south to north, with all holes loaded on July 2nd with 250 g of Pentex. The line was fired on the 3rd, 4th, and 5th of July. SEISLINE consisted of 39 shots (i.e. 3,040 m line length); the presence of crevasses at the north of the survey precluded extension of the line any farther. The elevation change over the line was a total of 20.5 m.

BANG

The second line deployed was BANG. This survey ran from 10 m downstream of a large crevasse and moulin in the mid-section of F-lake (which drained at the start of the month), in the direction it was estimated to have travelled following the lake tapping event. The purpose of BANG was to establish the topography of the basal terrain and characterize the composition and water content of any bed material, which would have implications for drainage development prior to, and during, the lake tapping event.

BANG ran approximately NE to SW. The line was drilled and loaded on July 9th and fired on July 10th. All holes were loaded with 250 g of Pentex. The line consisted of 46 shots, with a line length of 3,600 m. In addition, two passive seismic stations with three-component geophones were installed at two geophones (numbers 5 and 45) to provide S-wave velocities that may be applied to later AVO analysis. The maximum elevation change over the line was 36 m.

Table 2-6. Active seismic line properties.

	SEISLINE	BANG	BOOM	PLOP	SHBAM	SHR
Line length (m)	3,040	3,600	4,240	3,920	1,040	1,920
Line direction	S-N	NE-SW	SE-NW	WNW- ESE	NE-SW	W-E
Shotline start location	67.02888	66.99832	66.96989	67.04922		67.09998
(N,W)	–48.7269	–48.7237	–48.7226	–48.648		–49.96061
Shotline end location (N,W)	67.00158	66.97515	66.9964	67.02154		67.10005
	–48.72583	–48.7812	–48.7925	–48.5926		–49.93841
Start offset (from phone 1)	2,480	2,000	2,000	1,760	470	1,140
End offset (from phone 1)	560	1,600	2,240	2,160	570	780
No. of shots	39	46	54	50	14	33
No. of charges	1	1	1	2 (9 holes +1)	3	2 (27 holes +1)
Misfired shots	39 not triggered	n/a	24, 25,28 re-fired	30 re-fired	n/a	n/a
Date fired (July 2010)	3,4,5	9,10	16,17	19	27	31
Mean ice thickness (m)	1,271	1,054	1,070	1,160		~600
Mean elevation (masl)	1367.55	1355.23	1359.92	1395.36		709.82
Elevation change (m)	20.5	36	25.5	20.5		41.5
Section length (m)	1,750	2,079	2,450	2,000		1,075
Section start (N,W)	67.02672	66.99213	66.9759	67.04186		67.08347
	–48.7269	–48.7391	–48.7384	–48.6333		–49.92319
Section end (N,W)	67.01024	66.97876	66.9909	67.02777		67.08336
	–48.7263	–48.7723	–48.778	–48.6051		–49.95505

BOOM

BOOM was collected soon after BANG and ran orthogonal to it, with each line crossing perpendicularly at the halfway point of both geophone cable setups. The purpose of BOOM was to perpendicularly cross the likely path of subglacial water flow from the lake drainage event in order to establish the potential presence of any basal channels, the type of substrate, and the basal topography in the region of lake drainage.

BOOM ran approximately SE to NW, perpendicular to the general ice flow direction in this region (Figure 2-30). The line was drilled and loaded on July 15th and shot on July 16th and 17th. The line consisted of 54 shots, covering 4,240 m on the surface, with all holes loaded with 250 g Pentex. Similar to BANG, two passive seismic stations with three-component geophones were installed at geophones 5 and 45 to establish S-wave velocities. The total elevation change along BOOM was 25.5 m.

PLOP

The purpose of PLOP was to run an active seismic line over an area where a candidate subglacial lake had been identified in the spring of 2010 using 3Mhz radar. While radar studies can identify flat basal reflectors that might correspond to subglacial lake locations, active seismics can complement these studies by facilitating identification of any material filling subglacial basins, as well al the potential thickness, extent and volume of that material (whether water or sediment).

PLOP was set up in an ~WNW to ESE direction. The line was drilled and loaded on July 18th and fired on July 19th. All the holes were loaded with one 250 g Pentex stick and one 400 g dynamite stick. Nine holes were loaded with additional sticks of dynamite in order to provide better signal to noise ratio for later AVO analysis. The line consisted of 50 shots, running over 3,920 m. The maximum elevation change over the line was 20.5 m.

SHBAM

The configuration of SHBAM differed slightly from the preceding active seismic lines. The purpose of SHBAM was twofold: 1) to establish englacial and basal conditions downstream of BB moulin (which drained Z-lake), in the assumed direction of water flow, and 2) to record diurnal changes in the water content of the englacial and basal system (particularly if subglacial sediment is present) directly downstream of BB moulin.

The SHBAM line began immediately adjacent to BB moulin and ran NE to SW. The length of the seismic line was limited to 1,040 m (14 shots) by surface topography and a number of large impassable channels. The limited line length creates an insufficient offset for analyzing far-offset reflection amplitudes. However, with high signal-to-noise ratios, zero-offset reflection coefficients can be established if amplitudes of the direct reflection and the first multiple are used. To utilize this near-offset technique, a square array of 16 shots was set out between 80 m (shotpoint 2) and 480 m (shotpoint 7) from the start of the line, with a 10 m hole interval. The 14-shot line was drilled and loaded on July 26th. The holes were loaded with one 250 g Pentex stick and 2 × 400 g dynamite

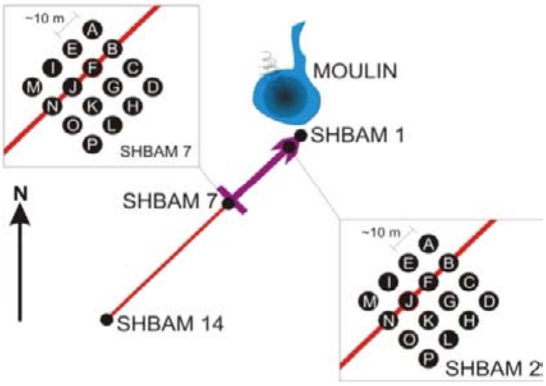

Figure 2-31. *Schematic ground-plan of SHBAM seismic line*

sticks and allowed to freeze overnight. Following detonation of the seismic line on July 27th, the entire 16-shot seismic array was loaded and fired every ~2 hours between 20:55 UTC on July 27th and 01:10 UTC on July 28th in alphabetical sequence (see Figure 2-31). Again, all holes were loaded with one 250 g Pentex stick and 2 × 400 g dynamite sticks.

SHR

The SHR active seismic line was located in the region of the AWI borehole ~10 km from Russell Glacier terminus. The purpose of the SHR seismic line was to provide basal topography/conditions for the bedrock drilling team at this site. The topography in this region is much more extreme than up-glacier at the F-lake and Z-lake sites, with ice ridges of up to several meters. In addition, there were a significant number of surface crevasses. As a result, much of the energy of the seismic shots likely did not travel into the ice, resulting in "noise" in the data. At this site, 24 geophones were used, which provides a smaller subsurface footprint that at the other sites but still allows for AVO analysis.

The SHR line ran west to east, with the 24-channel geophone cable placed ~50 m from the borehole. Shots were drilled 60 m apart, with the line covering 1,920 m (33 shots). All holes were loaded with 1 × 250 g Pentex charge and at least 1 × 400 g dynamite charge (some holes were loaded with 2 × 400 g dynamite sticks) on July 29th. The charges were left in place overnight to freeze. The shots were fired on July 30th. In addition to the shot-points being surveyed with GPS, the geophone locations were also surveyed. Due to topographical variations, the geophone spacing was sometimes reduced to less than 10 m.

Processing and preliminary results

PLOP

The PLOP active seismic data were processed in ReflexW (Sandmeier Software) using the following processing flow: 25 ms detonation delay removed; bandpass filter (cosine taper) to remove general noise; F-k fan filter to remove the groundroll; time mute >2,000 ms; predictive deconvolution to suppress multiples; 0 lag time deconvolution to concentrate wavelet energy closer to the surface; individual trace noise muting; time mute > 1,000 ms; elevation static corrections; constant velocity NMO stack; Stolt f-k migration; bandpass filter (cosine taper) to remove remaining noise.

A basin with three layers was visible post-processing (see Figure 2-32). In order to find the velocity intervals of these layers (to differentiate between ice, sediment, water and bedrock) single-gather layer velocities were manually picked and analyzed. Unfortunately, the time interval between the three layers is sufficiently small that it is not possible using this method to differentiate the interval velocities.

The next step is to create supergathers using ProMAX (Halliburton) and generate semblance plots to pick out the layer velocities. Following this, AVO analysis will be used to establish the layer velocities and properties within the subglacial basin. Amplitudes first have to be corrected for changes in surface conditions (using cross-correlation analysis), and P-wave attenuation (static correction). AVO analysis will then be carried out using Matlab scripts and models (to estimate matches between the amplitude data and modelled returns from different types of basal material).

SEISLINE, BOOM and BANG

The three F-lake active seismic lines are being processed in ProMAX using the following processing flow:25 ms detonation delay removed; Ormsby bandpass filter; top mute; surgical mute for groundroll suppression; predictive deconvolution; floating datum statics corrections; velocity analysis; elevation static corrections; automatic gain control; 2-D Kirchoff pre-stack time migration; Ormsby bandpass filter.

Results from SEISLINE show variable basal topography (elevation changes of ~175 m over the line). At the base of the steep incline, complex reflections may indicate the presence of sediment within the hollow (see Figure 2-33). BANG shows a basin tens of meters in depth (likely filled with sediment, as indicated by semblance analysis) and a potential out-of-plane event (see Figure 2-34). The bed dips fairly steeply away from the lake. BOOM also shows evidence of a basin that intersects with the BANG line. The topography on this across-flow line is bumpy, with a trough and an elevated section of bedrock also visible (see Figure 2-35). AVO analysis on the three F-lake lines will be commencing shortly in order to establish the basal material properties.

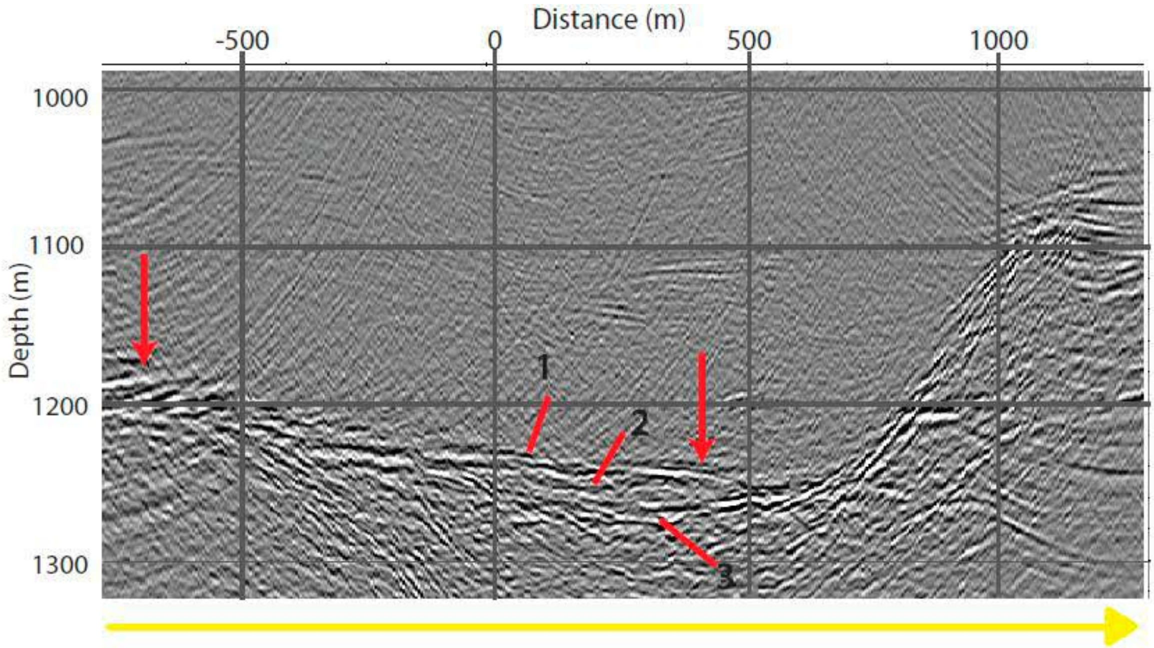

***Figure 2-32.** Brute stack migrated image of the PLOP active seismic line. The two arrows indicate where the potential subglacial lake would lie in relation to the feature identified in radar data collected in the spring 2010 campaign. The numbers point out three layers of interest within the basin.*

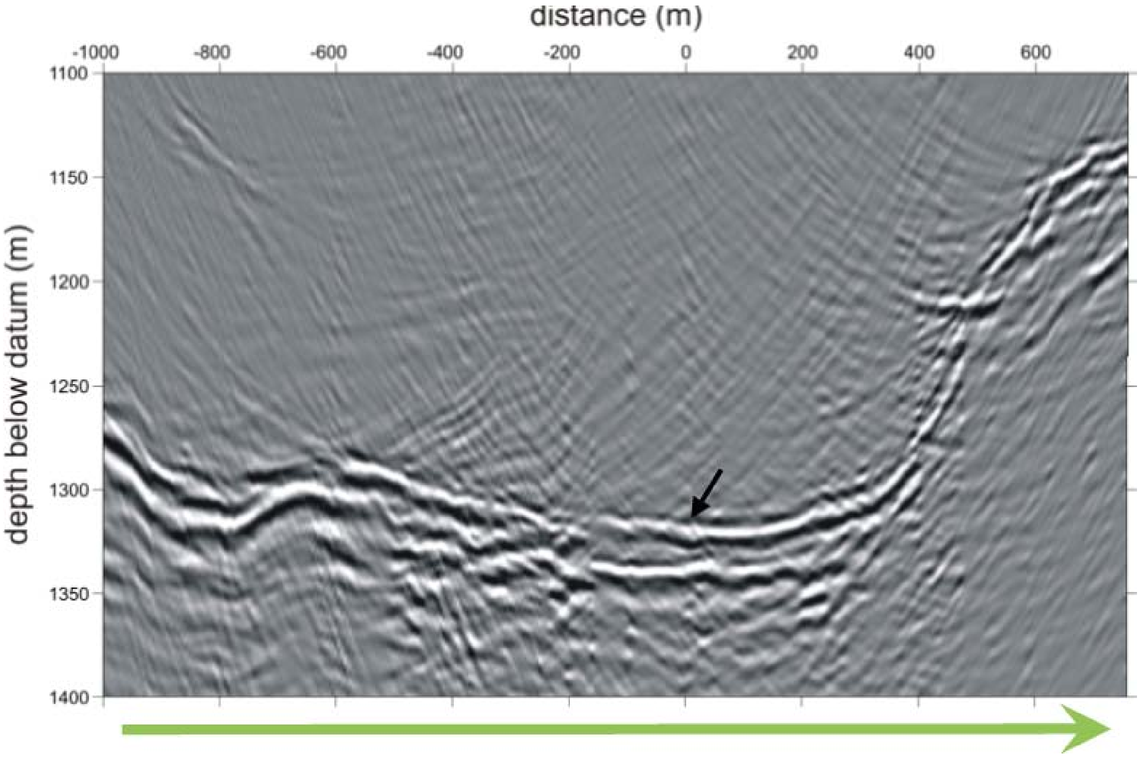

***Figure 2-33.** Pre-stack migrated image of the SEISLINE active seismic line. Arrow shows a reflection indicating sediment occurrence.*

SHBAM

The SHBAM active seismic line and temporal AVO data have not yet been analyzed. These data will be examined within the next six months and will be discussed in the 2011 annual report.

SHR

The SHR data have been partially processed. The data indicate a basal reflection at a maximum depth of around 660 m and an average of ~600 m. In comparison with the other active seismic lines from 2010, there appears to be limited basal topography at SHR. Full processing and AVO analysis will take place within the next 6 months.

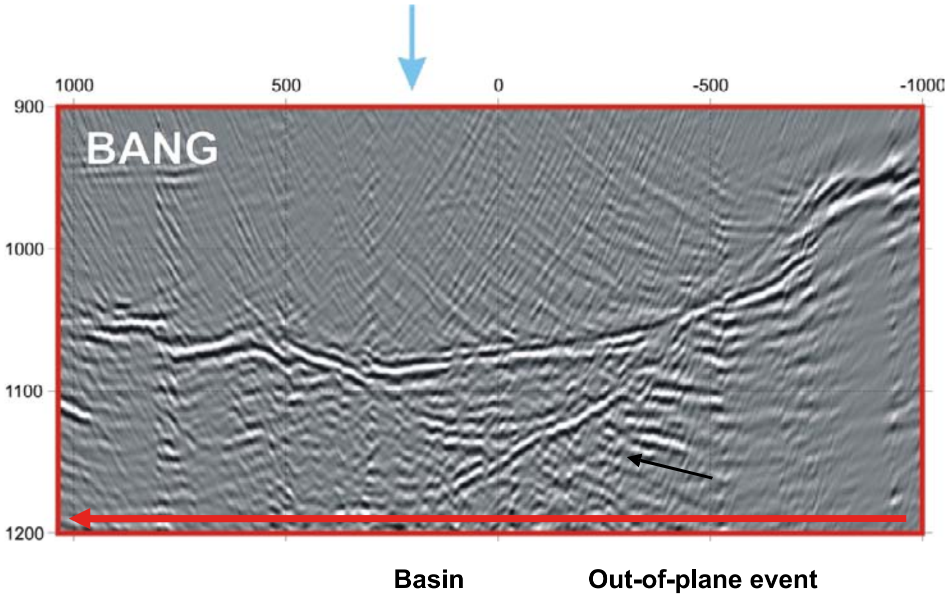

Figure 2-34. *Pre-stack migrated image of the BANG active seismic line. The blue arrow indicates the intersection with BOOM. The red arrow direction corresponds to that shown in Figure 2-30. X-axis shows distance in meters, and Y-axis depth in meters.*

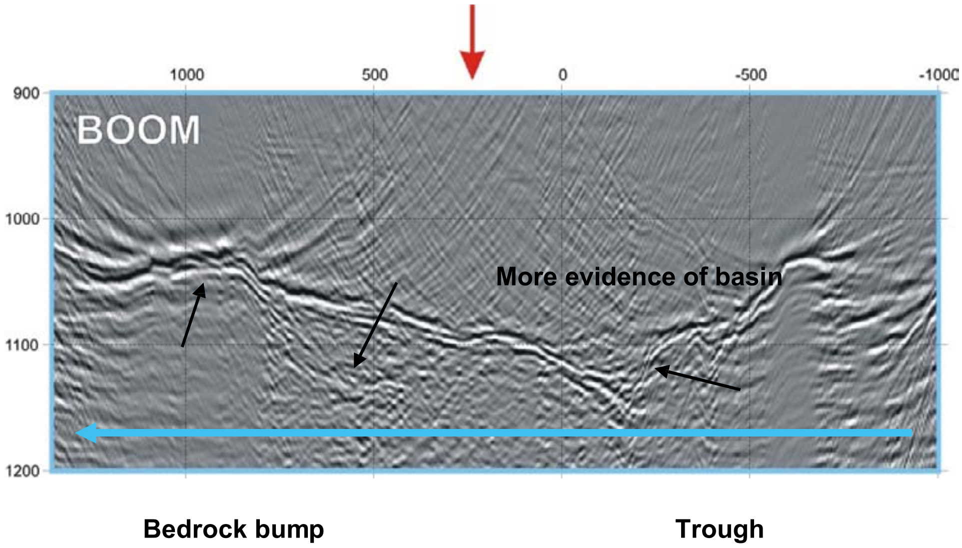

Figure 2-35. *Pre-stack migrated image of the BOOM active seismic line. The red arrow indicates the intersection with BANG. The blue arrow direction corresponds to that shown in Figure 2-30X-axis shows distance in meters, and Y-axis depth in meters.*

2.7 Passive seismics

The two main objectives of this campaign were to: 1) use passive seismics to monitor a lake drainage event and 2) image any structures or features associated with a moulin site and correlate these with other data, such as GPS and atmospheric forcing driving surface melt flux. Figure 2-36 is an overview of both moulin and lake field sites.

During the brittle failure of a crystalline material (e.g. rock ice), elastic strain energy in the form of an earthquake is released. Such deformation can be passively monitored by a network, or array, of seismometers, and has been successfully applied to a number of length scales and settings, such as laboratory rock deformation experiments, oil reservoirs and tectonic studies. In recent years, ice deformation has been successfully monitored using passive seismology (e.g. Roux et al. 2008, Walter et al. 2009, 2010).

There are numerous pathways that surface meltwater can take from the glacier surface to the bedrock. The first main type of drainage pathway is through the catastrophic drainage of a surface lake. During such an event, a large crevasse opens, allowing the contents of the lake to drain within a matter of hours. A second type of drainage pathway that the meltwater can take is through moulins (e.g. Zwally et al. 2002). These moulins vary in size from tens of centimeters to tens of meters in diameter and are, by far, the most important and efficient drainage pathway for surface meltwater. Although these features play a pivotal role in the drainage of meltwater, very little is known or understood about their internal structure, and to what extent the water penetrates the glacier.

Lake Drainage Site

The superglacial lake was selected on the basis of satellite data, which showed that drainage had occurred regularly and relatively rapidly within the past 4 years. kGPS analysis (skb4 installed in Autumn 2008) indicated a rapid displacement event, which coincided with this event in 2009 (Figure 2-39 to Figure 2-41). Further, helicopter reconnaissance showed the presence of a healed crevasse over 1 km in length within the lake. It is hypothesized that the crevasse running through the lake would be the main initiation point of drainage, and thus the array was optimized to focus on the crevasse. Initial plans for the monitoring of the lake site included a 12 station network, with the ability to remove 6 of the stations for a subsequent experiment focused on a moulin. The removal of 6 stations did not compromise coverage of the crevasse. The station network had an aperture of approximately 1–1.5 km, corresponding to 1–1.5 times the ice thickness. This aperture would allow for the imaging of seismic events from the bed-rock-glacier interfaces. However, the early initiation of the melt season, and late arrival of the equipment to Greenland, allowed for only 6 seismometers to be deployed prior to lake drainage.

An 18 channel RefTek acquisition system of six 4.5 Hz, 3-component geophones were deployed along with 4 GPS and 2 pressure transducers over a 12 hour period with helicopter support (Figure 2-37 and Table 2-7). The seismometers were deployed from June 26th until September 8th and ran in continuous mode with a sampling interval of 1,000 Hz. Due to the severity of the ablation, which resulted in dramatic changes in the terrain over the course of the summer melt season, deployment and servicing of the instruments was continuous and arduous. Additionally, ablation sometimes causes a shift in the position or orientation of the geophone after its deployment, In order to alleviate the effects of these movements, the geophones were mounted in concrete slabs, buried to a depth of 50 cm, and covered with ice chippings (Figure 2-38). Fifty centimeters depth corresponds to the firn water-table. The geophones were regularly serviced (approximately every 5 days). Traditionally the GPS timer and solar panel are mounted onto a large pole, however, previous field campaign experience showed that the pole tended to melt-out and generate noise as it moved. Based on such experience, it was decided that the solar panel and GPT timer should be mounted directly onto the box housing the RefTek data logger (Figure 2-38).

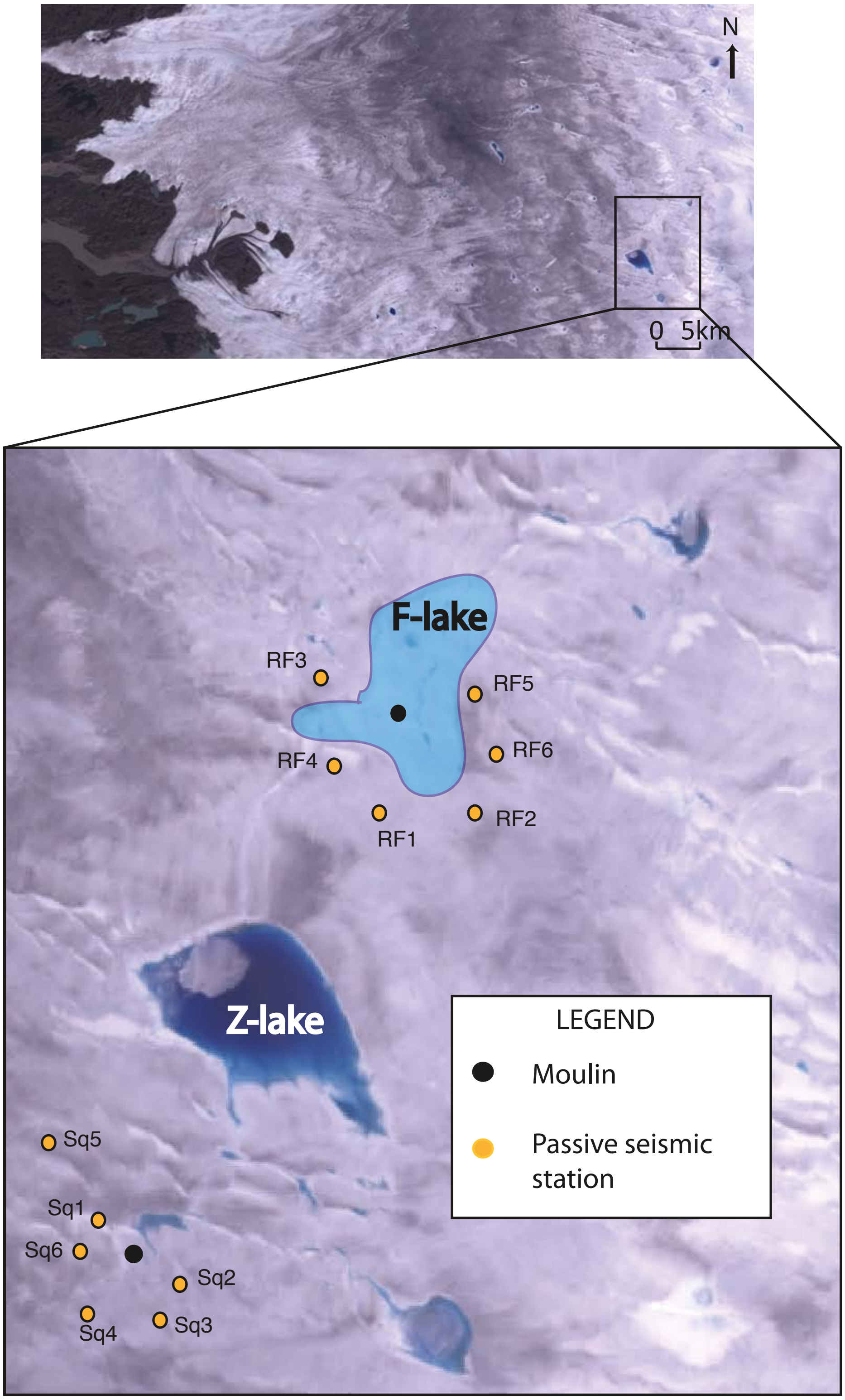

***Figure 2-36.** Landsat image of the passive seismic networks.*

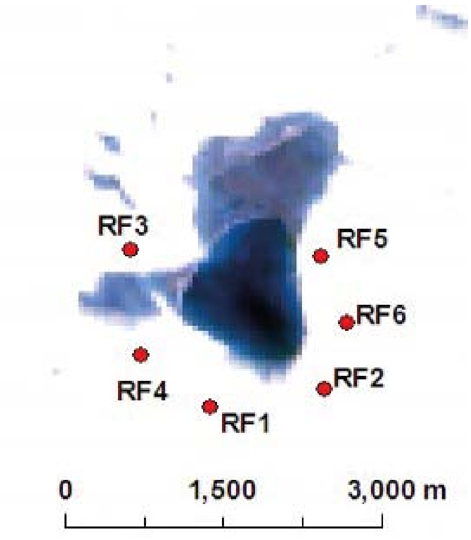

Figure 2-37. Landsat image of the passive seismic network and lake site.

Table 2-7. Location, deployment and notes regarding the data quality of the stations for the monitoring of lake drainage.

Station Name	Site Code	Latitude	Longitude	Altitude (m)	Deployment	Notes
a644	RF1	66:59.2732 N	48:43.5095 W	1,336	26/06/10–08/09/10	Data quality is good with high signal to noise ratios. Little movement of the geophone due to ablation ice creep effects.
a 514	RF2	66:59.3519 N	48:42.0099 W	1,335	26/06/10–08/0910	Data quality is good high signal to noise ratios. Little movement of the geophone due to ablation and ice creep effects.
a670	RF3	67:00.1500 N	48:44.4566 W	1,329	26/06/10–13/08/10	Data quality is good with high signal to noise ratios. Little movement of the geophone due to ablation and ice creep effects. Issue with geophone-logger connectivity between 18/07/10–25/07/10 leading to poor data quality for this period. The logger toppled over in late August after camp was closed for the season and hence power supply failed.
aa1a	RF4	66:59.5672 N	48:44.3694 W	1,327	26/06/10–08/09/10	Data quality is good with high signal to noise ratios. Some movement of the geophone due to ablation and ice creep effects.
a484	RF5	67:00.7980 N	48:41.9759 W	1,332	26/06/10–08/09/10	Suffered from poor coupling of the geophone after initial deployment leading to poor signal to noise and resonance of the signal during this period. The geophone experienced some severe ablation effects and movement early on in the season. On the whole the data quality is good.
aae9	RF6	66:59.7088 N	48:41.6750 W	1,341	26/06/10–30/08/10	Suffered from poor coupling of the geophone after initial deployment leading to poor signal to noise and resonance of the signal during this period. The geophone experienced some severe ablation effects and movement early on in the season. On the whole the data quality is good. The logger toppled over in late August after camp was closed for the season and hence power supply failed.

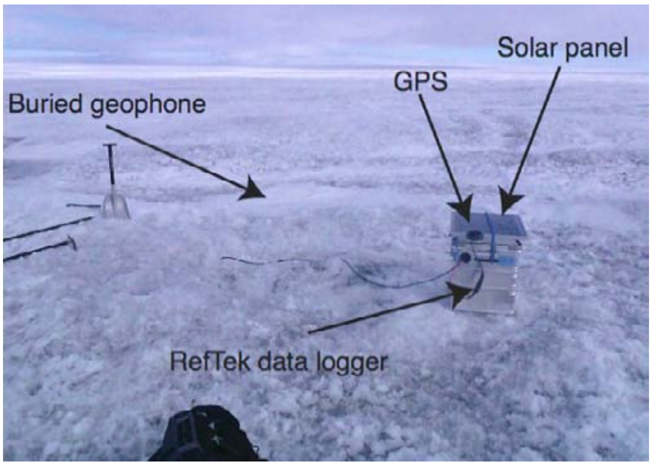

Figure 2-38. *Photograph of a deployed/serviced seismometer. The station has been buried up to the firn water-table and covered with ice chippings. Note that the GPS for the timing and solar panel are mounted directly onto the box housing the RefTek logger. Photograph by Glenn Jones.*

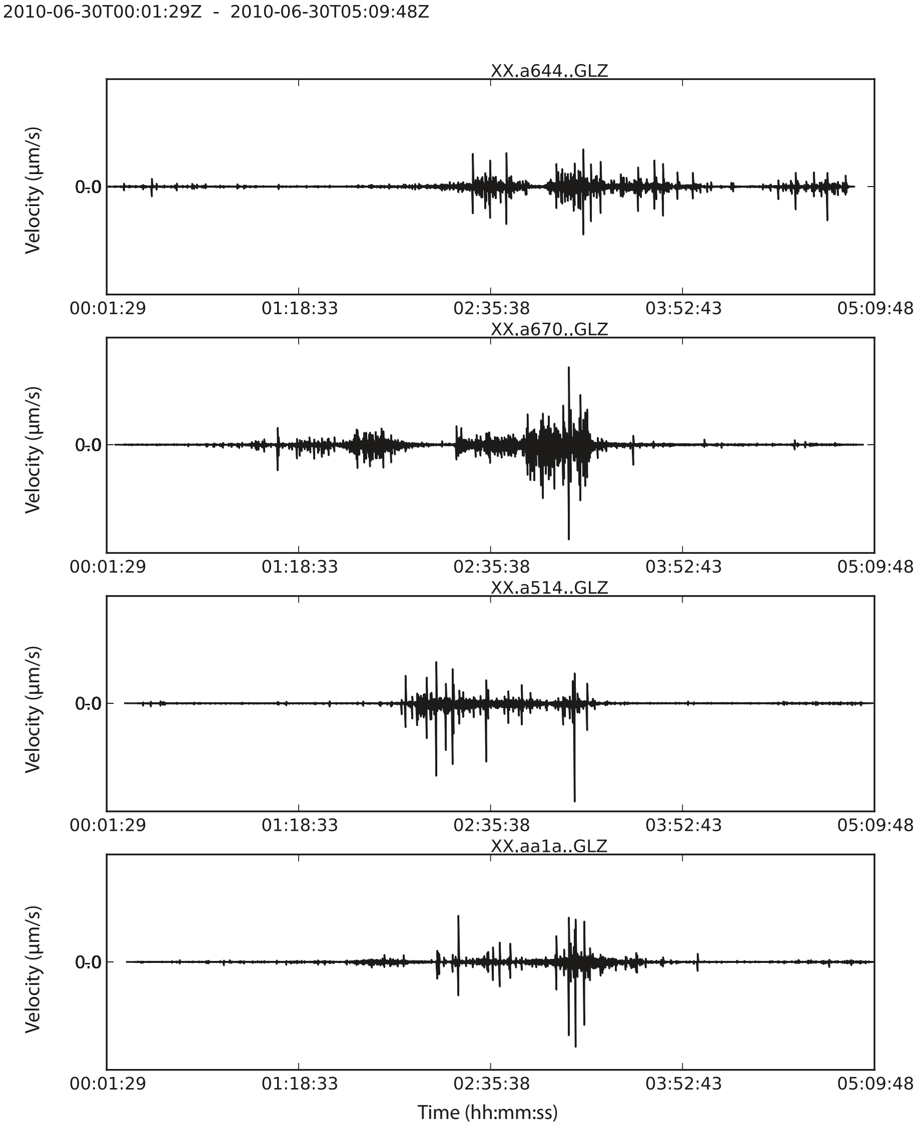

Figure 2-39. *Vertical component velocity seismogram of an approximate 4.5 hour period of lake drainage (30th of June, 2010). Notice the difference in the location of the seismic tremor associated with the lake drainage across the array. Also, large amplitude events are not necessarily seen from station to station.*

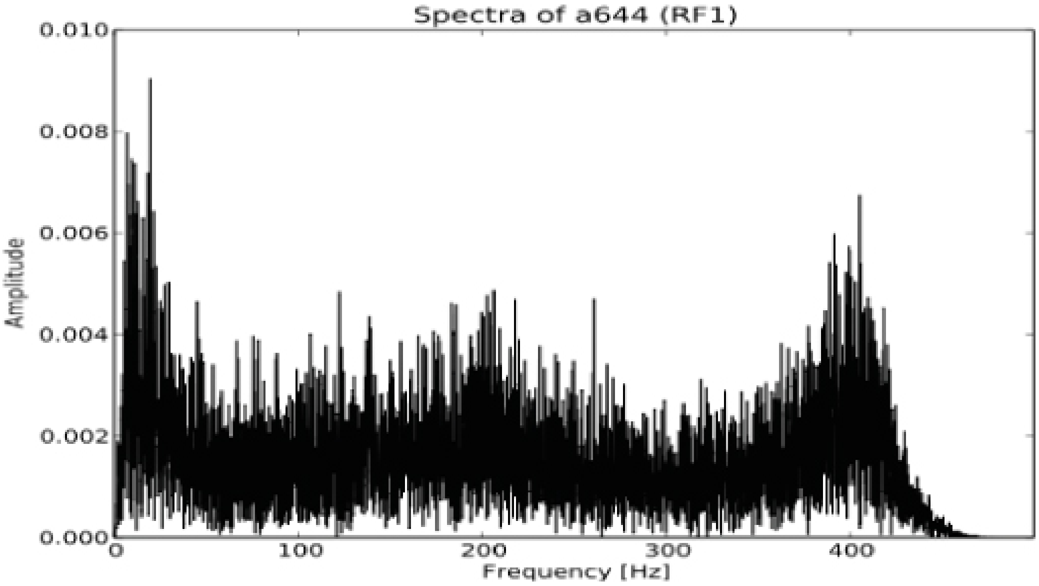

Figure 2-40. *Frequency spectra of the vertical component of station a644 (RF1) during the 4 hour period of lake drainage (01:00 to 05:00 30th of June, 2010). Note that the dominant frequency is < 50 Hz with a secondary peak at > 300 Hz.*

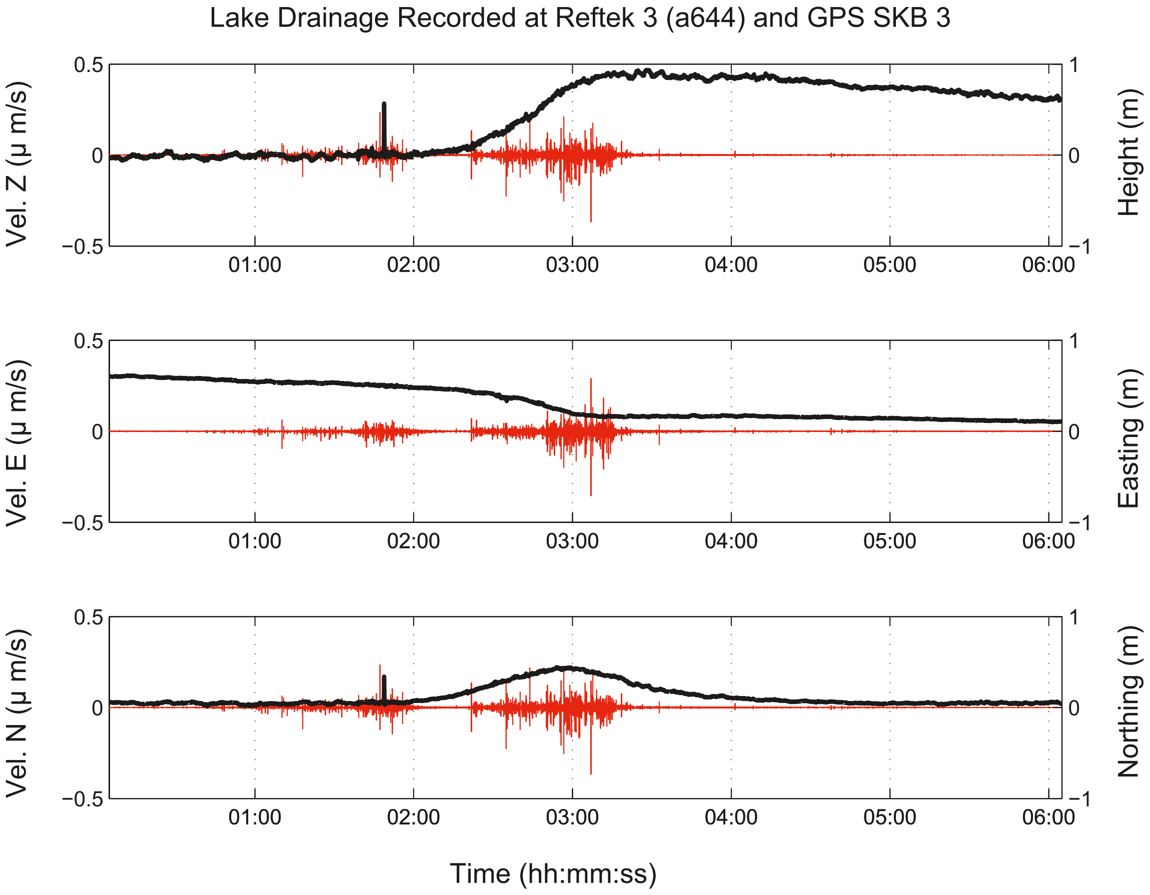

Figure 2-41. *Three-component velocity seismogram (red time series) recorded at a670 (RF3) and GPS (black time series) recorded at SKB3.*

Source location

The location of a seismic event (earthquake, microseismic event, or icequake) is the first and most basic step in any study of seismicity on any scale. In general, earthquakes are solved for their hypocentral parameters, defined by spatial coordinates (x_0, y_0, z_0) and origin time (t_0), assuming a velocity model and minimizing the difference between the observed and calculated travel times recorded on a number of stations (e.g. Lee and Stewart 1981). The first stage in this analysis is the accurate picking of the arrival times of the seismic event. Traditionally this function has been done by a trained analyst. Recent improvements in computer power and data storage have lead to the development of a number of automated techniques (e.g. the ratio of short- to long-term averages, STA/LTA; Withers et al. 1998).

An initial manual inspection of the data showed that many small and often overlapping events within the space of a few seconds were present. Figure 2-42a shows a 2-second time period during lake drainage. Three high frequency events are identified, with the largest amplitude events followed closely by a surface wave, suggesting that these events occurred close to the surface and to station a644. Sandwiched between the two large amplitude events is a small amplitude high frequency event. The lack of a surface wave following this event, and the low amplitude, suggest that this may have originated from depth or some distance away. It is also of note that there appears to be no clear S-wave in the data, suggesting that this has not yet had enough time to separate from the P-wave coda in the large amplitude high frequency events, or that the predominant mechanism of these types of events is tensile opening or closure producing little shear. The different waveforms are frequency dependent, with events associated with the fracturing of the ice having very high frequencies of > 300 Hz, whilst the surface waves have frequencies of < 50 Hz (Figure 2-42b). Some data loss through aliasing may occur as some of the signal bandwidth is close to the Nyquist frequency of 1 kHz sampling interval. However, we believe that the effect of aliasing is minimal. The frequency content of the waveforms seen in Figure 2-42 agree with the spectral content of the complete lake drainage time series in Figure 2-40 with the surface waves being the most abundant wave-type followed by the hydraulic fracture type events.

To detect and accurately pick the arrival times of different waveforms, and, in particular, the weak amplitude high frequency events, an automated procedure that would be sensitive to these properties was required. A wavelet transform based approach used in audio-engineering but not, to our knowledge, used in seismology, was applied (e.g. Bello et al. 2005). Wavelet transforms do not suffer from the trade-off between time and frequency localization experienced by traditional Fourier analysis. The wavelet transform is capable of "zooming" into a particular region of a signal using different wavelet scales (frequency bands). The rate of decay of a signal over a number of wavelet scales provides information about the "local" strength of the signal, which allows for the detection of weak amplitude seismic signals.

A wavelet coefficient tree is constructed using the "lifting" scheme and using a Haar wavelet. The Haar wavelet is a box-like wavelet, which is sensitive to sudden changes in the signal and therefore well suited to the onset detection of seismic signals. The detection function for the wavelet tree is known as the regularity modulus and is a local measure of the regularity of a signal, as defined in Bello et al. (2005). Tests against the commonly used STA/LTA picked (e.g. Withers et al. 1998) showed that the wavelet transform procedure yields comparable detection rates, with an improved arrival time pick accuracy.

Many thousands of events were detected during lake drainage, and further more detailed manual inspection of the data was conducted. It was noted that although it was possible to detect the onset of different waves, the association of these arrival times with a particular common event was almost impossible. Additionally, geometrical spreading effects lead to a loss in the amplitude of a given waveform (e.g. high frequency low amplitude event; Figure 2-42b) and may lead them to be overprinted by larger "local" events. This phenomenon of many thousands of overlapping events has been seen at other glaciers (e.g. Grubengletscher, Valais, Switzerland[1]). Due to this difficulty in the identification and association of various seismic phases with a discrete event, an alternative method to the determination of the seismic event hypocentre is required.

---

[1] Personal communication with A. Brisbourne, SeisUK

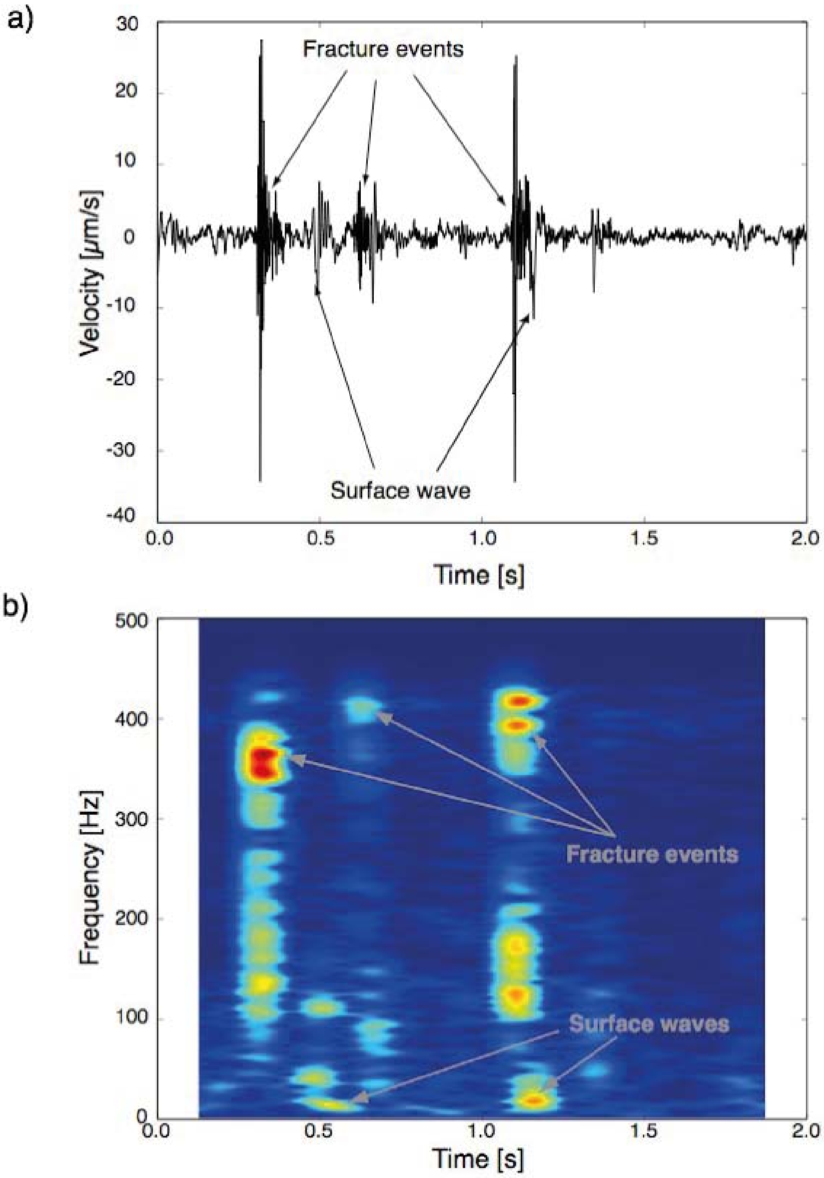

***Figure 2-42.** a) Example of a 2 second recording of the vertical component of station a644 (RF1) at approximately 2am (June 30th) during lake drainage. Three fracture events are seen in the seismogram. The two larger events are followed by a surface wave. Note that there are no clear S-wave separation with these events suggesting that they have not had time to separate from the P-wave, or that the predominant mechanism of these types of events is tensile opening or closure. b) Time-frequency representation of a). We note that the fracture events are typically high frequency with a broad frequency spectrum from 100 Hz to Nyquist with large amplitudes at >350 Hz. The surface waves have a narrow spectrum with frequency contents of <50 Hz.*

Recently, a number of migration based methods have been presented that do not require arrival times to be picked and are capable of locating weak and/or distal events with low signal to noise ratios. In general, these migration methods are based on back-propagating the signal in either time or space with the point of maximum energy being the hypocentre (e.g. Chambers et al. 2010). However, these methods tend to suffer from high computational cost and require a dense network of seismic stations to accurately perform the calculation. Another method of locating overlapping seismic events with low signal is by using the seismic amplitudes. This method has proven to be highly successful in mapping magma transport in active volcanoes (e.g. Battaglia and Aki 2003, Taisne et al. 2011). The physics of magma transport is similar to the process of hydraulic fracture, suggesting that the amplitude based approach would be applicable to the imaging of the lake drainage. The approach uses the differences in seismic amplitudes recorded at a number of different stations. The method relies on modelling the decay of the seismic amplitude along the ray-path and matching this to the observed amplitudes. The source is then the point which minimizes the observed and modelled amplitudes in a least-squares sense; this is also defined as the hypocenter (e.g. Battaglia and Aki 2003, Taisne et al. 2011).

Future Work

An amplitude source location procedure (e.g. Battaglia and Aki 2003, Taisne et al. 2011) has been written and is currently being implemented. The approach uses a preliminary grid search to find the initial source location and then uses the Levenberg-Marquardt algorithm to refine the solution. Once accurate hypocenters are determined, the data will be integrated with GPS and pressure sensor data to understand the hydrologic and dynamical response of the glacier to seismic events. More traditional source location procedures will be applied to the complete dataset, along with integration with the GPS data to understand the glacier relaxation response post-drainage. The microseismic hypocenters will serve as inputs into hydrological modelling.

Moulin Site

A large moulin site (Figure 2-43) was selected approximately 9 km south-west of the lake drainage site. The moulin has an approximate diameter of 10–15 m, with an estimated water input of 100 cumecs. An array of 6 geophones were deployed around the moulin to image any seismic activity associated with the downward movement of water. The array was positioned down-glacier flow of the moulin because it was hypothesised that any englacial conduit pathway would tend to flow in this direction. The aperture of the array was ~1 km, which corresponds to the approximate ice thickness, allowing for the accurate location of any events from the bed-rock-glacier interfaces.

The data were acquired using six 4.5Hz 3-component geophones and SAQS data-loggers (Figure 2-36, Figure 2-44 and Table 2-8) . The seismometers were deployed with GPS timers, from July 22nd until September 8th and ran continuously at a sampling interval of 1,000 Hz. Again, due to the high ablation rates, the solar panels and GPS timer were mounted directly on the box housing the data-logger. The geophones were regularly serviced (every 1–2 days) until August 10th.

Figure 2-43. *Photograph of the moulin at the moulin site. Photo by Glenn Jones.*

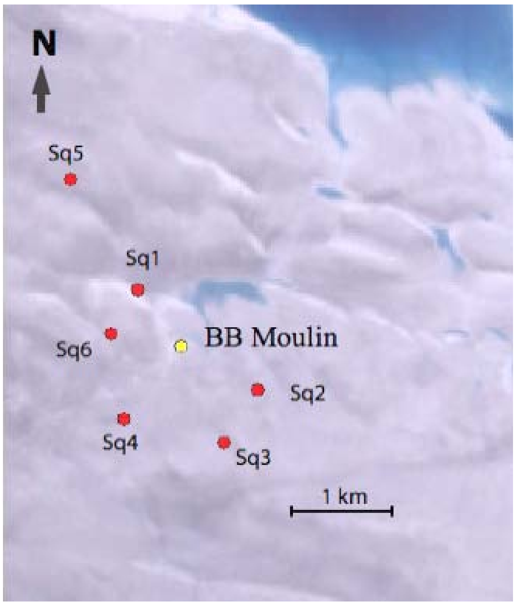

Figure 2-44. *Landsat image of the location of the moulin and seismic network.*

Table 2-8. Location of the stations for the monitoring of the moulin.

Site Code	Latitude	Longitude	Altitude (m)	Deployment	Notes
1	66:56.363 N	48:49.172 W	1,341	22/07/10 –08/09/10	Data quality is good
2	66:55.850 N	48:47.758 W	1,341	22/07/10–08/09/10	Data quality is relatively good
3	66:55.591 N	48:48.199 W	1,332	22/07/10–08/09/10	Data quality is relatively good
4	66:55.726 N	48:49.402 W	1,328	22/07/10–08/09/10	Data quality is relatively good.
5	66:55.912 N	48:49.954 W	1,339	22/07/10–08/09/10	Data quality is relatively good.
6	66:56.153 N	48:49.515 W	1,329	22/07/10–08/09/10	Data quality is relatively good.

Future Work

No processing has been done thus far on the data other than basic quality control. The first stage of any processing will be to locate any seismic events associated with the activity of the moulin. Detailed analysis of correlated high-frequency noise using seismic interferrometry (e.g. Wapenaar et al. 2010) may allow for the imaging of the moulin conduits, or steps in the conduit, and could provide further insight into the architecture of these features.

2.8 Coupled meltwater production – ice flow modelling

Understanding the non-linear relationship between surface meltwater and glacier speedup is essential in projecting glacier and ice sheet contributions to sea-level. Critically, the ice dynamic response to meltwater is dependent on subglacial drainage morphology and evolution. The key variable of interest at the ice-bed interface is the effective pressure because this controls the ability of the glacier to slide. The distribution of effective pressure (the difference between ice overburden and subglacial water pressure) at the glacier bed is directly related to the configuration of the subglacial drainage system. The effective pressure also acts at the subglacial and groundwater exchange and, thus, is of vital interest in aiding the study of groundwater flow beneath ice sheets.

Numerical Model

Subglacial Drainage

Subglacial drainage systems are usually classified into two distinct forms: distributed flow and channelized flow. A distributed drainage network consists of a network of interconnected cavities; this system exhibits inefficient ('slow') flow and is representative of the winter season. A channelized system consists of an arterial network of water-filled conduits; this is a more efficient ('fast') drainage system, typical of conditions in summer.

The inefficient system is modelled as an aerial averaged macroporous water sheet thickness, *h*:

$$\frac{\partial h^{\mathrm{s}}}{\partial t} + \frac{\partial q^{\mathrm{s}}}{\partial x} = \frac{Q_{\mathrm{G}} + u_{\mathrm{b}}\tau_{\mathrm{b}}}{\rho L} + \dot{b}^{\mathrm{s}} + \chi^{\mathrm{s:c}}, \qquad 2\text{-}1$$

with a non-linear Darcy Flux:

$$q^{\mathrm{s}} = -\frac{Kh^{\mathrm{s}}}{\rho_w g}\frac{\partial \psi^{\mathrm{s}}}{\partial x}, \qquad 2\text{-}2$$

and an empirical expression relating sheet thickness to subglacial water pressure:

$$P^{\mathrm{s}} = \rho g H\left(\frac{h^{\mathrm{s}}}{h^{s}_{c}}\right)^{7/2}, \qquad 2\text{-}3$$

The efficient drainage system is modelled as a semi-circular ice-walled (water-filled) conduit.

This system has a kinematic condition for the channel walls:

$$\frac{\partial S}{\partial t} = -\frac{Q^{\mathrm{c}}}{\rho L}\left(\frac{\partial \psi^{\mathrm{c}}}{\partial x} - c_{\mathrm{p}}\rho_{\mathrm{w}}\Phi\frac{\partial P^{\mathrm{c}}}{\partial x}\right) - 2AS\left(\frac{\rho g H - P^{\mathrm{s}}}{n}\right)^{n}, \qquad 2\text{-}4$$

A turbulent flow law:

$$Q^{\mathrm{c}} = -\left(\frac{8S^{3}}{P_{\mathrm{wet}}\,\rho_{\mathrm{w}}\,f_{\mathrm{R}}}\right)^{1/2}\frac{\partial \psi^{\mathrm{c}}}{\partial x}\left|\frac{\partial \psi^{\mathrm{c}}}{\partial x}\right|^{-1/2}, \qquad 2\text{-}5$$

And a balance equation for water mass:

$$\frac{\partial P^{\mathrm{c}}}{\partial t} = -\frac{1}{\gamma S}\left(\frac{\partial S}{\partial t} + \frac{\partial Q^{\mathrm{c}}}{\partial x} + \frac{Q^{\mathrm{c}}}{\rho_{\mathrm{w}} L}\left(\frac{\partial \psi^{\mathrm{c}}}{\partial x} - c_{\mathrm{p}}\rho_{\mathrm{w}}\Psi\frac{\partial P^{\mathrm{c}}}{\partial x}\right) - d_{\mathrm{c}}\left(\dot{b}^{\mathrm{c}} + \chi^{\mathrm{s:c}}\right)\right), \qquad 2\text{-}6$$

where *S* is channel cross-sectional area, *Q* the volume flux, P^c the water pressure in the conduit. The two drainage systems interact through the exchange term $\chi^{s:c} = \chi\ s{:}c\ (P^s - P^c)$. Further details on the model equations and particular parameters can be found in (Pimentel and Flowers 2010).

Ice Dynamics

Variability in basal topography, together with a patchwork of stick/slip zones and regions of fast basal sliding, suggest a strong contribution from longitudinal stresses to the force-balance along the Russell glacier flowline. These stresses are properly accounted for in the so-called higher-order ice dynamic models, of which we use the Blatter-Pattyn first-order approximation (Blatter 1995). This non-linear system requires successive iterations on flowline velocity, u = u(x; z), and viscosity, $\eta = \eta(x; z)$:

$$4\frac{\partial}{\partial x}\left(\eta\frac{\partial u}{\partial x}\right) + \frac{\partial}{\partial z}\left(\eta\frac{\partial u}{\partial z}\right) = \rho g\frac{\partial s}{\partial x}, \qquad 2\text{-}7$$

$$\eta = \frac{1}{2}A^{-1/n}\left[\left(\frac{\partial u}{\partial x}\right)^{2} + \frac{1}{4}\left(\frac{\partial u}{\partial z}\right)^{2} + \dot{\epsilon}_{0}^{2}\right]^{(1-n)/2n}. \qquad 2\text{-}8$$

Boundary Conditions

Effective pressure-dependent sliding at the base of an ice mass can have a leading-order effect on the mechanics of flow. A phenomenological sliding rule in the form of a regularized Coulomb friction law (Schoof 2005, Gagliardini et al. 2007) is used to dynamically couple the subglacial water pressure to basal sliding motion (Flowers et al. 2011, Pimentel and Flowers 2011, Pimentel et al. 2010):

$$\tau_b = CN \left(\frac{u_b m_{\max}}{\lambda_{\max} A N^n + u_b m_{\max}} \right)^{1/n}, \qquad 2\text{-}9$$

where $N = \rho g H - P^s$ is the effective pressure. The fixed ice surface s is treated as a stress-free interface:

$$4 \frac{\partial s}{\partial x} \frac{\partial u}{\partial x} - \frac{\partial u}{\partial z} = 0. \qquad 2\text{-}10$$

The fixed terminus position is prescribed with zero ice thickness and zero ice velocity, whereas the glacier head is considered an ice-divide, $u = 0$.

Input Data

A Russell glacier flowline representing planar flow has been extracted from a draft SPA radar data composite, which runs from the terminus to the ice-divide and bisects numerous kGPS and AWS stations. This flowline coincides with a DTU flight line for a large portion; however, the upper section extends beyond the extent of the DTU data, and therefore the SPA data and the Bamber DEM are used from 120 km distance from the ice terminus to the ice divide (Figure 2-45a). Meltwater and run-off for the Russell Glacier catchment have been generated from September 1st, 2008 to August 31st, 2010, plotted along the flowline (Figure 2-45b).

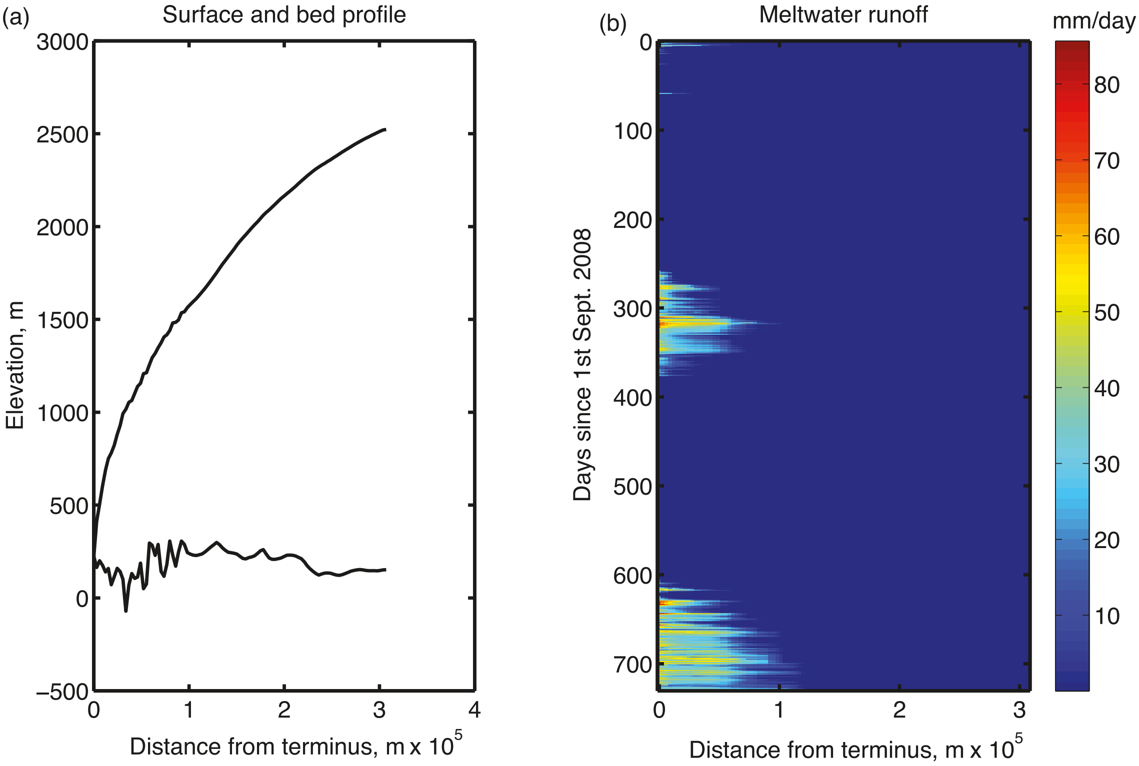

Figure 2-45. *a) Russell Glacier flowline surface and bed profile, (b) Russell Glacier catchment meltwater runoff.*

Preliminary Model Results

To give an idea of the sensitivity range of modelled velocities to ice softness, we show surface velocity with temperate ice (a homogenous value of flow-law parameter, $A = 2.4 \times 10^{24}$ Pa^{-3} s^{-1} [3], the black line in Figure 2-46) and colder ice (vertically averaged A values based on modelled ice temperatures derived from Brinkerhoff et al. 2011 does not include ice core data; the red line in Figure 2-46). Note that the surface velocities are derived using a no-slip basal boundary condition (i.e. deformational velocities only). Basal sliding is likely to be significant below the ELA, particularly during the early melt season. To incorporate basal sliding, the force-balance key friction law parameters, *m_max* and *λ_max,* need to be adjusted according to the minimum seasonal surface ice velocities observed.

The subglacial drainage system model (uncoupled from ice dynamics) has been forced using the 2009–2010 meltwater runoff (Figure 2-47). The response of the subglacial system to seasonal meltwater input can be modulated somewhat within the model by tuning parameters such as K, hs c, S. These parameters can be adjusted in hydrologically coupled ice-flow simulations to find the best model match to the timing and magnitude of seasonal speed-up, as observed from kGPS measurements along the flowline.

Future Modelling Plans

TerraSAR-X and GPS velocities along the flowline will be used to constrain model output and tune for unknown parameter values in the friction-law and subglaical drainage components. Hydrologically-coupled ice-dynamic model simulations, forced with the 2009 and 2010 meltwater runoff data, can then be conducted. The flowline model will be used to determine the extent of hydrologically-forced seasonally enhanced glacier flow speeds at Russell. A comparison of the modelled ice-dynamic response to meltwater production in 2009 and 2010 will be studied. A further step will be to direct meltwater into the modelled subglacial drainage network based on knowledge of lake drainage scenarios, and to examine whether these events play a significant role over a seasonal cycle.

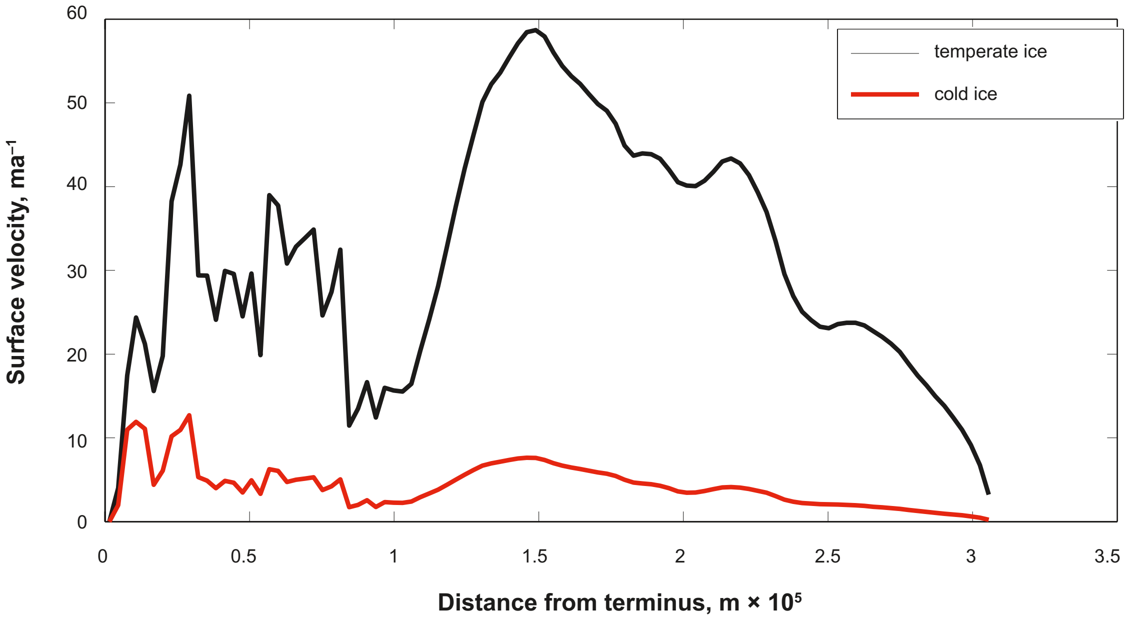

Figure 2-46. *Modelled surface velocities using a no-slip basal boundary condition and varying Glen's flow law parameter.*

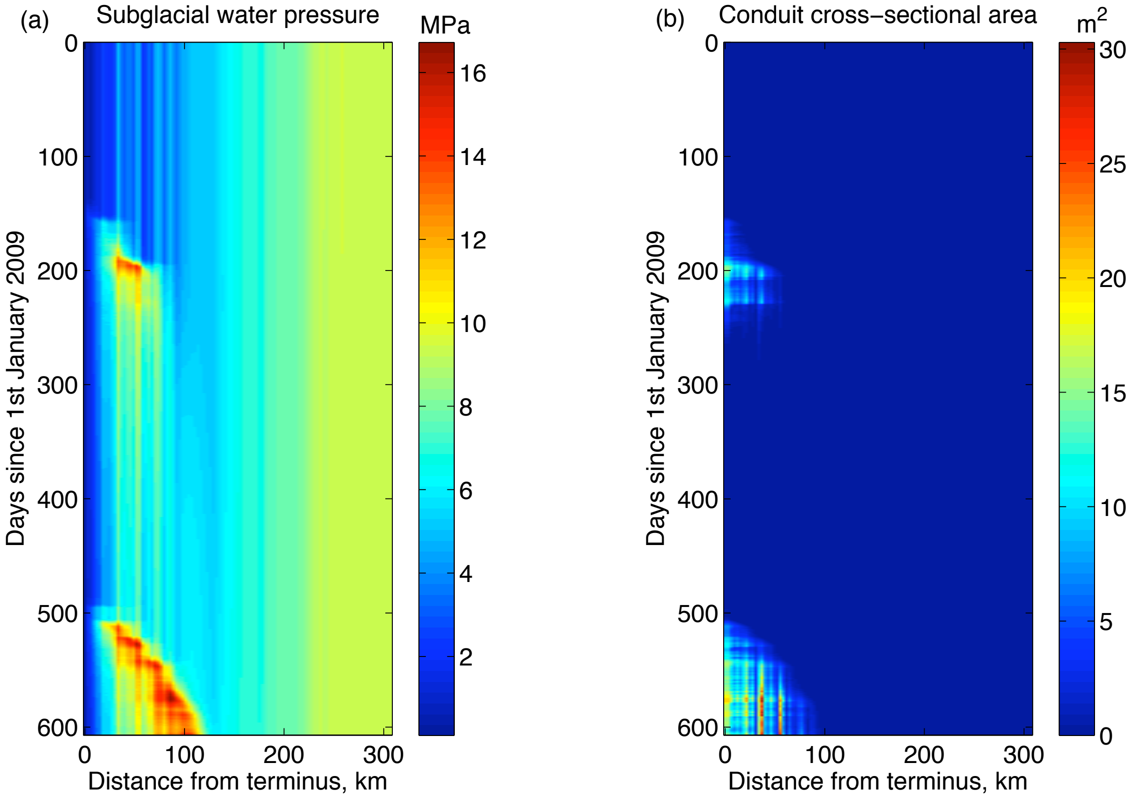

Figure 2-47. *Subglacial drainage dynamics for 2009–2010: (a) water pressure, (b) conduit cross–sectional area.*

2.9 Summary

Climate

- The three Automatic Weather Stations functioned perfectly over the year.
- Data indicate that 2010 was extremely warm in comparison with previous years.
- Melt in 2010 was at least double that of 2009, and was at least one month in advance.
- Distributed energy balance melt and bulk runoff modelling yields good agreement when compared with time-series of catchment wide (Watson River) discharge data.

Remote Sensing

- Additional Landsat7 scenes have been added to the existing remote sensing archive, permitting high-resolution mapping of lakes and surface structure.
- Automatic analysis of daily MODIS scenes has enabled temporal monitoring of the supraglacial lake area and meltwater volumes, in addition to capturing the timing and magnitude of lake drainage events.
- Nine successful TerraSAR-X time-slices from 2010 provide detailed information of spatial and temporal flow velocity patterns within the Russell glacier catchment.
- A structural-hydrological map of the Russell glacier catchment has been digitized from successful hydrological modelling, which adequately identifies moulins, lakes, surface channels and other structural flow features.

Ice Dynamics – kGPS

- Initial results from the kGPS analysis show ice surface velocity and height variations on diurnal, intra-annular, and lake tapping time scales.
- Surface meltwater forcing of basal dynamics and speed-up occurs at least 90 km inland.
- The kGPS, situated at S10, 150 km inland, shows little intra- or inter-annular variability in velocity, and represents an ice dynamic control point.
- Using TRACK software, a horizontal position uncertainty of ± 1.2 cm, vertical position uncertainty of ± 4 cm, and a velocity uncertainty of ± 7 m/yr, is achievable.

Radar

- Approximately 500 km of impulse radio-echo sounding data were collected (25% less than was planned) in short time window due to delayed logistics (Icelandic ash cloud) and the early onset of intense melt.
- The collected data is of high quality, and ice thickness and bed return power have been extracted from all the acquired profiles.
- Indication of the existence of a perennial subglacial water body under the Greenland Ice Sheet.
- DTU/GEUS airborne dataset of ice thickness is now available over Russell Glacier.
- The NASA ICEBridge airborne radar campaign designed to yield high density ice thickness and surface data over Russell glacier had limited success due to instrumental issues; analysis, however, is still on-going.

Active Seismics

- Six active seismic lines were collected at four sites on Russell Glacier during July 2010. One 26 hr AVO temporal experiment conducted to compliment these data.
- Five seismic sections have been processed using 2-D Kirchoff pre-stack migration in addition to noise removal filters. One section has been stacked with an NMO moveout function followed by Stolt f-k migration.
- All the sections presented here have been corrected for surface elevation factors. AVO analysis on these data is currently underway.
- Strong indication of the presence of a subglacial basin in the region of the subglacial lake identified in the spring 2010 radar campaign. AVO analysis is necessary to establish whether the basin is water- or sediment-filled, but initial analysis suggests that three distinct layers exist at the bed. Appears to be a mixture of sediment and bedrock at the ice-bed boundary with steep topography leading to a shallow basin.
- The basal topography is characterized by high variability in relief and saturation.

Passive Seismics

- The hydraulic fracture propagation associated with the rapid drainage (tapping) of a large supraglacial lake was successfully monitored using a network of kGPS and passive seismic stations.
- Many thousands of seismic events were detected over the duration of the lake tapping event, with a variety of different waveform characteristics suggesting different mechanisms at work during fracturing.
- Qualitative analysis of the kGPS and seismic time-series indicates that the fracture originated in the North-West and propagated towards the South-West of the lake.
- Seismic amplitude methods employed in volcanic studies have been adapted to locate the seismic events in three dimensions. This analysis will reveal the nature and rate of hydraulically driven englacial fracture propagation to the base of the ice sheet.

2.10 2011 plans

In 2011 SPA will continue to focus on remote-sensing and field-based monitoring and specific experimental campaigns to improve our knowledge and understanding of surface to basal hydrodynamic coupling. We wish to continue our aquistion of high temporal and spatial resolution remotely sensed data in the form of Terrasar-X, Landsat, MODIS and SPOT imagery/data. Analyses will be improved to yield velocity and surface lowering distributions, in addition to the mapping of the evolution of surface water storage and release in supraglacial lakes. SPA will also acquire high resolution terrestrial LIDAR data from the front of Russell Glacier in order to both calibrate and validate ARSF and Icebridge campaigns conducted in 2007, 2009 and 2010. These data will yield detailed residual maps of surface lowering from which the long term climatic/dynamic response of this sector of the Greenland Ice Sheet can be determined.

Field-based monitoring will continue with significant maintenance and improvement of the AWS and kGPS network. In April 2011, SPA will conduct a sustained ground based radar campaign to complement and extend the 2010 deep look radar acquisition. Ideally, we will retrieve an additional 1,500 km of profile, extending the 2010 transects up-glacier. Ample time and contingency for logistical difficulties is built in to this campaign and it is intended that the team will finish with a radar traverse to the upper Raven landing site, 250 km inland, where SPB propose to drill in 2012. The kGPS network will be extended, maintained and updated. We also wish to deploy a combined kGPS and passive seismic experiment focused on an ultra-large moulin that drains lake ice-T and was identified and instrumented at the end of 2010 with a pressure sensor and thermistor string. We will use high-rate kGPS (1Hz) to complement the passive seismological study of moulin initiation (and re-initiation). There are no published accounts of high-rate kGPS applied to ice dynamics and glaciology, but in combination with the passive seismics network, the technique is likely to reveal high temporal frequency data on stick-slip events and mechanical fracture. Shake-table tests of high-rate kGPS (up to 10 Hz) by Wang et al. (2009) et indicate that the accuracy of kGPS is independent of the sampling frequency. Depending on the nature of the melt-season, this equipment (on loan from SeisUK) will be re-deployed at a higher supraglacial lake site in order to capture a hydro-fracture event associated with rapid lake tapping at high temporal frequency.

3 Sub-project B activities 2010

3.1 Introduction and objectives

The Greenland Ice Sheet is a modern-day analog to future ice sheets that could cover Scandinavia and Canada as they have in the past. The Greenland setting, therefore, offers a unique opportunity for generating new scientific understanding about groundwater flow in the vicinity of ice sheets. This information is critical to successful design and risk assessment of nuclear waste repository sites located in northern regions susceptible to future glaciations.
Much remains to be learned about the glaciological processes and hydrology of the Greenland Ice Sheets. The interactions between ice, water beneath the ice, and the groundwater system near ice sheets are particularly poorly known. A comprehensive understanding of the ice sheet basal hydrology is an essential first step to understanding ice sheet/groundwater interactions. Unfortunately, the basal boundary of the Greenland Ice Sheet (and all ice sheets) has received very little prior investigation. Two related specific issues needing further investigation are the thermal state of the ice sheets bed, and the hydrological conditions at the bed. Both are related, and both potentially play a strong role in ice sheet/groundwater interactions.

Prior Information

Direct observation of basal temperature has been made only at the base of a few ice-coring holes drilled to the bed, and in several hot-water drilled holes near the margin of western Greenland. Frozen or melted conditions have been inferred from the analysis of reflectivity of radar bed returns (Oswald and Gogineni 2008), and from analysis of internal layer sequences (Fahnestock et al. 2001). Unfortunately, existing observations provide an incomplete picture of the overall basal conditions (Figure 3-1).

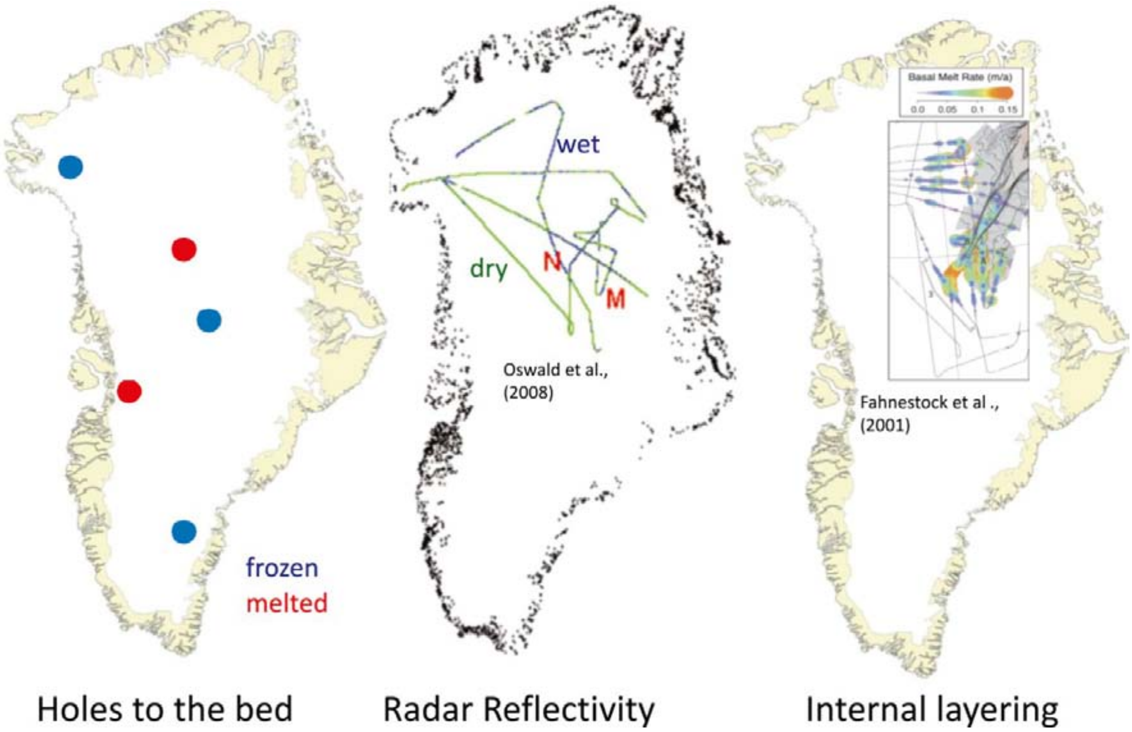

Figure 3-1. *Prior direct and indirect observations of the thermal state of the Greenland Ice Sheet bed. Left panel: red dots indicate melted conditions; blue dots indicate frozen conditions. Data interpreted from multiple sources related to ice core studies. Center panel: green lines indicate frozen bed conditions; blue lines indicate melted bed conditions. Figure compiled from Oswald et al. (2008). Right panel: basal melt rate indicated by color; no melt indicated by colorless solid line. Figure modified from Fahnestock et al. (2001).*

Measuring the basal conditions everywhere will never be possible. Remote sensing techniques have thus far been unsuccessful at quantifying basal temperature or water quantity, and there is little to suggest this problem will be solved soon. Modelling is therefore the only mechanism for extending the understanding of basal conditions away from the handful of point measurements; however, the model representation of basal conditions is dictated by numerous model assumptions and prescribed conditions, such as geothermal heat flux at the bed, ice deformation rate, basal sliding rate, surface climate, and surface mass balance. Relatively minor adjustments to the model representation of these factors can have a dramatic impact on model results. Not surprisingly then, modelled bed conditions do not necessarily agree with observations. In fact, different numerical models depict the basal temperature field of the Greenland Ice Sheet differently, owing to the complexities of the modelling and the lack of constraints on input data (Figure 3-2).

SPB Goals

Sub-project-B (SPB) has two primary research objectives, 1) to make in-situ measurement of subglacial hydrological conditions of the Greenland Ice Sheet, and 2) to conduct a suite of numerical modelling experiments focused on ice sheet dynamics with a particular focus on the basal boundary. The two objectives are closely related as the modelling work is used to direct field research, and the results from field research are used to improve the modelling work. The overarching purpose of both research objectives is to provide SKB-POSIVA-NWMO relevant information for nuclear waste disposal safety assessments; particularly, information related to basal conditions of the ice sheet which could impact groundwater flow beneath and adjacent to ice sheets. Specific results from this research are therefore directed toward this purpose, and research objectives remain flexible to react to new findings from project collaborators.

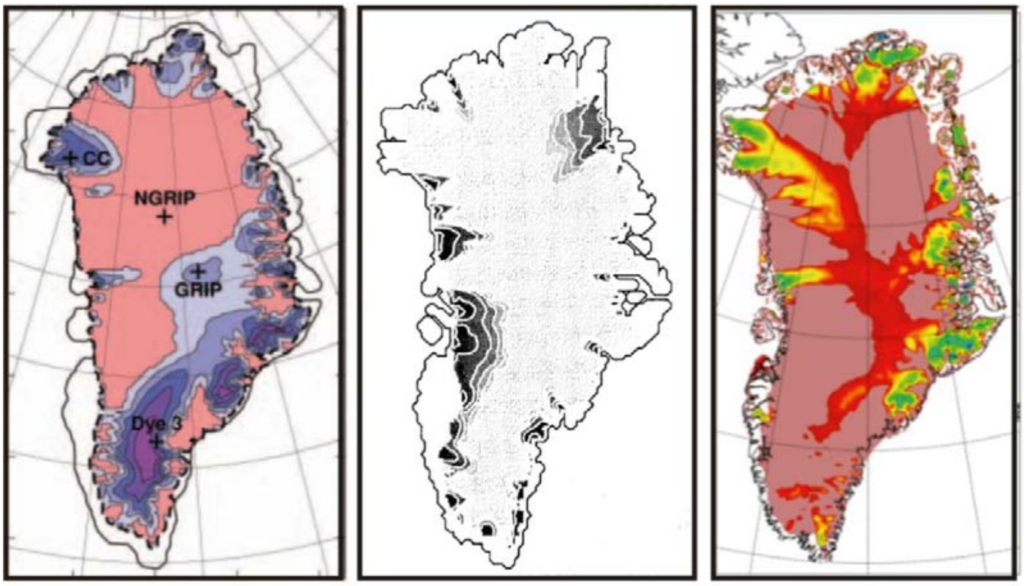

Greve (2005) Huybrechts (1996) CISM

Figure 3-2. *Three examples of melted bed conditions of the Greenland Ice Sheet bed as depicted by numerical ice sheet models. Left panel: the large pink area is at the melting point and other colors are colder. Figure modified from Greve (2005). Center panel: white stippled area is at the melting point, shaded gray areas are colder. Figure modified from Huybrechts (1996). Right panel: the large pink area is at the melting point and other colors are colder. Figure unpublished, generated for this project by J. Johnson.*

SPB Research Team

This project is directed by Dr. Joel Harper and Dr. Jesse Johnson at University of Montana, and Dr. Neil Humphrey at University of Wyoming. Toby Meierbachtol (Ph.D. candidate, University of Montana) is working on both modelling and field activities, thus providing a strong link between the two initiatives. Douglas Brinkerhoff (M.S. candidate, University of Montana) is conducting numerical modelling experiments and assisting with field research. Clair Landowski (M.S. candidate, University of Wyoming) is conducting field research focused on subglacial water chemistry. Luke Maddox and Chris Cox (M.S. candidates, University of Wyoming) have assisted with field research. Erin Johnson (B.S. candidate, University of Montana) assisted with field research, and is conducting a senior thesis related to satellite image tracking of snow melt and surface lake formation. Table 3-1 lists the sub-project B participants in 2010.

Table 3-1. List of SPB participants.

Participant	Position	Affiliation	GAP funding
Joel Harper, Ph.D.	Professor	University of Montana	x
Neil Humphrey, Ph.D.	Professor	University of Wyoming	x
Jesse Johnson, Ph.D.	Professor	University of Montana	x
Toby Meierbachtol	Ph.D. candidate	University of Montana	x
Claire Landowski	M.S. candidate	University of Wyoming	
Doug Brinkerhoff	M.S. candidate	University of Montana	
Chris Cox	M.S. candidate	University of Wyoming	
Luke Maddox	M.S. candidate	University of Wyoming	
Erin Johnson	B.S. candidate	University of Montana	

3.2 Activities

Research during the second year of SPB was focused on seven main activities. Each of the activities, and results from the work efforts, are described individually below.

3.2.1 Deep-ice hot water drill design and fabrication

Dr. Humphrey spent a substantial portion of the reporting period designing and overseeing fabrication of a new hot water drill built specifically for this project. The drill is designed to be capable of drilling to at least 1,000 m depth at a relatively high rate, while remaining light weight and simple enough to operate that it can be moved and used by a small crew of researchers. The design work included calculating specifications for the power plant, the pumping system, the drilling hose, and engineering a cutting-edge drilling tower. The drill hose required custom manufacturing and a suitable manufacturer had to be identified. Dr. Humphrey then worked closely with the company during the manufacturing process. Additional time during 2010 was spent researching specifications and manufacturers of various components of the drill's power plant, such as heaters and generators.

The drill tower is a unique design and required custom manufacturing by the University of Wyoming machine shop. The main design challenge was to engineer a capstan drive wheel that would not damage couplings, and would allow controlled lowering into the hole and rapid withdrawal from the hole (Figure 3-3). Dr. Humphrey oversaw manufacture of the drill tower with daily meetings with machinists.

In addition to the drill, the University of Wyoming machine shop designed and manufactured several other devises for borehole experiments. These included: 1) a basal water sampler, 2) a basal sediment corer (aka, "the glomometer"), 3) a bed penetrometer, and 4) a borehole dye injector. All of the devices were designed to work with a mechanical winching system for rapid lowering and raising in boreholes.

Figure 3-3. The main drive wheel of the Greenland drill, under construction in the University of Wyoming machine shop. The drive wheel is 4ft (1.2 m) in diameter, and was milled from an original 4ft square (1.2 m^2) plate of 1.5in (3.8 cm) thick aluminum. Photo by Neil Humphrey.

3.2.2 Radar reconnaissance of drilling sites

To prepare for the field drilling campaign, all available radar data collected by CReSIS (University of Kansas) airborne radars were acquired (Figure 3-4). Unfortunately, data are limited in the vicinity of Isunnguata Sermia, the research area. Two flight lines, passing up-ice sheet from the proposed drill sites in 2010, suggest a deep trough runs east-west and potentially intersects the region of the centerline boreholes (Figure 3-4).

Data from the NASA 2009 ICEBridge flights, which also has airborne radar, were also acquired and analyzed. Unfortunately, these data were not useful because the radar sensor was not operating properly when flights were conducted over the area of interest. Dr. Harper attended several phone conference meetings and drafted a flight request for 2010 ICEBridge flights with both radar and surface laser (ATM) measurements. These flights were flown in May of 2010 but data were not available during the reporting period.

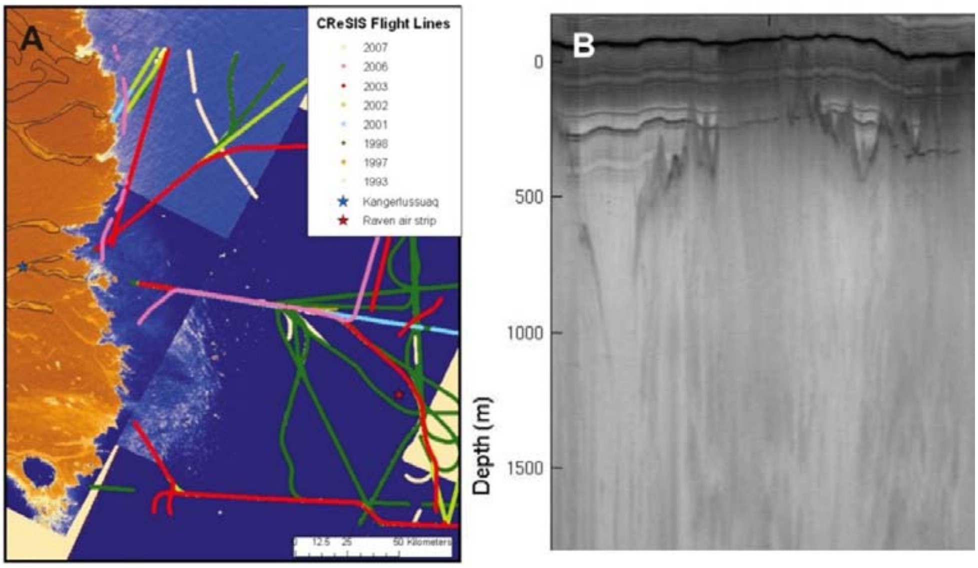

Figure 3-4. Map showing CReSIS radar data available for study area (left). Radargram from flight path crossing Isunnguata Sermia (right). Note the apparent deep topographic trough.

3.2.3 Transport of drill

In late March, a crew of five faculty and students packed the drilling and other field equipment into a rented cargo truck in Laramie, Wyoming. Dr. Humphrey then drove the truck to Stewart Airbase in Newburgh, New York. The equipment was offloaded and transported to Greenland on an Air National Guard C5A flight.

3.2.4 Sensor design and manufacture

Sensors and data loggers for the 2010 field campaign were custom designed and team members from both the University Wyoming and the University Montana manufactured them. The custom sensors and data loggers are low cost and have ultra low power consumption, which enabled installation of far more sensors than otherwise possible using commercially available equipment. The drawback of this approach is a substantial time investment in manufacturing the sensor strings. During the reporting period, the SPB team manufactured sensors and data loggers for the 2010 field campaign, including: 1) six water pressure transducers, 2) four thermistor strings, 3) one tilt meter string, 4) two borehole time-lapse cameras, and 4) a borehole video system. In addition, the team designed and worked with UNAVCO to design a fixed-monument GPS/weather station for installation in a high ice ablation (>4 m) location.

3.2.5 Field logistics planning

The SPB team devoted a significant portion of the reporting period to planning for the 2010 six week field campaign, the first field campaign of the project. Major planning initiatives included: 1) purchasing camping equipment and preparing other field camp logistics, 2) planning and purchasing food for the 8-person crew, 3) coordinating shipping of equipment from the USA to Greenland, and 4) planning helicopter support and ground transportation for the drilling equipment.

3.2.6 2010 summer field campaign

SPB conducted its first ice drilling campaign of the project from May 30th to July 11th, 2010. The six week campaign was carried out by an eight person crew: Dr. Harper, Dr. Humphrey, five graduate students, and one undergraduate student. The work effort consisted of: unpacking and preparing the equipment after shipping to Kangerlussuaq; moving the equipment by ground to a helicopter staging area near the ice sheet margin; transport of drilling equipment to three drilling sites and two camp sites; drilling and instrumenting 13 boreholes; ground transport of equipment back to Kangerlussuaq; and packing of the equipment for winter storage. See Section 3.5 for preliminary results of the campaign.

3.2.7 2010 fall field campaign

Dr. Harper and Dr. Humphrey returned to Greenland during the third week of September of 2010. The purpose of the trip was to download data from borehole data loggers and the GPS station, and to prepare data loggers and GPS instrumentation for winter. The first two sites were accessed by foot travel after driving to Pt 660 in a rented truck. The third site was accessed by helicopter charter from Kangerlussuaq.

3.2.8 Modelling activities

Modelling activities were initiated in autumn 2009. The team collected and processed boundary condition data sets, such as ice surface and bed topography, surface mass balance, and ice surface velocity measurements. A new steady-state, thermomechanically coupled, two-dimensional flowline model, which solves the Stokes equations, was developed. The model was applied to a profile through the study area extending from the ice divide to the terminus of Isunnguata Sermia. The modelling efforts investigated the sensitivity of the frozen/melted basal boundary to geothermal heat flux, and also cold ice advection resulting from ice motion, including basal sliding. The results were summarized in a manuscript which has been accepted for publication in Annals of Glaciology. For modelling results, see Appendix 1.

3.3 Field equipment and methods

3.3.1 Hot water drill

Hot water methods (Taylor 1984, Engelhardt et al. 1990, Humphrey and Echelmeyer 1990) were used to drill the boreholes. The Sub-project B drill was designed to create straight and vertical holes with smooth walls and constant diameter. To achieve this, a very heavy (~70 kg) drill stem is controlled by an electro-mechanical in-line drive. A load cell on the drill tower monitors the hanging weight of the drill stem to better than 1% precision, giving constant input to control the drilling speed. The 200 cm long drill stem has a tapered cross section along its length, from 3.4 to 1.4 cm. The unusually long and narrow stem causes turbulent mixing of hot water in the borehole, not just ahead of the drill tip, but also within upwelling water alongside the drill stem. The thermal decay length of the upwelling water is on the order of meters (Humphrey and Echelmeyer 1990), and, hence, the long and narrow end of the drill stem gives turbulent eddies space to grow as they move up the hole. Following drilling, the boreholes are inspected for smoothness and diameter using a borehole video camera (Harper and Humphrey 1995).

Water is heated and pumped to the drill stem by the power plant (Figure 3-5 and Figure 3-6). Water is captured in surface streams with a low pressure submersible pump. Two high pressure pumps raise the water pressure to about 1,100 psi, and four diesel-fired heaters raise the water temperature to about 80°C. A 4.5 kW gasoline generator supplies power for the heaters.

The entire drill system is as light weight and portable as possible, by design. No single component weighs more than 110 kg. This substantially reduces transportation costs, and enables the drill to be moved up to 100 m by a small field team (Figure 3-7). The penalty for the light weight design is that many components operate at design maximums, thereby creating some risk for failure.

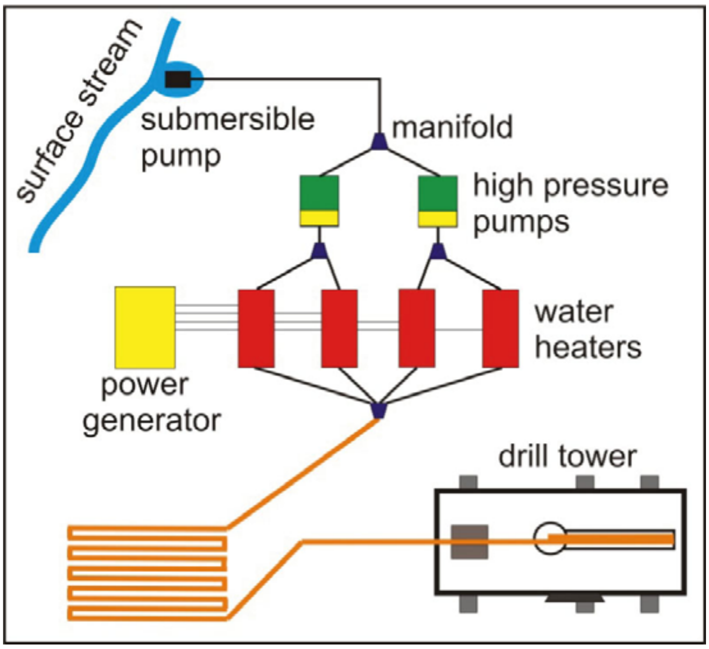

Figure 3-5. *Schematic of major hot water drill components.*

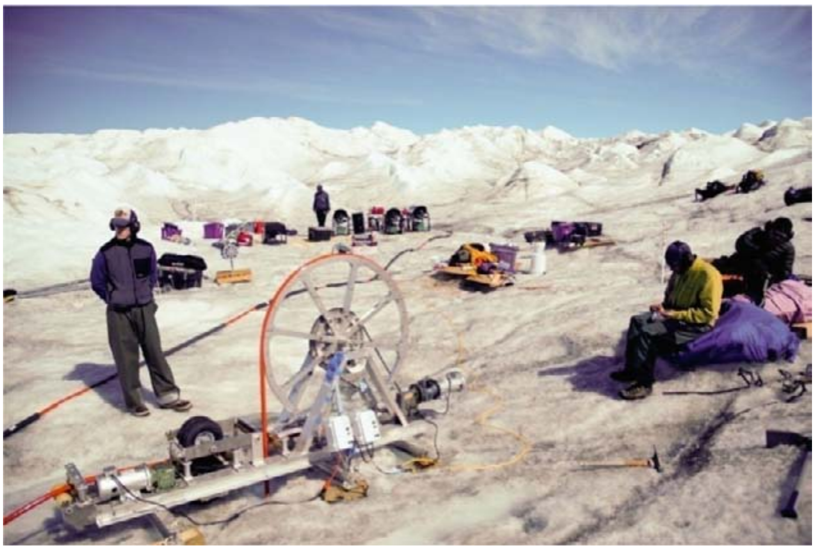

Figure 3-6. *Toby Meierbachtol and Chris Cox work next to the newly designed and fabricated drilling tower. The power plant for the drill is visible in the background. All equipment can be moved in 4 helicopter nets weighing 700 kg each (minus fuel). The equipment is easily setup for drilling by a small crew in one half-day, and can be operated with a crew of four persons. Total time for drilling a 700 m borehole is about 7 hours. Photo by Joel Harper*

Figure 3-7. *The drilling tower can be moved short distances by human power. Here, six persons manually move the drill tower 50 m over rough terrain. Photo by Joel Harper.*

3.3.2 Borehole sensors

Dr. Humphrey custom manufactured the borehole temperature strings for this project. The strings utilize temperature-sensing semiconductor chips which are soldered into long strands of CAT-5e cable (signal cable). The SPB team also custom manufactured water pressure sensor/cables for this project. Omega Engineering pressure transducers were installed on CAT-5e cable and potted in epoxy to make them water proof. Dr. Humphrey designed and manufactured the hardware and software for custom data loggers used to record borehole sensors (Figure 3-8). Two characteristics make these data loggers superior to commercially available loggers for purposes of this project: 1) they are very inexpensive, allowing for deployment of a large number of units at minimal cost; and 2) ultra low power, allowing for operation of sensors year-round with minimal cost and effort. A trade-off is the substantial labor involved in the building of the data loggers.

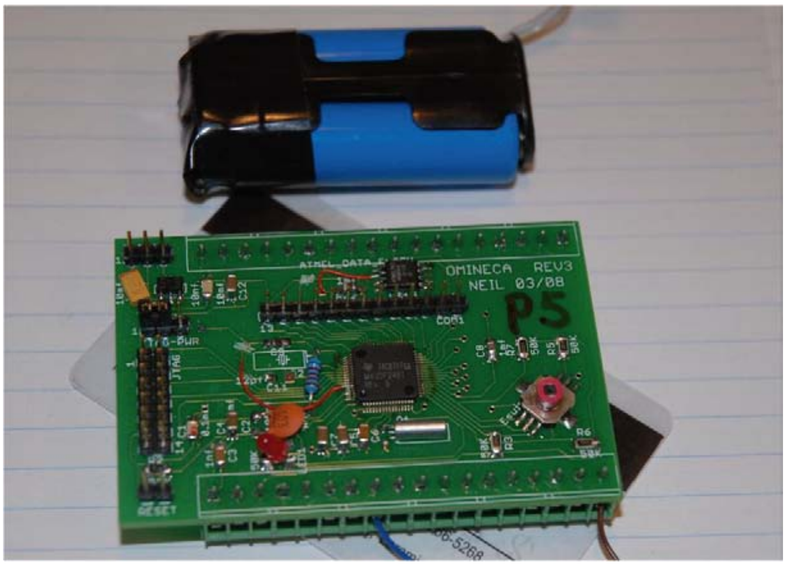

***Figure 3-8.** Photograph of data loggers built for this project. Credit card for scale. The self contained 32 channel data loggers can operate at a 30 minute time base for over 1 year on only two AA sized batteries (blue power pack). The data loggers are built in the laboratory at University of Wyoming for a cost of under $250 each. Photo by Neil Humphrey.*

3.3.3 GPS surface velocity

SPB involved the design and construction of a GPS/weather station for deployment on the ice sheet. The design goal was to create a system capable of continuous position measurements using a Trimble NetRS GPS receiver (Figure 3-9). Because the NetRS has a substantial power requirement, operation throughout the dark winter months requires substantial battery power. An additional design challenge was presented by high ablation: the field site receives over 4 m of ice ablation per year, causing settlement, melt-out, or sometimes causing instruments to become pedestaled on the ice surface. The solution was to place the very large battery array in a waterproof box which was then installed on a metal frame and allowed to float on the ice surface during ablation. The floating frame is separate from the GPS antenna, which was installed on a pole drilled deep into the ice and allowed to become elevated as ablation occurred.

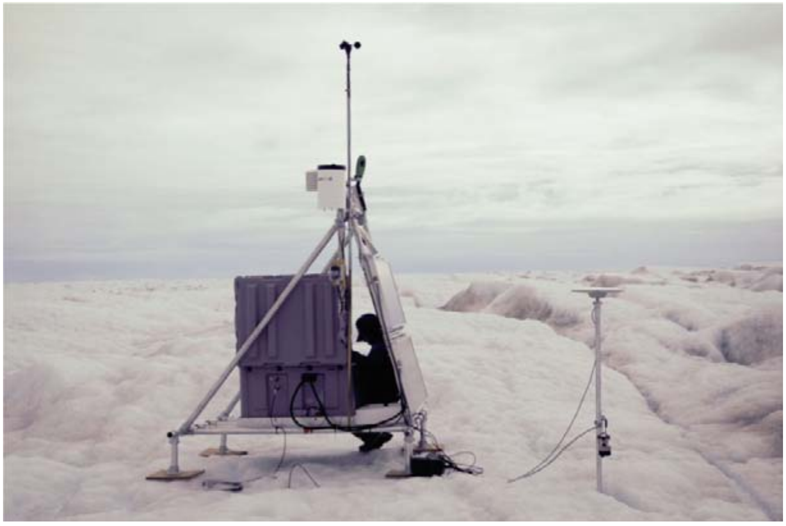

***Figure 3-9.** Photograph of GPS/meteorological installation. Data are stored at 15 sec to 15 minute intervals and will be retrieved in September, 2010, and spring, 2011. Photo by Joel Harper,*

3.3.4 Ice penetrating radar

To measure ice thickness and bed elevation, ice penetrating radar were collected using a Narod Geophysics type georadar transmitter and oscilloscope receiver. 5 MHz antennas were used and data were collected at 10 m spacing, where ice bumps and hummocks permitted. Often, hummocks or crevasses prevented data collection along multi-point transects, so data could only be collected at individual and scattered points. All points were georeferenced using a hand-held GPS receiver (accurate to about 5–10 m) with the vertical recorded by a 1 m accurate barometer. A two-way travel time was computed from the first reflection from the bed, and this travel time was transformed to ice depth using a constant radar velocity of 0.168 m ns^{-1}. Based on this velocity, a ¼ wavelength resolution of 8.4 m was calculated.

3.3.5 Water sampling

Basal water samples were collected from boreholes using an aluminum sampler that closes when it hits the bottom of the hole. For comparison to borehole waters, outlet stream samples were also collected from three points at the terminus of Isunnguata Sermia. Sites T1 and T2 (Figure 3-11) were accessed by climbing up onto the ice sheet and then descending between piles of sediment and dead ice to the base, where many small outlet streams emerge from beneath the glacier. Site T3 is the main stem of the terminus outlet, as close as is safely possible to the ice front. During the 2010 field season, only one day was available for sampling. The measurements from that day are single points and may or may not be representative of “average” conditions.

All water samples were split in two: one aliquot was reserved for geochemical analysis, while the other was analyzed immediately in the field for radon activity. The waters at Isunnguata Sermia contain two short-lived radioisotopes of radon: ^{222}Rn (half life 3.82 days) and ^{220}Rn (“Thoron;” half life 55.6 seconds), which can be quantified by counting the alpha decays of very short-lived daughter products using a Durridge Rad7 detector. The detector identifies the decay energy given off by the emitted alpha particle (Figure 3-10). A high water activity suggests a long water-rock interaction time; a low water activity is indicative of either a short water-rock interaction time or dilution by radon-free water (such as supraglacial melt). Englacial and subglacial melt inputs are assumed to be very small compared to supraglacial meltwater. Though radon is often used as a tracer in hydrothermal settings and groundwater studies, this is one of the first times that radon has been used in a glacial system. In addition to the water samples collected from boreholes and at terminus outlets, several water samples from a marginal outlet stream were assessed for radon activity in order to get some perspective on the variability of radon over a diurnal cycle.

Because of logistical constraints, not all the geochemical water samples from 2010 were filtered in the field. Water samples treated in the field were passed through a 0.45 µm syringe filter into an HCl-cleaned and rinsed HPDE bottle. Those not filtered in the field were stored in acid-washed-and-rinsed bottles and then filtered at 0.45 µm in the lab before solute analysis. All samples were acidified with ultrapure 16 M HNO_3 in the lab before analysis.

__Figure 3-10.__ Erin Johnson and Claire Landowski measure radon decay in a water sample collected from the bed of the ice sheet. Photo by Joel Harper.

Elemental concentrations were determined using an atomic emission mass spectrometer and inductively-coupled mass spectrometer at the USGS hydrogeochemistry labs (Drs. Howard Taylor and Kirk Nordstrom) in Boulder, Colorado; anions were measured using a Dionex ion chromatograph at the same facility.

3.4 Results, 2010 field campaigns

The primary objective of the first SPB drilling campaign was to drill 1-3 boreholes to provide information on ice sheet conditions in the region of the bedrock hole that is scheduled for drilling by SPC in 2011. It is anticipated that the ice sheet measurements will complement measurements made in a deep bedrock borehole by providing information about the ice conditions bounding the groundwater system.

The drill performed as designed and no major technical bugs emerged. Consequently, the drilling accomplishments exceeded expectations and 13 boreholes were drilled to the bed of the ice sheet at three different sites, including a 700 m deep borehole (Figure 3-11). The depth, drilling date, and location of these holes are presented in Table 3-2.

Once proficient, the SPB crew could ready the drill for operation within half a day after helicopter transport. The drill advanced the boreholes at rates of 100–120 m/hr. The drill hose and drill stem was easily retrieved from the 700 m borehole: pulling up from 700 m depth took 35 minutes and required just two people to manage the hose as it came out. In addition to drilling the boreholes, numerous experiments, both in the boreholes and in the region surrounding the boreholes, were conducted (Table 3-3). Results from some of these experiments are described below. Note that all times presented in this document are local Greenlandic time (GMT-2).

3.4.1 Water level impulse experiments

Three types of borehole impulse tests were performed to investigate basal hydrologic properties: 1) drilling water levels, 2) slug tests, and 3) constant-rate injection tests. The artificial perturbations to water levels through borehole impulse testing are being used to investigate the make-up and geometry of the basal drainage system tapped into by the boreholes. Numerical simulations are being created to reproduce the experimental response of the impulse tests. These simulations enable exploration of the fundamental elements of the drainage system moving water from the boreholes and along the bed. For example, the simulations of experimental response will elucidate the existence (or lack thereof) of high capacity conduits and/or interconnected low discharge cavities. The length and diameter of connecting pathways is also being explored through the numerical simulations. These results are important to interpreting the pressure records and incorporating information into ground water models. Development of the simulations is underway; results and interpretations will be presented in future reports. During 2010, three types of impulse experiments were conducted. Each type of impulse experiment is described below.

Table 3-2. Ice hole details.

Hole	Date	Depth (m)	Latitude (WGS 84)	Longitude (WGS 84)
GL10-1A	6/12/2010	98	67.162213	–50.064273
GL10-1B	6/13/2010	92.5	67.162137	–50.064433
GL10-1C	6/14/2010	91	67.162518	–50.063257
GL10-1D	6/14/2010	98.5	61.162385	–50.063314
GL10-1E	6/16/2010	91.9	67.162524	–50.062911
GL10-1F	6/17/2010	102	67.162662	–50.062037
GL10-2A	6/20/2010	144	67.167033	–50.066543
GL10-2B	6/21/2010	148.7	67.167093	–50.066535
GL10-2C	6/23/2010	146.3	67.167043	–50.066331
GL10-2D	6/23/2010	145.6	67.167119	–50.066171
GL10-2E	6/25/2010	148.7	67.167147	–50.066388
GL10-3A	6/30/2010	577.3**	67.19172	-50.02928
GL10-3B	7/2/2010	700.4**	67.191582	-50.02945

** Hole did not reach the bed.

Table 3-3. Data sets collected.

Dataset	Notes
Water level impulse experiments	3 types, at least one type in each of the 13 holes. Discussed in Section 3.4.1.
Basal water pressure	3 holes with continuous long term measurements; other holes measured intermittently during field campaign. Discussed in Section 3.4.2.
Borehole video/photography	Images of the bed and ice. Discussed in Section 3.4.3.
Ice temperature	Three holes fitted with thermistor strings; 2 holes fitted with DTS strings. Discussed in Section 3.4.4.
Ice penetrating radar	Over 100 point measurements concentrated near the Caribou site. Discussed in Section 3.4.5.
GPS surface velocity	One continuous running installation near the center of Isunnguata Sermia. Discussed in Section 3.4.6.
Water chemistry	Collected from both boreholes and streams; multiple analyses run. Discussed in Section 3.4.7.
Site 1-2 stake velocities	14 stakes located in the area of sites 1-2 were surveyed with a GeoXH GPS system 1–2 times per day for 10–15 days during June 2010. Data have not been processed and are not presented in this report.
Site 1-2 surface ablation	14 stakes located in the area of sites 1–2 were used to measure surface ice ablation 1–2 times per day for 10–15 days during June 2010. Data have not been processed and are not presented in this report.

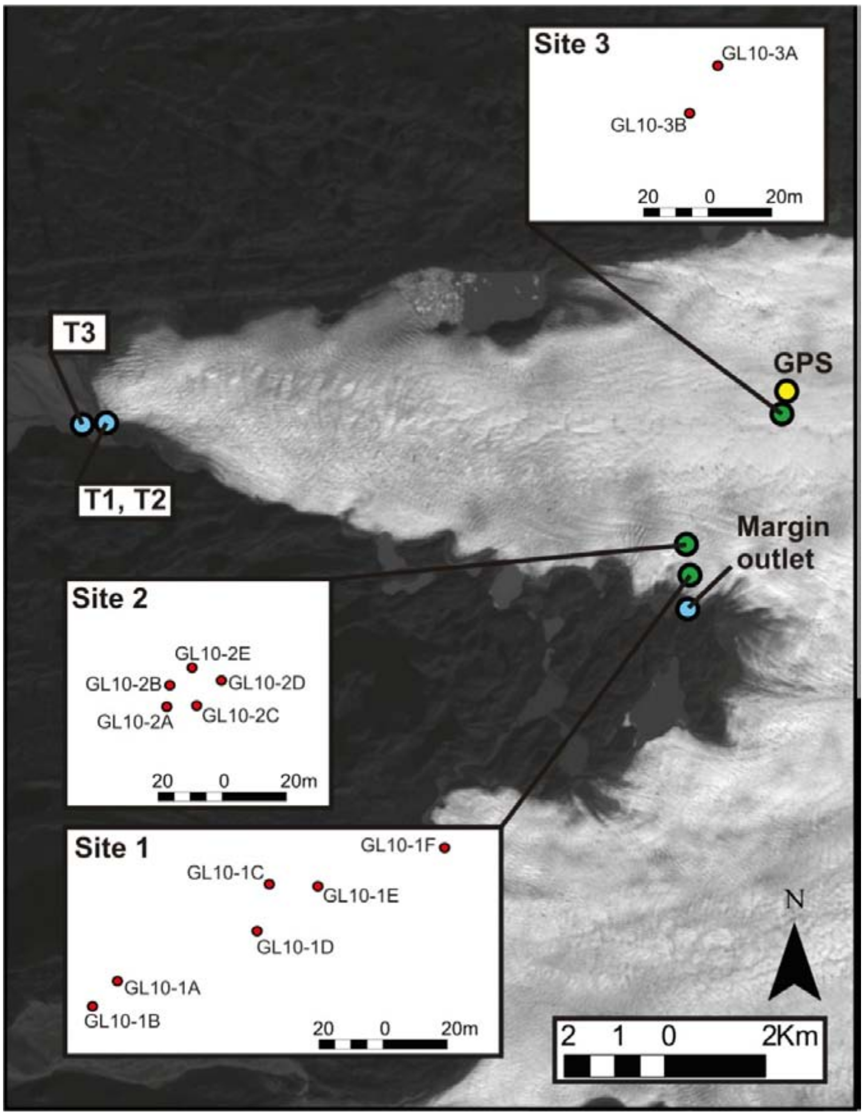

Figure 3-11. Isunnguata Sermia and locations of 13 boreholes drilled during the 2010 campaign. T1, T2, and T3 are sites of water sampling at terminus outlet streams.

Drilling Water Levels

During the drilling of all 13 boreholes, the water levels in the drill hole, and any existing adjacent boreholes, were closely monitored with pressure transducers (Figure 3-12). Sudden changes in the drill-hole water level indicated englacial or subglacial hydrological connections. In some cases, a sudden drop in the drill-hole water level corresponded to a sudden rise in an adjacent borehole, implying that water moved from the drill hole to the adjacent borehole through an englacial or subglacial hydrological connection. Preliminary analysis of the data suggests that englacial connections between the borehole and a transmissive drainage system do occur.

Slug-test Experiments

Hydraulic slug tests consist of applying a sudden pressure spike to a borehole and monitoring the subsequent water level recovery. In practice, this consists of rapidly pouring 150 liters of water into a borehole in a 20 second time interval while monitoring water levels in adjacent holes as well as the test hole. Such tests are simple to perform, easily repeatable, and yield useful information regarding subglacial drainage characteristics. Nine different boreholes were used to conduct 21 borehole slug tests (Figure 3-13). The slug experiments reveal information about the transmissivity of subglacial and englacial hydrologic connections. Preliminary data show very high transmissivity at the all areas of the bed. This includes an area that lacked diurnal water pressure variations, and is therefore assumed to have a poor connection to diurnally varying input of surface melt.

Constant-Rate Injection Tests

Constant-rate injection tests consist of introducing water to a test hole at a constant discharge rate for a set period of time. Here, water was pumped into a borehole with a well established connection to the basal drainage system at 75 l/min for a period of 2 hours (Figure 3-14). Two such experiments were conducted. These experiments reveal the transmissivity and capacity of the subglacial drainage system. The observations of the ability of the subglacial drainage network to respond to a controlled input reveals information on time scales of network evolution.

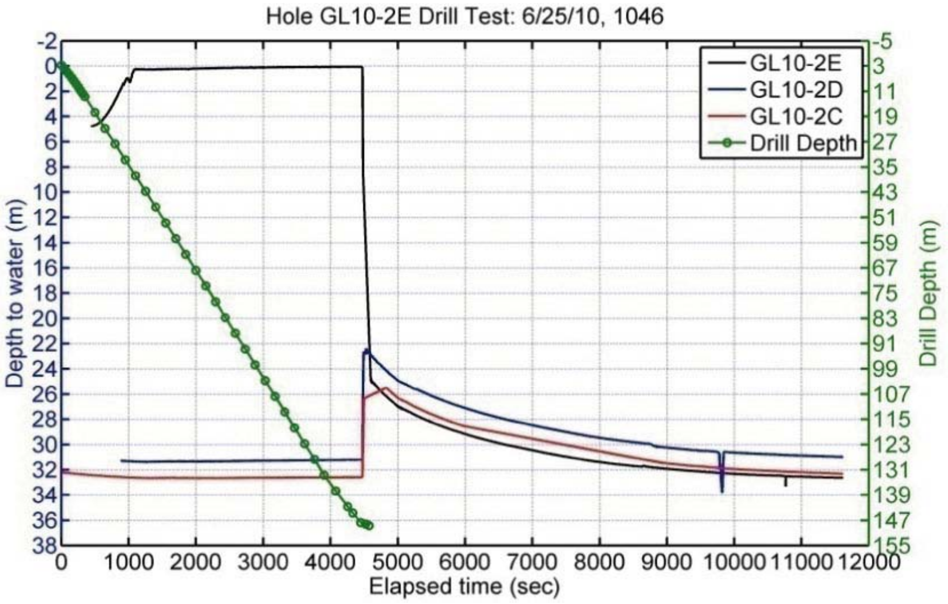

Figure 3-12. Results of drilling water level experiment. As the borehole intersected the bed (~4,600 sec), the water level in the drill hole GL10-2E dropped approximately 26 m. Simultaneously, the water levels in two nearby holes drilled previously, rose approximately 8 meters. The three holes then slowly drained to the level observed before drilling began.

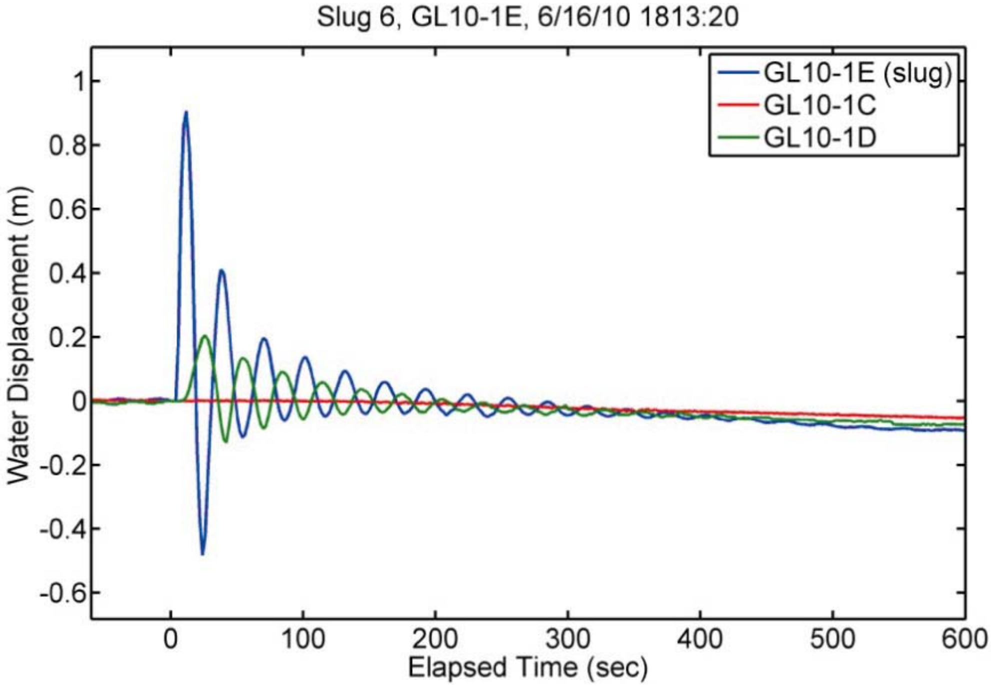

Figure 3-13. *Results from a slug experiment showing water level response in three boreholes separated by ~10 m. Hole GL10-2E received the slug and oscillated out of phase with GL10-2D, while hole GL10-2C showed an over-damped response.*

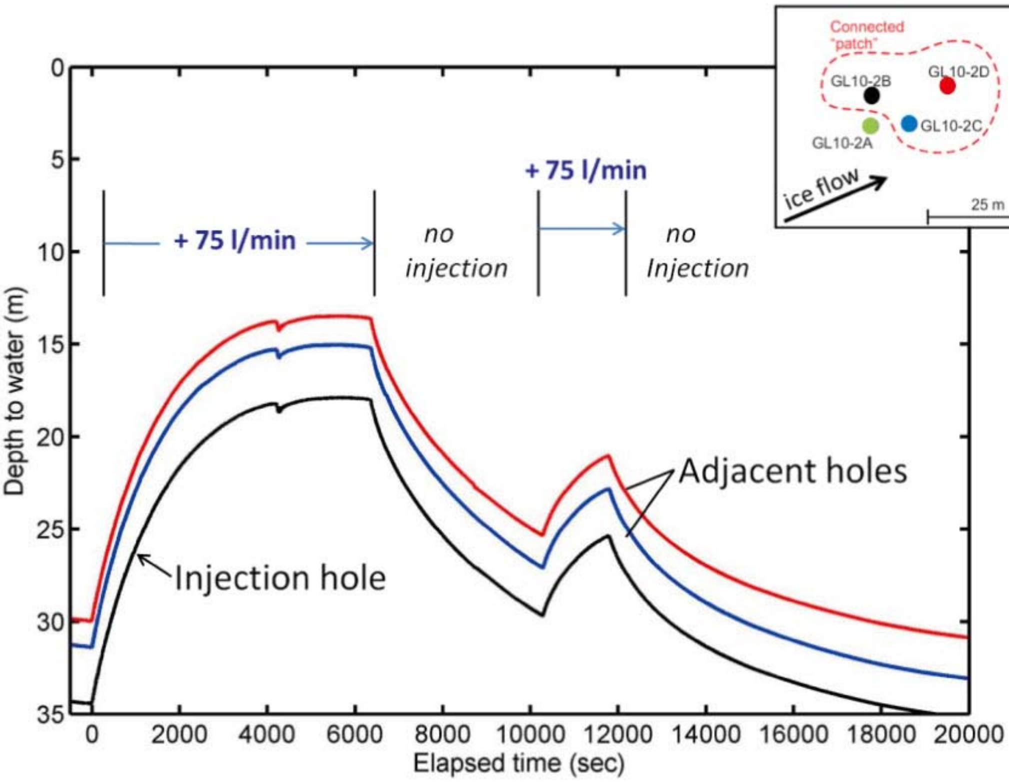

Figure 3-14. *Results of a constant-rate injection test. Water levels in three adjacent boreholes within a connected patch of the bed are shown (inset in upper right). When water was injected at a rate of 75 l/min the three water levels initially rose quickly. The subglacial drainage system slowly evolved to accommodate the increased water flux, causing the water levels to stop rising. The injection was stopped and the water levels began recovering. Hypotheses for subglacial water routing (i.e. the size and capacity of subglacial drainage elements) are being tested in numerical simulations using these data.*

3.4.2 Basal water pressure

Water levels were recorded in all 13 boreholes during the period of the field campaign. Three holes were selected for continuous water level measurements via a permanently installed pressure transducer near the borehole base and a data logger on the ice surface. These data are collected at 5 minute intervals. Data were retrieved in late September, 2010, yielding records lasting from July–September, 2010. The data loggers were left in place and in good working order, which should allow for the collection of additional data upon return to Greenland during the summer field campaign of 2011.

Existing records elucidate pressure variations during the summer to fall periods. Pressures reach values in excess of the ice overburden pressure for short periods of time, and fall to values as low as 25% of ice overburden for brief periods on a daily cycle (Figure 3-15). High frequency, but lower magnitude, variations were also observed (Figure 3-16) for several days.

3.4.3 Borehole video/photography

A submersible video camera was used to film all boreholes. In many holes, the lowest 5–10 m of the borehole could not be filmed due to turbidity caused by the drilling process. However, good images of the bed were obtained in several boreholes (Figure 3-17). These images suggest the ice near the bed is laden with sediment. The bed has a relatively thin covering of sediment (cm to decimeter thick, but not likely meters thick). A conceptual view of basal ice and the bed is shown in Figure 3-18. Note that other places of the ice sheet may differ.

Two borehole time-lapse cameras were specifically designed for this project by Dr. Humphrey. These low cost cameras were installed near the bed of two boreholes to provide repeat images of the basal boundary and allow for direct measurement of basal sliding rate (Figure 3-19 and Figure 3-20). The sliding speed over the 24 hour period was measured at 2.6 cm per day, with negligible difference in speed between two time periods: 0:00 to 17:30, and 17:30 to 23:45. Although the resolution is not sufficient to rule out some diurnal variation in sliding speed, it does suggest steady sliding, and also suggests that there is not the extreme variation in diurnal sliding that is often observed in mountain glaciers.

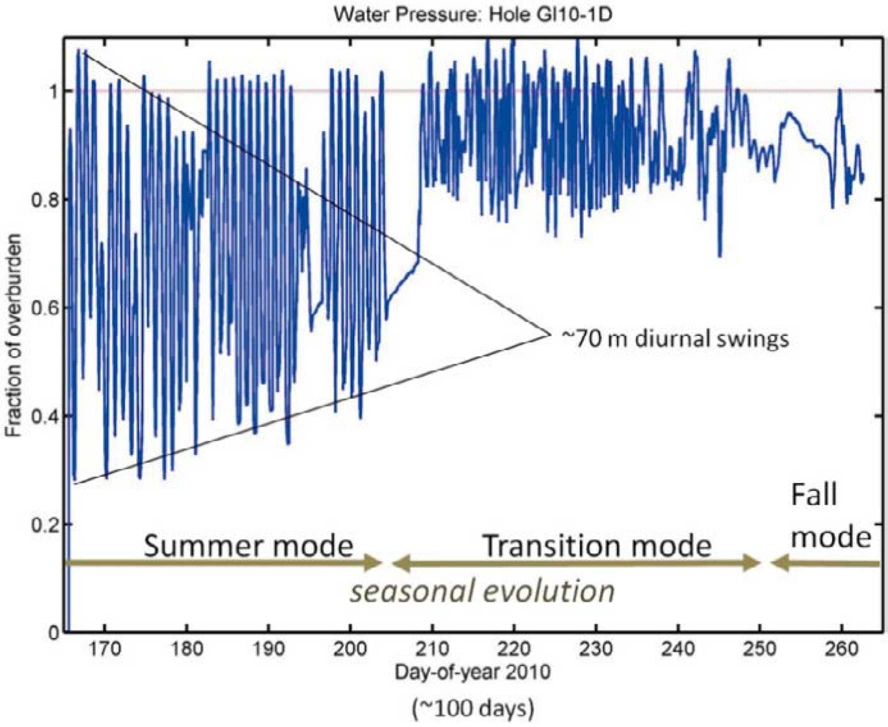

Figure 3-15. *Water pressure record from borehole 1D at GL10–Site 1. During mid-summer, the water levels show large diurnal swings, sometimes reaching 70 m in one cycle (Summer Mode). In late summer, the typical diurnal pattern breaks down and daily pressure variations become peculiar (Transition Mode, see Figure 3-16). In fall, repeated high frequency pressure variations cease (Fall Mode) and the pressure varies at differing time scales with a relatively high water pressure.*

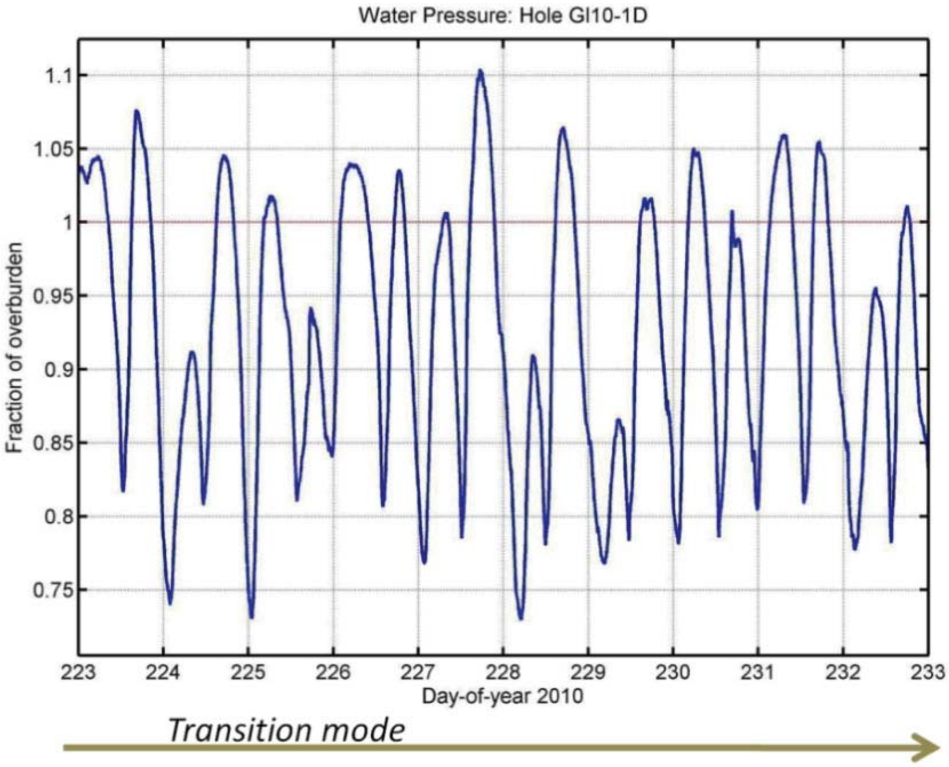

Figure 3-16. *Plot showing peculiar pressure variations during the transition mode between summer and fall. Water level variations occur during this ten day period on a cycle with two high pressure and two low pressure peaks each day. A multi-day period with six high and low values was also observed. As such, cycles are not driven by melt input variations; the pressure variability must be related to dynamics of the subglacial hydrologic system. Data from same borehole at site 2 as shown in Figure 3-15.*

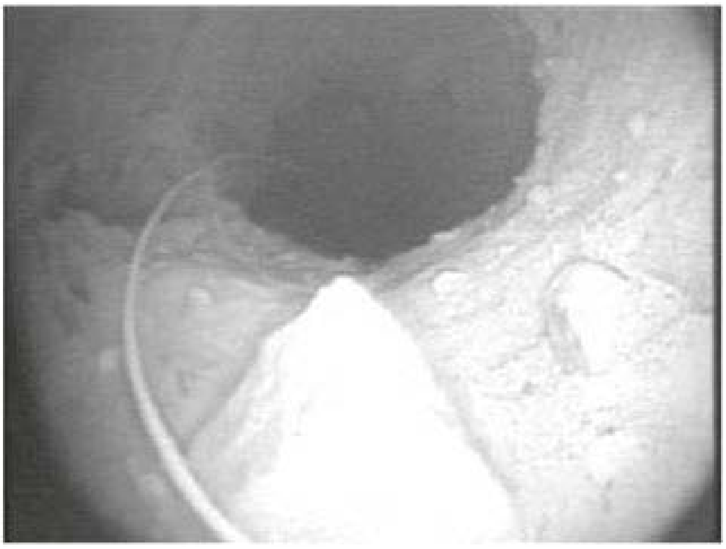

Figure 3-17. *Frame grab from borehole video camera showing from about 4 meters above the bed in borehole GL10-2D. The cable for a borehole pressure transducer is visible on left side of image, and has a diameter of a about 4.6 mm. Larger triangular rock protrudes from the borehole wall on bottom side of image. Other rocks are visible within the ice matrix of the borehole wall. Image acquired 25 June, 2010.*

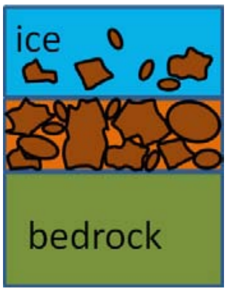

Figure 3-18. Conceptual view of the basal ice and bed within the region of sites 1-2. Ice 5–10 m above the bed is laden with sediment. Grain sizes from fine sand to 'rocks' 10–20 cm in diameter are common. The bed is covered by similar sized sediment in a layer that is cm to decimeter thick, but not likely more than 1 m thick. No evidence was found in this area for a thick layer of soft deformable bed material.

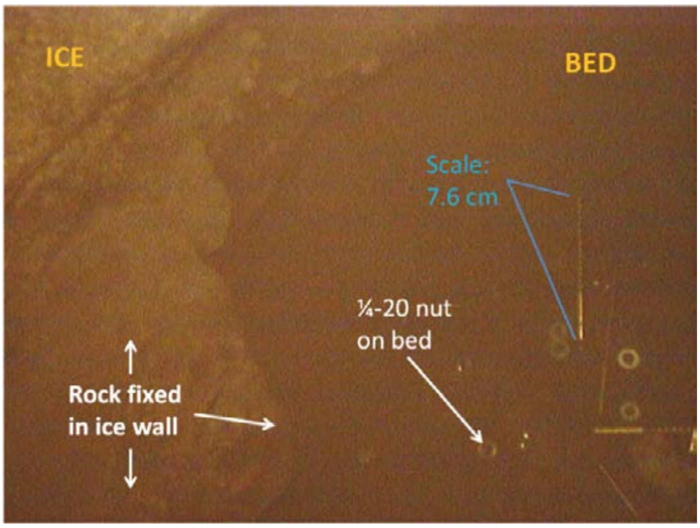

Figure 3-19. Example image from borehole camera from borehole GL10-2D. The walls are composed of dirty ice, with various sized rocks protruding. The bed is visible at the lower right. Several nuts and bolts have been dropped down the hole and are lying on the bed for scale. Image acquired 26 June, 2010.

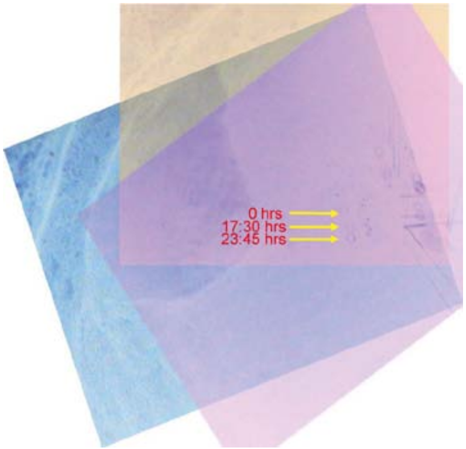

Figure 3-20. 24-hour sequence of processed images from the fixed borehole camera used to compute a basal sliding velocity in borehole GL10-2D. The images have been color shifted and made transparent to allow comparisons. The large rock (see Figure 3-19) was used to register the images to a common orientation and view. The bolts and nuts on the right side of the image record relative motion between each image. As an example the machine nut closest to the big rock shows that the ice was moving 'up' relative to the stationary bed.

3.4.4 Ice temperature

Three holes were fitted with thermistor strings for measuring ice temperature. Because temperatures within the ice can vary only over long time scales, these strings were not connected to data loggers. Rather, the data are collected manually during site visits. Once borehole temperatures have equilibrated to the perturbation following drilling, they are not expected to change during the duration of this project. A thermistor string was installed at each of the three sites, and data were collected in September 2010, after the boreholes had more than two months to equilibrate following drilling (Figure 3-21).

Two DTS (fiber optic) temperature measurement cables were also installed in two of the boreholes, one at site 1 and one at site 2. SPC team members made measurements on the site 1 cable using a DTS-reader. The temperatures obtained from the DTS-measurements are consistent with the temperatures obtained from the thermistor strings. Additional measurements may be taken during the 2011 field season.

Ice temperature at sites 1 and 2 is 'isothermal' (i.e. at the pressure melting point). These boreholes never completely froze closed during the field campaign. The ice temperature at site 3 is warm near the surface, cools with depth to a minimum of about –4.5 ˚C at 400 m depth, and then begins warming toward the bed. These temperatures are all substantially warmer than anticipated from previous modelling studies, likely due to shortcomings in the modelling, and unanticipated processes (see Section 3.5)

3.4.5 Ice penetrating radar measurements of ice depth

In an effort to map the bed and hydraulic potential of the study region, over 110 ice penetrating radar measurements were collected (Figure 3-22). Because of the extremely hummocky topography of this region, radar traces could not be collected using a standard towing/profile radar survey procedure. Instead, suitable locations within the hummocks had to be located, and antennas needed to be carefully draped in between the large bumps. The data collection was far more time consuming than is typical, and unusable traces with ambiguous reflections were more common than in other glacial and ice sheet settings. The radar data are being used to generate a detailed bed map of the study region, which will be utilized for 1) numerical modelling, 2) interpreting the hydraulic potential field in the region of the boreholes, and 3) generating a drilling plan for the deep bedrock hole (Figure 3-23).

3.4.6 GPS surface velocity

Data collected from the GPS station during the fall field campaign yield a record extending from July–September. Velocities averages about 40 cm/day along a westerly trajectory (Figure 3-24), with no strong diurnal variations. The data are preliminary. Resolution will hopefully be improved with more advanced processing techniques.

3.4.7 Basal water and sediment sampling

The sample locations are shown in Figure 3-25, and the concentrations of major, minor and trace metals are shown in Table 3-4. The standard deviations given are two sigma. In general, most borehole waters are significantly more concentrated than marginal and terminal outlets streams. Compared to published data sets for alpine glaciers, the meltwaters associated with the Greenland Ice Sheet at Isunnguata Sermia are more dilute and compositionally distinct. In other glacial systems, but perhaps most notably at Haut Glacier d' Arolla (HGA) in the Swiss Alps and the Bench Glacier in southwest Alaska, calcium is, by far, the most abundant cation in solution (Sharp et al. 1995, Tranter et al. 1997, Mitchell and Brown 2007, Anderson et al. 1999). At Isunnguata Sermia, though the concentration of calcium is higher than other cations, it measures as much as two orders of magnitude lower than at Bench and HGA. Other major species (K, Mg, Na, NO_3^-, SO_4^{2-}) at Isunnguata Sermia have concentrations that are similar to Ca (same order of magnitude), which is again unusual; in alpine glacial systems these major species are much more dilute in comparison to Ca.

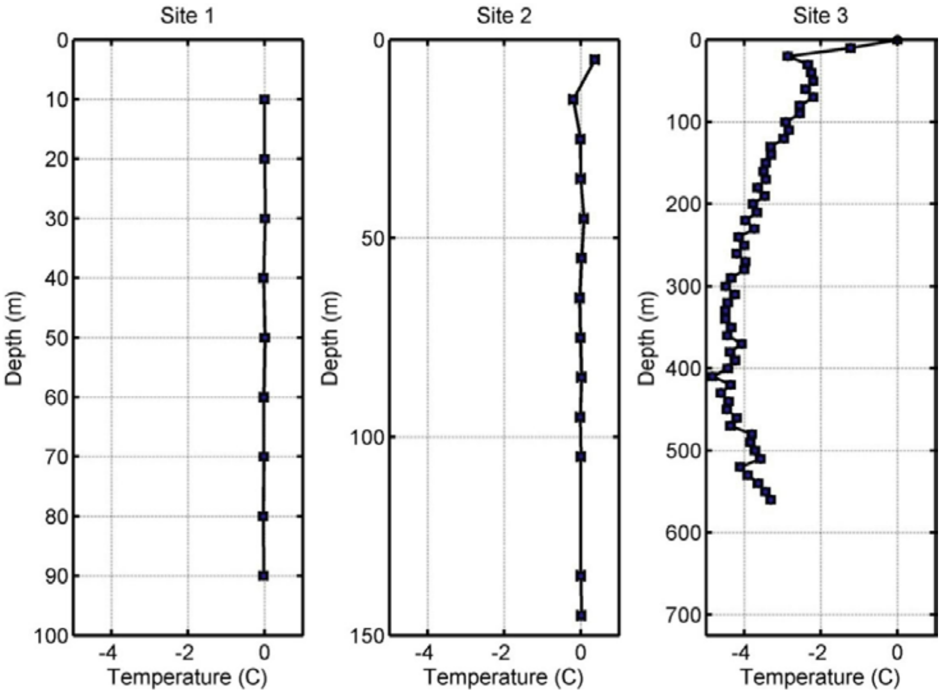

Figure 3-21. *Ice temperatures measured in boreholes at each of the three sites. Sensors were installed in June/July of 2010 and measured in September, 2010.*

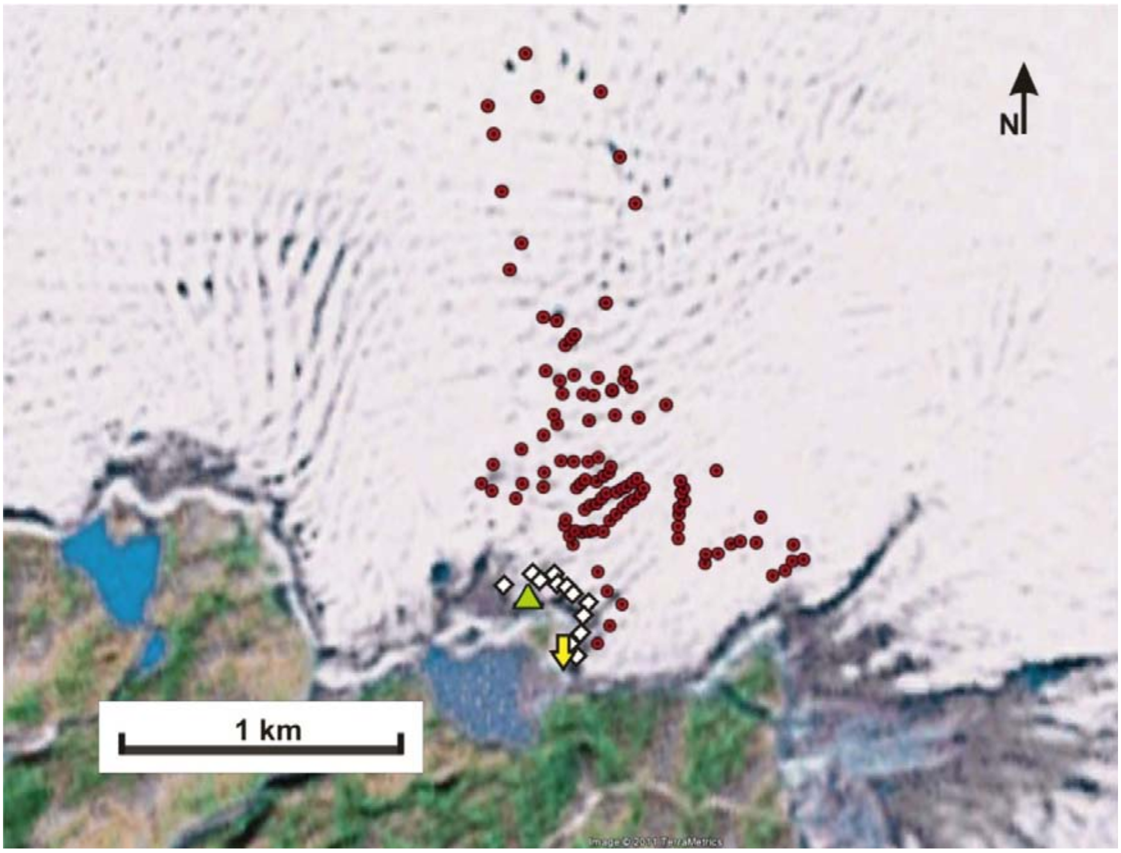

Figure 3-22. *Locations of ice penetrating radar measurements. Red circles show locations where a bed reflection is interpreted with reasonable confidence. White diamonds are locations along the 2010 ice margin with zero ice depth. Green triangle is location of one of SPB camps in 2010. Yellow arrow is outcropping bedrock.*

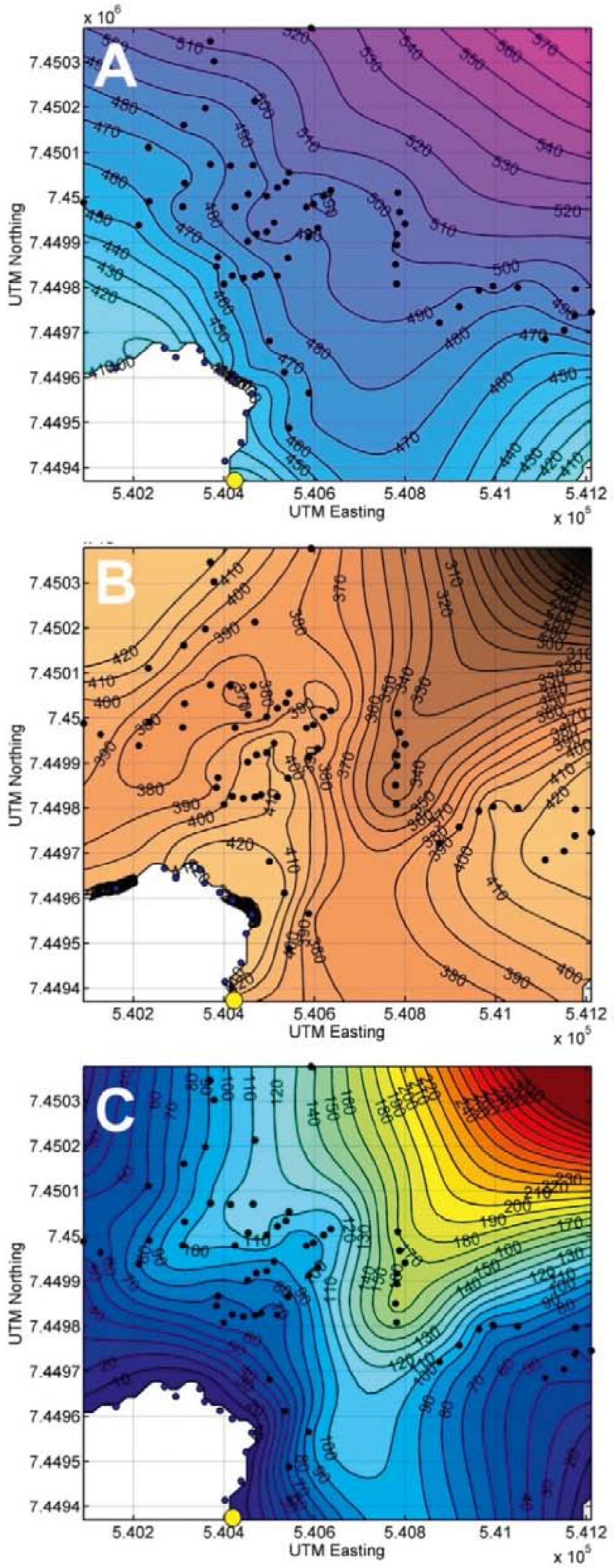

Figure 3-23. Surface, bed and ice thickness maps of the region of sites 1-2 and the site for the planned SPC bedrock hole. Yellow dot shows location of outcropping bedrock near the planned SPC bedrock hole. Black dots show locations of radar ice depth measurements, and surface elevation measurements. Note that in all maps interpolation is poorly constrained due to sparse and clustered data. A) Surface elevation determined from hand held GPS with elevation determined by barometer; B) Bed elevation determined by ice penetrating radar reflections, and C) Ice thickness determined by difference between A and B.

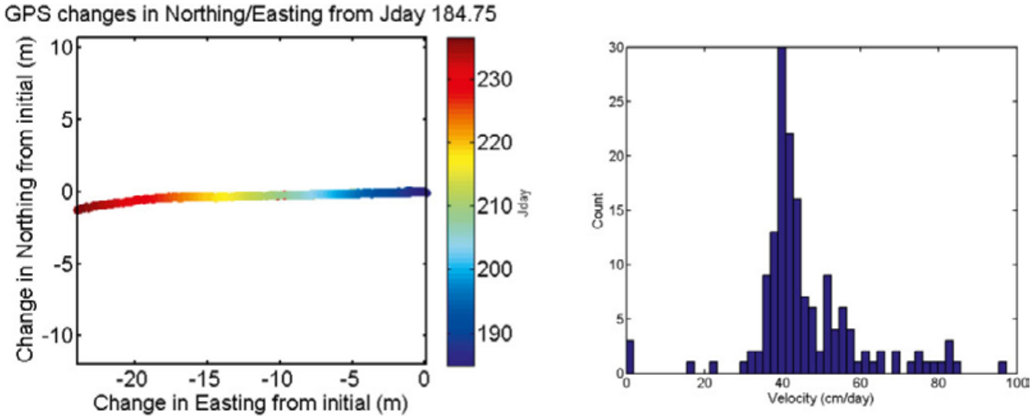

Figure 3-24. *GPS surface velocity data from center of Isunnguata Sermia. Left panel shows map plane trajectory of GPS station. Right panel shows velocity data binned by time intervals. The most common displacement over the time intervals corresponds to a velocity of about 40 cm/day. If strong diurnal velocity variations were present, more spread in the histogram would be expected.*

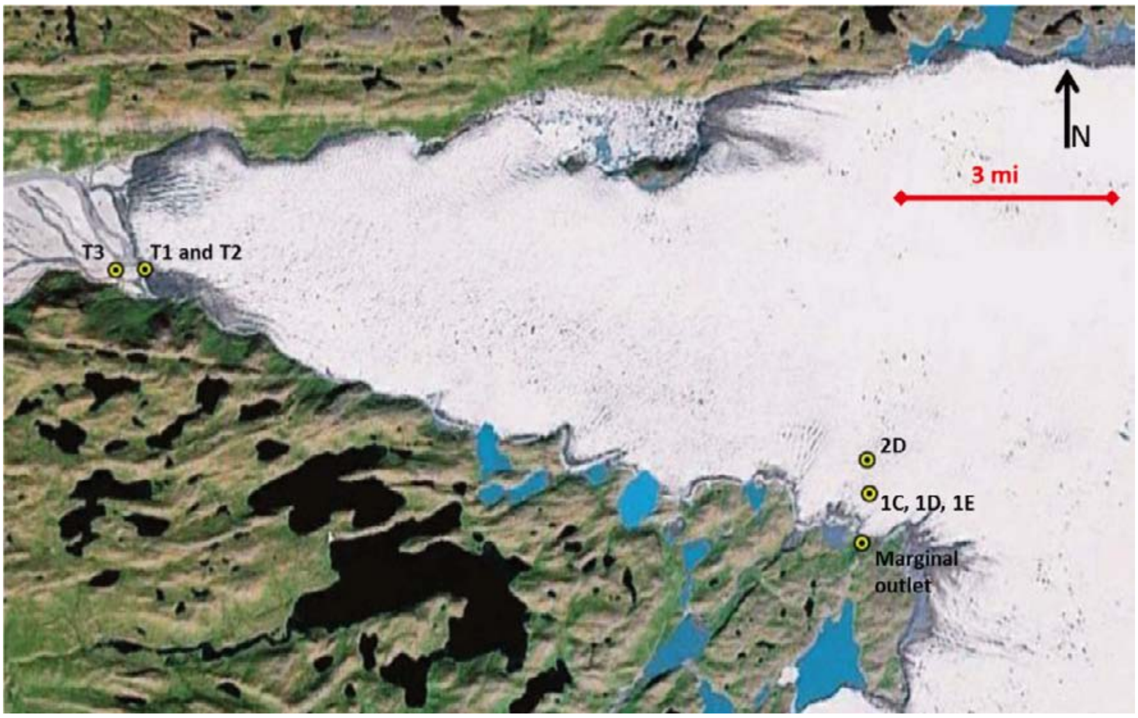

Figure 3-25. *Site map for water sampling during 2010 field season.*

Table 3-4. Geochemical data for borehole and terminus water samples. Total dissolved solids (TDS) are in units ppm; conductivity is given in µS. All elemental and ionic concentrations are in µg/L, and standard deviations are 2σ.

	1C	1C-R	1D	1D-R	1E	2D	2D-R	T1	T2	T3
Date	14-Jun-2010	14-Jun-2010	14-Jun-2010	14-Jun-2010	16-Jun-2010	25-Jun-2010	26-Jun-2010	17-Jun-2010	17-Jun-2010	17-Jun-2010
pH	7.5	6.66	5.25	---	6.31	5.82	5.62	5.48	5.09	---
TDS (ppm)	7.05	9.29	1.56	---	1.94	1.02	2.93	0.708	1.2	---
cond (µS)	15	18.5	3.1	---	3.88	2.07	5.67	1.427	2.35	---
Na (µg/L)	749 ± 47	1445 ± 22	567 ± 10	622 ± 6	177 ± 9	235 ± 11	251 ± 10	73 ± .4	52 ± 3	153 ± 12
Mg	675 ± 29	2154 ± 18	172 ± 4	290 ± 13	104 ± 2	160 ± 2	61 ± 1	27 ± .25	29 ± 1	180 ± 11
SiO_2	3251 ± 73	15536 ± 9	749 ± 16	2036 ± 53	455 ± 7	1053 ± 23	382 ± 2	149 ± 9	353 ± 13	2239 ± 246
K	1500 ± 16	2965 ± 12	674 ± 7	707 ± 11	311 ± 2	617 ± 6	270 ± 3	353 ± 2	230 ± 3	365 ± 5
Ca	1692 ± 41	5243 ± 48	700 ± 9	879 ± 33	406 ± 2	409 ± 11	316 ± 4	118 ± .7	116 ± 3	728 ± 2
Al	1120 ± 38	2520 ± 22	141 ± .9	291 ± 4	61 ± 4	307 ± 1	24 ± 2	34 ± .1	33 ± .8	168 ± 7
NO_3^-	---	1100	80	100	BD	420	450	BD	BD	BD
SO_4^{2-}	---	700	200	200	BD	200	200	100	BD	400
Cl^-	---	500	900	1000	200	700	1100	200	100	BD
HCO_3^-	---	24376	6116	6902	3976	2420	4594	2503	2343	4047
P	192 ± 5	244 ± 10	9.43 ± 3	31.1 ± .2	3.96 ± 1	14.9 ± 2	BD	BD	4.26 ± .3	23.9 ± 1
Sc	BD	.401 ± .1	BD	BD	BD	BD	BD	BD	BD	BD
Ti	47.4 ± 2	169 ± 2	2.60 ± .2	18.4 ± .04	3.63 ± .07	17.7 ± .5	.927 ± .2	2.47 ± .06	2.93 ± .3	19 ± .1
V	7.11 ± .06	12.3 ± .02	.412 ± .07	.761 ± .02	BD	.479 ± .08	BD	BD	.095 ± .09	.589 ± .04
Cr	1.36 ± .5	4.73 ± .02	.712 ± .08	.603 ± 04	BD	.848 ± .01	.238 ± .02	BD	BD	.219 ± .02
Mn	19.1 ± 1	55.4 ± .06	4.47 ± .1	8.39 ± .04	4.88 ± .1	3.91 ± .04	1.51 ± .05	.94 ± .04	1.84 ± .07	4.83 ± .04
Fe	1400 ± 3	3730 ± 117	83.8 ± 10	443 ± 38	93.9 ± 5	270 ± 3	23.5 ± 1	49.3 ± 5	60.9 ± 10	343 ± 49
Co	1.25 ± .1	2.98 ± .02	.896 ± .002	.558 ± .0009	.171 ± .004	.33 ± .009	.132 ± .005	.058 ± .004	0.138 ± .004	.182 ± .002
Ni	5.83 ± .5	12.8 ± .04	2.80 ± .03	2.59 ± .02	1.10 ± .04	2.03 ± .04	.859 ± .01	.273 ± .01	.783 ± .008	.663 ± .03
Cu	11.6 ± 1	24.8 ± .7	31.2 ± .05	15.0 ± .09	13.3 ± .003	22.7 ± .4	15.6 ± .02	.774 ± .02	0.737 ± .02	1.06 ± .008
Zn	15.6 ± 2	14.1 ± .03	36.2 ± .4	18.0 ± .4	50.5 ± .6	98.2 ± 2	99.6 ± .002	13.0 ± .2	6.14 ± .2	.744 ± .4
Rb	1.93 ± .06	5.53 ± .1	0.62 ± .009	1.01 ± .02	.284 ± .01	.571 ± .002	.282 ± .006	.158 ± .002	.186 ± .005	.851 ± .02
Sr	8.70 ± .6	26.7 ± 1	2.66 ± .02	4.09 ± .05	1.71 ± .01	1.80 ± .1	1.45 ± .01	.682 ± .03	.721 ± .05	3.24 ± .2
Ba	23.5 ± .3	49.7 ± 1	3.10 ± .006	9.71 ± .2	2.09 ± .07	4.34 ± .1	1.70 ± .008	1.64 ± .1	1.53 ± .03	4.13 ± .3
Pb	3.03 ± .09	2.38 ± .01	13.9 ± .02	12.3 ± .1	3.09 ± .1	12.5 ± .02	7.67 ± .02	.199 ± .03	.068 ± .005	.069 ± .01
U	0.039 ± .0009	.065 ± .0004	.009 ± .002	.011 ± .0001	.006 ± .002	.0087 ± .0001	.0029 ± .0002	.0061 ± .0008	.0029 ± 2E-5	.0088 ± .002

BD = concentration below the detection limits.
--- = quantity was not measured i.e. the borehole was sampled immediately after drilling concluded.
R = the borehole was re-sampled while the water level was rising in the borehole.

The concentration of Ca ranges from about 100 to 5,000 µg/L, which is extremely low compared to other published values. For all other major elements, the West Greenland waters are within an order of magnitude of other published values, though generally more dilute. Though the concentrations of Ca and HCO_3^- imply that some minor dissolution of calcite may occur in the subglacial system, the ternary diagram for cations (Figure 3-26) suggests that the more important processes in the subglacial system are feldspar and plagioclase weathering because all the water samples plot close to the region of plagioclase composition. The ternary diagrams imply that biotite dissolution is contributing only a moderate number of ions to solution, but the prevalence of potassium in solution, which would be removed from interlayer sites in biotite early in weathering, suggests that this process is still a primary control on water chemistry. Figure 3-27 plots [Ca] against [K], and suggests that, at Isunnguata Sermia, calcium and potassium weather out of bedrock at roughly the same rate. Calcium would be present in the water through the dissolution of calcite or plagioclase, and the relative importance of these weathering processes may be examined by comparing to a species that weathers only via silicate dissolution. Potassium was chosen because it is contributed primarily by biotite, which is an important phase in the bedrock at Isunnguata Sermia. The presence of calcite dissolution is exhibited by a datum that plots well above the 1:1 line, because calcite releases calcium ions much more readily than silicate minerals. In Figure 3-27, all other data are published values from alpine glaciers – to our knowledge, no other datasets yet exist for Greenland or Antarctic ice sheets. The distribution of alpine glacier waters suggests that the dissolution of secondary calcite seems to be an important process (i.e. compositions plot well above the 1:1 line). The compositions of Isunnguata Sermia waters all plot near the 1:1 line, demonstrating that there is relatively little contribution of calcium ion from calcite dissolution.

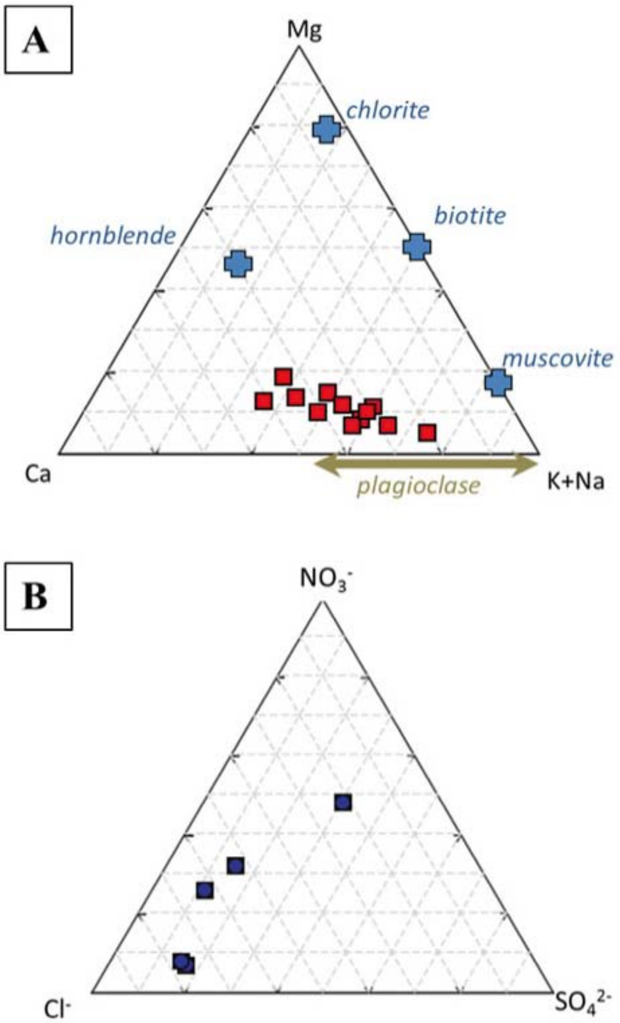

Figure 3-26. *Ternary diagrams for all samples. A: Cations (red boxes), plotted with minerals (blue crosses) observed in bedrock. B: Anions (blue boxes); data set is smaller because not all samples contained detectable nitrate and sulfate.*

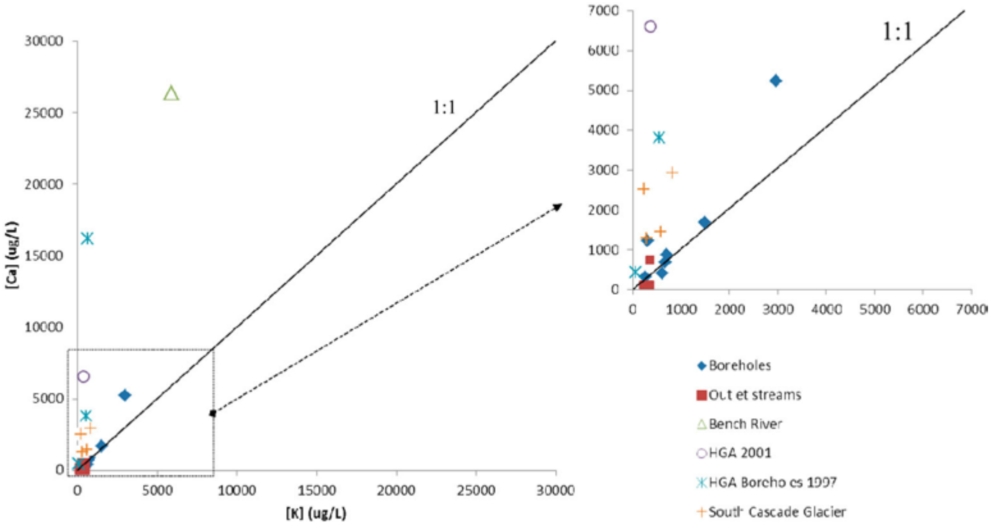

Figure 3-27. *Concentrations of calcium versus potassium for both Isunnguata Sermia 2010 (solid symbols) and other published values (open symbols). Bench River values are from Anderson et al. (1997), Bench Glacier outlet stream; HGA 2001 values are from Mitchell et al. (2001), Haut Glacier d'Arolla outlet stream; HGA boreholes 1997 are from Tranter et al. (1997), Haut Glacier d'Arolla boreholes; South Cascade Glacier values are from Drever and Hurcomb (1986); outlet streams and South Cascade Lake.*

The behavior of trace metals in this system may also be useful for understanding the nature of water-rock interaction in the subglacial system. Pb and U are considered as examples, though in principle, other elements like Cr, Cu, Zr, and others are also instructive. Experimental studies of granite dissolution (Harlavan and Erel 2002) have shown that most Pb released early in the weathering process originates in accessory minerals, and that dissolution of major minerals like plagioclase becomes the dominant source of Pb and REE after about 100 hours of water-rock interaction. The high concentrations of Pb and other trace metals in borehole samples, as compared to the terminus streams, suggests that near the margin of the ice sheet the residence time of water is relatively long. In terms of drainage system organization, it is likely that a distributed system or "slow flow" system is pervasive in this region and, that only during high-melt conditions, when the drainage system is flooded, may these channels drain. This interpretation is supported by data from boreholes where more than one sample was taken – there is little difference in concentration between the samples. In borehole 1D, for example, the concentrations of Pb are essentially the same both immediately after drilling, and, later, as subglacial water is flooding the borehole. This underlines the conclusion that Pb is released early in the weathering process and that only exceptionally fast drainage systems (i.e. closer to the terminus) will appear to be depleted in Pb. Isotopic analyses of Pb in these waters would help to identify the species contributing to the total Pb concentration and would help constrain the dissolution time. Uranium exhibits similar behavior; there is little difference between samples from the same borehole, and this is another case where the analysis of uranium isotopes would help to identify the order of mineral dissolution and estimate the residence time of water.

The results of the radon-counting experiment are found in Figure 3-28. In principle, this method may be utilized to estimate the length of water residence time in the subglacial system. ^{222}Rn (half-life of 3.2 days), the main target for analysis via this method, is produced by the alpha decay of ^{226}Ra (half life of 1,600 years), a daughter product in the reaction series of ^{238}U. ^{220}Rn (half life of 55.6 seconds), a product of the alpha decay of ^{224}Ra (half life of 3.66 days) in the ^{232}Th decay chain, may also be measured. These isotopes are present in water because of alpha recoil: as a radium atom decays, the energy emitted is split between the alpha particle produced and the daughter isotope. If the decay is sufficiently close to the edge of the mineral lattice, the alpha particle and the daughter product may exit the rock and enter the surrounding medium, which, in this case, is subglacial water. Theoretically, the residence time may be quantified by measuring several radioisotopes with different half-lives, but this data set is not yet large enough to be able to do this; instead, ^{222}Rn may be used as a relative proxy. A high activity in the sample water suggests a prolonged water-rock interaction time, and over the course of a day, the activity would be expected to rise and fall in relation to the amount of water in the subglacial system. Near Site 1, ^{222}Rn in a subglacial system outlet issuing from the margin of Isunnguata Sermia was measured. In Figure 3-28, these samples are denoted with blue diamonds labeled "Outlet stream." The blue line is the water level in a borehole at Site 1 that was well-connected to the basal hydrologic system; it is utilized here as a proxy for amount of water in the subglacial hydrologic system. When the water level is near the surface (a peak), the subglacial system should contain more water from surface melt.

The data suggest that during times of high flow in the subglacial system, the radon activity is low. This is because less water interacts with the bedrock or sediment below, and therefore fewer radon atoms are present per unit volume. During times of decreased flow, the water moves slower through the subglacial system and therefore the water-rock ratio decreases while water-rock interaction time grows, resulting in a higher activity. This pattern is particularly evident in the series of measurements made at the marginal outlet stream, where activity is highest in the early morning when melt is at a minimum and highest in the late afternoon during peak melt.

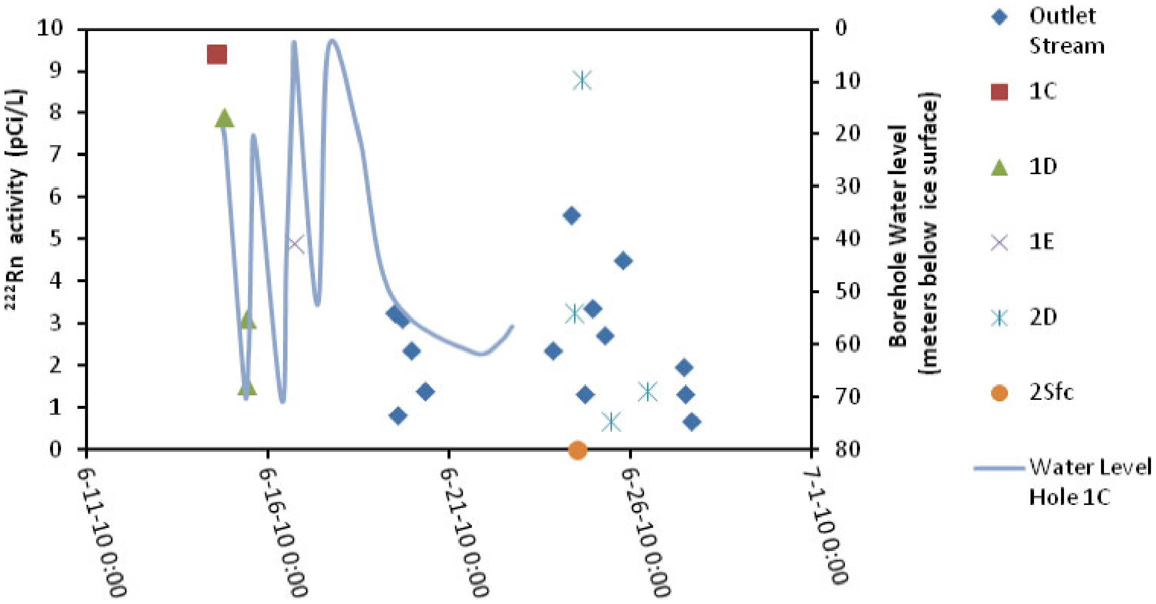

Figure 3-28. *Activity of ^{222}Rn for borehole and marginal outlet stream samples. Sample "2Sfc" is from a surface stream at site 2. The blue line is the water level in hole 1C; it is utilized here as a proxy for the amount of water in the subglacial system and in the outlet stream.*

3.5 Field campaign preliminary interpretations and conclusions

Key results and interpretations from the 2010 field research are preliminary and may be subject to change as ongoing analyses are completed.

Bed Characteristics

Three independent lines of evidence suggest the bed within the region of sites 1-2 consists of a relatively thin veneer of sediment on top of bedrock: 1) borehole video imaging shows sediment at the bed, but no soft and deformable till layer; 2) penetrometer tests failed to reveal a soft and deformable bed; 3) borehole slug tests suggest high transmissivity water flow at the bed.

Basal Water Drainage and Pressure

Observations of the subglacial hydrological system of this region of the ice sheet demonstrate many similarities to observations from mountain glaciers. The subglacial drainage system experiences diurnal water pressure variations, complex connection pathways, and very short residence times of basal waters. The water pressure exceeds ice overburden pressure at times, but also falls to less than 25% of overburden for short episodes. The basal water pressure also shows unusual high frequency variations for several days during the late summer. These variations are poorly understood 'valve-like' processes, perhaps related to elastic ice deformation, causing sudden changes in connections at the glacier bed.

Ice Temperature

Ice temperature is much warmer than expected or predicted by numerical models. Based on prior studies elsewhere in Greenland, and ice temperatures modelled by SPB and other workers, boreholes were expected to freeze closed in a matter of hours. Instead, the ice near the margin is nearly temperate (at the pressure melting point) and does not appear to be frozen to the bed. Further inland, at GL10-Site 3, the ice is temperate near the surface and bed, and only mildly cold (–4.5 degrees Celsius) at intermediate depths. Poor constraints on the modelling are likely to be partially responsible for the discrepancy between model results and observations. In addition, the ice is likely warmed by processes that are unaccounted for in the modelling because they have not previously been identified. Examples of processes that perhaps need inclusion in thermal-mechanical models include: latent heating from refreezing meltwater at the surface and within the ice, and high rates of basal sliding friction. Future work will address these issues by 1) additional ice temperature measurements, 2) improved numerical modelling via data assimilation methods, and 3) direct investigation of latent heating by refreezing meltwater.

Ice Depth

Ice depth near the center of this terrestrial terminating outlet glacier is much deeper than expected (i.e. the ice is >700 m deep and the bed is below sea level). A deep, and very steep-walled, trough runs through the outlet of Isunnguata Sermia and curves south higher up the ice sheet. The geometry of this trough is still poorly confined, but will hopefully emerge as more ICEBridge data become available.

3.6 2011 plans

Field Campaign

Boreholes will be drilled at two new sites during 2011 (Figure 3-29). At least three boreholes will be drilled at each site and fitted with sensors for measuring water pressure, ice temperature, and ice deformation rate. Basal water samples will be collected in at least one borehole at each site. Surface velocity will be measured at each of the two sites for a period of at least one year with a GPS station.

Modelling

Sub-project B will develop state-of-the-art adjoint based numerical methods to assimilate data collected from ongoing field campaigns into the thermo-mechanically coupled, higher-order ice sheet models. Team members will continue development of the two models: 1) a three-dimensional hybrid model, and 2) a full-stress profile model. The full stress model is important for estimating the errors in transition zones. The hybrid model provides continental-scale coverage, with high detail in critical regions. Both models are functioning to some degree, but require additional development. Using these models, research will focus on the basal temperature field and the basal melt rate.

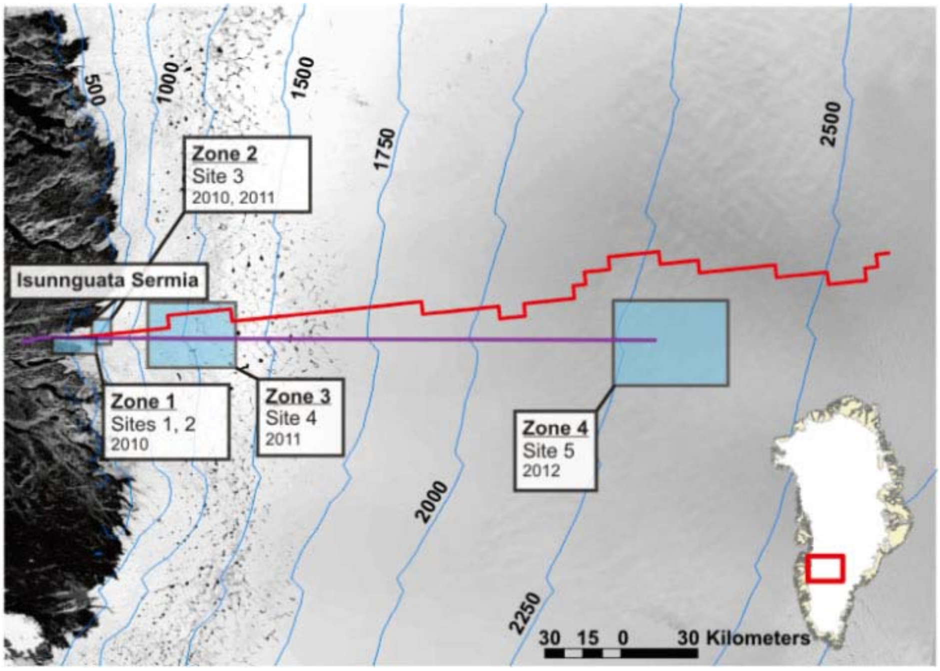

__Figure 3-29.__ Isunnguata Sermia and western Greenland drilling sites. The 2012 site is preliminary and subject to ice depth and logistical constraints. Boxes represent general field site vicinity and dates of completion. Red line shows the flowline defining the existing model profile described in modelling section. Purple line represents radar line flown by IceBridge in 2010.

4 Sub-project C activities 2010

The activities in 2010 have been divided into two categories: 1) planning of the 2011 drilling campaign and 2) continuation of the field investigations launched in previous years. The continued investigations include: hydrogeochemical sampling of borehole DH-GAP01 and surface waters; physico-chemical monitoring of borehole DH-GAP01; studies on the drillcores of boreholes DH-GAP01 and DH-GAP03; permafrost and talik investigations; and updating of the geological model (see Figure 4-1 for location of boreholes).

Planning of the 2011 Drilling Campaign

One of the main field objectives of the GAP, and consequently Sub-project C (SPC), is the drilling of the deep research borehole to allow for sampling and monitoring of groundwaters down to repository depth (i.e. about 500 m of vertical depth). Activities since 2008 have aimed to collect and provide sufficient background information to allow for the selection of the drilling site, as well as for the technical planning of the drilling and for the definition of the scientific targets of the campaign. These investigations have significantly increased our general understanding of the site area geology, structural geology, and hydrogeochemistry, and have been essential for the planning process (Aaltonen et al. 2010, SKB 2010).

The drilling plans have included the following: 1) review of the scientific aims; 2) selection of the drilling location; 3) planning of the borehole in 3D; 4) consideration of technical issues related to the drilling method; 5) hydraulic testing of the borehole,; and 6) questions related to logistics and budget.

At the same time, the challenges related to groundwater investigations in an Arctic environment have required special attention with respect to instrumentation design, motivating a thorough review of methods and components to be applied. In late 2009 a decision was made to subcontract the design and construction work to Geosigma AB, which has more than 20 years experience in downhole instrumentation and monitoring. Geosigma has been the main supplier for SKB instrumentations for many years and are also providing Posiva with field equipment solutions. Considerable communication is required to ensure that the scientific needs and the technical viability are met. Because long-term monitoring of the borehole is desired, a risk scenario assessment was done to identify the possible events that could compromise the durability of the instrumentation and its components.

Field Investigations

The field investigations included: 1) hydrogeochemical sampling from borehole DH-GAP01 and surface waters, 2) physico-chemical monitoring of DH-GAP01, 3) studies on the drillcores of boreholes DH-GAP01 and DH-GAP03, 4) permafrost and talik investigations, and 5) updating of the regional geological model.

Two field trips were conducted during the summer of 2010. The first one took place between the 6th and 13th of May, and the aim was to retrieve monitoring data and water samples that represent winter conditions with restricted meltwater production from surface or from the ice sheet. Borehole DH-GAP01 and the Leverett Spring (previously referred to as the Pingo Spring) were sampled. Physico-chemical data, recorded by the AquaTROLL in DH-GAP01, as well as the temperature and pressure data from the borehole weather stations, was collected. The temperature profiles in the talik hole (DH-GAP01) and in the permafrost hole (DH-GAP03) were measured. Temperature profiling was carried out in the Talik Lake (L26) to observe the undisturbed temperatures at the lake bottom. New data were used to update the geothermal model describing the talik.

The second field trip took place between August 31st and September 7th. DH-GAP01 was sampled for chemistry and also for microbial samples. Microbial sampling required filtering of a large volume of water and, hence, intense pumping. The pumping resulted in a significant lowering of the water level in the borehole. Recovery of the water table was monitored by the downhole instrumentation, and these data were used to calculate the transmissivity and water conductivity of the sub-packer borehole section.

The drillcores of DH-GAP01 and DH-GAP03 retrieved from the pilot boreholes in 2009 were shipped to Olkiluoto, Finland. In 2009, cores were photographed and logged in detail for lithology, the presence of fractures and fracture infillings. True orientation of fractures was measured and analyzed to aid both the drilling plans and the groundwater flow modeling. Drillcores DH-GAP01 and DH-GAP03 were sampled in May 2010 at Olkiluoto for detailed fracture infilling studies, crush and leach studies on matrix salinity and for petrophysical measurements.

The work to update the regional geological model was launched in 2010, as groundwater modelling groups identified the need for a better deformation zone model. Interpretation of the lineaments from topographical and geological data was expanded to cover the ice-free part of the defined modelling area. Airborne electromagnetic data was processed to support geophysical lineament interpretation. Major effort was made to find evidence of subglacial features.

The teams and main responsibilities of the 2010 SPC are given in Table 4-1. SPC is directed by Timo Ruskeeniemi at the Finnish Geological Survey (GTK). In addition to the overall GAP coordination, Lillemor Claesson Liljedahl (SKB) and Anne Lehtinen (Posiva) took care of the various instrumentations at the site, borehole sampling and monitoring, and had an essential role in the planning of the drilling and instrumentation design of the future research borehole. Jon Engström (GTK) did

Table 4-1. SPC personnel participating the field trips in 2010, the core logging and sampling in Olkiluoto and deformation zone modelling.

Field trip/activity	Name	Organization	Activity
May 6– 13	Claesson Liljedahl, Lillemor	SKB	Project coordination, geology, instrumentation and monitoring
	Engström, Jon	GTK	Geology, geomodelling , DTS-measurements
	Henkemans, Emily	Univ. Waterloo	Hydrogeochemistry
	Lehtinen, Anne	Posiva	Project coordination, hydrogeochemistry, instrumentation and monitoring
	Ruskeeniemi, Jari-Jussi	Aalto Univ.	Field assistant
	Ruskeeniemi, Timo	GTK	SPC coordination
August 31 – September 7	Aaltonen, Ismo	Posiva	Geology, geomodelling
	Claesson Liljedahl, Lillemor	SKB	See above
	Frape, Shaun	Univ. Waterloo	Hydrogeochemistry, water-rock interaction
	Hardisty, Dalton	Univ. Indiana	Microbiology
	Henkemans, Emily	Univ. Waterloo	See above
	Hirschorn, Sarah	NWMO	Project coordination
	McKelvie, Jennifer	NWMO	Microbiology
	Ruskeeniemi, Timo	GTK	See above
Drill core logging and sampling	Drake, Henrik	Univ. Gothenburg	Bedrock redox front studies (parallel research project)
	Engström, Jon	GTK	See above
	Frape, Shaun	Univ. Waterloo	See above
	Lehtinen, Anne	Posiva	See above
	Makahnouk, Mike	Univ. Waterloo	Water-rock interaction
	Pere, Tuomas	Posiva	Bedrock geology, core logging
	Ruskeeniemi, Timo	GTK	See above
	Smellie, John	Conterra	Bedrock redox front studies (parallel research project)
	Tullborg, Eva-Lena	Terralogica	Bedrock redox front studies (parallel research project)
Geological modelling	Aaltonen, Ismo	Posiva	See above
	Claesson Liljedahl, Lillemor	SKB	See above
	Engström, Jon	GTK	See above
	Follin, Sven	SF GeoLogic AB	Modelling coordination
	Klint, Knud Erik	GEUS	Geomodelling, contacts with authorities, logistics
	Lehtinen, Anne	Posiva	See above
	Paananen, Markku	GTK	Geophysics, geomodelling
	Ruskeeniemi, Timo	GTK	See above
	Stigsson, Martin	SKB	Geomodelling

DTS temperature profiling and was responsible for the geomodelling task. Shaun Frape and Emily Henkemans (University of Waterloo) conducted hydrogeochemical studies of surface water and groundwaters. Mike Makahnouk (University of Waterloo) focused on mineralogical studies. Knud Erik Klint (GEUS) participated in the geomodelling work and managed the contacts with local authorities, and was responsible for the permits.

Co-operation with the SKB- and Posiva-funded project entitled, "Detection of the near-surface redox", which investigates the nature of the redox fronts observed in drill core material from DH-GAP01 and DH-GAP03 is conducted. This redox study is carried out in collaboration with the water-rock interaction team of the University of Waterloo.

The main activities conducted in 2010 and the current status of investigations are described in the following chapters. The different data types produced during 2010 are presented in Table 4-2.

Table 4-2. Data types produced in 2010.

Activity	Data type	Status
Geology		
– Drill core	Drill core logs: lithology, fractures, fracture orientation, fracture infillings	
	– DH-GAP01	Reported
	– DH-GAP02	Not logged
	– DH- GAP03	Reported
– Bedrock mapping	Lithologies, tectonic measurements	Reported
– Petrophysics	density, matrix porosity, thermal conductivity, magnetic susceptibility, remanent magnetization, seismic P-wave velocity and specific resistivity	Reported
Physical monitoring		
– DH-GAP01	DTS temperature profile	Data collected in May 2010
– DH-GAP03	DTS temperature profile	Data collected in September 2010
– DH-GAP01	AquaTROLL: pressure, temperature, electrical conductivity. Record since June 2009	Data collected in May and September 2010
– Talik Lake (L26)	Temperature profiling of the water column	Reported
Hydrogeochemistry	(chemistry, isotopes)	
– DH-GAP01	Hydrogeochemical analyses, 2 sampling rounds in 2010	Analyzed
– Surface waters (Leverett spring, lakes)	Hydrogeochemical analyses, 2 sampling rounds in 2010, Spring gas composition	Analyzed
Weather data	Pressure and temperature from the sites of DH-GAP01 and DH-GAP03. Record since September 2009	Data collected in May and September 2010

4.1 Planning of the deep research borehole

The aim of the deep research borehole is to provide groundwater sampling and monitoring opportunities down or below the hypothesized 'repository depth'. This depth was defined as 500 m of vertical depth. Preferentially, the hole should extend beneath the ice sheet and it should intersect geological units which are representative for repository sites. The diameter and dip of the hole should be such that instrumentation with a multi-packer system would be feasible.

Selection of the drilling site was based on the investigations carried out since 2008. Geological and structural studies were initiated by detailed mapping of selected key areas, which provided information on the variability of the rock types and deformation in the area considered feasible for the GAP studies (Aaltonen et al. 2010). After evaluating the gathered information and considering the logistical, environmental and safety aspects, SPC suggested that the area called *Caribou* would be the most promising area for research drilling (see Figures 4-1 and 4-2).

The borehole will be DH-GAP04, the drilling length will be approximately 700 m and the dip 70º. Drilling orientation will be northwards, but small adjustment may be made depending on how the drilling rig is positioned. Figure 4-3 shows how the borehole is located relative to the ice sheet.

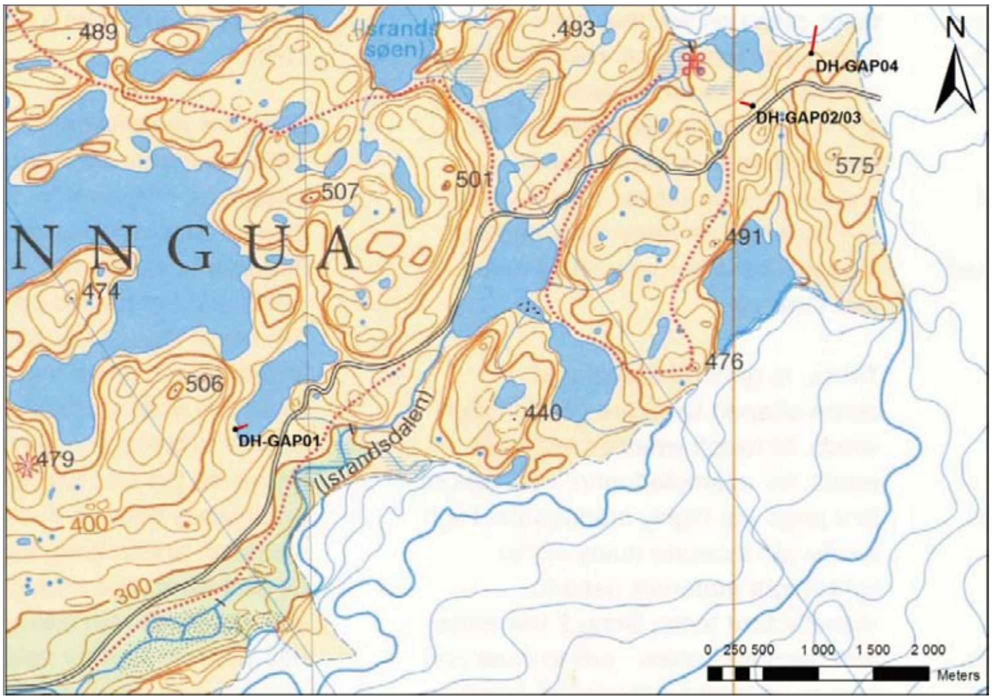

Figure 4-1. *Location of the deep research borehole DH-GAP04 relative to boreholes DH-GAP01 and DH-GAP03. Base map: Hiking Map 1:100 000, © Greenland Tourism a/s.*

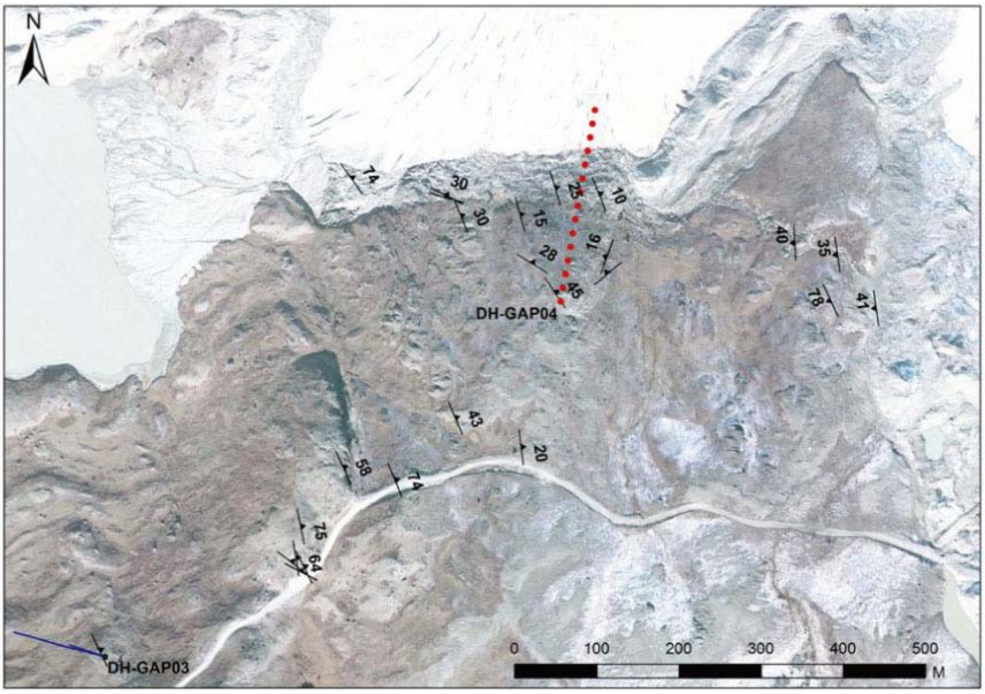

Figure 4-2. *Possible orientation of DH-GAP04 (red dotted line). Drilling will be planned so that the borehole cuts the foliation and the main fracture sets in an optimal manner. DH-GAP03 is located in the lower left corner, about 600 m SW from DH-GAP04.*

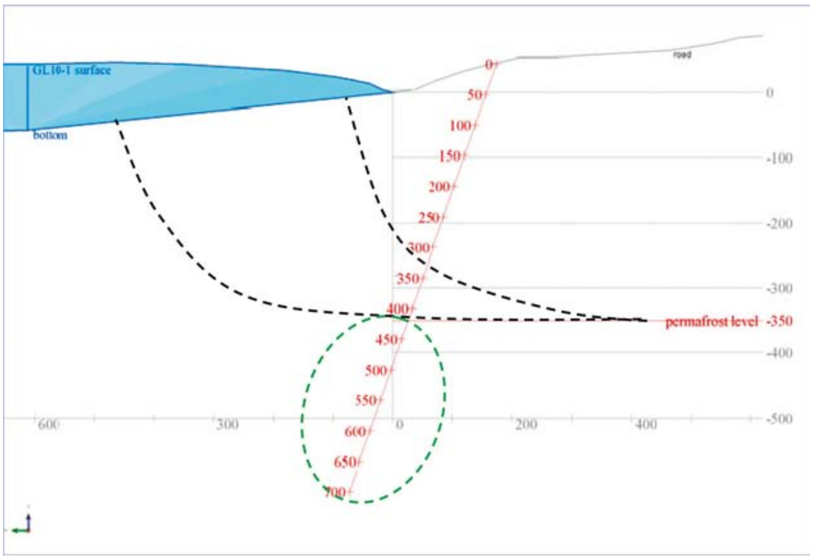

Figure 4-3. Schematic cross-section showing how the 700-m long borehole is located relative to the ice sheet. The assumed drilling angle is 70 degrees. Dashed black lines indicate two different scenarios as to how the permafrost could distribute beneath the ice sheet. Because there is not enough information available yet to judge which one is more likely, the planning is based on the deep penetration scenario. Green dashed oval indicates the most probable zone for groundwater sampling.

The drilling will be done using double tube WL-76 (wire line) equipment, providing 76 mm hole and 57 mm core. Lake water will be applied as drilling offlushing water. In order Because the drilling will be done in th frozen ground, the drilling water will be warmed to 60°C. Heating will also keep the borehole open for hydraulic testing and instrumentation. The flushing water will use sodium fluorescein for tracering.

Information about the location of water conducting fractures in the borehole is important for successful downhole instrumentation, so that the sampling sections can be positioned where possible meltwater recharge routes have been identified. SPC will conduct the hydraulic testing of the borehole by using the Posiva Flow Log (PFL).

Instrumentation of the deep research borehole is a challenging task, and therefore the preparations for these activities began late in 2009. The construction includes two inflatable packers, which isolate a section with a fixed length of 10 m. Water sampling uses a combination of two pieces of tubing connected to a U-coupling, and a check valve which allows purging of samples with nitrogen gas. One tube is pressurized with gas to close the check valve, and the water is squeezed to the surface through the other tube. A purge will provide 5 to 7 liters (depending on final installation depth) of water and samples can potentially be collected from three sections: above, between and below the packers. Each sampling section will have a pressure sensor and an electrical conductivity sensor. Additionally, the fixed section will have a temperature sensor. Data will be collected in a logger and transmitted via satellite modem to a data server. A continuous down-hole temperature profile (from the surface, through permafrost, down to the fixed section) will read by a fiber optic cable (DTS).

A heating cable will be installed in the hole down to the base of the expected permafrost depth. The cable must be powered a few days before water sampling in order to melt the potentially frozen sampling lines.

Field activities related to drilling of the deep research borehole are scheduled to take place between early June and mid July, 2011.

4.2 Hydrogeochemical investigations

The goal of the hydrogeochemical studies is to investigate if glacial meltwater penetration into the bedrock takes placeoccurs and how the mixing of melt water affects the chemical nature of deep groundwaters. To reach this goal, and to increase the understanding of the functioning processes, information is required for the potential end members: meltwaters, surface waters and the deep groundwaters. In addition, hydrogeological conditions have an important role in the evolution of the local groundwater flow system. Particularly, the fracture network and permafrost conditions are controlling the groundwater flow and the mixing behavior of the different water types in bedrock. Since 2008, significant efforts have been made to investigate these topics. The studies included extensive hydrogeochemical sampling from surface water, and diamond drilling and instrumentation of two research boreholes (DH-GAP01, DH-GAP03) in 2009 (Aaltonen et al. 2010, SKB 2010).

Groundwater sampling from borehole, DH-GAP01, and the Leverett spring, see Figure 4-5, were the main targets of the 2010 hydrogeochemical investigations. Studies on surface waters were continued with more emphasis on the saline lakes (Hunde Sø, Braya Sø, Little Hun Store Saltsø located at the head of the fjord (see Figure 4-4). Additionally the Talik Lake (L26) was profiled for temperature and depth (see Chapter 4.7.2). From the selected profiles of, pH and EC, ,two water samples were taken for the transition zones of the temperature profile.

Hydrogeochemical investigations were supported by monitoring the physical and chemical conditions in the packered-off section in DH-GAP01 (Figure 4-6). Pressure, temperature and EC data are recorded with pre-set frequencies (see Chapter 4.4.1).

Figure 4-4. *Locations of saline lakes sampled around Kangerlussuaq from 2008 to 2010. © Google Earth.*

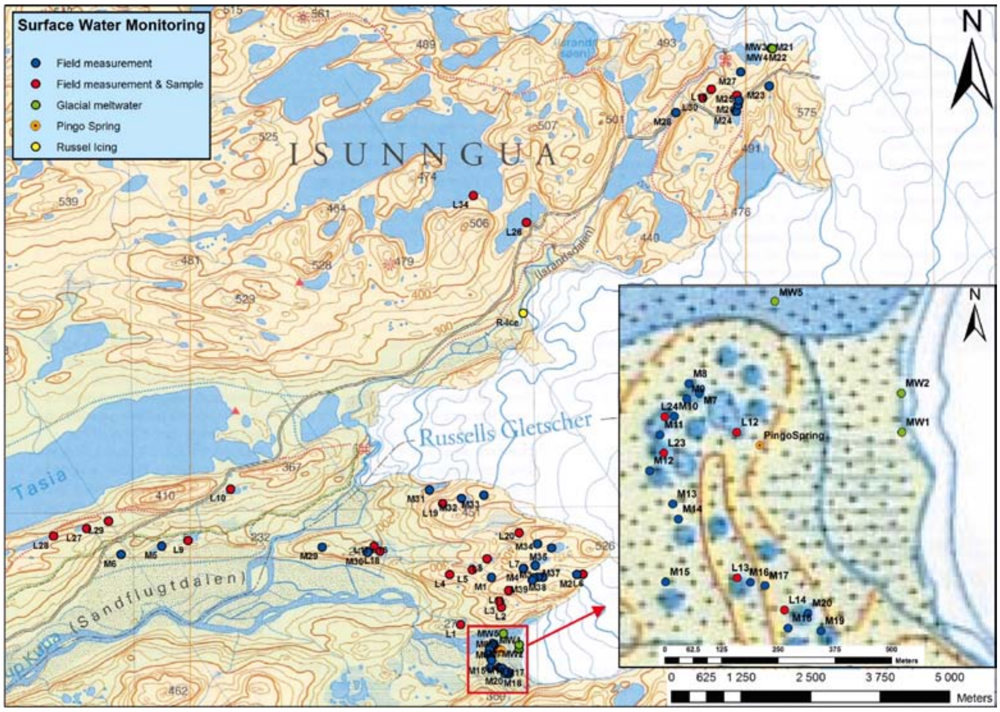

Figure 4-5. Sampling locations from 2008 to 2010 along the ice sheet margin, including locations where surface water samples were collected (red dot with L code) or only field measurements were conducted (blue dot with M code). MW codes with pink dots stand for meltwater sampling locations. Leverett Spring is located in front of the ice tongue at the lower edge of the figure. Base map: Hiking Map 1:100 000, © Greenland Tourism a/s.

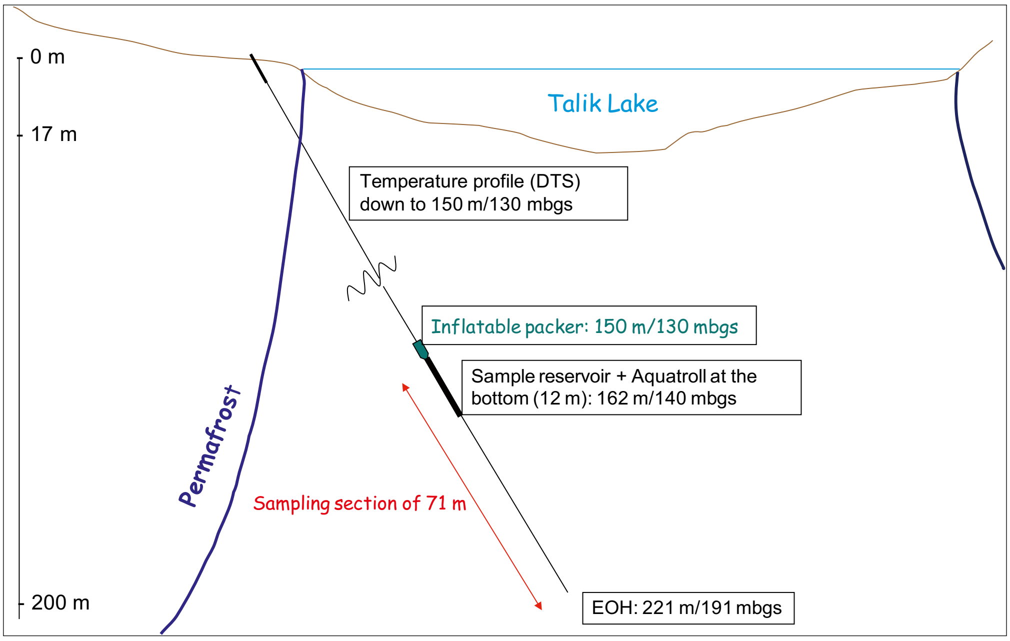

Figure 4-6. Schematic plan of the borehole DH-GAP01, the instrumentation and the hydrogeological context. Mbgs = meters below the ground surface, 0 m is the ground surface at the wellhead. EOH = end of the borehole.

4.2.1 Status of the hydrogeochemical investigation

After completing the drilling of DH-GAP01 in 2009, the borehole was outfitted with a U-tube sampler (Freifeld et al. 2005) at a vertical depth of 130 m. The system consists of a pneumatic packer, a U-tube sampling system with a sample fluid reservoir, and pressure/temperature/conductivity sensors. For the technical description of the sampler, see the GAP yearly report 2009 (SKB 2010). The sampling section is 150–221 m borehole length (i.e. 130–191 mbgs), i.e. the section between the packer and the bottom of the hole (Figure 4-6). Water samples are purged using nitrogen gas. A pressure of about 350 PSI was applied in order to get water from the sampling section. The borehole has been purged a total of 54 times from June, 2009 to September, 2010. Given that one purge yields 11.8 L water, we have extracted approximately 640 L water in total from the borehole as of September, 2010. This means that we have completed approximately 4 cleaning cycles of the section below the packer (the section below the packer is 71 meters, with a diameter of 56 mm, giving a section volume of 175 L). During drilling, a significant decline of flushing water pressure was observed at 203 m of borehole length, indicating the presence of an open fracturing. This fracture(s) could also be found also from the drill core. We assume that this zone dominates the inflow into the borehole. Stabilization of the chemistry, and the reduction of flushing water contamination from major to minor within two years, demonstrate that the flushing has been effective. In addition to the description of the instrumentation of DH-GAP01, Figure 4-6 illustrates the hydrogeological context of the Talik Lake area.

Samples collected between July and September of, 2009 contained tritium, a short-lived ($t_{1/2}$ = 12.43 years) radioactive isotope of hydrogen whose presence indicates recently recharged waters, and sodium fluorescein tracer used in the drilling waters. Preliminary sampling of DH-GAP01 in 2009 showed that drilling waters had not yet been flushed from the system (SKB 2010). Sampling of DH-GAP01 was conducted successfully in both May and September, 2010, and showed an absence of tritium and tracer concentrations (< 5% initial concentration), indicating that the borehole has recovered and drilling waters have been flushed from the system. Samples were analyzed for geochemistry as well as several isotopic parameters: $\delta^{18}O$, $\delta^{2}H$, ^{3}H, $^{87}Sr/^{86}Sr$, $\delta\,^{37}Cl$, and $\delta\,^{34}S$ and $\delta^{18}O$ of SO_4.

Prior to May, 2010, it was unknown whether or not the Leverett spring (previously referred as the Pingo Spring) flowed throughout the winter. It was discovered in May, 2010, that the spring continued flowing throughout the winter and a large mound of ice had built up over the spring outlet. A manual ice drill was used to drill through ice mound (Figure 4-7). Water immediately began to flow from the hole upon puncturing of the ice cap (Figure 4-13), indicating the groundwater system remains under pressure throughout the winter.

While the pond that accumulates around the Leverett spring during the summer months has a rust-red color, the water flowing from the spring through the ice hole in May was clear, indicating that the iron in the spring water was unoxidized. Additional observations include the smell of H_2S gas and a water temperature of 0.3°C. Water samples were collected for geochemical and isotopic analyses.

In May, 2010, it was observed that the drive point piezometers installed in the previous summer had been heaved out by the freezing pingo over the winter and were, unfortunately, no longer functional.

The Leverett spring was re-visited in September, 2010, with the collection of additional gas samples as the first priority. Water samples were also collected for additional isotopic analyses ($d^{34}S$ and $d^{18}O$ of SO_4, $d^{37}Cl$ and $d^{81}Br$); however, the sample volume was not enough to obtain a reliable ^{81}Br analysis at the low concentrations (0.9–1 mg/L) of the spring water.

4.2.2 Hydrogeochemical sampling and analysis methods

Samples were obtained from DH-GAP01 in May, 2010 and again in September, 2010. Heating of the hole to melt the ice formed in the sampling line within the permafrost zone (upper 20 m of drill hole length) had to be performed during both campaigns. Water samples were collected for the chemical and isotopic analyses. Additionally, in September, 2010, a large amount of water was pumped and filtered for microbial sampling (Chapter 4.3). The intense pumping was used as a modified ‘slug test’ to retrieve data to calculate hydraulic transmissivity and conductivity for the sampling section. The outcome from the modified ‘slug test’ is reported in Chapter 4.4.3 and in more detail in Appendix 3.

Figure 4-7. Ice mound covering the Leverett spring in May, 2010. A hand powered ice auger was used to drill through over 1.2 meter of ice. Photo by Emily Henkemans.

Surface water samples were collected from the shoreline of lakes, avoiding andshallow or partially enclosed areaswere . A portable Oakton pH, electrical conductivity and temperature meter was used to measure field parameters at sampling locations.

Water samples for isotopic and anion analyses were collected in plastic Nalgene bottles and were not filtered or otherwise treated. Cation samples were filtered with 0.45 µm filters and acidified with nitric acid. Samples collected for analysis of the tracer, sodium fluorescein, were wrapped in aluminum foil to prevent deterioration of the tracer from light. Samples for dissolved organic and inorganic carbon were filtered with 0.45 µm filters, and the DOC samples were acidified using phosphoric acid.

Gas samples from the Leverett spring were collected using a large funnel inverted and held underwater over the location where bubbles have been consistently observed in the spring pond and water can be seen rising to the surface. The funnel feeds into an inverted glass bottle that has been filled with water from the spring pond (Figure 4-8). Water is displaced as the gas sample is collected and the bottle is capped with a teflon septum equipped cap underwater; some water remains in the inverted bottle to help seal the gas sample. 500 mL and 1 L glass bottles have been used with approximately 1/3 of the volume occupied by water and 2/3 occupied by the gas. A potential source of oxygen in the gas samples is release of atmospheric gas from bubbles in melting ground ice in the till. Bottles were transported in an inverted position.

Isotope analyses were performed at the University of Waterloo Environmental Isotope Lab. Geochemical samples were analyzed at Labtium Oy in Finland, except for the sodium fluorescein samples, which were analyzed at Teollisuuden Voima (TVO) lab in Finland. Gas samples were analyzed at the University of Waterloo Organic Geochemistry Lab. Microbial samples were analyzed at the Microbial Analytics Sweden Ab in Gothenburg.

Figure 4-8. Gas sampling method: funnel and mouth of bottle are held underwater as gas displaces water in the glass sampling bottle. Bottle is then capped underwater and kept inverted. Photo by Emily Henkemans.

4.2.3 Hydrogeochemical analysis results and discussion

Surface Waters

Surface water studies continued to build on the work done in 2008 and 2009, but with a more focused approach. The goals of surface water sampling in 2010 were 1) to examine the saline lakes located close to the head of the fjord (see Figure 4-4) to determine the source of salinity and the potential for groundwater contribution to those lakes ; and 2) to further constrain the geochemical processes affecting the chemical composition of lakes further inland. Lakes are defined as saline and dilute after Anderson et al. (2001) where saline refers to lakes with electrical conductivities greater than 800 mS/cm and dilute as less than 800 mS/cm. Lakes in the region all fall within the range of fresh (< 1,000 mg/L) or brackish (1,000–10,000 mg/L) waters (Davis 1964).

The saline lakes located close to the head of the fjord have been previously studied (e.g. Williams 1991, Anderson et al. 2001, Leng and Anderson 2003, Aebly and Fritz 2009). These lakes include Hunde Sø (L21), Braya Sø (L22), Limnea Sø and Store Saltso (L32). These studies suggest that the elevated salinity in these lakes comes from evaporative concentration.

Figure 4-9 shows that the saline lakes Hunde Sø, Braya Sø and Store Saltsø fall along a local evaporation line. However, these saline lakes also show the effects of very long residence times of around 8,000 years (Aebly and Fritz 2009). Tritium levels in Store Saltsø and in Hunde Sø are lower than that would be expected from evaporative concentration, and, in fact, are lower than tritium levels found in local precipitation (13.8 TU from July, 2009 snow sample). Store Saltsø and Hunde Sø had tritium concentrations of 8.3 and 12.1 TU, respectively. The maximum tritium concentration of a lake can be diminished with respect to ^{3}H levels in precipitation by dilution with tritium free pre-bomb waters (Herczeg and Imboden 1988). Closed basin lakes, such as Store Saltsø, may have long residence times and low tritium inputs due to the low yearly precipitation and the removal of water only by evaporation.

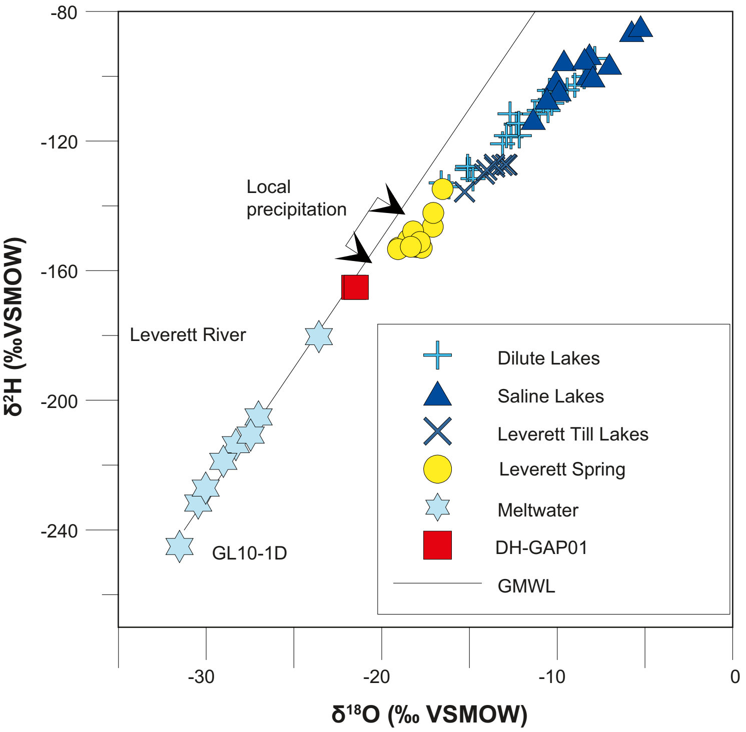

Figure 4-9. *Plot of $\delta^{18}O$ versus $\delta^{2}H$ of ground and surface waters in the study area. Surface waters describe a local evaporation line with a slope less than the global meteoric water line (GMWL). DH-GAP01 samples only from 2010 are shown, as 2009 samples were contaminated with drilling water.*

Anderson et al. (2001) suggest the aeolian transport of marine deposits from around the fjord, as well as of loess, as contributing salts to the saline lakes. Isotopic analyses of $\delta^{34}S$ and $\delta^{18}O$ of SO_4 in saline lake samples, indicate that marine salts are a source of salinity in the lakes close to the fjord. Hunde Sø has a $\delta^{34}S$ of sulphate that is enriched by over 20‰ compared to the inland lakes. Hunde Sø has 23‰ of $\delta^{34}S$ of sulphate, which is similar to the sea water value of 21‰. It is likely that the sulphate in Hunde Sø and the other fjord lakes originates as sea salt aerosols. The $^{87}Sr/^{86}Sr$ ratio of Hunde Sø (0.730) is less than that of other lakes in the area, which fall between 0.74 and 0.76. This could be due to the geological influence (plagioclase feldspar) or the mixture of marine ($^{87}Sr/^{86}Sr$ (0.7091,) (Clark and Fritz 1997) and geological sources of salinity.

Crush and leach experiments on the drillcores have shown that the anionic composition of the dilute lakes (<800 mS/cm) is generally similar to that of the waters derived from crush and leach (Figure 4-10). Waters extracted from three sections of core have around 30% of chloride (in total milliequivalents), and 4 samples have about 30% of sulphate. Crush and leach experiments suggest that sulphate, and chloride, in the more dilute lakes which are located away from the fjord are geologic origin. The terrestrial sulphate signature of $\delta^{34}S$ and $\delta^{18}O$ (Figure 4-14) in the dilute lakes suggests that the oxidation of sulphides from local bedrock and till are the sources of sulphate in these lakes (Clark and Fritz 1997).

During the temperature profiling of the Talik Lake (Chapter 4.7.2), pH and electrical conductivity were measured at several of the profiling points: two at the deepest part of the lake and one in a shallower area. The pH decreased with depth (from 8.3 at the surface to 7.7 at 28 m depth) and the electrical conductivity increased with depth (from between 210–214 to 232–233 µS/cm at 28 m of depth). These measurements confirmed the stratification of the lake and the presence of a slightly higher conductivity and lower pH at the bottom layer. A sample taken at 28 m depth in September, 2010 showed similar isotopic and geochemical properties as a sample taken at 8 m depth in July, 2009 (SKB 2010).

Initially, it was planned that Lake Ferguson (L33) (for location see Figure 4-4) would also be profiled in May, 2010, but the early and rapid melt that was occurring during the field trip rendered the ice unsafe before this goal could be accomplished. It was noted that Lake Ferguson had no observed flow in May 2010.

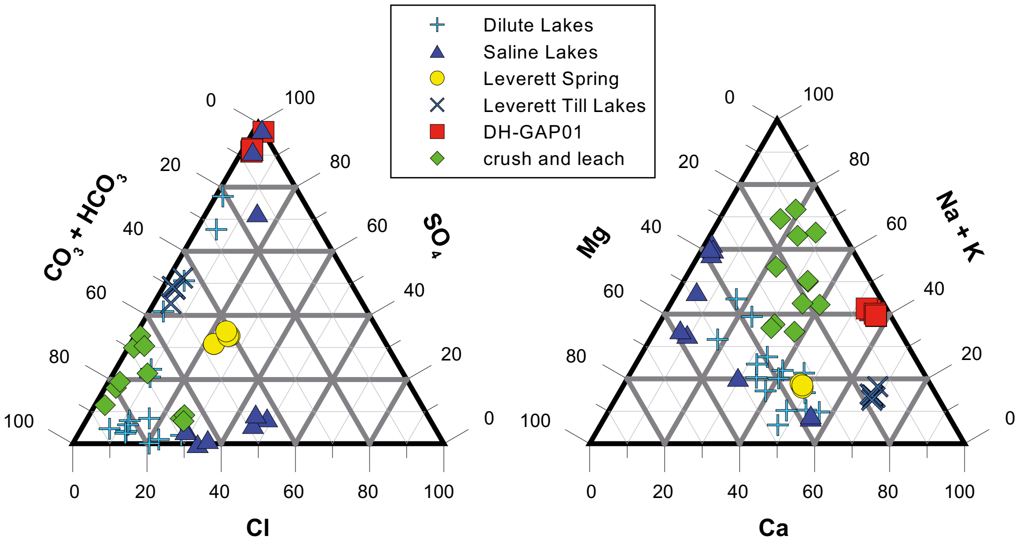

__Figure 4-10.__ Ternary plots of crush and leach, ground and surface waters as mol percent of total for major cations and anions.

Glacial Meltwater

Four meltwater samples were collected from Russell and Leverett glaciers in 2008 (SKB 2010) and are indicated by the designation "MW" in Figure 4-5. In September, 2010, a sample was collected from the main meltwater river emerging from beneath Leverett glacier at, as close to its point of emergence as safely possible. This sample was analyzed for δ^{18}O and δ^{2}H and was found to be approximately 7–10 ‰ enriched in δ^{18}O over the meltwater samples collected in 2008 (Figure 4-9). The river sample contained 1.5 TU, thus, its enrichment in the stable isotopes is likely due to a larger contribution of melt from the surface where more recent snow contributes enriched and tritiated waters. In addition, a sample provided from the ice-hole GL10-1D by SPB (see Chapter 3.4.7) was also analyzed for δ^{18}O and δ^{2}H and was found to be more depleted than the 2008 meltwater samples by 1–3‰ in δ^{18}O (Figure 4-9). It is clear that there is a large amount of variation in meltwaters in terms of their stable isotopes. Constraining the glacial meltwater end member is important in this system if the extent of connection between meltwater and groundwater is to be understood. Therefore, it is important toto explore further the full range of variation.

Russell Icing

The Leverett spring was the only iron-rich feature observed in the study area prior to May, 2010. However, during fieldwork in May, 2010, a stream of reddish colored ice similar in appearance to the ice covering the pingo, was observed at Russells glacier near the Talik Lake (Figure 4-11). Unfortunately, the feature was no longer flowing and no water sample could be taken to compare to the Leverett spring waters.

Figure 4-11. Icing feature observed in May, 2010 at Russells Glacier near the Talik Lake. Photo by Emily Henkemans.

DH-GAP01 (Talik Hole)

Figure 4-12 shows the isotopic and geochemical evolution of DH-GAP01 as the drilling water (Talik Lake water) is progressively purged and replaced by waters more representative of the formation. In the 2010 samplings, the average total dissolved solids (TDS) was 580 mg/L, which is higher than the Talik Lake water (185 mg/L). According to David's (1964) TDS classification, groundwater ,samples are fresh waters (TDS < 1,000 mg/L). The water type for DH-GAP01 is Ca-Na-SO_4 in all samples taken in 2010.

DH-GAP01 waters become more depleted in both $\delta^{18}O$ and $\delta^{2}H$ and move toward the Global Meteoric Water Line (GMWL) as the well recovers from drilling activities in 2009 (Figure 4-9). Isotopic values for DH-GAP01 water samples collected in May and September of 2010 locates on the GMWL, at values slightly more depleted than local precipitation but more enriched than glacial meltwater (Figure 4-9). A potential explanation for the isotopic composition of the DH-GAP01 waters is that they represent meteoric waters recharged during a cooler climatic period, when precipitation was more isotopically depleted in $\delta^{18}O$ and $\delta^{2}H$ than modern precipitation. The lack of tritium in DH-GAP01 also indicates that waters were recharged more than 50 years before present.

The waters extracted from the crush and leach experiments had $^{87}Sr/^{86}Sr$ ratios considerably lower (0.706–0.713) than the lakes (0.730–0.757). However, DH-GAP01 waters have a $^{87}Sr/^{86}Sr$ ratio of 0.7075 falling within the range of the crush and leach waters. This indicates that the chemistry of DH-GAP01 groundwater is strongly related to the chemistry of the bedrock. The higher lake $^{87}Sr/^{86}Sr$ ratios (0.730–0757) may represent that Sr is obtained from glacially pulverized and weathered rock material where K-feldspars and micas (with , ($^{87}Sr/^{86}Sr$ of 0.74–0.76,; from McNutt et al. 1990) have greater influence on the Sr isotope ratio, in particular, the weathering of biotite (Blum and Erel 1997).

When the DH-GAP01 waters are compared to the chemistry of the crush and leach waters, the borehole groundwaters shows higher mol percentages of sulphate and calcium out of total anions and cations, respectively (Figure 4-10; Figure 4-12). DH-GAP01 waters have high concentrations of SO_4 compared to the Pingo Spring (Leverett Spring) waters and the majority of surface waters.

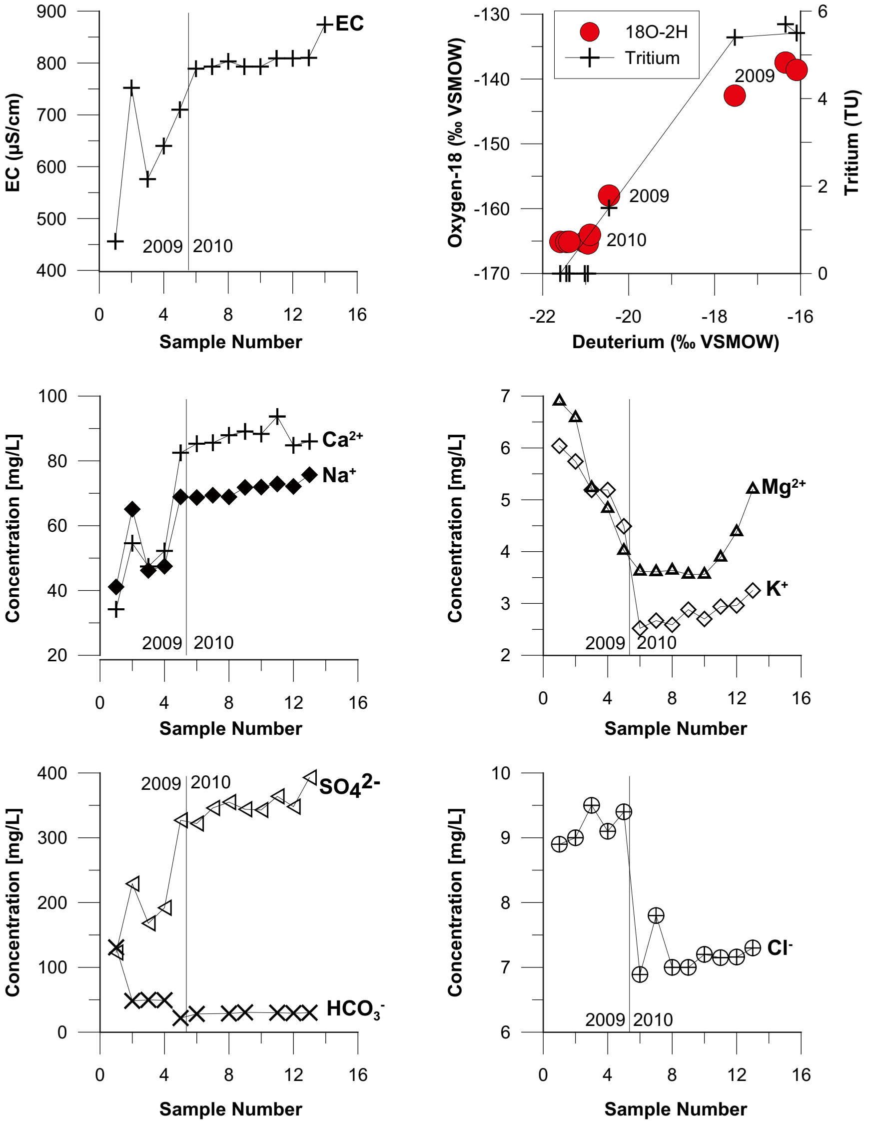

Figure 4-12. Geochemical and isotopic evolution of the groundwaters sampled from the DH-GAP01 borehole in 2009 and 2010.

Stotler et al. (2010) reported δ^{37}Cl of –0.78 to +1.52‰ SMOC (standard mean ocean water) for groundwaters in the Canadian and Fennoscandian Shields. DH-GAP01 groundwater has similar but slightly negative δ^{37}Cl value of –0.05‰ as the other shield groundwaters. Negative values of δ^{37}Cl (–0.2 to –0.4‰) have been observed in thelakes impacted by evaporation in the Kangerlussuaq area. These values fall within the range of marine salts and shield rock. At this time, DH-GAP01 water cannot use the d^{37}Cl values to distinguish its origin between these sources or the effects of fractionation that occurs during evaporation and the precipitation of salts. DH-GAP01 waters are not impacted by evaporation because there is no enrichment of δ^{18}O and δ^{2}H, as is typically seen in evaporated waters (Clark and Fritz 1997).

The isotopes of sulphate, δ^{34}S and δ^{18}O, indicate that there is enrichment in both the heavy isotopes for sulphur and oxygen in DH-GAP01 waters relative to lakes located away from the influence of marine sulphate (Figure 4-14). Enrichment in d^{34}S and d^{18}O of sulphate may indicate that bacterial sulphate reduction is occurring (Clark and Fritz 1997). However, microbial analysis did not reveal the presence of sulphate reducers in 2010 samplings (see Chapter 4.3). The DH-GAP01 waters do fall within the range of d^{34}S/ d^{18}O values observed in sulphate in groundwaters of the Canadian Shield (e.g. Fritz et al. 1994). Further study of the sulphur bearing minerals found in the bedrock could help determine the source of sulphate in groundwaters.

Leverett Spring

One aim of SPC in 2010 was to constrain whether or not the oxygen measured in gas samples collected from the Leverett spring (previously referred as the Pingo Spring) is from the groundwater system or is the result of contamination by air during or after sampling. Gas samples have been collected each year for the GAP project, starting in the preliminary reconnaissance trip in 2008 (Table 4-3). The quality of the 2008 sample was questionable and was likely contaminated by air. In the subsequent years, samples have shown a small percentage of oxygen in each sample with althoughusing the improved collection methods have been used. The two samples collected in September, 2010 were analyzed for $\delta^{18}O$ of the gas phase to further constrain the source of the gas. However, results indicated that microbial activity had caused fractionation of the oxgen isotopes in the gas phase and so the results could not be considered representative. Samples taken in 2011 will be kept cool during transport and storage to eliminate this issue.

A deep source for the oxygen is unlikely as previous studies suggest oxygen is consumed within 50 to 120 m of the surface (e.g. Spiessl et al. 2008, Drake et al. 2009). A potential source of oxygen is from air bubbles trapped in melting ice in the till. It was observed, while collecting gas samples, that small pieces of clear ice containing bubbles would emerge from the spring (Figure 4-7).

In addition, a final trip to the Leverett spring is planned for April of 2011 when the ice cover of the spring will be used to further limit the possibility of contamination by the atmosphere.

Comparing the chemistry of samples ,from the hole drilled through the ice (Figure 4-12) collected in May 2010 to that of samples collected in June, July or September, it reveals that the chemistry is mostly the same. The major difference is that the water collected from the ice covered (less aerobic) spring in May has more iron – 14.8 mg/L compared to an average of 8.9 mg/L in samples collected from the open pond. The formation of oxyhydroxides, resulting in the reduction of dissolved iron, likely accounts for the difference.

Figure 4-9 shows that small variations, outside of analytical uncertainty, occurring in the $\delta^{18}O$ and $\delta^{2}H$ values of the Leverett spring waters. At this time, there is no discernable relationship between these variations and the time of year. The spring waters differ from the DH-GAP01 waters in this respect, because the waters collected from the DH-GAP01 borehole did not vary outside of analytical uncertainty during either of the May or September sampling episodes in 2010.

The Leverett spring waters are enriched in $\delta^{18}O$ over local precipitation, but fall below the local evaporation line that is described by the lakes in the Kangerlussuaq region (Figure 4-9). Scholz and Bauman (1997) suggest that the source of the spring waters is hydrothermal. Enrichment in oxygen-18 over precipitation can indicate hydrothermal waters (Clark and Fritz 1997). Scholz and Bauman (1997) state that there are elevated levels of fluoride, aluminum and gold, which are often associated with hydrothermal systems. However, the measured value for aluminum of 451 µg/L (Scholz and Bauman 1997) is much higher than the 10–25 µg/L consistently measured in the spring in this study. Fluoride is also not present in high concentrations (<0.1 to 0.1 mg/L), nor is lithium (0.6 to 0.8 µg/L).

Table 4-3. Composition of gas samples collected at the Leverett spring from 2008 to 2010. Multiple samples taken in 2009 and 2010 are averaged in this table but did not vary greatly (Oxygen range 0.85–1.44% in 2009 and 1.28–1.79% in 2010).

	% Oxygen	% Nitrogen	%CO2	% Methane	Total %
Atmosphere	20.95	78.08	0.04	0	99.07
Spring 2008	10.96	85.52	0.36	ND	96.83
Spring 2009 (Avg)	1.26	92.29	0.92	0.11	94.59
Spring 2010 (Avg)	1.53	93.69	1.88	0.03	97.13

Leverett spring waters show an enrichment of $\delta^{34}S$, 5–10‰ richer than inland lakes analyzed (Figure 4-14). Along with the observed smell of H_2S during sampling from the spring when it is covered with ice in May, the enrichment in ^{34}S may be evidence for bacterial sulphate reduction. Figure 4-14 shows that DH-GAP01, the Leverett spring, lake 0023W and the saline lake Hunde Sø have $\delta^{18}O$ of SO_4 values that falls within a narrow range (3.4 to 6.0 ‰). The $\delta^{18}O$ of sulphate approaches a constant value during the later stages of reaction (Fritz et al. 1989) which may explain the narrow range of sulphate values found for those waters impacted by sulphate reduction.

Similar to the lakes in this area, the $^{87}Sr/^{86}Sr$ of the Leverett spring is 0.74283, falling within the range expected for Sr derived from K-feldspar and micas (0.74 to 0.76) (McNutt et al. 1990). The Leverett spring, as well as Lake 13L, which is located on the Leverett till plain approximately 50 m from the spring (see Figure 4-5), have slightly positive $\delta^{37}Cl$ values (0.06 and 0.03, respectively). These values fall in line with those observed in groundwaters in the Canadian and Fennoscandian Shield which range from –1 to +2‰ (Stotler et al. 2010).

Figure 4-13. *Water flowing from the hole drilled through the ice covering Leverett spring. Photo by Emily Henkemans.*

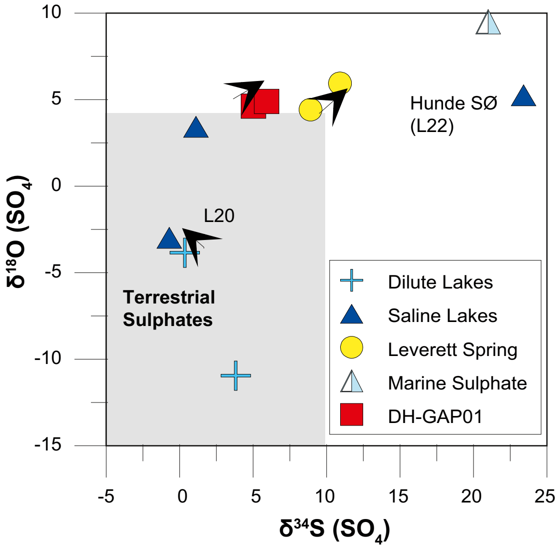

Figure 4-14. *The $\delta^{18}O$ and $\delta^{34}S$ of sulphate in lakes and groundwaters. Arrows indicate multiple sampling episodes with the arrow head pointing towards the most recent sample. Terrestrial sulphate range from Clark and Fritz 1997.*

4.3 Microbial investigations

A microbial investigation was performed that analyzed DNA extracted from borehole DH-GAP01 groundwater and lake water. Microscopic and molecular methods were also applied to analyze number of cells (TNC and qPCR) as described in Appendix 2, where detailed results can be found.

DNA sequences obtained from the borehole groundwater were mostly related to strict anaerobic or facultative anaerobic microorganisms. In opposite, the lake water contained sequences mostly related to aerobic microorganisms including species of Cyanobacteria that typically requires light for growth. The number of observed unique sequences for the lake was twice of that observed for the borehole groundwater. The observed sequence diversity in the borehole groundwater did not overlap the diversity observed in the lake. These observations suggest that the lake water had not mixed recently with the borehole groundwater. In addition, the dominance of sequences related to strict anaerobes in the borehole groundwater was indicative of predominantly anaerobic conditions at the sampled depth. Analysis of numbers of microorganisms did not show a significant difference between borehole groundwater and lake water.

This microbial investigation should be regarded as a pilot study rather than a full microbial study. To fully engage the capacity of microbial diversity and numbers for analyses of water samples more powerful methods should be applied such as microarrays of metagenome analysis. This analytical approach is still under development with good results along the way in very different research areas ranging from deep biosphere marine sediments to the human body and diseases. In conclusion, the pilot study presented here suggests that a full genomic investigation could provide information about origin and mixing of water types at the studied site.

4.4 Downhole monitoring in boreholes DH-GAP01 and DH-GAP03

4.4.1 Pressure, temperature and conductivity monitoring of DH-GAP01

The U-tube sampler in DH-GAP01 is equipped with downhole sensors (Aqua TROLL 200) allowing for water sampling and monitoring of pressure (P), temperature (T) and electrical conductivity (EC). The technical specifications of the Aqua TROLL 200 are described in Campbell (2007) and the GAP 2009 yearly report (SKB 2010). The P/T/EC sensors are located below the inflatable packer at a vertical depth of 140 meters, and are connected to the surface via a non-vented cable (Figure 4-6). A TROLL Com cable, in combination with the Win Situ software, is utilized to communicate with the Aqua TROLL and to download data.

The Aqua TROLL is running on an internal battery and has been operating since the June 28th, 2009, with different monitoring frequencies. Because permafrost exists in the upper part of the borehole, it is impossible to replace the battery, which means that the lifetime of the Aqua TROLL is limited. The logging frequency has, therefore, been changed over time in order to ensure 1) satisfying data resolution, and 2) a sufficiently long monitoring lifetime of the Aqua TROLL. During the initial monitoring period (i.e. summer 2009 following drilling), it was considered important to have a detailed monitoring frequency (every 15 minutes) so that the recovery of the borehole following drilling could be monitored. After September, 2009, it was considered sufficient to have a monitoring frequency of every 6 hours, and in September, 2010, the frequency was changed to every 12 hours. This means that with the current monitoring frequency, the Aqua TROLL is expected to be able to operate for a few more years.

Figure 4-15 shows the pressure and temperature variations from June, 2009 to September, 2010. After drilling, the initial downhole temperature was ca 3.3°C and the pressure was ~14.2 bars. However, a considerable drop in both temperature and pressure is observed over the few weeks following the installation of the U-tube and sensors. These initial changes are related to stabilization of the borehole, because large volumes of hot drill water was pumped down into the system during drilling. In September, 2009, the downhole temperature stabilized around ~1.3°C. The purging of the borehole is indicated by temperature increase and synchronous significant decreases in pressure (see June-09, Sep-09, May-10 and Sep-10).

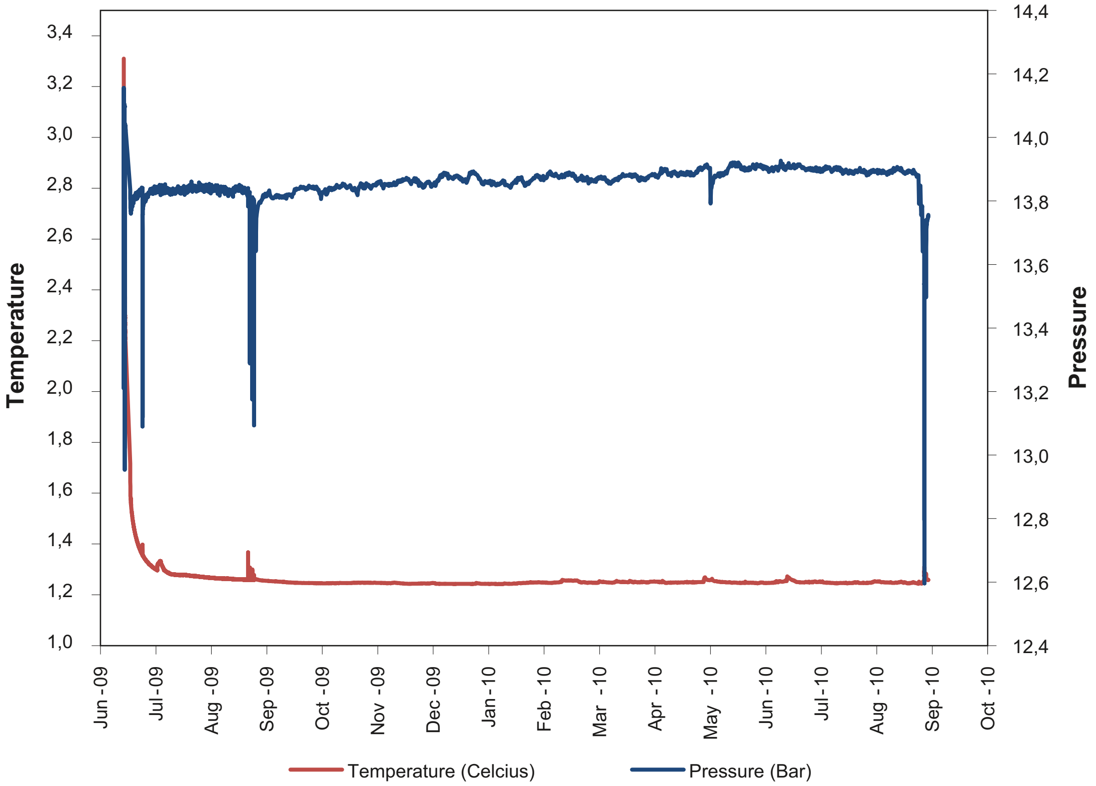

Figure 4-15. *DH-GAP01 pressure and temperature variations over time. The logging frequency has not been constant over time. From the June 28th to September 6th, 2009 the frequency was 15 minutes. From the September 7th, 2009 to September 6th, 2010 the frequency was 6 hours. During short intervals, i.e. during purging of the borehole, the frequency has been set to 1–10 minutes. No barometric pressure correction has been applied.*

Figure 4-16 shows the pressure and specific conductivity variations from June, 2009 to September, 2010. The purging of the borehole is seen as significant specific conductivity peaks and synchronous decreases in pressure (June-09, Sep-09, May-10 and Sep-10). A notable increase in conductivity is observed over the monitoring period. The initial conductivity was ~265 µS/cm, and, during the summer of 2010, the conductivity stabilized around ~800 µS/cm. Because lake water, with a conductivity of ~200 µS/cm, was used as drill fluid, the increase in conductivity implies that the borehole has recovered from drill water contamination and that the downhole water is significantly different from the lake water.

4.4.2 Temperature and barometric pressure at DH-GAP01

As the logged pressure data originates from a non–vented Aqua TROLL, the pressure sensor measures all pressure forces exerted on the strain gauge, including atmospheric pressure (PSIA units measured with respect to zero pressure). To account for the effects of changes in barometric pressure, post–corrections of absolute (non-vented) variations are necessary in order to obtain the real pressure at depth. To monitor the variations in air temperature and barometric pressure, a pressure/temperature logging station (Solinst Junior Levelogger, model 3001) was installed next to DH-GAP01 in September, 2009 (Figure 4-17). The logging frequency is every 15 minutes. Besides providing data allowing for pressure corrections of the downhole pressure, the Solinst station will also allow comparison with other weather records in the area. The aim is to compare the records from the Kangerlussuaq airport and from the ice margin to assess the influence of the ice sheet, as well as higher elevation, on climatic forcing. Figure 4-18 shows the temperature variation at the ground surface from September, 2009 to December, 2010 at DH-GAP01. The coldest recorded temperature during this time interval was –29.9°C (in Nov-09) and the warmest was 14.8°C (in May-10).

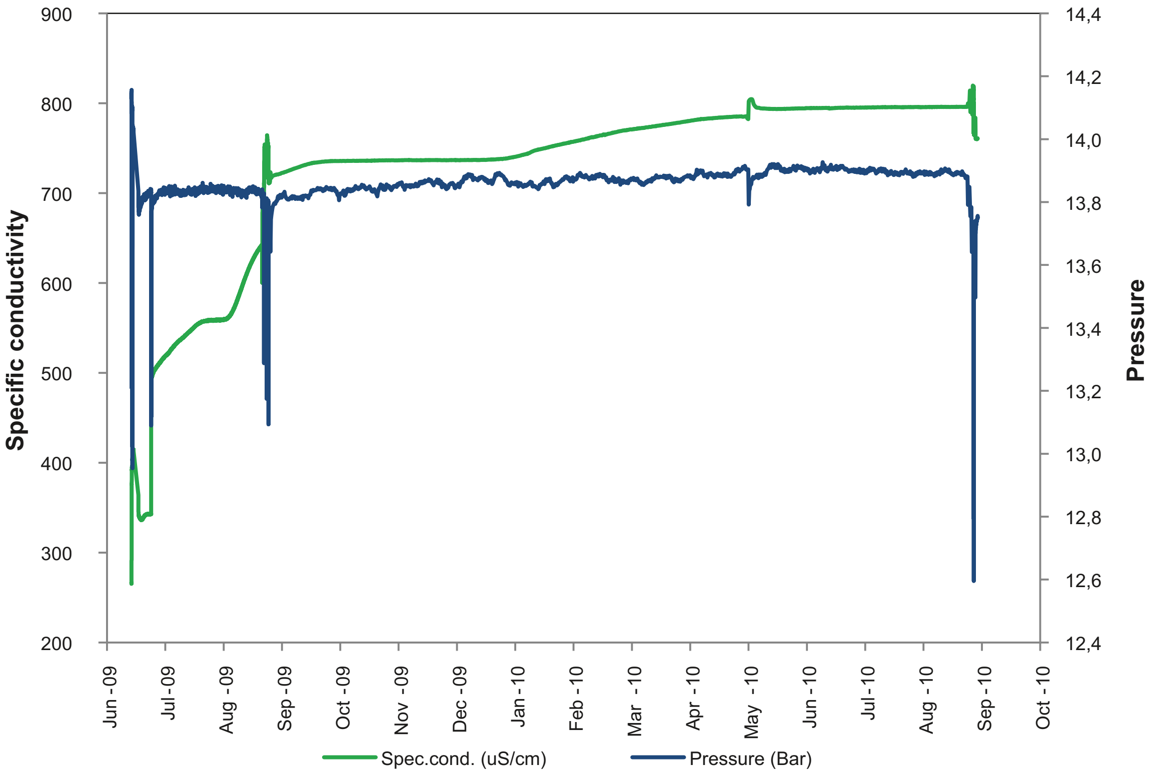

Figure 4‑16. *DH-GAP01 pressure and specific conductivity variations over time. The logging frequency has not been constant over time. From 28th June to September 6th, 2009, the frequency was 15 minutes. From September 7th, 2009 to September 6th, 2010 the frequency was 6 hours. During shorter intervals, i.e. during purging of the borehole, the frequency has been set to 1–10 minutes. No barometric pressure correction has been applied.*

Figure 4‑17. *Solinst pressure and temperature logger next to DH-GAP01. Photo by Lillemor Claesson Liljedahl.*

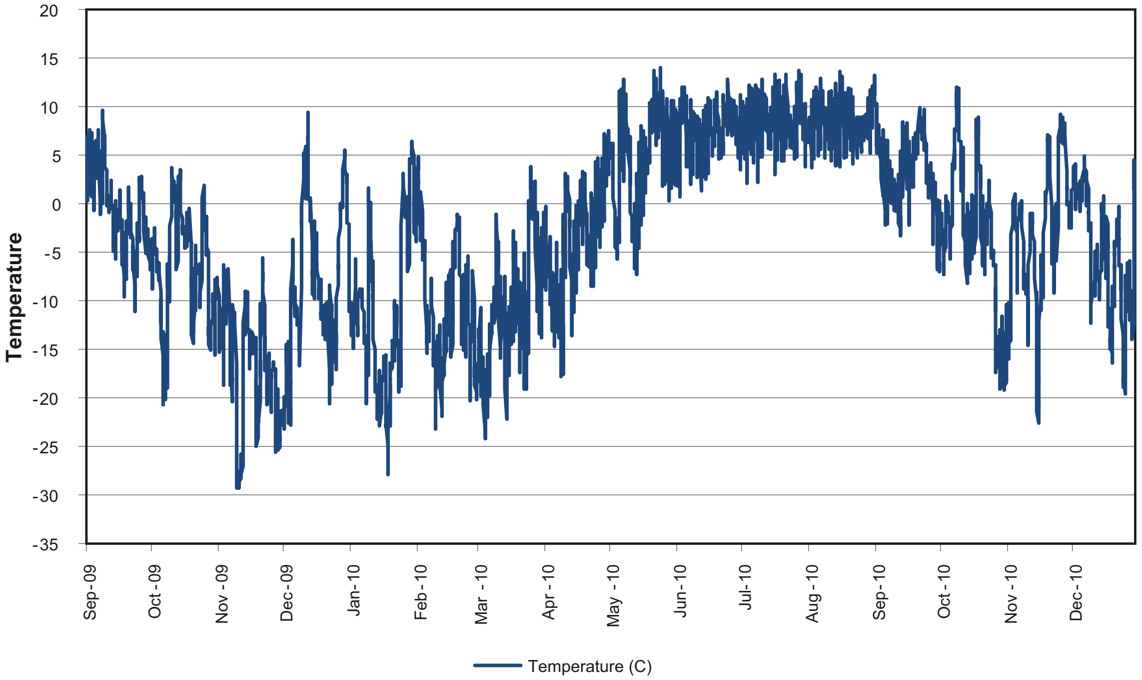

Figure 4-18. *Temperature over time from the Solinst logger next to DH-GAP01.*

Figure 4-19 shows the pressure corrected data from DH-GAP01 from September, 2009 to September, 2010. The correction smoothes out the pressure profile to some extent, however, the overall pressure pattern remains the same after barometric correction.

Table 4-4 shows snapshots of five different data readouts from DH-GAP01 in 2009 and 2010. These results, in combination with hydrogeochemical and microbial results (see Chapters 4.2 and 4.3), clearly show that the borehole has recovered from drill water contamination and it confirms the existence of a water reservoir chemically distinct from the surface waters. The DTS monitoring, in combination with temperature monitoring with the Aqua TROLL, has confirmed the existence of a talik beneath the lake (see Chapter 4.7.1). As there are currently no clear indications of downhole P/T/EC changes supporting vertical flow in the talik, the question whether this talik is an open or through talik still remains. Longer time-series will allow detailed analysis of the borehole data and will add valuable information to help clarify whether the talik is open only to surface or extends through the permafrost.

Table 4-4. P/T/EC readings from the Aqua TROLL in DH-GAP01 at five different times through June, 2009 to September, 2010.

Date and time	28 June 2009, 1:58PM	7 Sep. 2009, 7:58PM	1 Dec. 2009, 1:58 AM	1 May, 2010, 1:58 AM	1 Sep. 2010, 1:58AM	Change from initial reading
Pressure (Bar)	14.08	13.77	13.85	13.88	13.88	–0.2
Temperature (C)	3.31	1.26	1.24	1.25	1.25	–2.06
Specific conductivity (µS/cm)	265.74	712.42	736.74	784.48	795.96	+530.22

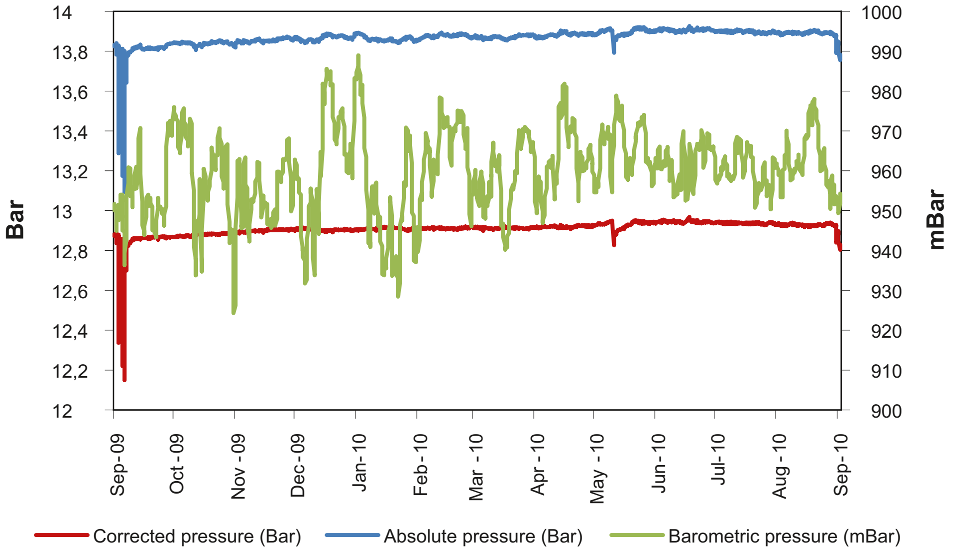

Figure 4-19. *DH-GAP01 pressure and temperature variations over time, including corrected (red line) and non-corrected/absolute (blue line) downhole pressure. The green line shows the barometric pressure variation over time at the ground surface. Barometric pressure obtained from the Solinst logger (Figure 4-17). Note that this graph shows data from September, 2009 to September, 2010. Because no barometric information is available from June–September, 2009 no correction could be made for this time period.*

4.4.3 Hydrotest of DH-GAP01

Two pressure-response tests, associated with water withdrawal from borehole DH-GAP01, were performed in September, 2010. The tests were attempts to obtain data for evaluation of hydraulic properties, transmissivity (T) and hydraulic conductivity (K), of the rock surrounding the borehole. For a detailed description of these tests, and the results of the data evaluation, see Appendix 3. When water is removed from the borehole for chemical sampling, the downhole pressure responses are monitored with the Aqua TROLL pressure sensor. From this data set, the pressure recovery following water removal was evaluated, which allowed calculation of transmissivity and hydraulic conductivity (i.e. slug tests). The tests had short durations and involved small water volumes, implying that the evaluated parameters relate to the rock immediately surrounding the borehole. It is important to note that single-hole test data are associated with large uncertainties regarding the storativity values (S).

The recovery data were evaluated using the AQTESOLV software and the following commonly employed methods: Cooper-Bredehoeft-Papadopulos (Cooper et al. 1967), Bouwer-Rice (Bouwer and Rice 1976) and Hvorslev (1951). Potential influence of borehole skin was tested using the KGS method (Hyder et al. 1994), whereas the Barker-Black method (Barker and Black 1983) was used to evaluate the transmissivity of fractures and the hydraulic conductivity of the rock mass between fractures. Measured pressures p (bar) were converted to pressure heads h (m) by the relation, using ρ (density of water) = 1,000 kg/m^3 and g = 9.81 m/s^2.

The results of the evaluation of the two pressure-response tests suggest a total fracture transmissivity (i.e. the transmissivity of all fractures intersecting the borehole) of approximately 10^{-6} m^2/s and a rock-mass hydraulic conductivity of approximately 10^{-8} m/s.

4.4.4 Pressure, temperature and conductivity monitoring of DH-GAP03

Due to problems arising during the instrumentation of borehole DH-GAP03 in July, 2009, it was not possible to instrument this borehole with a U-tube system. Instead, the borehole was instrumented with an Aqua TROLL and a DTS cable and two heating cables. Testing of the Aqua TROLL was carried out before deployment. The Aqua TROLL, DTS and heating cables were lowered by hand to a depth of 329 meters (309 meters vertical depth).

Data was recovered from the Aqua TROLL in September, 2009. Figure 4-20 shows the variations in pressure and temperature over time. It is observed that the pressure displays an overall decrease, whereas temperature displays an initial drop followed by a continuous increase, with a drastic increase around mid-July. Because the downhole temperature was ~17.5°C, it is deduced that the sensor readings are erroneous. Attempts to reset the Aqua TROLL failed and after communication with the sensor manufacturer (In Situ), we concluded that the Aqua TROLL had experienced an internal failure. The cause of the sensor failure is likely related to the fact that we did not penetrate the permafrost when drilling DH-GAP03, which resulted in a position of the Aqua TROLL in a zone of semi-frozen water, which may have caused the sensors to freeze and collapse. Due to the ~300 meters of ice in the borehole above the sensors, it was not feasible to replace the Aqua TROLL. However, it is still possible to obtain downhole temperatures in DH-GAP03 using the DTS fiber (see Chapter 4.7.1).

Table 4-5 shows snapshots of three different data readouts from DH-GAP03 during 2009, including the first and last readouts. Pressure decreased from ca. 28 to 20 bar during this period, while at the same time, the temperature increased from ca. 5 to 18 degrees Celsius. This high temperature at the bottom of the hole, which does not represent actual temperatures within the borehole, indicates that there has been some internal failure of the temperature sensor downhole. After September 7, 2009, it has been impossible to connect to the Aqua TROLL.

Table 4-5. First three and the final readings from Aqua TROLL in DH-GAP03. Logging frequency 135 minutes.

Date and time	6 July 2009, 21:07	7 July 2009, 01:37	7 September 2009, 18:06	Change from initial reading
Pressure (Bar)	27.99	27.90	19.96	–8.03
Temperature (C)	4.68	4.71	17.61*	12.93
Actual conductivity (µS/cm)	229.30	347.23	0	–229.30
Specific conductivity (µS/cm)	374.68	566.95	0	–374.68

* suspected malfunction of the temperature sensor

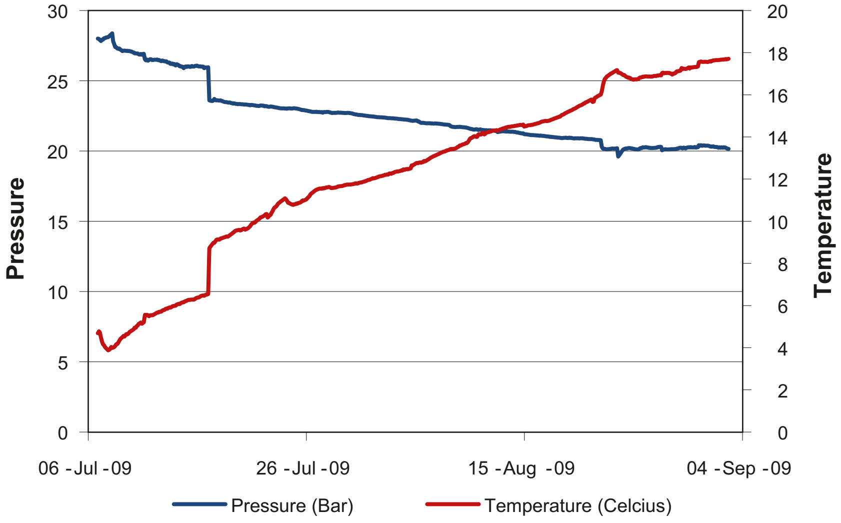

Figure 4-20. DH-GAP03 pressure and temperature variations over time. The logging frequency was 135 minutes. No barometric pressure correction has been applied.

4.5 Drill core investigations

DH-GAP01, DH-GAP02 and DH-GAP03 were drilled in 2009 (SKB 2010). The cores were shipped to Posiva's drill core depot in Olkiluoto, Finland, where drill cores DH-GAP01 and DH-GAP03 were logged and documented. The records include lithologies, fracture characteristics, fracture orientations and fracture infillings.

Drill cores DH-GAP01 and DH-GAP03 provided an opportunity to launch various investigations related either to general site characterization or to the planning of future activities. In most cases, these drill core investigations were designed to fill knowledge gaps with respect to the subsurface geology in the GAP study area, which could not have been determined without the drilling of the pilot holes. The most significant goals related to the structural geology, where information such as fracture density with depth, and the orientation of the main fracture sets, could be obtained through examination of the drill core. modelling.

Fracture infillings contain the records of the area's fluid evolution over geologic time. Calcite is the most common infilling mineral and it provides a means to study the chemistry of the fluid from which it was formed and also the formation conditions (progress in water-rock interaction studies is reported in Chapter 4.6). A project focused on redox fronts was conducted in parallel with the drill core investigations, and targeted materials in the core that could be used for studies on redox sensitive elements (U, Ce, Fe) and provide evidence regarding changes in near-surface redox conditions (Chapter 4.6.3).

Variations in rock types, and in their physical properties, have impacts on many of the features investigated in GAP. For example, growth of permafrost and development of active layer are linked to the thermal properties of the rock and, in this case, to lesser extent to the porosity of the rock. Matrix waters and fracture waters are interacting, and the amount of accessible pore volume determines its significance. Geophysical interpretation is based on contrasts, e.g. in magnetic properties or density. At the time of preparation of this report, only airborne magnetic data was available for the SPC study area, but it was successfully applied in the lineament interpretation (see Chapter 4.8). If site specific data is missing, literature values can be used, but that is not ideal. The essential parameters required in thermal modelling and in geophysical investigations can be readily measured from rock samples.

Salinity of the matrix pore water is of interest in systems where recharge of fresh waters has potentially influenced the composition of fracture waters. At the matrix porosity-scale, diffusion is occurring as a natural response to geochemical or other changes that have taken place in the fracture network This process is slow enough to allow the formation of disequilibrium fronts within the rock mass. It has been attempted to trace these features with a crush and leach method, where the sample is crushed and sieved to different grain size fractions. The rock powder is leached with pure water and the dissolved species are analyzed.

A three day core review and sampling campaign took place between May 25th and 27th, 2010. The following sample types were taken:

- Fracture infillings for mineralogical, stable isotope and fluid inclusion studies (University of Waterloo)
- Fracture infillings for detailed geochemical studies: minor elements, uranium series disequilibrium (Redox front project, Terralogica and University of Gothenburg)
- Rock samples for petrophysical properties (GTK)
- Rock samples for crush and leach studies (University of Waterloo).

The samples for crush and leach were taken immediately adjacent to the samples selected for petrophysical investigations in order to ensure that the measured porosity numbers could be considered representative for crush and leach samples as well (Figure 4-21).

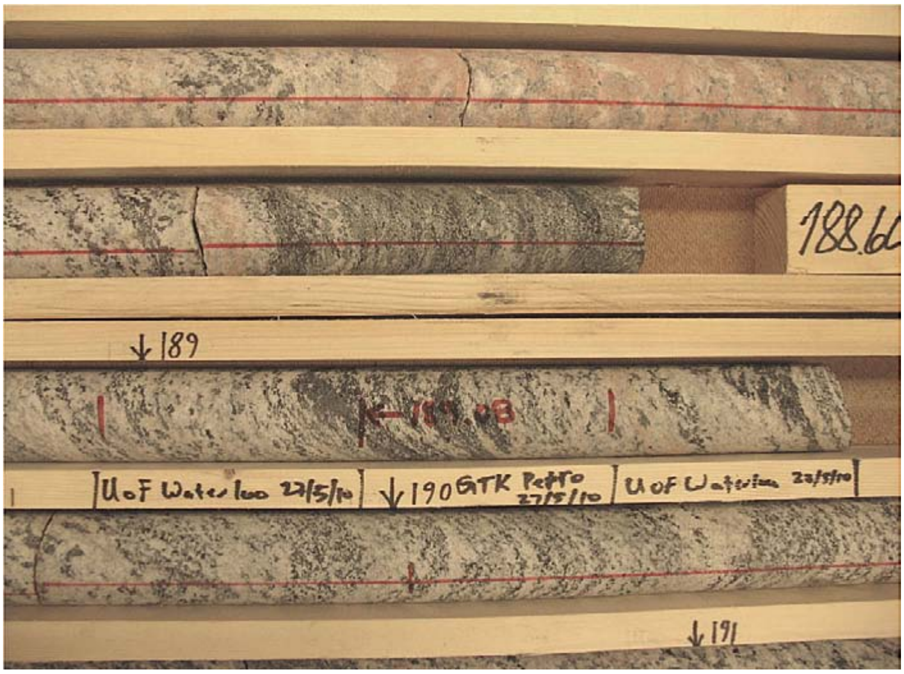

Figure 4-21. Sampling strategy for the petrophysical and crush and leach samples. The continuous red line is related to the orientation of the core. Photo by Timo Ruskeeniemi.

4.5.1 Lithological and fracture loggings

DH-GAP01 consists mainly of feldspar-rich felsic gneisses, interlayered with shorter sections of mafic, amphibole-rich gneisses; intermediate compositions also occur. The rock is foliated throughout the whole length of the core (221 m). The beginning of the core is generally more fractured, and these fractures are filled primarily with drill cuttings and only thin fracture fillings occur. A few distinct fracture zones and fault zones were mapped from the core (Figure 4-22). These zones are slightly altered and the fault zones contain cohesive breccia and intensive alteration on the fracture surfaces with chlorite, calcite and clays. The total number of fractures in DH-GAP01 is 496, and the fracture frequency is thus 2.24 fractures/m (SKB 2010).

DH-GAP03 consists mainly of amphibole-rich mafic gneisses interlayered with shorter sections of amphibole-poor intermediate gneisses and feldspar-rich felsic gneisses. Single pegmatite veins were also logged from the drillcore. The felsic gneisses are located primarily in the middle portion of the 341-m long core, while mafic gneisses are found both in the deeper levels and closer to ground surface. Iron hydroxides and oxides occur on the fracture surfaces close to the ground level, continuing to approximately 40 m borehole depth. These 'rusty' fractures were interpreted as open fractures that have been subjected to surface water circulation in the past (Figure 4-23).

The fracture frequency in DH-GAP03 is relatively dense throughout the hole. The most intense fracturing is concentrated in more mafic sections, while felsic gneisses are typically intact and relatively unfractured. The lowest 100 meters of core is very densely fractured and the section contains three fault/deformation zones. In many places, marker horizons indicate that slip had occurred, even though it was not possible to determine the exact amount of slip. The total amount of fractures identified in DH-GAP03 is 1,080, and the fracture frequency is thus 3.17 fractures/m (SKB 2010).

The dark green, glossy coatings mapped from many fracture surfaces in DH-GAP03 consist of lamellar chlorite. Clay minerals were mapped also from several fractures, and another typical fracture-filling mineral was calcite. Calcite occurs typically in small amounts (less than 0.5 mm) as partial coating on fracture surfaces; some occurrences of multi-phase calcites with several distinct layers were also mapped (Figure 4-24).

The cores were orientated during drilling, so that true foliation and fracture orientations could be extracted from the core. The procedure for measuring the orientation of planar features in core is explained by Holcombe et al. (2011). Some parts of the cores could not be oriented due to difficulties with the initial marking of the core orientation during drilling, and therefore some of the fractures

Figure 4-22. *Photo showing the main fault zone in DH-GAP01, located in between 84.30 m–89.55 m of borehole length. Photo by Tuomas Pere.*

Figure 4-23. *Iron oxyhydroxide precipitation on top of calcite infilling in DH-GAP03 at 28.54 m. Photo by Timo Ruskeeniemi.*

Figure 4-24. *Thin white calcite coating on a sheared (chlorite bearing) fracture surface (DH-GAP03, 139.42 m). Photo by Jon Engström.*

lack orientation. In DH-GAP01, it was possible to orientate 80% of the core, and in DH-GAP03, it was possible to orientate 75%. The foliation measurements were performed approximately at every five meters in both cores.

The foliation in DH-GAP01 is generally dipping towards NW, with a sub-vertical dip, while the foliation in DH-GAP03 has moderate to steep dip and dips towards NE. This clearly illustrates the heterogenic nature of the study site and demonstrates the existence of major fold structures in the area.

4.5.2 Petrophysics

Measurement of petrophysical properties is best from fresh, non weathered rock samples, and in sufficient amount to achieve statistical significance over the natural variability within the sample set. During the drill core sampling campaign, 12 samples were taken from the core DH-GAP01 and 18 from DH-GAP03; this means, roughly, a sample for every 20 m. The aim was to cover the main rock types distinguished by their mineralogical and textural characteristics. A 10 cm sample was cut from the core by a diamond saw. Care was taken that the sample was representative of the specific rock unit and did not include fractures or other anomalous features. In addition, two hand specimens from the proposed Caribou drilling site were considered to represent the rock type assumed to be dominant in DH-GAP04. In total, 10 subsamples were cored from the two hand specimens for measurement.

Petrophysical determinations were conducted in the Petrophysical Laboratory of the Geological Survey of Finland. The determinations included: density (kg/m^3), matrix porosity (%), thermal conductivity (W/mK), magnetic susceptibility (10^{-6}SI), remanent magnetization (A/m), seismic P-wave velocity (m/s) and specific resistivity (Ω/m).

The following protocols were applied in the laboratory determinations:

Densities were determined by weighing the samples in air and water and calculating the dry bulk density. The accuracy of the scale is 0.01 g and the repeatability for weighing of average-size (200 cm^3) specimens is better than 0.01%.

Porosities were determined by water saturation method. Water-saturated (three days at room temperature and pressure) samples are weighed before and after drying (three days at 110ºC) in an oven. The accuracy of the scale used for porosity measurements is 0.01 g.

Thermal conductivity was measured with the steady-state divided bar method, using an apparatus built at the Geological survey of Finland (GSF). Disks with 7 mm thickness were prepared from the 39 mm diameter core samples. Thermal conductivity was measured after keeping the samples in a water bath a room temperature and pressure for at least two days. Inaccuracies for the thermal conductivity values are considered to be smaller than 5%.

The ***magnetic susceptibility*** was measured with low-frequency (1,025 Hz) AC-bridges, which are composed of two coils and two resistors. The measuring field parallel to the coil axis is roughly of the same intensity as the Earth's magnetic field. For nearly isotropic, weakly magnetic (susceptibility < 0.001), 200 cm^3-sized samples, the standard error of repeated measurements stays generally below 20×10^{-6} SI-units. For more strongly magnetic and anisotropic block samples, the measuring result can vary by more than 10% if the sample position and direction is varied within the measuring coil.

The intensity of the ***remanent magnetization*** was measured with fluxgate magnetometers inside magnetic shielding. The accuracy is ca. 3 mA/m for weakly magnetic samples of typical size (200 cm^3).

Seismic P-wave velocity was measured by using sonar (ultrasonic transducers) elements. Measurements at GFS are done at room pressure and temperature. The accuracy of measured P-wave velocity is approximately 10 m/s, but the time of water immersion has a great effect on the measuring result: a longer immersion time increases the P-wave velocity. Used immersion time was 3 days.

The ***specific resistivity*** was measured by galvanic method. The galvanic equipment includes 2- or 4-point systems with wet electrodes and different frequencies (e.g. 0.1, 10 and 500 Hz), which allow for the determination of the Induced Polarization (IP) effect. The measuring range is ca.10–200,000 ohm.

As an example, Figure 4-25 shows the variation in the density and thermal conductivity of the 30 drill core samples. The felsic (lower density) and more mafic (higher density) rock types plot in distinct density fields, but, as a whole, the thermal conductivity does not seem to correlate with density.

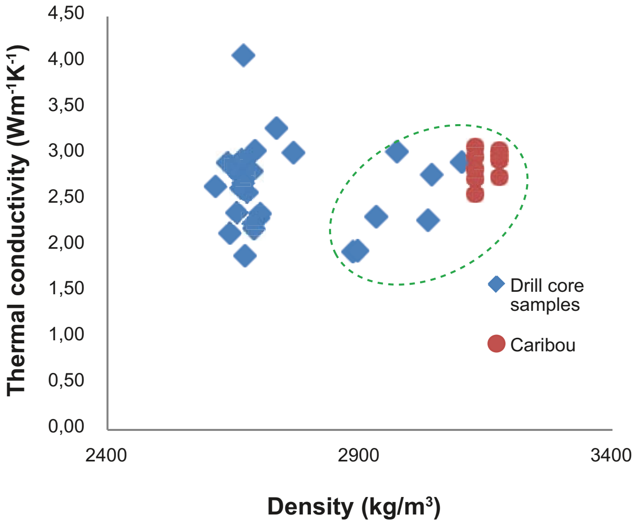

Figure 4-25. *Thermal conductivity versus density measured from drill cores DH-GAP01 and DH-GAP03 and from the subsamples from the two Caribou hand specimens. The more mafic rock are outlined by the dashed line.*

However, there is some variation in the thermal properties within both felsic and mafic rocks. Felsic rocks have a relatively narrow range of densities, but the thermal conductivity is variable, whereas in the mafic group, the thermal conductivity has positive correlation with the density. The results suggest that cooling behavior is similar in the encountered felsic and mafic rock units.

The average matrix porosity (diffusion porosity) for 30 unweathered drill core samples, representing the felsic and mafic rock varieties, is 0.48%.

4.6 Water-rock interaction studies

Fracture networks are distributed throughout crystalline rock and present potential migration pathways from the deep subsurface to the far-field environment. Fracture minerals that have precipitated in these conduits possess information about paleo-hydrological processes, such as metamorphic or glacial events (Blyth et al. 2004, Drake et al. 2009). Consequently, fracture mineral investigations provide a useful analytical method for understanding the past evolution of a site. Characterization of minerals, such as calcite, can yield information regarding past fluid chemistry and isotope signatures, as well as temperature and pressure of the environment when these minerals formed. Fluid inclusion studies of calcite can estimate paleo-fluid salinities from observed eutectic temperatures. Furthermore, fluid inclusion studies coupled with $\delta^{13}C$ and $\delta^{18}O$ isotopic analyses have given rise to methodology that can establish the formation temperatures of calcite within fractures (Blyth et al. 2000, 2004). This technique can be used as a proxy to distinguish between waters that are of magmatic or meteoric origin.

4.6.1 Fracture infilling investigations

The research completed for the GAP water-rock interaction studies was only at early stages of analysis at the time of report preparation. A brief highlight of completed research is presented, and direction and steps forward are given. Greenland is a glacial terrain and fractures that have potentially been activated by recent glacial unloading could have created conduits for glacial waters or seawater to penetrate the bedrock.

A summary of mineralogy, as well as $\delta^{13}C$ and $\delta^{18}O$ isotope geochemistry of the fracture fillings of calcite throughout DH-GAP01 and DH-GAP03, is given in Tables 4-6, 4-7, and 4-8. Further, the isotopic geochemical data of the Greenland drill cores is presented in Figure 4-26 and 4-27, showing how the data compare to other sites (as classified by Blyth et al. 2009). The comparison plot in Figure 4-27 illustrates where the Greenland data lies relative to sites of similar geology.

One important finding from the Greenland drill cores is that there are fracture fillings (DH-GAP01: 168.4 m, DH-GAP03: 246.73–246.76 m) that are intermixed with calcite and dolomite. A possible explanation of the fractures mixed with calcite and dolomite is that a fluid that that was saturated (or super-saturated) with respect to magnesium was precipitated in an older, reactivated calcite infilling. Work is ongoing to separate the two carbonate phases so that filling temperatures can be determined for both calcite and dolomite in these fractures. Finally, multiple generations of calcite have been identified in the fillings of fractures at 260.46 m and 293.71 m by optical microscopy and stable δ^{13}C and δ^{18}O isotope analyses (Table 4-8).

Table 4-6. Fracture fillings mineralogy for DH-GAP01.

Length (m)	Minerals
74.25	calcite, quartz (~50/50)
85.67	calcite, <10% quartz
89.34	calcite
98.75	calcite
128.75	calcite, <10% quartz
161.0	quartz, albite, montmorillonite, <10% calcite
168.4	calcite, dolomite (~2:1)

Table 4-7. Fracture fillings mineralogy for DH-GAP03.

Length (m)	Minerals
28.54	calcite, goethite
40.04	albite, calcite, quartz
41.10	calcite, unidentified clay
47.08	calcite (magnesian) – $(Ca_x, Mg_{1-x})CO_3$
77.50	calcite
83.15	calcite
90.15A	calcite, <10% quartz
90.15B	quartz, calcite, possible albite
97.04	dolomite
117.43	calcite, albite and quartz (trace)
142.39	calcite, albite and quartz (<10%)
158.74	calcite, quartz (trace)
173.72	calcite, <10% quartz
184.92	quartz, calcite (~30%)
208.73	calcite
218.89	calcite, <5% albite, fluorite (trace)
221.38	calcite, quartz
246.73–.76	dolomite (major), ~10% calcite, quartz (trace)
275.77	calcite
328.84	calcite
328.91	calcite

Table 4-8. Fracture fillings in DH-GAP03 with multiple generations of calcite.

Length (m)	Minerals
260.46 A	calcite
260.46 B	quartz, <25% calcite
260.46 C	calcite, quartz (trace)
293.71 A	calcite
293.71 B	calcite, < 10% quartz
293.71 C	calcite, < 10% quartz
293.71 D	quartz, < 25% calcite

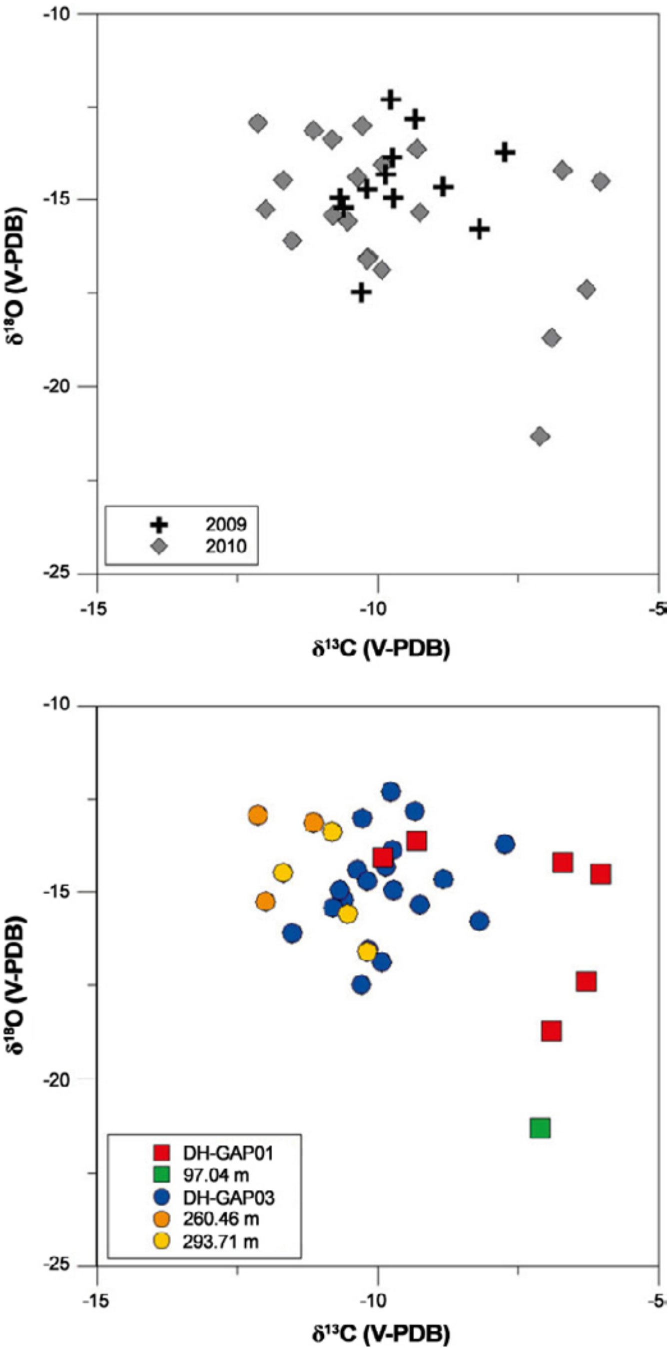

Figure 4-26. *$\delta^{13}C$ versus $\delta^{18}O$ for calcites sampled from the DH-GAP boreholes and results divided into DH-GAP01 (talik hole) and DH-GAP03 (permafrost hole). Note: Depths 260.46 m and 293.71 m correspond to multiple generations of calcite fillings, and depth 97.04 m is the signature of a dolomite filling.*

The Greenland calcite data is comparable to the Olkiluoto site, and is more depleted in $\delta^{18}O$ compared to the Canadian Whiteshell URL site. There is a vertical trend in the oxygen isotope geochemical data (Figure 4-27). Such trends have been attributed to calcites of magmatic/hydrothermal origin in other studies. Such signatures have been demonstrated to result from fractionation due to cooling and calcite precipitation (Blyth et al. 2009). Mineral phases intermixed with the calcite, such as quartz and fluorite, are typical for hydrothermal mineralization from a cooling magmatic fluid that has degassed as the magma is became emplaced in the wall-rock. This process is also supported by the presence of a solid solution product of calcite, where diffraction data confirms magnesium substitution for calcium in the calcite lattice; very typical of mineralization at elevated temperatures.

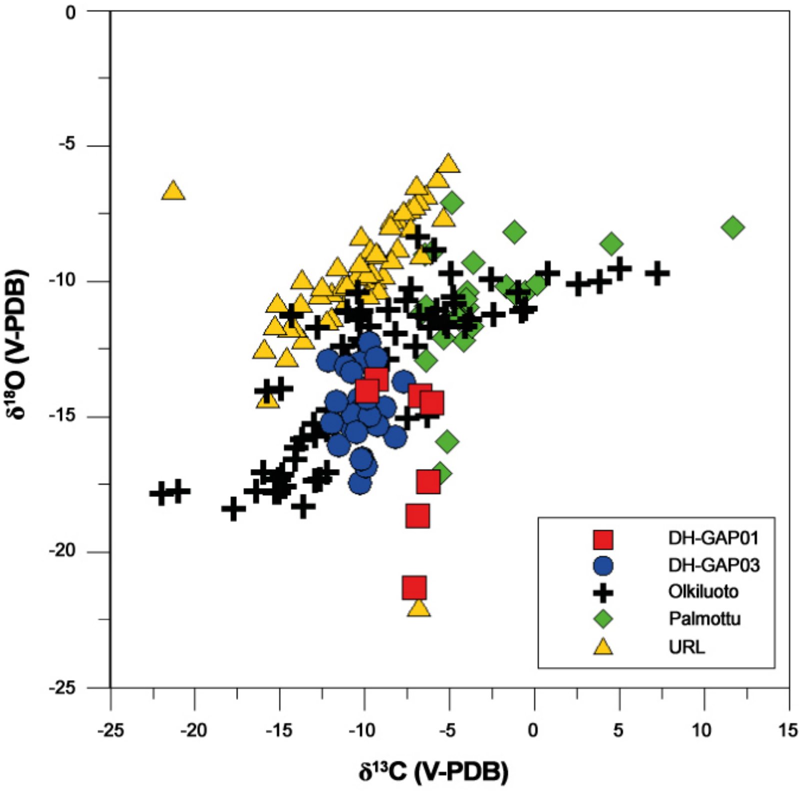

***Figure 4-27.** $\delta^{13}C$ and $\delta^{18}O$ geochemical comparison of granitic gneiss sites (from Blyth et al. 2009) with the Greenland calcites.*

Fluid inclusion analysis will be able to provide direct evidence to distinguish hydrothermal fracture fillings from calcites that are in equilibrium with present day fluids. Interestingly, DH-GAP01 is enriched in carbon-13 when compared to fracture fillings of DH-GAP03.

More information about the dolomite phases must be obtained in order to determine if the dolomite formed from water-rock interaction processes with Mg-rich solutions. Strontium is well-established in the literature as a conservative tracer in hydrological systems because it does not fractionate during geochemical processes, and therefore is used to identify or constrain end-members of parent fluids. Calcium has been shown to fractionate at high magmatic temperatures (Huang et al. 2010), and research will be completed on the fracture calcites to evaluate whether the $^{44/40}Ca$ signature can be used to identify geological processes that control calcite mineralization.

Fractures logged at 260.46 m and 293.71 m of DH-GAP03 contained layers of calcites observed with the naked eye. Stable $\delta^{13}C$ and $\delta^{18}O$ isotope geochemistry confirms the presences of multiple generations of calcite, and interestingly enough, both of these fractures are situated in bedrock of similar geology (as classified in the Posiva core log). Another interesting fracture was the infilling at 90.15 m, where the calcite infilling has been subdivided into 90.15 A and B. As summarized in Table 4-7, there are different minerals present within the fracture located at 90.15 m; but that could be easily attributed to the heterogeneity within the fracture. X-ray diffraction however, supports two different crystallization events in this fracture and this is confirmed by comparing the signal to noise ratios in the two diffraction patterns of the filling minerals. The diffraction pattern of filling 90.15A has sharp reflection lines and a flat baseline, which suggests a high-degree of crystallinity within the sample. The powder of filling 90.15B had a diffraction pattern with more background noise, a low signal to noise ratio, and broader reflection lines; all indicative of crystallites containing a low-degree of crystallinity. A possible explanation of this difference could be the presence of both and old and a young generation of calcites; the low degree of crystallinity could be related to low temperature precipitation with small crystallites.

4.6.2 Crush and leach

Crush and leach experiments were completed at the University of Waterloo in 2010. Eleven sections of core were used: five samples from DH-GAP01 and six samples from DH-GAP03. The sections of core were pulverized into a fine powder using a ball-mill rock crusher. Nano-pure water was added to the fine powder in a mixing ratio of 1 mL of water to 1 mg of rock. These samples were then placed on a shaker for 24 hours, after which the sediment was allowed to settle before waters were extracted for analyses. Sections of approximately 10 cm were taken from either side of the samples used for petrophysical analyses. These two sections were combined so that 20 cm of core was used for each crush and leach set up, and are referred to in the following paragraphs by the depth of the first 10 cm segment used.

Crush and leach waters were analyzed for major and minor trace elements and several sections were also analyzed for $^{87}Sr/^{86}Sr$. X-ray diffraction was also used to identify minerals in DH-GAP01 at 139.75 m. Water derived from the crush and leach experiments were generally of the composition Na > Ca > Mg, however several sections had chemistries that were Na > Ca, Mg (see Figure 4-10). The majority of sections had SO_4 > Cl, with the exception of three sections which had Cl at 30% of total anions. Further discussion of the crush and leach experiments in relation to the chemistry of surface and ground waters can be found in Chapter 4.2.3.

Chloride is a conservative tracer and the ratios of Na to Cl and Br to Cl can be used to delineate waters with different sources or that have undergone various geochemical processes (Fritz and Frape 1982). Figure 4-28 shows the crush and leach waters compared to surface and groundwaters, along with their $^{87}Sr/^{86}Sr$ ratios. Neither the DH-GAP01 groundwaters nor the Leverett spring waters resemble the crush and leach derived waters. Several of the more dilute lakes, including L8 and L6, have similar Na/Cl–Br/Cl ratios to fluids derived from crush and leach, which suggests that the local bedrock chemistry may be a significant control on the evolution of surface and other waters.

Na/Cl–Br/Cl ratios are included for crush and leach experiments performed on rocks from the Canadian and Fennoscandian Shield for comparison (Stotler et al. 2010). While the Br/Cl ratio for the DH-GAP01 and DH-GAP03 sections is similar to that observed in the Canadian and Fennoscandian Shields, the GAP crush and leach samples are considerably enriched in Na than the presented Shield samples.

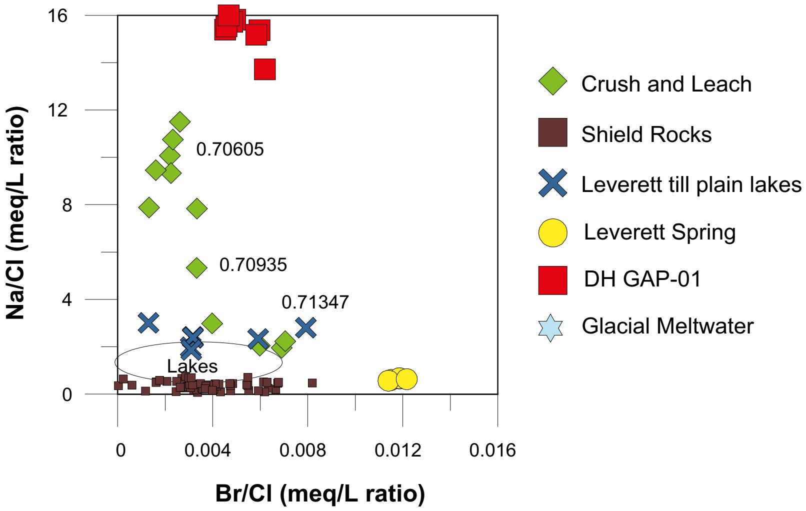

Figure 4-28. Ratios of Na/Cl and Br/Cl for surface waters, ground waters and crush and leach samples from Kangerlussuaq, Greenland. $^{87}Sr/^{86}Sr$ in leachate is given for three crush and leach samples. Samples from the Canadian and Fennoscandian Shields are included for comparison from Stotler et al. (2010).

Water from three sections of core were analyzed for $^{87}Sr/^{86}Sr$: DH-GAP01 149.90 m, DH-GAP03 80.80 m, and DH-GAP03 139.75 m. The strontium isotopic ratios for the crush and leach segments ranged from 0.706 to 0.713. The less enriched values of strontium isotopes likely indicate an influence of lower temperature Na plagioclase feldspar mineralization (McNutt et al. 1990).

An example of the mineralogical work related to crush and leach was completed in 2010 for borehole DH-GAP03, Sections 139.75–.80 m and 139.9–140.03 m. The powder was analyzed by X-ray diffraction to identify minerals within the matrix; a $^{87/86}Sr$ ratio of 0.70605 was measured from the pore water obtained from the crush and leach method. This value is slightly lower than present day seawater and is low in comparison to waters analyzed from crystalline rock environments (McNutt et al. 1990).

4.6.3 Observations on redox conditions based on fracture infillings in DH-GAP01 and DH-GAP03

The aim of the study is to use mineralogy and geochemistry to determine possible changes in redox conditions from the surface down further into the bedrock. Hydrogeological models have indicated that oxygenated glacial meltwater may be introduced into the bedrock during a deglaciation phase. Using fracture infillings to study redox conditions in the GAP drillcores will provide information as to the depth to which oxygenated water has penetrated the bedrock in this area. Below is given a brief summary of the analyses carried out and the preliminary results to date.

1) Changes in mineralogy: the oxidative leaching of pyrite and the formation of Fe-oxyhydroxide have been found to be very useful for depicting the changes in redox conditions. During the sampling campaign on the GAP cores at Olkiluoto, detailed macroscopical mapping in order to look for this transition was performed (see results in Figure 4-29)
2) Samples for detailed studies were collected to cover the transition from oxidizing to reducing conditions (13 samples from DH-GAP01 and 27 samples from DH-GAP03).
3) All fracture surfaces have been examined using SEM microscopy. In addition, 5 thin sections have been prepared and examined for wall rock alteration. The results show that Fe-oxyhydroxides (probably goethite) are present on many fracture surfaces from shallower depths than 40 m, whereas pyrite is absent. Goethite is very abundant in many samples and shows characteristic spherulitic aggregates (mostly <5 um in diameter (Figure 4-30) of platy crystals. In addition, Mn-oxides (or oxyhydroxides), also indicative of oxidizing conditions, are observed, but in much smaller amounts than goethite. Thin sections show that in the uppermost part of the bedrock oxidizing fluids have penetrated up to 6 mm into the wall rock, shown by goethite-filled micro-fractures and partial alteration of wall rock pyrite to goethite. At greater depth (> 40 m) pyrite is fresh and unaltered on the fracture surfaces (although present in small amounts). Chlorite and clay minerals dominates the fracture coatings along with calcite and wall rock fragments.
4) Fracture coatings have been scraped off the fracture surface and analyzed as bulk samples for chemistry using ICP-AES/QMS (27 samples). The results show typical trends representative for changes in redox conditions (e.g. in behavior of Ce), which show positive Ce-anomalies in the upper 40 m indicative of Ce^{4+} (Figure 4-31), and leaching U (indicating mobilization of oxidized U^{6+}) in the upper 20 m (Figure 4-32).
5) XRD identification has been performed on 6 of the bulk samples for identification of clay minerals. Some of the analyzed samples indicate the presence of swelling clay minerals of smectite type.
6) A subset of samples (11) was selected for uranium series analyses. The uranium content is very low and it is also obvious that the mobile part of the uranium is significantly lower. The remaining samples will be analyzed with mass spectrometry in 2011.

Some of the key results to date are:

A redox transition is recognized in the GAP drill cores similar to what have been earlier found at Äspö and Laxemar. Here it is found at somewhat greater depth (at ~40 m, well within the upper 100 m). It is, however, important to remember that from the Laxemar/Äspö area we have on the order of 20 drill cores with different orientations, whereas for the GAP there are only 2 thus far.

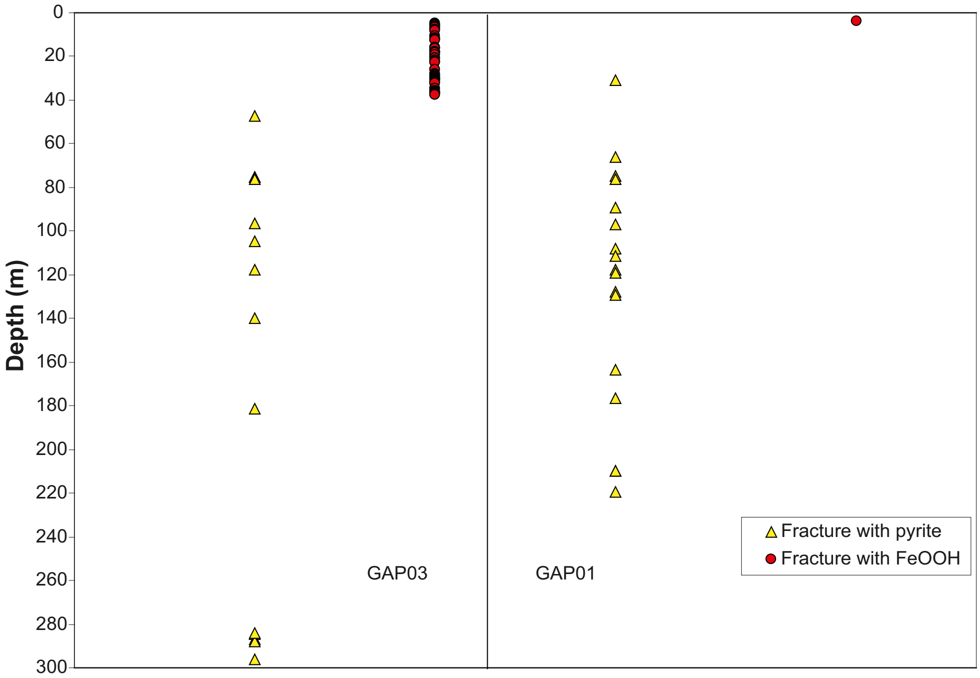

Figure 4-29. *Mapping of fracture minerals goethite (FeOOH) and pyrite versus depth.*

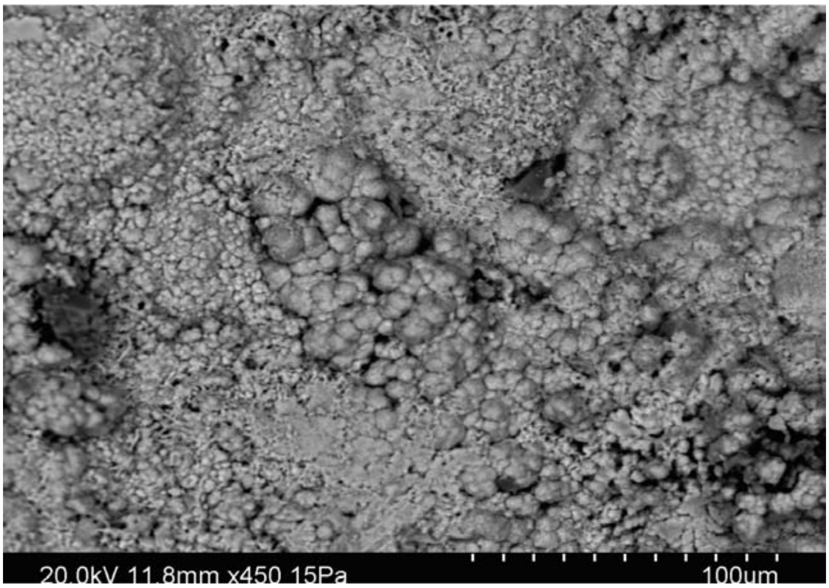

Figure 4-30. *Back-scattered SEM-image of spherulitical goethite aggregates from sample DH-GAP03-34.65 m. Photo by Henrik Drake.*

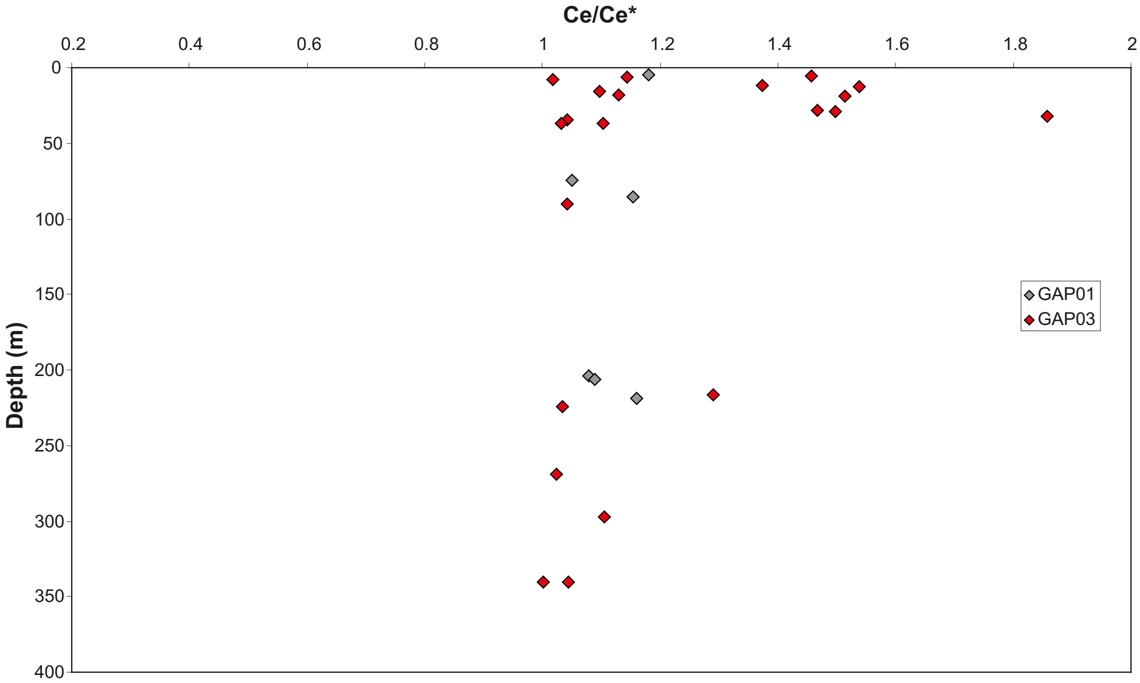

Figure 4-31. *Ce-anomalies (Ce/Ce*) in fracture coatings versus depth. Ce* is the normalized value; the normalized line between REE with higher and lower atomic number than Ce (i.e. La and Pr). Ce*= (La*Pr)^1/2. Ce-anomalies are visualized by looking at how the measured Ce values relate to Ce*.*

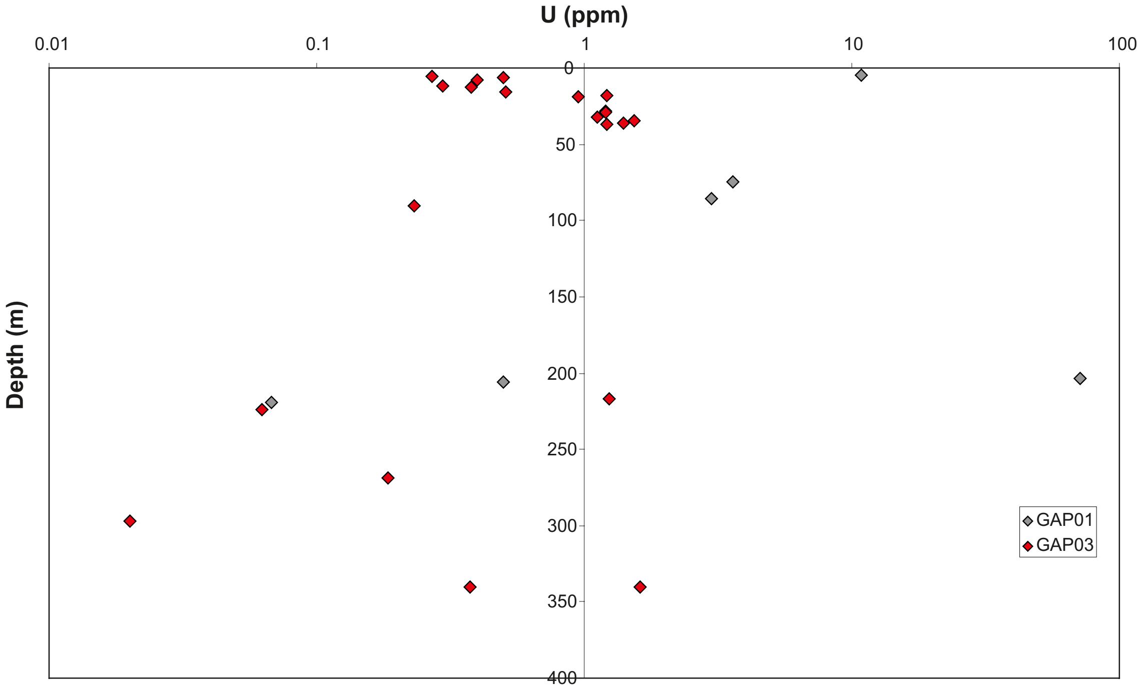

Figure 4-32. *Concentrations of U in bulk fracture coatings versus depth.*

4.7 Permafrost investigations

4.7.1 Temperature profiling with Distributed Temperature Sensing (DTS)

The Distributed Temperature Sensing (DTS) utilizes a passive optical fiber acting as temperature sensor, which allows monitoring of exact temperature profiles along the optical fiber. The DTS-measurement is based on the proven Raman-Optical Time-Domain-Reflectometry technique. An optical laser pulse propagating through the fiber sends scattered light back to the transmitting end, where it is analyzed. By measuring the difference in the signal intensity of the backscattered light, an accurate temperature measurement can be made along the whole length of the optical fiber. DTS provides a method to monitor bedrock temperatures in permafrost areas, where the freezing of boreholes prevents the use of any conventional measuring techniques.

An Agilent DTS device from AP Sensing and an Oryx DTS device have been utilized in the GAP (SKB 2010). The accuracy of the Agilent DTS device is one meter for spatial resolution and 0.1°C for temperature resolution. To achieve this accuracy a minimum time of 15 minutes per measurement is required. In order to get the actual temperature, the device has to be calibrated against a known external temperature source (e.g. an ice-bath) for every measurement.

DTS Measurements in DH-GAP01 and DH-GAP03 during 2010

Both boreholes were equipped with a steel coated optical BRUsteel FRNC cable designed for harsh environments immediately after the drilling was completed. The DTS-cable at DH-GAP01 was lowered together with the sampling device, thus it is located above the packer at 0–150 m of borehole length (see Figure 4-6). The temperature data from DH-GAP01 is therefore acquired only down to 130 m vertical depth, though the borehole was drilled to 192 m vertical depth. The AquaTROLL sensor, providing an independent temperature reference, is located at 140 m of vertical depth. The DTS-cable at DH-GAP03 was lowered successfully together with the AquaTROLL sensor to about 300 m of vertical depth. Unfortunately the AquaTROLL failed and thus all measurements are referenced from an ice-bath at surface (SKB 2010).

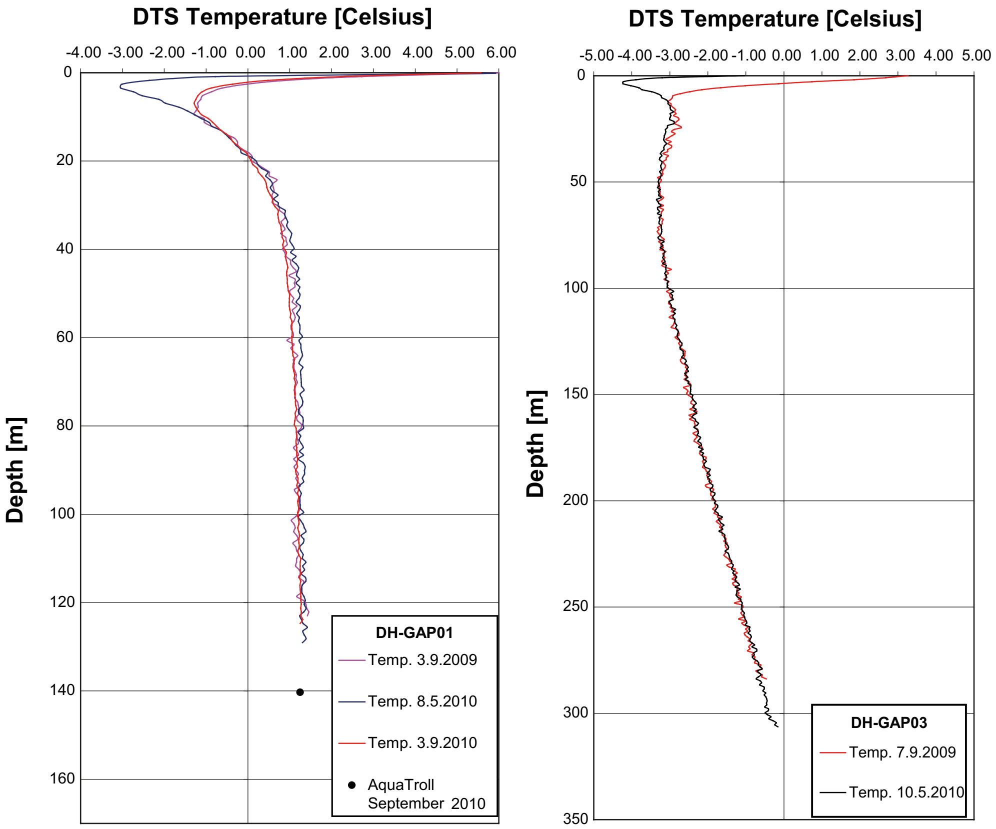

Figure 4-33. *Temperature profiles in DH-GAP01 (left) and DH-GAP03 (right) calculated for vertical depths. Note that the vertical depth extension is not the same in the two figures.*

In 2010, DTS measurements in DH-GAP01 were performed during the field trips in May and in September, whereas DH-GAP03 was measured only in May (Figure 4-32).

The measurements in DH-GAP01 confirm that the Talik Lake is indeed underlain by a talik. By definition a through talik is a talik both open to the top and unfrozen layers beneath the permafrost. An open talik is open to the top. The first 20 m of the borehole is in frozen ground, but when the borehole extends under the lake the temperature rises above the freezing point. In both holes, the seasonal variation is pronounced and it extends down to about 10 m depth. In May 2010, the coldest temperature in DH-GAP01 was –3.0°C at 3.5 m depth, while at the same depth in DH-GAP03, the temperature was –4.2°C. The difference in temperature may be partly explained by the location of the boreholes. DH-GAP01 is situated next to a talik at 350 m elevation, whilst DH-GAP03 is in a permafrost region at 450 m elevation. The soil cover and vegetation are also somewhat different at these respective locations.

DTS measurements in 2010 confirm the initial interpretations based on the data collected in 2009. The base of the permafrost is at approximately 335 meters depth, extrapolated from the DH-GAP03 profile. Lakes of sufficient size are able to support the formation of through-taliks in the investigation area (see Chapter 4.7.3). The data obtained from DTS profiling is important for the planning and successful completion of the deep research borehole and for the general understanding of permafrost distribution at the research area.

4.7.2 Temperature profiling of the Talik Lake

During the May field trip, the lake beneath which DH-GAP01 intersects the talik was profiled for depth and temperature. The purpose of this task was to establish the undisturbed temperature profile of the water column. Therefore, the sounding was scheduled for a period when the lake had been ice covered for more than 6 months and the melting season had not yet begun to feed water into the lake. The steady state temperature at the lake bottom is a critical boundary condition for talik formation and is of interest for geothermal modelling. Another aim was to investigate whether water discharging from the talik into the lake was detectable at any location in the lake, interpreted through temperature anomalies. Water from the talik would likely be a different, slightly cooler temperature than the lake water based on temperatures measured in the borehole and would, thus, appear as an anomaly in the temperature profile.

The study was accomplished by drilling ice holes along four profiles, three across the shorter width of the lake and one lengthwise down the middle of the lake, Figure 4-34. Profile 1 followed the trace of borehole DH-GAP01. An Antares (0.001°C resolution) temperature probe was lowered on a measuring tape at regular intervals, allowing the temperature probe time to calibrate at each measuring depth. Data from the Antares was then processed to create temperature profiles with depth.

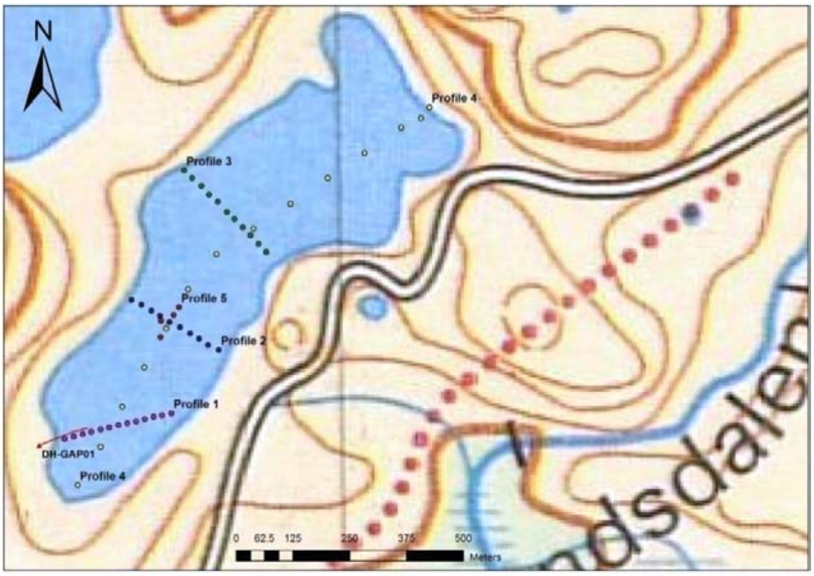

Figure 4-34. Locations of profiles used to assess the distribution of temperature and depth of the Talik Lake. Base map: Hiking Map 1:100 000, © Greenland Tourism a/s.

The four profiles on the Talik Lake are shown in Figure 4-34. Four additional holes (called profile 5) were drilled at the deepest part of the lake. All profiles showed cooler temperatures at the surface immediately beneath the ice. The maximum depth of Profile 1 was 15.4 m and bottom temperature was 3.65°C (Figure 4-35). Temperatures were fairly homogenous with depth. In Profile 2, which has a greater depth, temperatures decrease from around 3.6°C to 3.2°C between 15 and 20 m depth. There is a return to slightly warmer temperatures, around 0.1 to 0.3°C higher, at the lake bed. Similar temperature profiles were noted for each site on the lake where depths were equivalent. A comparable unstratified temperature pattern, down to depths around 13 m, was seen in the profiling done by boat in September, 2009, but under open water conditions, and after the temperate season, the temperatures were about 5 degrees higher (i.e. 8.9°C) (SKB 2010). The Talik Lake appears to stratify during the ice-covered winter months, with the transition between layers occurring between 15 and 20 m depth. Whether this is the case in the summer also is not known because in 2009 none of the monitoring points were deeper than 13 m. While there are cooler temperatures at depths greater than 15 m in the lake, this is to be expected in a stratified lake and the minimum temperature observed was 3.28°C. The temperature-depth profiles of the Talik Lake demonstrate that if flow from the talik into the lake occurs, it is likely to be very small volumes due to the low transmissivity of the crystalline rock, and thus does not cause any appreciable temperature anomaly, or the discharge is very localized or time dependent and was not captured with the rather coarse grid used for soundings. The AquaTROLL data logger installed in DH-GAP01 gives a temperature of 1.3°C at a depth of 140 m.

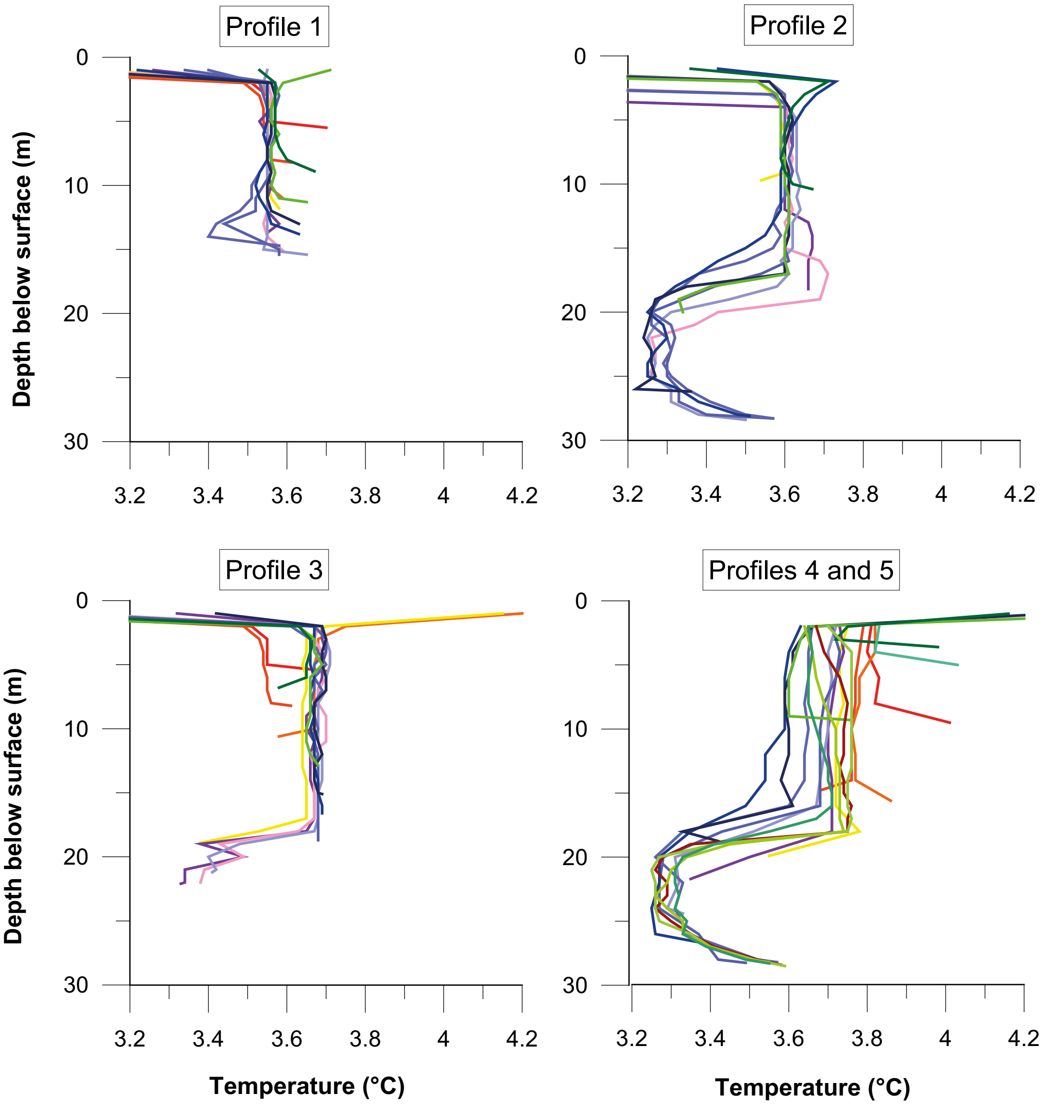

Figure 4-35. *Temperature and depth profiles of the Talik Lake showing stratification occurring in the deeper areas of the lake. Colors indicate different observation points in each profile.*

4.7.3 Geothermal modelling

New site-specific data obtained in 2010 allowed us to further interpret the measured bedrock temperature profiles and to refine the previously reported permafrost/talik models (SKB 2010). The determination of the thermal properties of the main rock types (Chapter 4.5.2), and the Talik Lake temperature profiling (Chapter 4.7.2), in particular, produced useful information for further modelling considerations.

Heat Flow Density

Model calculations, DTS temperature profiling and petrophysical data from DH-GAP03 were used to obtain the first estimate for the steady state Heat Flow Density (HFD). The upper 150 m of the temperature data was omitted to reduce the influence of the recent (past 15 years) warming observed in the upper part of the profile (Figure 4-36). Using the temperature gradient, 13.9 mK/m, determined at 150–300 m, and the average measured thermal conductivity values (9 determinations) for the rocks in the test section, 2.50 ± 0.13 W/mK, resulted in a HFD value of 34.8 ± 1.9 mW/m^2. It should be noted that this value is not the deep undisturbed steady-state heat flow value and is still affected by the temperature fluctuation induced by the past glacial stages and Holocene variations (extends down to 1–2 km).

Development of Taliks

Borehole DH-GAP01 was drilled in 2009 under a lake to seek confirmation that the assumed talik exists and to observe the hydrogeochemical and physical conditions in such a structure (SKB 2010). Repeated temperature profiling of the borehole shows that as soon the borehole advances beneath the lake basin the bedrock temperature increases above zero and stabilizes quickly to about 1.3ºC. This temperature is maintained along the profile down to the depth of 140 m, which is our deepest monitoring point. Geothermal modelling was applied to investigate the nature of this talik and determine whether it extends through the permafrost or is just an open talik which closes deeper down. The constraints for the talik formation were also of interest: how large the lake should be, how long does it take to develop into a talik, and how the chosen boundary conditions affect the results?

The heat transfer in bedrock was studied by 2D conductive models using the simulation code, Processing Shemat (Clauser 2003). In 2009, the modelling was based on assumptions about the thermal parameters and the lake bottom temperatures. A preliminary temperature profiling of the

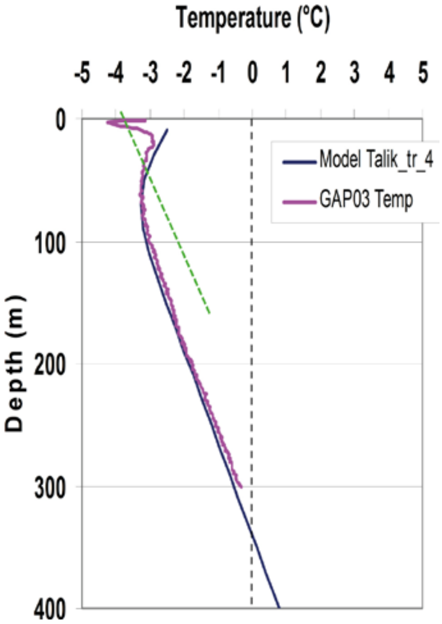

Figure 4-36. DTS temperature profile from DH-GAP03 (pink) and a model curve fitting (blue) used for HFD calculation. The green dashed line suggests that initial ground surface temperature has been about –4.4ºC during the growth of deep permafrost.

lake water basin was conducted in September, 2009. It turned out that in the upper 15 meters the water column is totally mixed and the temperatures were almost uniformly about +8°C (SKB 2010). This is not an accurate representation of conditions year round and therefore a more comprehensive monitoring was conducted from the lake ice in May, 2010 (Chapter 4.7.2) in order to refine the model. The results show that the minimum temperatures in the lake bottom are above +3.4°C, confirming the concept of talik formation (Figure 4-35).

The temperature data from DH-GAP03 indicates that the present permafrost has grown when the climate was cooler than present (Figure 4-36). The long-term records from Kangerlussuaq give a mean annual air temperature of –5.7°C for the period 1960–1990 (Danish Meteorological Institute). In the observed temperature profiles, the present ground temperature not affected by the annual variation is about –3°C, while the value extrapolated from the deep permafrost is –4.4°C.

In the updated talik simulations the basal heat flow is 38 mW/m^2. Because it is reasonable to assume that both the Talik Lake, and the talik beneath, have been there for a long time, –4.4°C was taken as the initial ground surface temperature and +4°C was used as the upper boundary condition (lake bottom temperature) for the talik. Latent heat of pore water is ignored due to very low porosity (average 0.48%) measured from the GAP drill core samples (see Chapter 4.5.2).

The main conclusion regarding the development of taliks was that under the steady-state conditions, as defined above, through-taliks are likely to form through a 300 m deep layer of permafrost, if the lake is wider than about 200 m. Open taliks (open to surface, confined by frozen ground beneath) are forming beneath lakes which are about 100 m wide. It is noteworthy that, according to our model, taliks form rather quickly in low-porosity crystalline rocks. If a large enough lake basin is formed on frozen ground, an open talik can be observed in less than 100 years, and a through-talik can form in less than 500 years (Figure 4-37). Surface water bodies influence the distribution of permafrost and the talik-related recharge-discharge areas, and the variations can be very rapid in comparison to geological time scales.

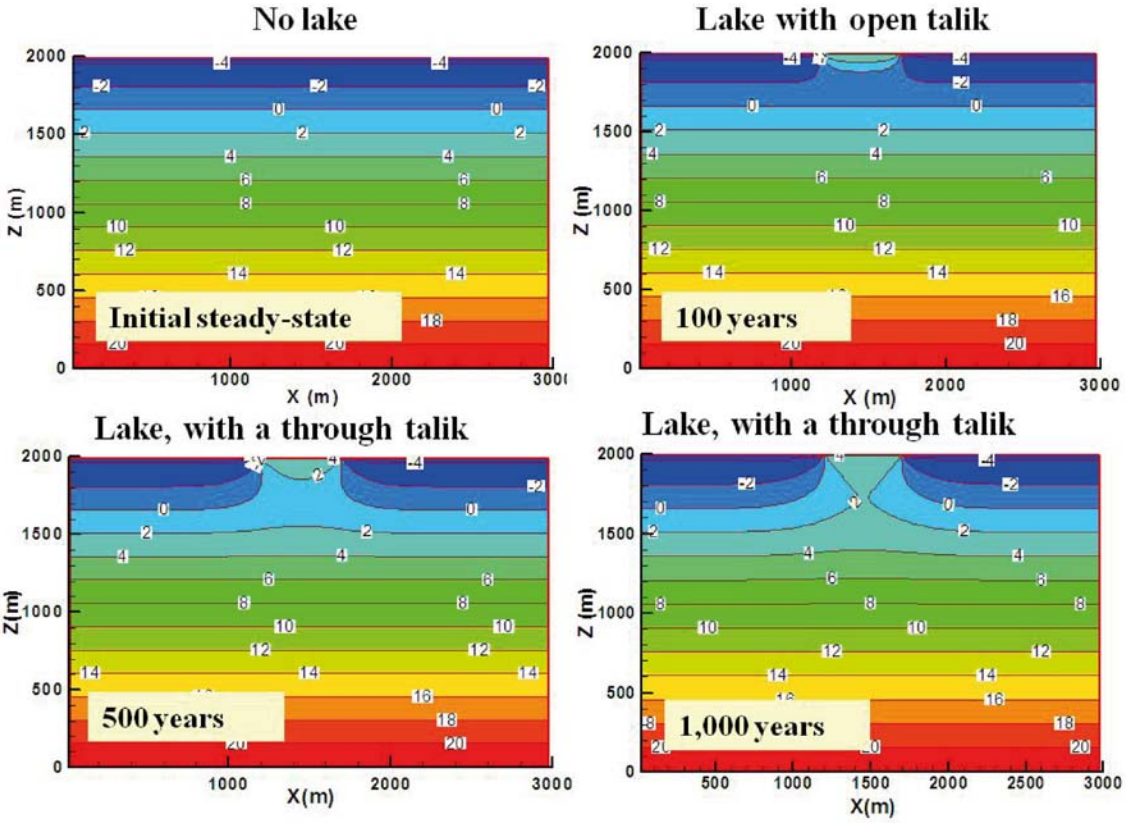

Figure 4-37. Development of a talik through a 300 m deep layer of permafrost. Initial ground surface temperature is assumed to be –4.4°C and the lake bottom temperature +4°C appears at year zero. Basal heat flow of 38 mW/m^2, thermal conductivity of 3 W/mK and porosity 0% were applied for the simulation.

4.8 Structural geology and geomodelling

Structural geology has been an important part of SPC activities since the first reconnaissance field trip in 2008 (Aaltonen et al. 2010, SKB 2010). In crystalline bedrock, the fracture network provides the space and routes for groundwater flow and, therefore, it is important to understand the brittle deformation of the bedrock. Direct applications of this information have been used for the planning of the deep research borehole. The focus and the scale of the field observations have been such that these data needs have been satisfied in sufficient degree. However, some limited effort has been also made in 'semi-regional' scale to identify the major lineaments crossing the study area.

In 2010, significant progress in understanding the nature of brittle fracturing was made when the fracture orientation data from the DH-GAP01 and DH-GAP03 cores became available. Chapter 4.8.1 reports the analysis of this data set.

A deformation zone model is an important input in hydrogeological modelling. A very simple and stochastic deformation zone model already exists, which is based on superficial interpretation of site-scale lineaments and the mapping data collected from small key areas in 2008 (Aaltonen et al. 2010) and this model has been used by, for example, the In2Earth modelling team (Jaquet et al. 2010). The modelling teams have requested an updated geological map and deformation zone model of the field area around Kangerlussuaq. The target area of the full-scale hydrogeological modelling is very large compared to the field area of SPC, and a significant part of it is covered by ice. In order to respond to the modelers request, so that the updating could rest on sound argumentation, a sub-model area about 70 km by 110 km was defined that was mainly in the ice free region (see Figure 4-43). In the east, the sub-model area is restricted by the availability of the airborne geophysical data at about 40 km east of the ice margin. Work with the updated model started in autumn, 2010 and will be completed by March, 2011. Outline of the GAP Geomodel is given in Chapter 4.8.2.

4.8.1 Fracture orientation analysis of drill cores DH-GAP01 and DH-GAP03

Fracturing controlled by foliation is common in both drill cores. Part of the fracturing in DH-GAP01 shows the same trend as the foliation, with a sub-vertical dip towards the NW (Figure 4-38). Fracturing parallel to the foliation is not as prominent in DH-GAP03, but still forms a distinguishable set of fractures (Figure 4-39). Both drill cores provide evidence of a sub-horizontal fracture set, but, due to the rather limited amount of drilling, the nature and orientation of this set remains somewhat uncertain.

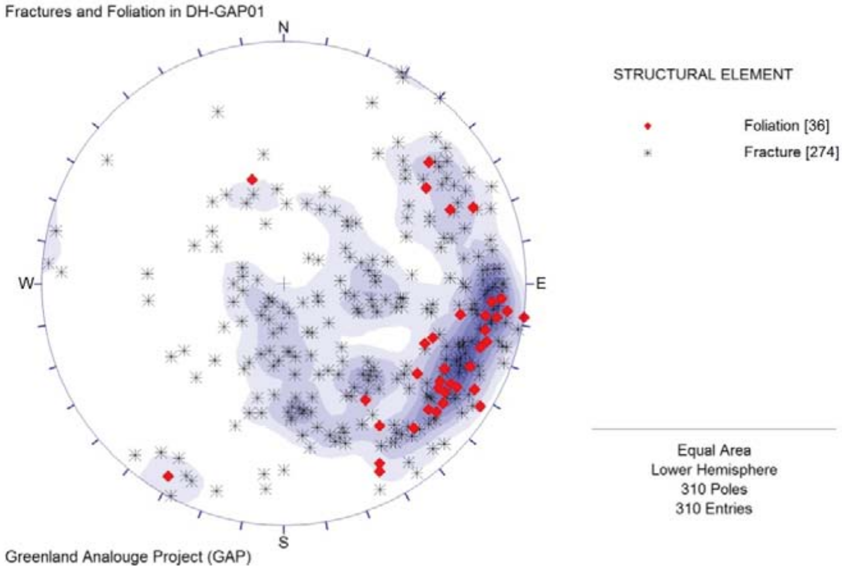

Figure 4-38. *Fracturing and foliation in DH-GAP01, presented as a stereographic plot (equal area, lower hemisphere projection).*

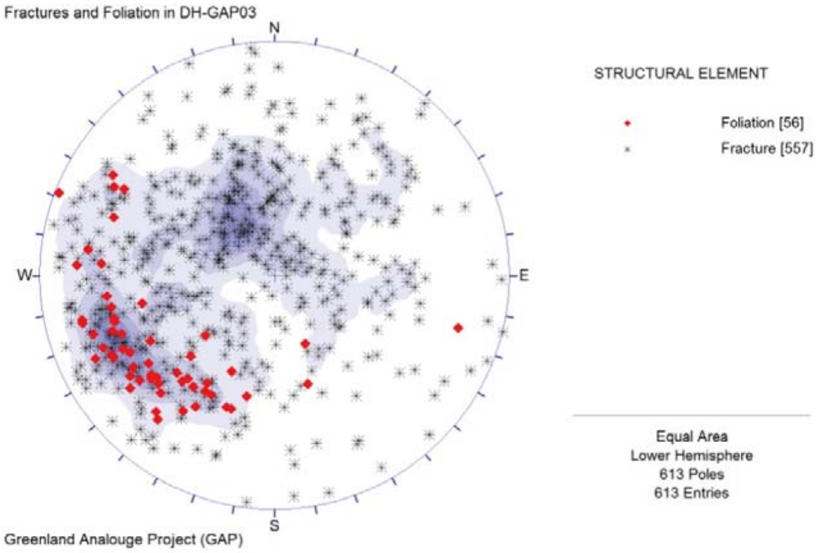

***Figure 4-39.** Fracturing and foliation in DH-GAP03, presented as a stereographic plot (equal area, lower hemisphere projection).*

DH-GAP01 intersects fault zones/deformation zones which are indicated by increased fracture densities. The first evident fault zone was seen at approximately 85 m of borehole length and it is dipping moderately towards WSW (Figures 4-22 and 4-40). Two other apparent fault zones are recognized at approximately 155 m and at 218 m of borehole length. The upper zone is trending N-S with a dip towards the E, while the other has a sub-vertical dip towards NE.

DH-GAP03 is intersected by four fault zones/deformation zones, which show signs of increased fracturing and/or slickenside fractures showing signs of movement. The first fault zone was discovered at approximately 91 m of borehole length, dipping sub-vertically towards NE (Figure 4-41). The three other zones are recognized in the bottom part of the hole, the first one at 246 m of borehole length. This zone is dipping moderately towards SW. The third zone is dipping moderately towards

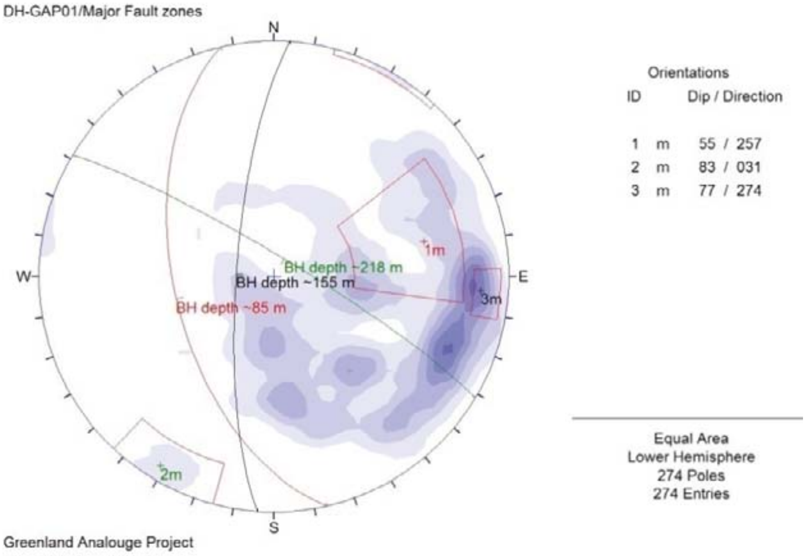

***Figure 4-40.** The major fault zones in DH-GAP01, presented as a stereographic plot (equal area, lower hemisphere projection). Darker shade indicates a higher number of observations.*

the E at borehole depth of 296 m. The borehole ends in a major deformation zone, which is defined by intense fracturing of the core for the last 15 m (Figure 4-42). The orientation of the deformation zone is based on a fracture set that appears when the deformation zone is approached (at approximately 327 m of borehole depth). These fractures indicate that the zone dips moderately towards SE (Figure 4-41).

4.8.2 GAP Geomodel

The updated GAP Geomodel utilizes all available information in order to improve the accuracy of the model, especially beneath the ice sheet. The aim of the geomodelling work was to start with the large scale features and then work towards more detailed scales. The modelling area was divided into two scales: the regional scale area and the site scale area (Figure 4-43). The site scale refers to the area where surface mapping has been performed, and where DH-GAP01 and DH-GAP03 were drilled in 2009 (Aaltonen et al. 2010, SKB 2010).

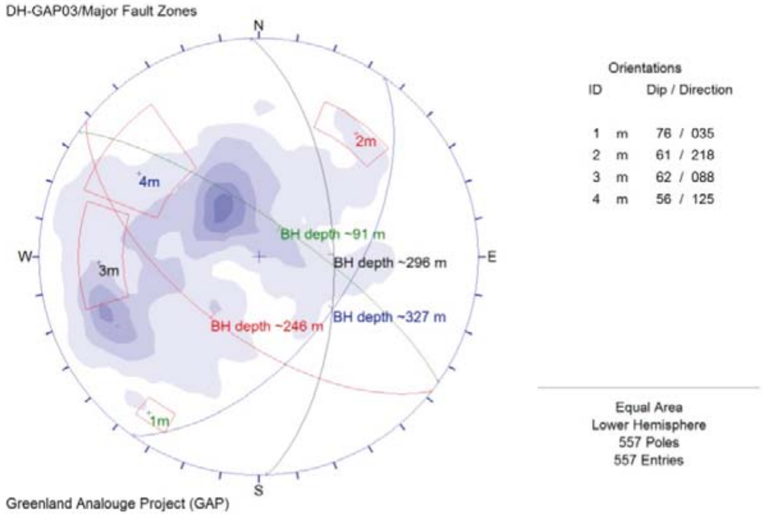

Figure 4-41. The major fault zones in DH-GAP03, presented as a stereographic plot (equal area, lower hemisphere projection).

Figure 4-42. Photo showing part of the main fault zone in DH-GAP03, located in between 326.87 m–341.20 m of borehole length. Photo by Tuomas Pere.

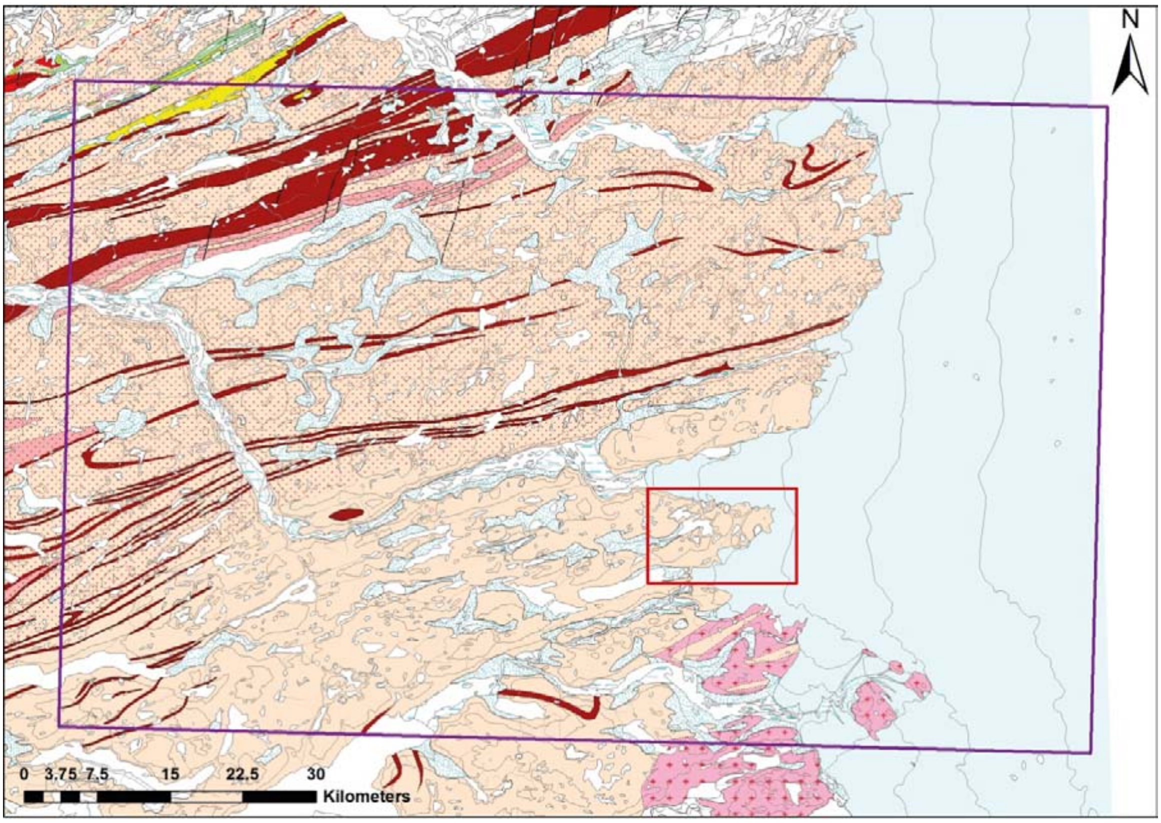

Figure 4-43. Regional modelling area for the GAP Geomodel (shown in lilac) and the site-scale area (shown in red). Geology is adapted from Escher (1971).

The work on the Geomodel included processing of geological mapping data SPC collected in 2008–2010, together with the recently updated geological map over West Greenland (Escher 1971). A regional lineament map was produced by integrating geological information and the topographical indications. Four different sets of faults or deformation zones were identified. To confirm their locations, and increase the confidence of the interpretation, an independent geophysical interpretation was done on aeromagnetic data purchased from GEUS. This data was especially valuable when looking for the subglacial lineaments.

Integrated interpretation resulted in a model consisting of 158 deformation zones or fault zones in the regional area. Out of these, 18 occur within the site-scale area shown in Figure 4-43 and most of them are supported by field observations. The most prominent features in the region are the ductile/brittle, roughly ENE-WSW trending, Type 1 zones (lilac) crosscutting the area, butand also the Type 3 zones (blue) and the Type 4 faults (black) (Figure 4-44).

To confirm and validate the regional model, a comparison with the site area was carried out. The mapping data from all three years (2008–2010) were compiled into a database. Special emphasis was put on the analysis of faults and slickenside fractures to compare them to the recognized regional large-scale features. The four faults or deformation types could be identified also in the site-scale data. In addition to these four sets, a fifth set of fractures was found from the drill core data. A group of sub-horizontal fractures are shown in red and referred to as Type 5. Sub-horizontal fractures and faults are not readily observed in outcrops and, hence, they are undervalued in mapping data. Virtually all of the observations are coming from the two drillcores, and therefore, it is not actually known how widespread thise fault set is in the study area. However, based on the experience from Finland and Sweden, it is known that this type of feature is common and that they have an important role in water conductivity in the upper 200 m (Olofsson et al. 2007, Löfman et al. 2009).

The color codes in the stereographic plot in Figure 4-45 are the same as in the regional model: Type 1 (lilac), Type 2 (green), Type 3 (blue), Type 4 (black) and Type 5 (red). The most distinct fault set in the stereographic plot is the E-W (ID=1) trending sub-vertical feature (Type 1), which shows a sub-vertical

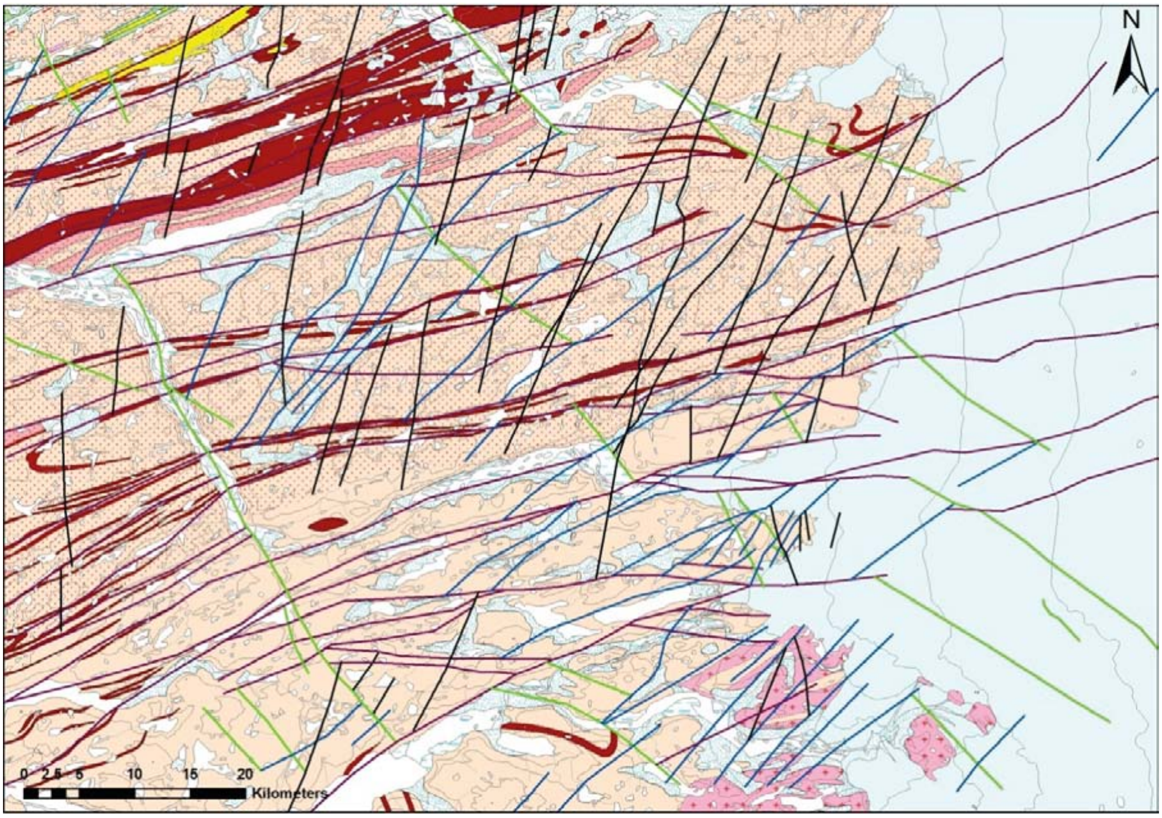

Figure 4-44. Regional map showing the final interpretation with the four distinct types of deformation zones and faults; Type 1=Lilac, Type 2=Green, Type 3=Blue and Type 4=Black. Geology is adapted from Escher (1971.)

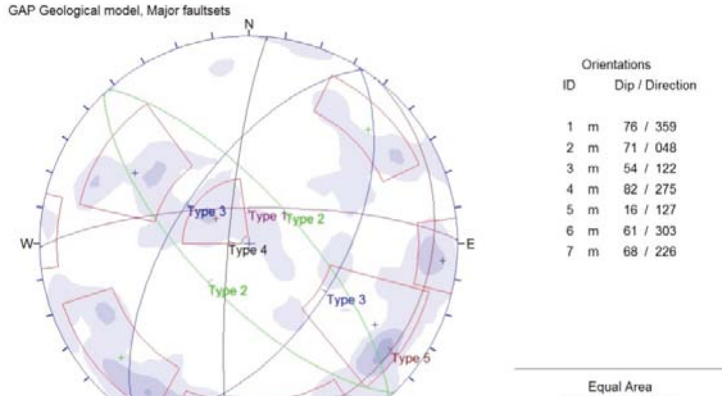

Orientations

ID		Dip / Direction
1	m	76 / 359
2	m	71 / 048
3	m	54 / 122
4	m	82 / 275
5	m	16 / 127
6	m	61 / 303
7	m	68 / 226

Figure 4-45. Stereographic plot of the major fault sets interpreted from the slickenside fractures mapped by SPC from the site area (equal area, lower hemisphere projection). The measurements, together with the interpreted planes, are shown. Type 1 (lilac), Type 2 (green), Type 3 (blue), Type 4 (black) and Type 5 (red).

dip towards the N. Type 2 faults dip either to NE (ID=2) or to SW (ID=7). Dips to NE dominate (75%) over the SW direction (25%). Type 3 faults have a more diverse character, exhibiting moderate dips towards SE (ID=3) and NW (ID=6), statistically in equal frequency. Type 4 feature trends NNE-SSW (ID=4) showing a sub-vertical dip both towards the E and W. As mentioned before, Type 5 faults are identified only from drillcores DH-GAP01 and DH-GAP03. Dip of these fractures seem to be towards SE (ID=5), but the small number of measurements leaves some uncertainty to the interpretation.

4.9 Conclusions

- Continued DTS and AquaTROLL temperature monitoring in borehole DH-GAP01 confirmed the existence of a talik beneath the investigated lake. The water basin is 1,200 m long, 300–400 m wide and up to 32 m deep. The bedrock temperature profile beneath the lake remains constant and is 1.26ºC at 140 m of vertical depth. Water temperature at the bottom of the lake remains above 3ºC year round.
- Geothermal modelling supports the idea that the investigated lake has a through talik beneath it, penetrating the 330 m of frozen ground recorded in borehole DH-GAP03. There are numerous other lakes in the area, which are likely to support taliks as well. Geothermal modelling suggests that thawing a talik through the permafrost takes less than 500 years under the conditions recorded at the investigation site.

  Model calculations using DTS temperature profiling and petrophysical data from DH-GAP03 were used to determine the first estimate for the steady state Heat Flow Density (HFD). A HFD value of 34.8 ± 1.9 mW/m^2 was obtained. However, this value is probably somewhat affected by the temperature fluctuation induced by past glacial stages.
- Groundwater sampling from the talik borehole (DH-GAP01) show that the water reservoir in the talik is chemically and isotope geochemically distinct from surface waters. The $Ca\text{-}Na\text{-}SO_4$ –type talik waters have higher amount of dissolved solids and a depleted stable isotope composition (d^2H, $d^{18}O$) compared to the lake water. Lack of tritium indicates that mixing with meteoric waters has been limited or non-existent at least for the past 50 years. Most microbial DNA signatures indicated anaerobic conditions in the borehole and aerobic conditions in the Talik Lake.
- Pressure-response tests associated with water withdrawal from borehole DH-GAP01 and use of the AquaTROLL pressure sensor were made to obtain data for evaluation of hydraulic transmissivity and hydraulic conductivity of the rock surrounding the borehole. The results of the evaluation of the two pressure-response tests suggest a total fracture transmissivity of approximately 10^{-6} m^2/s and a rock-mass hydraulic conductivity of approximately 10^{-8} m/s. The tested interval was 130–191 m of vertical depth.
- Five regional, potentially brittle deformation zones can be identified from the area. All these zones can be observed in the site-scale fracture data as well. The compiled Geomodel provides an input for hydrogeological modelling.

4.10 2011 plans

1) The research work in 2011 will focus on the drilling of the deep research borehole, DH-GAP04, and related activities. The aim is to produce a ca. 500 meter deep borehole with a diameter of 76 mm. In relation to the drilling campaign, physico-chemical data (AquaTROLL) will be collected from DH-GAP01 and sampling will be conducted if the new data indicates changes in water composition.

Two field trips are planned in connection to DH-GAP04. Drilling, hydraulic testing of the borehole, and the instrumentation, will take place between mid-June and mid-July, 2011. The function of all the different components (sampling system, heating cables, sensors, loggers, satellite link, etc.) will be tested immediately after the installation. In order to obtain reasonable understanding of 1) the duration of sampling per section, 2) consumption of nitrogen and 3) the cleaning behavior in the sections, a one-week pumping campaign will be conducted. The first samples will be taken on this occasion. A more comprehensive sampling will be performed in September, after the borehole has had some time to recover from disturbances associated with drilling. It is expected that natural groundwater inflow will have diluted the drilling water contamination and additional pumping prior to sampling will further improve the quality of the samples. The temperature disturbance caused by the drilling is assumed to be smoothened away and the temperature profile in the bedrock will be measured using DTS cable.

2) The investigations at the Leverett spring will most likely be finalized this year. A fieldtrip will be scheduled in April when the spring is assumed to be covered by thick ice, providing an opportunity to study redox conditions and to take uncontaminated samples. The spring has been sealed out from the atmosphere for months and based on the observation in May, 2010, overpressure prevails in the pool. A hole will be drilled through the ice into the pool and a packer system will be installed to manage the water flow. Hydraulic head and redox conditions will be measured, and both water and gas samples will be collected. A substantial effort will be made to confirm the gas phases, to estimate the recharge temperature based on rare gas composition, and to obtain reliable recharge dates.

3) Other studies will include the following tasks:
   - **a)** DTS profiling of DH-GAP04 will be conducted through the instrumentation until the hole is frozen to learn about drilling in frozen ground. The undisturbed temperature profile will be measured before the sampling campaign in September. Possibly, DH-GAP01 and DH-GAP03 will be measured again, mainly to obtain support for the definition of the depth of zero annual amplitude.
     In 2010, DTS cables were installed into two ice holes drilled close to the ice margin. In co-operation with SPB, the temperature profiles will be measured in September, if temporally and technically feasible.
   - **b)** Geochemical characterization of meltwater lakes will be attempted as a co-operation between SPA, the University of Waterloo and GTK. SPA will collect water samples from ten spatially distributed lakes and they will be analyzed for isotopes and chemistry to define the recharge end member. This work has a link to the hydrogeochemistry of both the drill holes and the Leverett spring.
   - **c)** Core and fracture mineral investigations will be continued at the University of Waterloo using the samples collected from DH-GAP01 and DH-GAP03 drill cores. Fracture infillings are studied for mineralogy, stable isotopes of the calcites, and fluid inclusions in calcites. The aim is to characterize the fluid history at the site and provide background data for the meltwater-related water-rock interaction investigations. The composition of rock matrix fluids has been studied using the crush and leach method, and further testing will be conducted with the new drill core. DH-GAP04 can be sampled only in very late 2011 or early 2012 after the detailed documentation in the Posiva core logging facility. However, review of potential sampling sections will be performed at the drilling site
   - **d)** The physico-chemical data recorded by the down-hole sensors in DH-GAP01 will be collected and compared with the weather station data.

5 Summary

This chapter gives a short summary of the investigations carried out by the GAP project during 2010. The GAP sub-projects were active in the field throughout the period May to September, 2010, but were also engaged in preparatory work, data processing and modelling work throughout the year.

5.1 Sub-project A

Two field campaigns focused on improving the understanding of ice sheet hydrology through indirect observations were completed by SPA. These campaigns involved the following investigations: maintenance of the AWS and GPS stations network; acquisition of deep-look radar profiles; and passive and seismic experiments. Remote-sensing processing, data processing, as well as melt- and ice flow-modelling were also carried out in parallel with the field campaigns.

A number of remote sensing activities were undertaken to study the evolution of supraglacial lakes and surface structures, and to acquire information about ice flow velocity patterns of the RGC. By combining different remote sensing archives, a structural-hydrological map of the RGC was produced, which together with ArcGIS tools and GPS results can be used to understand the input of meltwater into englacial and subglacial systems and catastrophic lake drainage events.

Three AWS stations were installed on the ice in the melt zone in an east-west section during 2008 and 2009. These stations complement the weather station transect monitored by the IMAU group in the Netherlands. As a result, the Kangerlussuaq part of the Greenland Ice Sheet has the highest density of weather stations, which allow highly detailed temporal surface mass budget variability studies. The three weather stations have performed well since their installation and have provided 100% temporal data coverage. 2010 work involved data download and field maintenance of AWS network. The last decade has been warm in Greenland, but 2010 was a record year, where all months displayed above-average temperatures. This resulted in a lower surface mass budget than in 2009. Data from the AWS network was used as input data for melt modelling of the entire RGC area. The results show that the melt season in 2010 was longer and that the total volume of freshwater running of the ice sheet was at least double that of 2009.

SPA manages a GPS network covering the RGC, with 20 stations, including a base station situated in front of the Russell Glacier. About 10 of these stations have been running since 2007, and the other 10 were installed in 2010. Maintenance and revamping work in 2010 aimed to solve the previously reported power and memory capacity problems that have led to some data acquisition interruptions. The velocity data indicates that velocity increases tend to coincide with the timing of peak melt. Moreover, the Greenland Ice Sheet experiences strong diurnal variations forced by surface melting; the surface meltwater forcing of basal dynamics and speedup occur at least 90 km inland. Data from the station 150 km inland shows very little annular variability.

In order to obtain ice thickness information, and to be able to identify englacial hydrological features and characterize the subglacial topography and thermal conditions, two impulse radio-echo sounding systems were deployed in 2010. The eruption of the Eyafjallajökull volcano in Iceland in March–April, 2010 significantly delayed and shortened the planned radar work, but 500 km of high resolution radar profiles was able to be collected. The processed data indicate that the ice thickness ranges from 200 to 1,600 m. Preliminary results indicate the presence of a subglacial water body, which would be the first to be observed in Greenland.

Active and passive seismic investigations were carried out in order to identify and characterize: 1) englacial hydraulic processes; 2) sub glacial hydraulic transients; 3) basal motion triggered by the ingress of surface meltwaters to the glacier bed; and 4) deeper seismic activity related to tectonic processes in the geosphere. From the obtained active seismics data it was possible to support the likely existence of a subglacial basin where the radar indicated a potential subglacial water body. Through passive seismics, it was possible to capture the hydraulic fracture propagation associated with the drainage of supraglacial lakes. Further processing of the extensive data sets will provide important support for numerical models on ice sheet hydrology and the rheological controls on meltwater routing.

5.2 Sub-project B

Research during the second year focused on activities such as: deep-ice hot water drill design and fabrication, radar reconnaissance of drilling sites, transport of drill, sensor design and manufacture and field logistics planning. In addition, modelling activities were carried out throughout the year. SPB conducted two field campaigns. The first campaign in May–July (totally six weeks campaign) was the first ice drilling campaign in the GAP. In September 2010, a team returned to the fieldwork site to winterize the equipment and to download data from borehole data loggers and the GPS station.

A total of 13 boreholes were drilled to the bed of the ice sheet at three different sites with depths ranging from ~100 to 700 meters. Due to unexpectedly deep ice at site 3, the two holes here did not reach the bed. Once the holes were drilled they were instrumented and borehole impulse tests were carried out to study the basal hydrological processes.

The results from bed characterisation such as borehole video imaging, penetrometer tests and borehole slug test suggest that at site 1 and 2 there is a relatively thin layer of sediment on top of bedrock.

One key area of interest within the GAP and SPB is the characteristics of the basal water drainage system. The basal pressures in the ice boreholes show diurnal water pressure variations, complex connection pathways and very short times of basal waters. For short times the water pressures exceed ice overburden pressures, and can for short periods fall to values as low as 25% of the ice overburden. These results suggest that the investigated part of the Greenland Ice Sheet show many similarities with observations made from mountain glaciers.

The ice temperature profiles from the thermistor strings are isothermal, which means that the temperature is much warmer than expected and predicted by numerical models. The reason for this discrepancy are partly related to poor constraints on the modelling and the ice gets probably warmed by unidentified processes.

Besides the ice drilling, SPB carried out a radar survey. This was done in order to map out the bed, ice thickness and the hydraulic potential.

Basal water samples were collected from the bottom of the ice holes and from outlet stream waters at the terminus of Isunnguata Sermia. The main objective here is to study the nature of water-rock interaction beneath the Greenland Ice Sheet. The results suggest that the borehole waters have a higher ionic strength than the marginal and terminus samples. Comparing these water samples with other glacial systems the water at Isunnguata Sermia is more dilute and compositionally distinct.

Bed Characteristics

Three independent lines of evidence suggest the bed within the region of sites 1-2 consists of a relatively thin veneer of sediment on top of bedrock: 1) borehole video imaging shows sediment at the bed, but no soft and deformable till layer; 2) penetrometer tests failed to reveal a soft and deformable bed; and 3) borehole slug tests suggest high transmissivity water flow at the bed.

Basal Water Drainage and Pressure

Observations of the subglacial hydrological system of this region of the ice sheet demonstrate many similarities to observations from mountain glaciers. The subglacial drainage systems experience diurnal water pressure variations, complex connection pathways, and very short residence times of basal waters. The water pressure exceeds ice overburden pressure at times, but also falls to less than 25% of overburden for short episodes. The basal water pressure also shows unusual high frequency variations for several days during the late summer. The latter are poorly understood ‘valve-like’ processes, perhaps related to elastic ice deformation, causing sudden changes in connections at the glacier bed.

Ice Temperature

Ice temperature is much warmer than expected or predicted by numerical models. Based on prior studies elsewhere in Greenland and ice temperatures modelled by Sub-project B and other workers, boreholes were expected to freeze closed within hours. Instead, the ice near the margin is nearly temperate (at the pressure melting point) and does not appear to be frozen to the bed. Further inland at GL10- Site 3, the ice is temperate near the surface and bed, and only mildly cold (–4.5 degrees Celsius) at intermediate depths. Poor constraints on the modelling are likely to be partially responsible for the discrepancy between model results and observations. In addition, the ice is likely warmed by processes so far unaccounted for in the modelling because they have not previously been identified. Examples of processes that perhaps need inclusion in thermal-mechanical models include latent heating from refreezing meltwater at the surface and within the ice, and high rates of basal sliding friction. Future work will address these issues by: 1) additional ice temperature measurements, 2) improved numerical modelling via data assimilation methods, and 3) direct investigation of latent heating by refreezing meltwater.

Ice Depth

Ice depth near the center of this terrestrial terminating outlet glacier is much deeper than expected (i.e. the ice is >700 m deep) and the bed is below sea level. A deep and very steep walled trough runs through the outlet of Isunnguata Sermia and curves south higher up the ice sheet. The geometry of this trough is still poorly confined, but will hopefully emerge as more IceBridge data become available.

5.3 Sub-project C

The activities in 2010 have been divided into two categories: 1) Planning of the 2011 drilling campaign and 2) continuation of the field investigations launched in previous years. The continued investigations include: hydrogeochemical sampling of borehole DH-GAP01 and surface waters, physico-chemical monitoring of borehole DH-GAP01, studies on the drillcores of boreholes DH-GAP01 and 03, permafrost and talik investigations, and updating of the geological model.
SPC conducted two field trips during the summer, 2010. The first one took place from May 6–13th, aiming to retrieve monitoring data and water samples representing winter conditions with restricted meltwater production from surface or from the ice sheet. The second field trip took place between August 31st and September 7th. DH-GAP01 was sampled for chemistry and also for microbial analysis.

The main aim of the SPC during 2010 was to continue the collection of information supporting the planning of the deep drilling of borehole DH-GAP04 to be carried out in 2011. The detailed planning involved technical and logistical planning, outlining drilling targets, as well as design and construction of the donwhole instrumentation that will allow hydrogeochemical sampling and monitoring.

SPC's two field campaigns focused on continued hydrogeochemical sampling and monitoring of borehole DH-GAP01, the Leverett spring and surface water bodies. In parallel to the field campaigns, logging of drillcores DH-GAP01 and DH-GAP03 was carried out, together with mineralogical studies, geothermal modelling, and updating of the geologic model of the GAP field area.

Continued monitoring of P/T/EC and hydrogeochemistry in DH-GAP01 confirmed the existence of a chemically distinct reservoir under the lake, suggesting that a talik exists. Microbiological DNA signatures in DH-GAP01 and the overlying lake showed anaerobic conditions in the borehole and aerobic conditions in the lake water, confirming that the borehole water is different from the lake water. Indications of vertical flow have not been observed in the talik under DH-GAP01. However, by a combination of DTS temperature data from DH-GAP03 and petrophysical data from the DH-GAP03 core, geothermal heat transfer modelling suggests that a through talik can exist under the lake and that it will take less than 500 years to develop a through-talik.

During the field work at Leverett spring in May 2010, it was discovered that the spring was flowing and that the system was under pressure throughout the winter. The Leverett spring was re-visited in September, 2010 and in addition to water samples, gas samples were also collected. Despite of the improved gas collection method a small percentage of oxygen was found from the gas samples. A potential source of oxygen is observed from air bubbles trapped in melting ice in the till. Water chemistry in the spring has remained largely the same during the different sampling years.

Water-rock interaction studies on calcites from the drill cores indicate that the calcites have a magmatic/hydorthermal origin and that the GAP site is comparable to the Olkiluoto site. Crush-and leach experiments on rock powder from the drillcores showed agreement between Br/Cl ratios from the Canadian and Fennoscandian Shield, whereas Na was enriched over the Shield samples. Through mineralogical analysis of fracture infilling a redox transition was recognized in the drillcores, suggesting a depth of approximately 40 meters, which is in agreement with what has been found in cores from Äspö and Laxemar in Sweden.

5.4 2011 plans

All three GAP sub-projects will be active in the field in 2011 and the main activities include a second ice drilling campaign, targeting two new sites, the drilling of the deep bedrock borehole DH-GAP04, and to collect an additional ~1,500 km of radar echo-sounding profiles toward the ice divide. Additional fieldwork includes: maintenance work of the AWS/GPS-network, active/passive seismics, and continued monitoring of DH-GAP01 and surface waters. Apart from fieldwork, the following activities will be carried out during 2011: continued water-rock interaction studies, melt modelling, geothermal modelling and remote-sensing analysis.

Ice sheet modelling will be carried out parallel to the GAP fieldwork. SPB is planning to develop a state-of-the-art adjoint model to assimilate field data into the thermo-mechanically coupled, higher-order ice sheet models, and continuing development of the 3D models to gain understanding of the temperature field and basal melt rate. SPA is planning to constrain and tune their coupled meltwater production-ice flow model using remote sensing and GPS velocities, and through information obtained from lake drainage events which force meltwater into the subglacial drainage network.

Groundwater modelling will continue to, on different scales, investigate the conditions and processes impacting recharge of glacial meltwater into the geopsphere, in particular to repository depth in fractured crystalline rock, as well as over safety assessment time scales.

Finally, through a range of field and modelling activities from 2009 to 2010 the GAP has been able to obtain direct observations of hydrological, hydrogeological, hydrogeochemical and glaciohydrological processes from a land-based terminus portion of the Greenland Ice Sheet. Future activities in the GAP will add information required to obtain a substantial and relevant understanding of the conditions and processes associated with the recharge of glacial meltwater into the geosphere within the time frame that is considered relevant to repository safety.

6 References

SKB's (Svensk Kärnbränslehantering AB) publications can be found at www.skb.se/publications.

Aaltonen I, Douglas B, Claesson Liljedahl L, Frape S, Henkemans E, Hobbs M, Klint K E, Lehtinen A, Lintinen P, Ruskeeniemi T, 2010. The Greenland Analogue Project, Sub-Project C. 2008 field and data report. Posiva Working Report 2010-62, Posiva Oy, Finland.

Aebly F A, Fritz, S C, 2009. Palaeohydrology of Kangerlussuaq (Søndre Strømfjord), West Greenland during the last ~8000 years. Holocene, 19, pp 91–104.

Anderson N J, Harriman R, Ryves D B, Patrick S T, 2001. Dominant factors controlling variability in the ionic composition of West Greenland lakes. Arctic, Antarctic, and Alpine Research, 33, pp 418–425.

Anderson S P, Drever J I, Humphrey N F, 1997. Chemical weathering in glacial environments. Geology, 25, pp 399–402.

Barker J A, Black J H, 1983. Slug tests in fissured aquifers. Water Resources Research, 19, pp 1558–1564.

Barns S M, Cain E C, Sommerville L, Kuske C R, 2007. Acidobacteria phylum sequences in uranium-contaminated subsurface sediments greatly expand the known diversity within the phylum. Applied Environmental Microbiolology, 73, pp 3113–3116.

Bartholomew I, Nienow P, Mair D, Hubbard A, King M A, Sole A, 2010. Seasonal evolution of subglacial drainage and acceleration in a Greenland outlet glacier. Nature Geoscience, 3, pp 408–411.

Battaglia J, Aki K, 2003. Location of seismic events and eruptive fissures on the Piton de la Fournaise volcano using seismic amplitudes. Journal of Geophysical Research, 108, 2364. doi:10.1029/2002JB002193

Bello J P, Daudet L, Abdallah S, Duxbury C, Davies M, Sandler M B, 2005. A tutorial on onset detection in music signals. IEEE Transactions on Speech and Audio Processing, 13, pp 1035–1047.

Blatter H, 1995. Velocity and stress fields in grounded glaciers: a simple algorithm for including deviatoric stress gradients. Journal of Glaciology, 41, pp 333–344.

Blum J D, Erel Y, 1997. Rb-Sr isotope systematics of a granitic soil chronosequence: the importance of biotite weathering. Geochimica et Cosmochimica Acta 61, 3193–3204.

Blyth A R, Frape S K, Blomqvist R, Nissinen P, 2000. Assessing the past thermal and chemical history of fluids in crystalline rock by combining fluid inclusion and isotopic investigations of fracture calcite. Applied Geochemistry, 15, pp 1417–1437.

Blyth A R, Frape S K, Ruskeeniemi T, Blomqvist R, 2004. Origins, closed system formation and preservation of calcite in glaciated crystalline bedrock: evidence from the Palmottu natural analogue site, Finland. Applied Geochemistry, 19, pp 675–686.

Blyth A R, Frape S K, Tullborg E-L, 2009. A review and comparison of fracture mineral investigations and their application to radioactive waste disposal. Applied Geochemistry, 24, pp 821–835.

Bouwer H, Rice R C, 1976. A slug test for determining hydraulic conductivity of unconfined aquifers with completely or partially penetrating wells. Water Resources Research, 12, pp 423–428.

Box J E, Ski K, 2007. Remote sounding of the Greenland supraglacial melt lakes: implications for subglacial hydraulics. Journal of Glaciology, 53, pp 257–265.

Brinkerhoff D J, Meierbachtol T W, Johnson J V, Harper J T, 2011. Sensitivity of the frozen/melted basal boundary to perturbations of basal traction and geothermal heat flux: Isunnguata Sermia, western Greenland. Annals of Glaciology, 52, pp 1–7.

Campbell T, 2007. Aqua TROLL 200 operator's manual. Fort Collins, CO: In-Situ Inc.

Chambers K, Kendall J-M, Brandsberg-Dahl S, Reuda J, 2010. Testing the ability of surface arrays to monitor microseismic activity. Geophysical Prospecting, 58, pp 821–830.

Chen G, 1998. GPS kinematic positioning for the airborne laser altimetry at Long Valley, California. PhD thesis. Massachussets Institute of Technology.

Clark I D, Fritz P, 1997. Environmental isotopes in hydrogeology. Boca Raton, FL: Lewis Publishers.

Clauser C (ed), 2003. Numerical simulation of reactive flow in hot aquifers. SHEMAT and Processing SHEMAT. Berlin: Springer.

Cooper H H Jr, Bredehoeft J D, Papadopulos I S, 1967. Response of a finite-diameter well to an instantaneous charge of water. Water Resourources Research, 3, pp 263–269.

Das S B, Joughin I, Behn M D, Howat I M, King M A, Lizarralde D, Bhatia M P, 2008. Fracture propagation to the base of the Greenland ice sheet during supraglacial lake drainage. Science, 320, pp 778–781.

Davis S N, 1964. The chemistry of saline waters: discussion. Ground Water 2, 51.

Dever J I, Hurcomb D R, 1986. Neutralization of atmospheric acidity by chemical weathering in and alpine drainage in the North Cascade Mountains. Geology, 14, pp 221–224.

Drake H, Tullborg E-L, MacKenzie A B, 2009. Detecting the near surface redox front in crystalline bedrock using fracture mineral distribution, geochemistry, and U-series disequilibrium. Applied Geochemistry, 24, pp 1023–1039.

Engelhardt H, Humphrey N, Kamb B, Fahnestock M, 1990. Physical conditions at the base of a fast moving Antarctic ice stream. Science, 248, pp 57–59.

Escher A, 1971. Geologisk kort over Grønland 1:500.000. Kort nr. 3 Søndre Strømfjord – Nûssuaq. København: De Nationale Geologiske Undersøgelser for Danmark og Grønland.

Fahnestock M, Abdalati W, Joughin I, Brozena J, Gogineni P, 2001. High geothermal heat row, basal melt, and the origin of rapid ice how in central Greenland. Science, 294, pp 2338–2342.

Flowers G E, Roux N, Pimentel S, Schoof C G, 2011. Present dynamics and future prognosis of a slowly surging glacier. The Cryosphere, 5, pp 299–313.

Freifeld B M, Trautz R C, Kharaka Y K, Phelps T J, Myer L R, Hovorka S D, Collins D J, 2005. The U-tube: a novel system for acquiring borehole fluid samples from a deep geologic CO_2 sequestration experiment. Paper LBNL-57317, Lawrence Berkeley National Laboratory, Berkeley.

Fritz P, Frape S K, 1982. Saline groundwaters in the Canadian shield – a first overview. Chemical Geology, 36, pp 179–190.

Fritz P, Basharmal G M, Drimmie R J, Ibsen J, Qureshi R M, 1989. Oxygen isotope exchange between sulphate and water during bacterial sulphate reduction of sulphate. Chemical Geology: Isotope Geoscience Section, 79, pp 99–105.

Fritz P, Frape S K, Drimmie R J, Appleyard E C, Hattori K, 1994. Sulfate in brines in the crystalline rocks of the Canadian Shield. Geochimica et Cosmochimica Acta 58, 57–65.

Gagliardini O, Cohen D, Råback P, Zwinger T, 2007. Finite-element modelling of subglacial cavities and related friction law. Journal of Geophysical Research, 112, F02027. doi:10.1029/2006JF000576

Ginzinger D G, 2002. Gene quantification using real-time quantitative PCR: an emerging technology hits the mainstream. Experimental Hematology, 30, pp 503–512.

Gordon S, Sharp M, Hubbard B, Smart C, Ketterling B, Willis I, 1998. Seasonal reorganization of subglacial drainage inferred from measurements in boreholes. Hydrological Processes 12, 105–133.

Greve R, 2005. Relation of measured basal temperatures and the spatial distribution of the geothermal heat flux for the Greenland ice sheet. Annals of Glaciology, 42, pp 424–432.

Gudmundsson G H, 2007. Tides and the flow of Rutford Ice Stream , West Antarctica. Journal of Geophysical Research, 112, F04007. doi:10.1029/2006JF000731

Harper J T, Humphrey N F, 1995. Borehole video analysis of a temperate glacier's englacial and subglacial structure: implications for glacier flow models. Geology, 23, pp 901–904.

HCO, 2011. Oriented drillcore: measurement and calculation procedures for structural and exploration geologists. HolcombeCoughlinOliver Consultants. Available at: http://www.holcombecoughlinoliver.com/downloads/HCO_oriented_core_procedures.

Herczeg A L, Imboden D M, 1988. Tritium hydrologic studies in four closed-basin lakes in the Great Basin, U.S.A. Limnology and Oceanography 33, 157–173.

Hobbie J E, Daley R J, Jasper S, 1977. Use of nucleopore filters for counting bacteria by fluorescence microscopy. Applied and Environmental Microbiology, 33, pp 1225–1228.

Huang S, Farkaš J, Jacobsen S B, 2010. Calcium isotopic fractionation between clinopyroxene and orthopyroxene from mantle peridotites. Earth and Planetary Science Letters, 292, pp 337–344.

Humphrey N, Echelmeyer K, 1990. Hot-water drilling and bore-hole closure in cold ice. Journal of Glaciology, 36, pp 287–298.

Huybrechts P, 1996. Basal temperature conditions of the Greenland ice sheet during the glacial cycles. Annals of Glaciology, 23, pp 226–236.

Hvorslev M J, 1951. Time lag and soil permeability in ground-water observations. Bulletin 36, Waterways Experiment Station, Miss., U.S. Army Corps of Engineers.

Hyder Z, Butler J J, McElwee C D, Liu W, 1994. Slug tests in partially penetrating wells. Water Resources Research, 30, pp 2945–2957.

Iken A, Röthlisberger H, Flotron A, Haeberli W, 1983. The uplift of Unteraargletscher at the beginning of the melt season – a consequence of water storage at the bed. Journal of Glaciology, 29, pp 28–47.

Inagaki F, Tsunogai U, Suzuki M, 2004. Characterization of C1-metabolizing prokaryotic communities in methane seep habitats at the Kuroshima Knoll, southern Ryukyu Arc, by analyzing pmoA, mmoX, mxaF, mcrA, and 16S rRNA genes. Applied and Environmental Microbiology, 70, pp 7445–7455.

Jaquet O, Namar R, Jansson P, 2010. Groundwater flow modelling under ice sheet conditions. Scoping calculations. SKB R-10-46, Svensk kärnbränslehantering AB.

Joughin I, 2002. Ice-sheet velocity mapping: a combined interferometric and speckle-tracking approach. Annals of Glaciology, 23, pp 195–201.

Jägevall S, Rabe L, Pedersen K, 2011. Abundance and diversity of biofilms in natural and artificial aquifers of the Äspö Hard Rock Laboratory, Sweden. Microbial Ecology, 61, pp 410–422.

Lee W H K, Stewart S W, 1981. Principles and applications of microearthquake networks. New York: Academic Press.

Leng M J, Anderson N J, 2003. Isotopic variation in modern lake waters from western Greenland. Holocene, 13, pp 605–611.

Löfman J, Pitkänen P, Mészáros F, Keto V, Ahokas H, 2009. Modelling of groundwater flow and solute transport in Olkiluoto – update 2008. Posiva Working Report 2009-78, Posiva Oy, Finland.

Madigan M T, Martinko J M, 2006. Brock biology of microorganisms. 11th ed. London: Pearson Prentice Hall.

McNutt R H, Frape S K, Fritz P, Jones M G, MacDonald I M, 1990. The $^{87}Sr/^{86}Sr$ values of Canadian Shield brines and fracture minerals with applications to groundwater mixing, fracture history, and geochronology. Geochimica et Cosmochimica Acta 54, 205–215.

Mitchell A C, Brown G H, 2007. Diurnal hydrological-physicochemical controls and sampling methods for minor and trace elements in an Alpine glacial hydrological system. Journal of Hydrology, 332, pp 123–143.

Mitchell A C, Brown G H, Fuge R, 2001. Minor and trace element export from a glacierized alpine headwater catchment (Haut Glacier d'Arolla, Switzerland). Hydrological Processes, 15, pp 3499–3524.

Nettles M, Larsen T B, Elósegui P, Hamilton G S, Stearns L A, Ahlstrøm A P, Davis J L, Andersen M L, de Juan J, Khan S A, Stenseg L, Ekström G, Forsberg R, 2008. Step-wise changes in glacier flow speed coincide with calving and glacial earthquakes at Helheim Glacier, Greenland. Geophysical Research Letters, 35, L24503. doi:10.1029/2008GL03612.

Olofsson I, Simeonov A, Stephens M, Follin S, Nilsson A-C, Röshoff K, Lindberg U, Lanaro F, Fredriksson A, Persson L, 2007. Site descriptive modelling Forsmark, stage 2.2. A fracture domain concept as a basis for the statistical modelling of fractures and minor deformation zones, and interdisciplinary coordination. SKB R-07-15, Svensk Kärnbränslehantering AB.

Oswald G K A, Gogineni S P, 2008. Recovery of subglacial water extent from Greenland radar survey data. Journal of Glaciology, 54, pp 94–106.

Pedersen K, Ekendahl S, 1990. Distribution and activity of bacteria in deep granitic groundwaters of southeastern Sweden. Microbial Ecology, 20, pp 37–52.

Pedersen K, Arlinger J, Erlandson A-C, Hallbeck L, 1997. Culturability and 16S rRNA gene diversity of microorganisms in the hyperalkaline groundwater of Maqarin, Jordan. In Pedersen K (ed). Investigations of subterranean microorganisms and their importance for performance assessment of radioactive waste disposal. Results and conclusions achieved during the period 1995 to 1997. SKB TR 97-22, Svensk Kärnbränslehantering AB, pp 239–261.

Pedersen K, Arlinger J, Edlund J, Eriksson S, Lydmark S, Johansson J, Jägevall S, Rabe L, 2010. Microbiology of Olkiluoto and ONKALO groundwater. Results and interpretations, 2008–2009. Posiva Working Report 2010-60, Posiva Oy, Finland.

Pimentel S, Flowers G E, 2010. A numerical study of hydrologically driven glacier dynamics and subglacial flooding. Proceedings of the Royal Society A, 467. doi:10.1098/rspa.2010.0211

Pimentel S, Flowers G E, Schoof C G, 2010. A hydrologically coupled higher-order flow-band model of ice dynamics with a Coulomb friction sliding law. Journal of Geophysical Research, 115, F04023. doi:10.1029/2009JF001621

Pimentel and Flowers 2011. A numerical study of hydrologically driven glacier dynamics & subglacial flooding. Proceedings of the royal society A 467 537–558.

Roux P-F, Marsan D, Metaxian J-P, O'Brien G, Moreau L, 2008. Microseismic activity within a serac zone in an alpine glacier (Glacier d'Argentiere, Mont Blanc, France). Journal of Glaciology, 54, pp 157–168.

Shapiro A M, Hsieh P A, 1998. How good are estimates of transmissivity from slug tests in fractured rock? Ground Water, 36, pp 37–48.

Sharp M, Tranter G, Brown G H, Skidmore M, 1995. Rates of chemical denudation and CO_2 drawdown in a glacier-covered alpine catchment. Geology, 23, pp 61–64.

Scholz H, Baumann M, 1997. An 'open system pingo' near Kangerlussuaq (Søndre Strømfjord), West Greenland. Geology of Greenland Survey Bulletin, 176, pp 104–108.

Schoof C, 2005. The effect of cavitation on glacier sliding. Proceedings of Royal Society of London, Series A, 461, pp 609–627.

Schoof C, 2010. Ice-sheet acceleration driven by melt supply variability. Nature, 468, pp 803–806.

Shepherd A, Hubbard A, Nienow P, King M, McMillan M, Joughin I, 2009. Greenland ice sheet motion coupled with daily melting in late summer. Geophysical Research Letters, 36, L01501. doi:10.1029/2008GL035758

SKB, 2010. The Greenland Analogue Project. Yearly report 2009. SKB R-10-59, Svensk Kärnbränslehantering AB.

Sneed W A, Hamilton G S, 2007. Evolution of melt pond volume on the surface of the Greenland Icesheet, Geophysical Research Letters, 34, L03501, doi: 10.1029/2006GLD28697.

Spiessl S M, MacQuarrie K T, Mayer K U, 2008. Identification of key parameters controlling dissolved oxygen migration and attenuation in fractured crystalline rocks. Journal och Contaminant Hydrology 95, 141–153.

Stotler R L, Frape S K, Shouakar-Stash O, 2010. An isotopic survey of δ^{81}Br and δ^{37}Cl of dissolved halides in the Canadian and Fennoscandian Shields. Chemical Geology, 274, pp 38–55.

Sugiyama S, Bauder A, Weiss P, Funk M, 2007. Reversal of ice motion during the outburst of a glacier-dammed lake on Gornergletscher, Switzerland. Journal of Glaciology, 53, pp 172–180.

Sundal A V, Shepherd A, Nienow P, Hanna E, Palmer S, Huybrechts P, 2011. Melt-induced speed-up of Greenland ice sheet offset by efficient subglacial drainage. Nature, 469, pp 521–524.

Taisne B, Brenguier F, Shapiro N M, Ferrazzini V, 2011. Imaging the dynamics of magma propagation using radiated seismic intensity. Geophysical Research Letters, 38, L04304. doi:10.1029/2010GL046068

Taylor P L, 1984. A hot water drill for temperate ice. In CRREL Special Report 84-34, Cold Region Research and Engineering Laboratory, Hanover, NH, pp 105–117.

Tranter M, Sharp M J, Brown G H, Willis I C, Hubbard B P, Nielsen M K, Smart C C, Gordon S, Tulley M, Lamb H R, 1997. Variability in the chemical composition of in situ subglacial meltwaters. Hydrological Processes, 11, pp 59–77.

van den Broeke M, van de Wal R, Smeets P, 2011. The seasonal cycle and interannual variability of surface energy balance and melt in the ablation zone of the west Greenland ice sheet. Cryosphere Discussions, 5, pp 779–809.

Ventura M, Canchaya C, Tauch A, Chandra G, Fitzgerald G F, Chater K F, van Sinderen D, 2007. Genomics of Actinobacteria: tracing the evolutionary history of an ancient phylum. Microbiology and Molecular Biology Reviews, 71, pp 495–548.

Walter F, Clinton J F, Deichmann N, Dreger D S, Minson S E, Funk M, 2009. Moment tensor inversions of icequakes on Gornergletscher, Switzerland. Bulletin of the Seismological Society of America, 99, pp 852–870.

Walter F, Dreger D S, Clinton J F, Deichmann N, Funk M, 2010. Evidence for Near-Horizontal Tensile Faulting at the Base of Gornergletscher, a Swiss Alpine Glacier. Bulletin of the Seismological Society of America, 100, pp 458–472.

Wang G, Blume F, Meertens C, Ibanez P, 2009. An assessment of accuracy of 10-samples-per-second kinematic GPS based on a sets of six-degree-of-freedom shake table tests. (Submitted to Journal of Geophysical Research).

Wapenaar K, Slob E, Snieder R, Curtis A, 2010. Tutorial on seismic interferometry. Part II: Underlying theory and new advances. Geophysics, 75, pp 75A211-75A227.

Williams W D, 1991. Comments on the so-called salt lakes of Greenland. Hydrobiologia, 210, pp 67–74.

Withers M, Aster R, Young C, Beiriger J, Harris M, Moore S, Trujillo J, 1998. A comparison of select trigger algorithms for automated global seismic phase and event detection. Bulletin of the Seismological Society of America, 88, pp 95–106.

Zwally H J, Abdalati W, Herring T, Larson K, Saba J, Steffen K, 2002. Surface melt-induced acceleration of Greenland ice-sheet flow. Science, 297, pp 218–222.

7 Bibliography

SPA Publication output

Manuscripts

Booth A D, Kulessa B, Hubbard A, Gusmeroli A, Clark R, Doyle S, Dow C, Jones G, Murray T, in prep. Seismic characterisation of subglacial drainage channels beneath the West Greenland Ice Sheet. In preparation for Nature Geoscience.

Doyle S, Hubbard A, in prep. Variations in the flow of land-terminating Russell Glacier Catchment, SW Greenland on diurnal, seasonal and lake tapping time scales, determined using geodetic GPS. In preparation for Journal of Glaciology.

Doyle S, Jones G, Hubbard A, Kulessa B, Dow C, in prep. Integration of kinematic GPS with passive seismology for the study of hydraulically driven crevasse propagation during both rapid lake drainage and moulin initiation on the Greenland Ice Sheet. In preparation for Nature Geoscience.

Jones G A, Doyle S, Kulessa B, Dow C, Hubbard A, 2011. Spatial mapping of superglacial lake drainage in West Greenland using seismic amplitudes. In preparation for Journal of Geophysical Research.

Smeets P, Boot W, Hubbard A, Wilhelms F, van den Broeke M, van de Wal R, submitted. Instruments and methods: a wireless subglacial probe for deep ice applications. Submitted to Journal of Glaciology.

Conference abstracts

Booth A, Kulessa B, Gusmeroli A, Doyle S, Dow C, Jones G, Murray T, Clark R, Hubbard A, 2011. Seismic characterisation of subglacial media around a supraglacial meltwater lake, Russell Glacier, West Greenland. European Geosciences Union General Assembly, Vienna, Austria, 3–8 April 2011.

Dow C F, Doyle S H, Jones G A, Booth A D, Kulessa B, Hubbard A, 2010. Field measurements of rapid supraglacial lake drainage in the Russell Glacier catchment, SW Greenland. Oral presentation at Swansea University Postgraduate Researchers' Science Conference, Swansea, December 2010.

Dow C F, Jones G A, Doyle S H, Booth A D, Kulessa B, Hubbard A, 2011. Geophysical measurements of a catastrophic supraglacial lake drainage event in the Russell Glacier catchment, SW Greenland. Invited talk, Visible Lunch Series, Computer Science Department, Swansea University, February 2011.

Doyle S H, Dow C F, Gusmeroli A, Jones G A, Kulessa B, Booth A D, Hubbard A, 2010. Field observations of rapid supraglacial lake drainage in the Russell Glacier catchment, SW Greenland. Oral presentation at International Glaciological Society British Branch Meeting, Aberystwyth, September 2010.

Jones G A, Doyle S, Dow C, Kulessa B, Hubbard A, 2010. Accurate seismic phase identification and arrival time picking of glacial icequakes. American Geophysical Union Fall Meeting 2010, abstract C21A-0512.

SPB Publication output

Conference abstracts

Brinkerhoff D, Meierbachtol T, Johnson J, Harper J, 2010. Sensitivity of the frozen-melted basal boundary to perturbations of basal traction: Isunnguata Sermia, western Greenland. International Glaciological Society, 2010 Symposium on Disappearing Ice, abstract 59A065.

Brinkerhoff D J, Johnson J V, Meierbachtol T W, Harper J T, 2010. Modelled dynamic sensitivity of Isunnguata Sermia, Western Greenland to the perturbation of basal boundary conditions. Paper presented at American Geophysical Union, Fall Meeting 2010, San Francisco, 13–17 December 2010, abstract C23B-0605.

Harper J T, Humphrey N F, Johnson J V, Meierbachtol T W, Brinkerhoff D J, Landowski C M, 2010. Integrating borehole measurements with modelling of englacial and basal conditions, Western Greenland (Invited). Paper presented at American Geophysical Union, Fall Meeting 2010, San Francisco, 13–17 December 2010, abstract C42A-03.

Landowski C M, Humphrey N F, Harper J T, Sims K W, 2010. Geochemical characterization of subglacial water from the West Greenland Ice Sheet. Paper presented at American Geophysical Union, Fall Meeting 2010, San Francisco, 13–17 December 2010, abstract C21B-0539.

Meierbachtol T W, Harper J T, Humphrey N F, 2010. Perturbations to subglacial water storage through integrated borehole impulse testing: Western Greenland. Paper presented at American Geophysical Union, Fall Meeting 2010, San Francisco, 13–17 December 2010, abstract C21B-0540.

SPC Publication output

Reports

Aaltonen I, Douglas B, Claesson Liljedahl L, Frape S, Henkemans E, Hobbs M, Klint K E, Lehtinen A, Lintinen P, Ruskeeniemi T, 2010. The Greenland Analogue Project, Sub-project C: 2008 field and data report. Posiva Working Report 2010-62, Posiva Oy, Finland.

SKB, 2010. The Greenland Analogue Project. Yearly report 2009. SKB R-10-59, Svensk Kärnbränslehantering AB.

Conference abstracts

Claesson Liljedahl L, Lehtinen A, Ruskeeniemi T, Engström J, Kukkonen I T, Frape S, Henkemans E, 2010. Instrumentation and monitoring of a talik in Kangerlussuaq, West Greenland (Electronic resource). In Thermal state of frozen ground in a changing climate during the IPY : abstracts from the Third European Conference on Permafrost (EUCOP III), Svalbard, Norway, 13–17 June 2010. Longyearbyen: The University Centre in Svalbard, 238. Optical disc (CD-ROM).

Frape S K, Henkemans E, Stotler R L, Ruskeeniemi T, 2010. Sources of salinity in crystalline rocks: the role of cryogenic processes associated with permafrost conditions and proximity of continental ice sheets. In Reaching new peaks in geoscience: 2010 GSA Annual Meeting and Exposition, Denver, Colorado, 31 October – 3 November 2010. Geological Society of America. Abstracts with Programs 42, 487.

Henkemans E, Frape S K, Ruskeeniemi T, Hobbs M, Lintinen P, Makahnouk M, 2009. Geochemical and isotopic characterization of surface waters, Kangerlussuaq, Greenland. Poster at Symposium on Applied Isotope Geochemistry, 2009.

Lehtinen A, Claesson Liljedahl L, Näslund J-O, Ruskeeniemi T, 2010. Future glaciations and the challenges related to long time management of nuclear waste : Greenland Analogue Project (Electronic resource). In Thermal state of frozen ground in a changing climate during the IPY : abstracts from the Third European Conference on Permafrost (EUCOP III), Svalbard, Norway, 13–17 June 2010. Longyearbyen: The University Centre in Svalbard, 63. Optical disc (CD-ROM).

Makahnouk M, Henkemans E, Frape S, Ruskeeniemi T, Lintinen P, Hobbs M, 2009. Geochemical and isotopic characterization of surface and ground water from an area of continuous permafrost adjacent to the Greenland Ice Sheet, Kangerlussuaq, Greenland. Presentation at Portland GSA Annual Meeting, 2009.

Ruskeeniemi T, Lehtinen A, Näslund J O, Belfadhel Mahrez B, Aaltonen I, Claesson Liljedahl L, Hobbs M, Pratt L, Puigdomench I, Selroos J-O, Vähänen M, 2008. Ice sheet hydrology and its impact on deep groundwaters - research project in western Greenland. In Congress of the International Polar Year 2007/08 : IPY 07/08 celebration of Finnish geoscientific studies in Polar areas, GTK, Espoo, Finland, 12–13 November 2008: program and abstracts. Espoo: Geological Survey of Finland, 44.

Stackhouse B T, Onstott T C, Ruskeeniemi T, Claesson Liljedahl L, Lehtinen A, Freifeld B M, Hardisty D, Pratt L, 2010. Chemical and microbial analysis of a talik in western Greenland. Poster at the AGU Fall Meeting, 2010.

Seminars etc.

Henkemans E, Frape S, Makahnouk W M, Lehtinen A, Claesson Liljedahl L, Näslund J-O, Ruskeeniemi T, 2009. Future ice ages and the challenges related to final disposal of nuclear waste: the Greenland Analogue Project. NWMO Geoscience Seminar, 2009.

Henkemans E D, Frape S K, Makahnouk M, Ruskeeniemi T, Engström J, Claesson Liljedahl L, Lehtinen A, Hobbs M, Lintinen P, 2010. Geochemical and isotopic characterization of surface and groundwater from an area of discontinuous permafrost adjacent to the Greenland Ice Sheet, Kangerlussuaq, Greenland. NWMO Geoscience Seminar, 2010.

Makahnouk M, Frape S K, Henkemans E D, Ruskeeniemi T, Engström J, Claesson Liljedahl L, Lehtinen A, Hobbs M, Lintinen P, 2010. Fracture mineral investigations: 2010 Update. NWMO Geoscience Seminar, 2010.

Appendix 1

Reprinted with permission from Annals of Glaciology

Annals of Glaciology 52(59) 2011 1

Sensitivity of the frozen/melted basal boundary to perturbations of basal traction and geothermal heat flux: Isunnguata Sermia, western Greenland

Douglas J. BRINKERHOFF,[1] Toby W. MEIERBACHTOL,[2] Jesse V. JOHNSON,[1]
Joel T. HARPER[2]

[1] *Department of Computer Science, University of Montana, 32 Campus Avenue, Missoula, MT 59812-5256, USA*
E-mail: douglas.brinkerhoff@umontana.edu
[2] *Department of Geosciences, University of Montana, 32 Campus Avenue, Missoula, MT 59812-5256, USA*

ABSTRACT. A full-stress, thermomechanically coupled, numerical model is used to explore the interaction between basal thermal conditions and motion of a terrestrially terminating section of the west Greenland ice sheet. The model domain is a two-dimensional flowline profile extending from the ice divide to the margin. We use data-assimilation techniques based on the adjoint model in order to optimize the basal traction field, minimizing the difference between modeled and observed surface velocities. We monitor the sensitivity of the frozen/melted boundary (FMB) to changes in prescribed geothermal heat flux and sliding speed by applying perturbations to each of these parameters. The FMB shows sensitivity to the prescribed geothermal heat flux below an upper threshold where a maximum portion of the bed is already melted. The position of the FMB is insensitive to perturbations applied to the basal traction field. This insensitivity is due to the short distances over which longitudinal stresses act in an ice sheet.

INTRODUCTION

At geologic timescales, high-latitude countries in the Northern Hemisphere will likely experience future glaciations. The long-term storage of nuclear waste in deep geologic repositories can potentially be impacted by a glaciation via the ice sheet's influence on the subglacial and proglacial groundwater system. It is therefore important to consider subglacial hydrological processes and the role ice sheets play in driving groundwater systems when designing safe storage systems in northern locations. Subglacial hydrological processes become active and recharge the groundwater system only where the bed of an ice sheet is melted. Understanding the spatial pattern of thermal conditions of an ice sheet's bed is therefore an important design criteria for responsible nuclear waste disposal in countries such as Sweden, Finland and Canada.

The Greenland ice sheet (GrIS) is a present-day analog to future ice sheets in Scandinavia and Canada. The thermal state of the bed of GrIS and the accumulation of subglacial water has been investigated by a variety of methods, but remains poorly constrained. Direct observations via drilling show that melted conditions exist near the western margin (Lüthi and others, 2002), as well as at a north-central location near the ice-sheet divide (Andersen and others, 2004). Conversely, frozen conditions have been noted at point locations spanning the ice sheet from Camp Century near the northwest margin (Weertman, 1968), to the centrally located GRIP core and the southeast Dye 3 core (Dahl-Jensen and others, 1998). The spatial extent of melted bed conditions, as determined by the few point observations, has been extended via interpretation of ice-penetrating radar. Fahnestock and others (2001) derived spatially variable basal melt rates $>0.15\,\mathrm{m\,a^{-1}}$ in central GrIS through interpretation of internal radar layering. Using bed reflectivity power as a proxy for basal water content, Oswald and Gogineni (2008) suggested a spatially heterogeneous basal water distribution along radar transects of the GrIS.

Spatially comprehensive estimates of basal conditions are offered by ice-sheet model output. Greve and Hutter (1995) investigated the sensitivity of the basal temperature field on the Greenland ice sheet to variations in a uniform geothermal heat flux. Their results suggest that, while increasing heat flux caused an inland migration of temperate basal conditions, the interior remained frozen, even under the highest heat flux scenario ($54.6\,\mathrm{mW\,m^{-2}}$). This was complemented by a follow-up investigation of the basal temperature field, matching geothermal heat flux to point observations, which implied that the majority of the ice-sheet bed was at the pressure melting point (Greve, 2005). In addition to geothermal heat flux, the sensitivity of GrIS basal conditions to changes in surface temperatures and mass balance was investigated by Huybrechts and others (1996), who found basal conditions show a pronounced sensitivity to steady-state changes in temperature and mass balance; e.g. a 10°C drop in surface temperature resulted in a freezing of the majority of the ice-sheet bed, however, the drop in surface mass balance associated with a 10°C lowering of surface temperature resulted in temperate conditions over nearly 60% of the bed. Transient simulations over the last two glacial cycles show most of GrIS exhibits frozen conditions at the bed at some point in time. While the models employed by both Greve and Huybrechts were three dimensional, both were mechanically limited to the shallow-ice approximation.

In summary, previous studies suggest a spatially distinct frozen/melted boundary (FMB). The location of the FMB at the bed is the result of a balance between heat sources concentrated near the bed (frictional heat from sliding, geothermal heat flux and strain heating) and the introduction of colder ice through diffusive and advective processes. In the present study, we investigate the sensitivity of the FMB not only to geothermal heat flux, but also to

igs.cls v2.01 February 23, 2011 Article ref t59A065 Typeset by Sukie Proof no 1

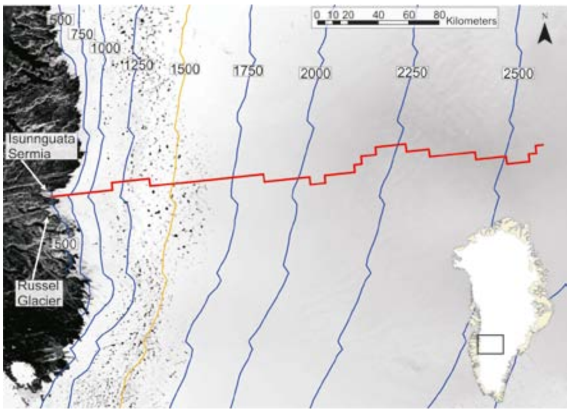

Fig. 1. Study site displaying model profile (red line) from the ice-sheet divide through Isunnguata Sermia to the western margin. Surface elevation contours (blue lines) are given in meters above sea level, and interpolated from Bamber and others (2001). The yellow contour at 1500 m a.s.l. represents the approximate equilibrium line altitude (ELA), according to Van de Wal and others (2008).

changes in cold ice advection resulting from ice motion, including basal sliding. Sensitivity is investigated with a steady-state, thermomechanically coupled, two-dimensional flowline model which solves the full-stress equations (a vertically explicit solution that includes membrane stresses). We apply this model to a profile of Isunnguata Sermia (Fig. 1), a terrestrially terminating glacier in western GrIS. The model is brought into agreement with observation by using adjoint methods for evaluating gradients of an objective function. Motivation for selecting a terrestrially terminating glacier stems from the fact that the majority of the GrIS is land terminating, and such a profile removes additional physical complexities relating to marine-terminating ice. Using the steady-state glacier geometry and surface velocity field, we examine the interactions of heat sources that dictate the stability of the FMB under different assumptions about geothermal heat flux and the basal traction fields. **Fig.1**

METHODS

Field equations

Our model is built upon the continuum mechanical formulation of the laws of conservation of mass, momentum and energy for an incompressible fluid. These are, respectively,

$$\nabla \mathbf{u} = 0, \tag{1}$$

$$\rho \frac{\mathrm{d}\mathbf{u}}{\mathrm{d}t} = \nabla \sigma + \rho \mathbf{g}, \tag{2}$$

$$\frac{\mathrm{d}\theta}{\mathrm{d}t} = \frac{1}{\rho c_\mathrm{p}} \nabla k_\mathrm{i} \nabla \theta - \mathbf{u} \nabla \theta + \frac{\Phi}{\rho c_\mathrm{p}}, \tag{3}$$

where $\mathbf{u}$ represents the velocity vector, σ the stress tensor, θ the temperature and Φ sources of heat generation in the ice. Physical constants c_p, k_i, ρ and $\mathbf{g}$ are defined in Table 1. Analysis is restricted to the x-z plane, or the vertical profile, making $\nabla = \frac{\partial}{\partial x}\hat{i} + \frac{\partial}{\partial z}\hat{k}$, where $\hat{i}$ and $\hat{k}$ are unit vectors in the x and z directions, respectively. **Tbl 1**

Table 1. Parameters and physical constants used in the model

Parameter	Symbol	Value
Gravitational acceleration	$\mathbf{g}$	$9.81\ \mathrm{m\,s^{-2}}$
Thermal conductivity of ice	k_i	$2.1\ \mathrm{W\,mK^{-1}}$
Density of ice	ρ	$911\ \mathrm{kg\,m^{-3}}$
Heat capacity of ice	c_p	$2093\ \mathrm{J\,kg^{-1}\,K^{-1}}$
Latent heat of fusion of ice	L	$3.35\times10^{5}\ \mathrm{J\,kg^{-1}}$
Triple point of water	T_0	273.15K
Pressure dependence of melting	b	$-9.8\times10^{-8}\ \mathrm{K\,Pa^{-1}}$
Universal gas constant	R	$8.314\ \mathrm{J\,mol^{-1}\,K^{-1}}$
Seconds per year	—	31 556 926
Glen's flow law exponent	n	3
Viscosity regularization	$\dot{\epsilon}$	$10^{-30}\ \mathrm{Pa\,s}$

Conservation of momentum and mass

The constitutive relation for ice takes the form

$$\tau_{ij} = 2\eta\dot{\epsilon}_{ij}, \tag{4}$$

where τ_{ij} is the ij element of the deviatoric stress tensor, which is defined by $\tau_{ij} = \sigma_{ij} - p\delta_{ij}$, with δ_{ij} the Kronecker delta function. Isotropic pressure is defined as $p = -\frac{1}{3}\sum_i \sigma_{ii}$.**[AUTHOR: Later, eq (20), p is used again. It might be better to use a different symbol here, to avoid any possible confusion.]** $\dot{\epsilon}_{ij}$ represents the corresponding element of the strain-rate tensor and η the viscosity. The strain-rate tensor is given by, and related to, velocity gradients as follows

$$\dot{\epsilon}_{ij} = \frac{1}{2}\left(\frac{\partial u_i}{\partial x_j} + \frac{\partial u_j}{\partial x_i}\right). \tag{5}$$

A non-Newtonian rheology is used for ice

$$\eta = \frac{1}{2}A(\theta^*)^{-1/n}\left(\dot{\epsilon}_{\text{II}} + \dot{\epsilon}_0\right)^{(1-n)/n}, \tag{6}$$

with $\dot{\epsilon}_{\text{II}}^2 = \frac{1}{2}\Sigma_{ij}\dot{\epsilon}_{ij}\dot{\epsilon}_{ij}$, or the second invariant of the strain-rate tensor, and $\dot{\epsilon}_0$ a regularization parameter introduced to avoid a singularity at zero strain rate. Glen's flow law (Paterson, 1994) gives $n = 3$. $A(\theta^*)$ is the flow law rate factor, given by Paterson and Budd (1982):

$$A(\theta^*) = \begin{cases} 3.61\times10^{-13} & \mathrm{e}^{-6.0\times10^4/R\theta^*}, \quad \theta^* \le 263.15\mathrm{K}, \\ 1.73\times10^{3} & \mathrm{e}^{-13.9\times10^4/R\theta^*}, \quad \theta^* > 263.15\mathrm{K}, \end{cases} \tag{7}$$

where θ^* is the homologous temperature, defined by $\theta^* = \theta + bp$ and R is the universal gas constant.

Under the assumption of steady state, the velocity of the ice is then determined from Stoke's flow confined to the x-z plane

$$\nabla\sigma = \rho\mathbf{g}, \tag{8}$$

and the conservation of mass, $\nabla\mathbf{u} = 0$.

Conservation of energy

Φ, the term in Equation (3) which represents internal heat generation, is computed as

$$\Phi = 2\eta\dot{\epsilon}_{\text{II}}^2. \tag{9}$$

Under the assumption of steady state and uniform thermal conductivity, the temperature of the ice is given by:

$$0 = \frac{k_\mathrm{i}}{\rho c_\mathrm{p}}\nabla^2\theta - \mathbf{u}\,\nabla\theta + \frac{2\eta\dot{\epsilon}_{\text{II}}^2}{\rho C_\mathrm{p}}. \tag{10}$$

Boundary conditions

Boundary conditions are applied to three distinct regions on the boundary of Isunnguata Sermia: (1) the surface; (2) the bed and (3) a vertical boundary at the ice divide.

Conservation of momentum and mass boundary conditions

The surface of the glacier upholds the neutral or stress-free boundary condition:

$$\sigma \widehat{\mathbf{n}} = 0, \tag{11}$$

where $\widehat{\mathbf{n}}$ is the outward normal unit vector.

The bed of the glacier is subjected to a Weertman-style sliding law, where basal velocity and shear stress are related as

$$\tau_b = \beta^2 \mathbf{u}\,\widehat{\mathbf{t}}, \tag{12}$$

where β^2 is a positive scalar, spatially variable parameter representing the magnitude of frictional forces at the bed and τ_b is given by

$$\tau_b = \sigma \widehat{\mathbf{n}} \tag{13}$$

evaluated at the base of the glacier. We constrain the sliding velocity to be tangential to the bed, that is $\mathbf{u}\,\widehat{\mathbf{n}} = 0$.

The vertical boundary at the divide is subject to a symmetry boundary condition:

$$\widehat{\mathbf{n}}\,\mathbf{u} = 0 \tag{14}$$

$$\sigma\,\widehat{\mathbf{t}} = 0, \tag{15}$$

where $\widehat{\mathbf{t}}$ is the unit vector tangent to the divide.

Conservation of energy boundary conditions

The bed of the glacier is subject to an inward heat flux given by

$$Q = q_g + q_f - q_l, \tag{16}$$

where q_g is the geothermal heat flux, q_f is heating due to sliding friction and q_l is latent heat associated with the melting of ice. q_g is taken as 42 mW m^{-2}, unless otherwise stated. Frictional heat is calculated as

$$q_f = \mathbf{u}\,\tau_b. \tag{17}$$

Latent heat is given by

$$q_l = \begin{cases} q_f + q_g + k_i \frac{\partial \theta}{\partial z}, & \theta^* \geq 273.15\text{K}, \\ 0, & \theta^* < 273.15\text{K}. \end{cases} \tag{18}$$

[AUTHOR: I have added units for the temperatures in the equation above. OK? The temperature is 263.15K in equation (7). Does anything need to be changed?]This heat interacts with the ice via the Neumann boundary condition

$$-\widehat{\mathbf{n}}\,k_i \nabla \theta = Q. \tag{19}$$

Note that the inclusion of the latent heat term serves as a temperature constraint on the ice by counteracting the inward flux from geothermal heat and frictional heat when the basal ice is at the pressure melting point.

The surface temperature of the glacier is inferred from the dataset of Ettema and others (2009), and is imposed as a Dirichlet boundary condition. The vertical boundary at the divide is thermally insulated such that $\widehat{\mathbf{n}}\,[-k_i \nabla \theta] = 0$.

Table 2. Quantities of importance for model numerics

Quantity	Value
Mesh elements	632
Degrees of freedom	4686
Element type	Lagrange quadratic
Initial damping factor	1×10^{-4}
Minimum damping factor	1×10^{-8}
Criterion for convergence	$<1 \times 10^{-6}$

Model domain

The geometry for the model domain was derived from the surface elevation and thickness data of Bamber and others (2001). Since the model used here considers only a vertical profile, we selected a streamline from the surface velocity data presented by Joughin and others (2010). We employed cubic splines to interpolate the glacier geometry between data points, which were spaced at 5 km.

Due to the discrete nature of the original dataset, the profile surface contained numerous artifacts, manifested as irregularities in slope. In order to produce a more reasonable surface, we implemented a free-surface evolution scheme, and allowed the model geometry to relax for 50 years. The high driving stresses associated with the slope irregularities quickly diffused, yielding a surface free from the original artifacts, but still consistent with the data and model physics.

Numerical considerations

The model uses the finite-element method to solve the field equations subject to the boundary conditions. Lagrange quadratic elements are used (Hughes, 2000), allowing second derivatives of the velocity to be computed accurately. The nonlinearity resulting from the viscosity (Equation (6)) is resolved using the modified Newton's method iterative solver (Deuflhard, 1974). The resulting linear systems were solved with UMFPACK (Davis, 2004). Model-specific parameters are summarized in Table 2. All numerical work was carried out in the *Comsol Multiphysics* modeling environment, a commercial package for finite-element analysis of general partial differential equations. **Tbl 2**

Modeling assumptions

Several assumptions were made in the development of this model, and results must be understood with these in mind. The assumptions are as follows:

The datasets used in the generation of the model domain geometry are sufficiently accurate, and the surface smoothing used to reduce artifacts does not introduce additional errors larger than those resulting from artifacts in surface geometry.

Stresses acting transverse to the dominant flow direction are small. This is necessary due to the effect that these stresses, and associated strains, have on the rheologic properties of the ice. Given the profile's location at the center of the ice catchment, and the uniform width of the streaming feature, this assumption is likely to be valid.

The steady-state solution generated by the data-assimilation process is a reasonable representation of a long-term configuration for the model domain. This

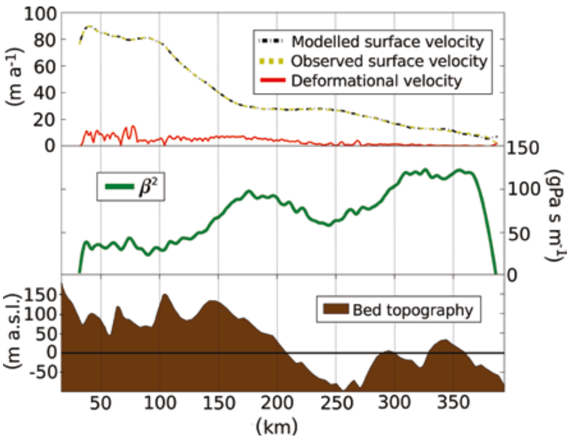

Fig. 2. Top: modeled and observed velocity, as well as the portion of the modeled velocity accounted for by internal deformation. Middle: the β^2 field derived from the data-assimilation procedure. Bottom: the topography underlying the modeled ice profile.

assumes that the modeled region of the GrIS was not in a transient state at the time the data was collected.

A constant geothermal heat flux is an appropriate parameterization of the real phenomenon across the modeled domain. This is to say that, given the spatial scale under consideration, variability in geothermal heat flux is either of a sufficiently low resolution to be considered in an average sense, or of a sufficiently large scale that it is essentially constant.

Steady-state solutions which include the data-assimilation process are sufficient for probing the sensitivities of the system with respect to changes in the basal boundary. A more complete treatment would entail the evolution of the free surface to determine the ultimate outcome of the perturbation, but that is beyond the scope of this work.

Data assimilation and model initialization

When modeling ice dynamics, there are two issues that must be addressed before numerical experiments can be conducted. Firstly, fields which have not been directly measured but are significant in computing flow must be estimated. For instance, the internal distribution of temperatures are critical to ice dynamics, but are at best known at a few boreholes. We will refer to this process as 'model initialization'. Secondly, the initialized model should be in agreement with measurements that are available. We refer to this as 'data assimilation'.

Our strategy in this paper will be to use steady-state solutions to conservation equations to initialize the model, subject to the constrains introduced by the data-assimilation process. This is not a new idea, MacAyeal (1993) introduced control methods in the context of ice-sheet modeling. Here, we extend the concepts to solutions which incorporate the full flowline stress balance.

For data assimilation, we use the adjoint of the linear operator to compute derivatives of an objective function, and use these slopes to minimize the function. We have defined an objective function in terms of difference between the observed, $u^{\mathrm{obs}}(\mathbf{x})$, and modeled, $u^{\mathrm{mod}}(\mathbf{x})$, surface velocities,

$$g(u,p) = \sum_{i=1}^{N} \left(u^{\mathrm{obs}}(\mathbf{x_i}) - u^{\mathrm{mod}}(\mathbf{x_i}) \right)^2, \tag{20}$$

which will be differentiated with respect to a parameter, p, that we vary in order to minimize the objective function. In this case the parameter will be $p = \beta(x)^2$, or the basal traction. Our introduction follows that of Strang (2007, p. 678–684).

'Chain rule' differentiation yields

$$\frac{\mathrm{d}g}{\mathrm{d}p} = \frac{\partial g}{\partial u}\frac{\partial u}{\partial p} + \frac{\partial g}{\partial p}, \tag{21}$$

where u is a solution vector containing both velocities and temperatures. The key to efficient calculation of the derivatives of the objective function is writing

$$\frac{\partial g}{\partial u} = c^{\mathrm{T}} \tag{22}$$

or, recognizing that the objective function is linear in u. It is now possible to write the gradient as

$$\frac{\mathrm{d}g}{\mathrm{d}p} = c^{\mathrm{T}}\frac{\partial u}{\partial p} + \frac{\partial g}{\partial p} = c^{\mathrm{T}}A^{-1}\frac{\partial b}{\partial p} + \frac{\partial g}{\partial p}, \tag{23}$$

where $c^{\mathrm{T}}A^{-1}$ is the result of solving the 'adjoint' linear system, $A^{\mathrm{T}}\lambda = c$ for $\lambda^{\mathrm{T}} = c^{\mathrm{T}}A^{-1}$. Note that the original problem is assumed to be represented by the system of linear equations, $Au = b$. Hence, the gradient for each step of an optimization algorithm (we use quasi-Newton) requires a single extra linear solve, rather than a linear solve for each of the many parameters, p. This saving makes it possible to do large inverse problems, such as computing a basal traction for each point in the model domain (Fig. 2). Figure 3 corresponds to the initialized velocity and temperature field, or the steady-state solutions to the field equations that assimilate the data. This will provide the starting point for all numerical experiments. In some cases, such as determination of the sensitivity to q_{g}, the entire assimilation/initialization process is repeated with different values.

Fig.2
Fig.3

NUMERICAL EXPERIMENTS

Sensitivity of the FMB to basal heat flow

In order to determine the sensitivity of the location of the FMB to different values of geothermal heat flux, we performed the data-assimilation procedure over a range of possible values. This experiment is motivated by the observation that basal sliding represents a significant portion of the total modeled surface velocity, and we wish to determine the geothermal heat flux required to produce a completely melted bed, in line with the assumption that the bed must be at the melting point for sliding to occur. We conducted model runs every 5 mW m^{-2} within the range 0–120 mW m^{-2}. Figure 4 shows the location of the FMB as a function of the prescribed geothermal heat flux. The FMB asymptotically approaches the divide as geothermal heat flux is increased, although the entire bed is not at the melting point under any of the parameter values considered, even for fluxes which seem unreasonably high. For comparison, previous authors have used a value of 42 mW m^{-2} (Pattyn, 2003), and a structural similarity model by Shapiro and Ritzwoller (2004) indicates a mean geothermal heat flux of ~58 mW m^{-2} along our flowline.

Fig.4

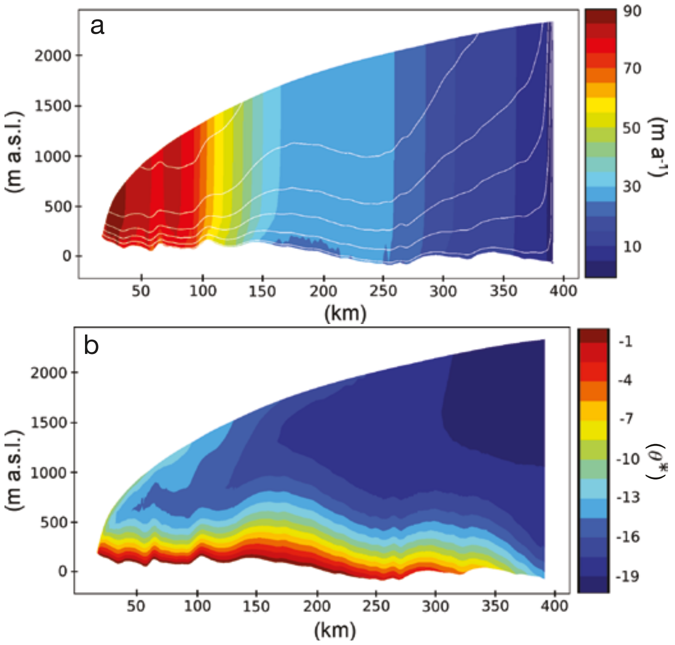

Fig. 3. (a) Velocity and (b) temperature fields produced by the data-assimilation process. White lines on the velocity figure indicate flowlines within the velocity field.

Previous work suggests that seasonal changes in the glacial drainage system below the ELA can contribute to changes in basal traction, leading to changes in surface velocity (Zwally and others, 2002; Joughin and others, 2008; Van de Wal and others, 2008; Bartholomew and others, 2010). There is little agreement between these workers regarding the magnitude of proposed changes in surface velocity. Joughin and others (2008) suggest that terrestrially terminating glaciers in the region south of Jakobshavn Isbræ (of which Isunnguata Sermia is one) experience 25% increases in surface velocity as a result of surface meltwater lubricating the bed. Bartholomew and others (2010) suggest speed-ups as great as 200%, and that a warming climate and associated surface lowering will expose greater portions of the bed to surface meltwater, increasing the fraction of the ice sheet exposed to summer speed-ups. Van de Wal and others (2008) acknowledge these seasonal variations, but present data showing an overall 10% decrease in surface velocities between 1990 and 2007. They also note that surface ablation and velocity show no correlation.

Regardless of the magnitude and sign of such changes in surface velocity, we sought to determine whether perturbations to the basal traction field, β^2, downstream from the ELA, such as those which would be induced by increased surface meltwater production, would have an impact on the basal thermal regime, specifically the location of the frozen melted boundary. We tested this by inflicting constant multiplicative perturbations to β^2 downstream from the ELA, ranging between 50% and 200% of the value produced by the data-assimilation process. The location of the FMB was insensitive to all these perturbations. The reason for
Fig.5 this is shown in Figure 5. Notable changes in the surface velocity field ($>1\,\mathrm{m\,a^{-1}}$) extend only 20 km, or ~10 ice thicknesses, upstream from the extent of the perturbation. Thus, the advection of heat away from the bed, the dominant mechanism accounting for heat flux at the bed, as shown in Figure 6, is unchanged 90 km upstream, at the location **Fig.6** of the FMB. This short coupling distance within the velocity field is corroborated by other studies (Price and others, 2008; Bartholomew and others, 2010).

Sensitivity of the FMB to sliding

Heat budget

In order to track the dominant factors which dictate the thermal regime at the bed, we calculated a heat budget of sources and sinks in terms of flux to the ice-sheet base. We performed this calculation for a model scenario with optimized β^2 and a geothermal heat flux of $42\,\mathrm{mW\,m^{-2}}$; results are displayed in Figure 6. Upstream of the FMB, frozen conditions are controlled by the advection of cold ice.

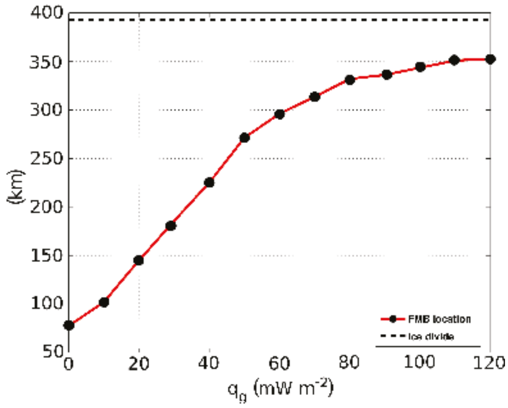

Fig. 4. Sensitivity of FMB location to variations in the geothermal heat flux.

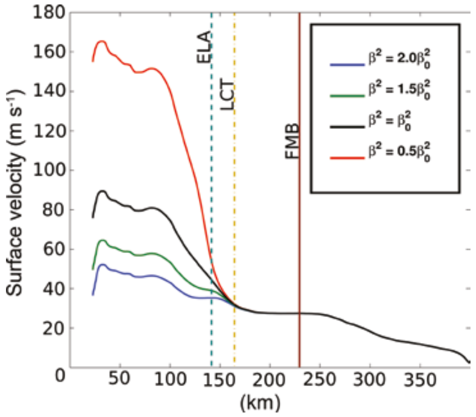

Fig. 5. Sensitivity of surface velocity to perturbations to the basal traction field, β^2. Equilibrium-line altitude (ELA) is ∼1500 m a.s.l. We interpret the longitudinal coupling threshold (LCT) to be the location at which the difference between any two surface velocity profiles is $\leq 1\,\mathrm{m\,a^{-1}}$.

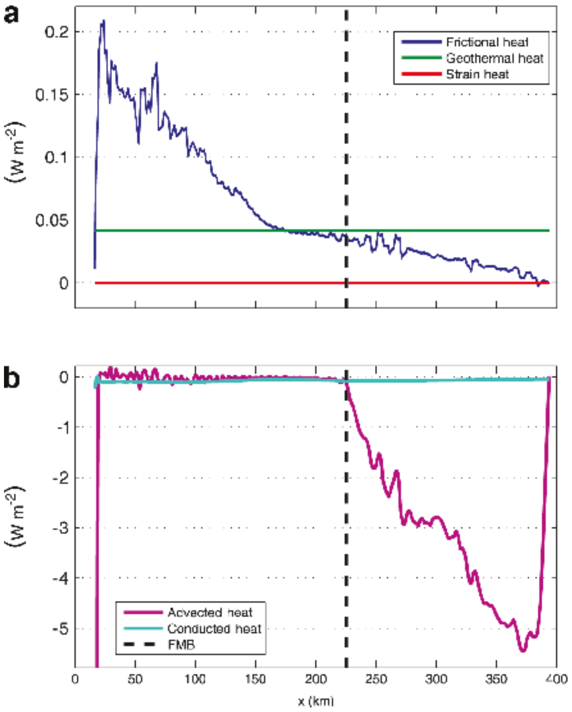

Fig. 6. Budget of (a) heat sources and (b) sinks along the profile basal boundary. Latent heat generation (not shown), is a negative nonzero term below the FMB, and accommodates excess heat generated from (a). Strain heat is a positive nonzero term, but negligible compared to frictional and geothermal heat sources.

Near the divide this advection is predominantly vertically directed from the surface. Moving downstream, advection becomes bed-parallel, so the advective flux decreases to zero at the FMB as heat sources raise the ice temperature as it flows along the bed. Throughout the frozen zone, and some kilometers beyond the FMB, the primary source of heat along the bed is geothermal heat flux. We find that heat generation due to straining at the bed is a positive contributor, but negligible compared to geothermal and frictional sources. Downstream of the FMB, excess heat generation is accommodated by the consumption of latent heat associated with the phase transition from ice to water as basal melt occurs. Basal melting initiates at the FMB and steadily increases to a maximum of $\sim 20\,\mathrm{mm\,a^{-1}}$ near the terminus.

DISCUSSION

The sensitivity experiments described above indicate strongly different responses by the FMB to perturbations in geothermal heat flux and basal sliding. The direct response of the basal thermal regime to changes in geothermal heat flux is an expected result. However the diminishing sensitivity of the FMB to increasingly higher heat fluxes is worth noting, and likely reflects the inability of the added heat to overcome cold advected from upstream.

In contrast, longitudinal coupling effects from sliding perturbations below the ELA do not propagate far enough up-glacier to influence the FMB. The location of the FMB is consequently insensitive to such perturbations. This interpretation hinges on the assumption that sliding perturbations apply only below the ELA, which is reasonable considering that the effect of increased surface melt input to the basal hydrologic system is not likely to propagate a significant distance upstream along the bed. We hypothesize that the limited distance over which longitudinal coupling occurs is a result of stress being dissipated at the basal boundary. It is important to note that sliding in our model is not limited to below the ELA. In fact, our optimization scheme produces a β^2 field with sliding above the FMB to the ice divide, albeit the upstream sliding is small relative to that occurring near the margin. Migration of melted conditions to the divide does not occur under very high values of geothermal heat flux, thus the representation of sliding in our modeled frozen zone needs some explanation.

If the bed is in fact frozen we see several potential explanations for our modeled sliding. Firstly, sliding has been observed over a frozen bed consisting of a till layer (Engelhardt and Kamb, 1998), or hard bedrock (Echelmeyer and Wang, 1987; Cuffey and others, 1999). Additionally, substantial deformation has been observed within a frozen till layer, both within the body of the till itself (Echelmeyer and Wang, 1987; Engelhardt and Kamb, 1998) and along discrete shear planes (Echelmeyer and Wang, 1987). This mechanism may be taking place if such a layer exists beneath GrIS. Secondly, and perhaps more likely, our model could under-represent velocity from ice deformation, requiring our optimization scheme to over-represent sliding to maintain the observed surface velocity. Changes in flow due to variable impurity and water content and grain size of ice are not accounted for in our model, however, elsewhere in Greenland, a layer of soft pre-Holocene ice has been observed to enhance flows 1.7–3.5-fold (Paterson, 1994; Lüthi and others, 2002). Alternatively, but in the same vein, the standard constitutive law we use could under-represent grain-scale ice deformation processes (Goldsby and Kohlstedt, 2001). Finally, the velocity field itself could potentially depict a velocity field out of balance with the current ice-sheet geometry. We have no basis to eliminate any of these possibilities. However, if the magnitude of sliding over frozen bed computed here is not real, it is likely to be principally accounted for by spatial changes in geothermal heat flux, anisotropies within the ice, or a combination of the two.

An alternative scenario is therefore a partitioning of the observed surface velocity with enhanced ice deformation and reduced sliding velocity. Our heat budget along the basal boundary suggests the implementation of sliding has a significant influence on the location of the FMB by increasing the advection of cold ice along the bed. Under this alternative scenario, the associated drop in sliding velocity combined with additional interior heat generation from enhanced straining may modulate the cold contribution from advection, pushing the FMB further upstream. These processes would likely be countered by a decrease in frictional heating, which would force the FMB towards the margin. A model exploration of FMB migration from this interaction of heat sources is beyond the scope of this paper, but will be the focus of future work.

CONCLUSIONS

We have developed a thermomechanically coupled, two-dimensional flowline model and applied it to a terrestrially terminating glacier profile located in western Greenland. We extracted geometric information for the model domain from a dataset presented by Bamber and others (2001), which we believe to be the best data available at present for the Greenland ice sheet. We used adjoint methods to optimize the basal traction field, such that modeled surface velocities matched observed values (Joughin and others, 2010) to within 1 m a^{-1}.

With an optimized model in hand, we conducted experiments in order to determine the sensitivity of the frozen/melted boundary (FMB) to perturbations in the basal heat flux and basal traction downstream of the ELA. We found that the FMB migrates easily under different assumptions about geothermal heat flux. At values close to 0 mW m^{-2}, the FMB moves very close to the terminus, but part of the bed remains unfrozen due to frictional heating from sliding. At high values, the FMB asymptotically approaches the ice divide. We found that for reasonable perturbations to basal traction downstream from the ELA, such as might be expected from an increase in surface meltwater production and associated bed lubrication, the FMB was insensitive. This is a result of the short length scale over which longitudinal stress coupling in the ice operates ($\sim$10 ice thicknesses). The FMB is significantly further upstream from the ELA than the perturbations to the velocity field extend, thus advective heat fluxes are unchanged. Our model predicts that, under most assumptions about geothermal heat flux, sliding occurs over a frozen bed. We see two possible explanations for this: (1) that this sliding is real, and follows one of the mechanisms proposed by Echelmeyer and Wang (1987), Engelhardt and Kamb (1998) or Cuffey and others (1999) (2) anisotropies or variability in hardness within the ice result in a preferential flow direction and increased deformation. Additional work is needed to quantify the sensitivity of the basal thermal regime to the second of these factors.

ACKNOWLEDGEMENTS

Funding for this work was provided by the Greenland Analogue Project (GAP), a collaborative project funded by the nuclear waste management organizations in Sweden (Svensk Krnbrnslehantering AB), Finland (Posiva Oy) and Canada (NWMO). It was also funded by grants from the US National Science Foundation: NSF-CMG-0934404 (JVJ) and NSF-OPP-0909495 (JTH).

REFERENCES

Andersen, K.K. *and 50 others*. 2004. High-resolution record of Northern Hemisphere climate extending into the last interglacial period. *Nature*, **431**, 147–151.

Bamber, J.L., R.L. Layberry and S.P. Gogineni. 2001. A new ice thickness and bed data set for the Greenland ice sheet. 1. Measurement, data reduction, and errors. *J. Geophys. Res.*, **106**(D24), 33 773–33 780.

Bartholomew, I., P. Nienow, D. Mair, A. Hubbard, M.A. King and A. Sole. 2010. Seasonal evolution of subglacial drainage and acceleration in a Greenland outlet glacier. *Nature Geosci.*, **3**(6), 408–411.

Cuffey, K.M., H. Conway, B. Hallet, A.M. Gades and C.F. Raymond. 1999. Interfacial water in polar glaciers and glacier sliding at −17°C. *Geophys. Res. Lett.*, **26**(6), 751–754.

Dahl-Jensen, D. *and 6 others*. 1998. Past temperatures directly from the Greenland ice sheet. *Science*, **282**(5387), 268–271.

Davis, T. 2004. A column pre-ordering strategy for the unsymmetric-pattern multifrontal method. *AMS Transactions in Mathematical Software*, **30**, 165–195.

Deuflhard, P. 1974. A modified Newton method for the solution of ill-conditioned systems of nonlinear equations with application to multiple shooting. *Numerical Mathematics*, **22**, 289–315.

Echelmeyer, K. and Z. Wang. 1987. Direct observation of basal sliding and deformation of basal drift at sub-freezing temperatures. *J. Glaciol.*, **33**(113), 83–98.

Engelhardt, H. and B. Kamb. 1998. Basal sliding of Ice Stream B, West Antarctica. *J. Glaciol.*, **44**(147), 223–230.

Ettema, J. *and 6 others*. 2009. Higher surface mass balance of the Greenland ice sheet revealed by high-resolution climate modelling. *Geophys. Res. Lett.*, **36**(L12501). (10.1029/2009GL038110.)

Fahnestock, M., W. Abdalati, I. Joughin, J. Brozena and P. Gogineni. 2001. High geothermal heat flow, basal melt, and the origin of rapid ice flow in central Greenland. *Science*, **294**(5550), 2338–2342.

Goldsby, D.L. and D.L. Kohlstedt. 2001. Superplastic deformation of ice: experimental observations. *J. Geophys. Res.*, **106**(B6), 11 017–11 030.

Greve, R. 2005. Relation of measured basal temperatures and the spatial distribution of the geothermal heat flux for the Greenland ice sheet. *Ann. Glaciol.*, **42**, 424–432.

Greve, R. and K. Hutter. 1995. Polythermal three-dimensional modelling of the Greenland ice sheet with varied geothermal heat flux. *Ann. Glaciol.*, **21**, 8–12.

Hughes, J.R. 2000. *The finite element method: linear static and dynamic finite element analysis*. Mineola, NY, Dover Publications.

Huybrechts, P., T. Payne and the EISMINT Intercomparison Group. 1996. The EISMINT benchmarks for testing ice-sheet models. *Ann. Glaciol.*, **23**, 1–12.

Joughin, I., S.B. Das, M.A. King, B.E. Smith, I.M. Howat and T. Moon. 2008. Seasonal speedup along the western flank of the Greenland Ice Sheet. *Science*, **320**(5877), 781–783.

Joughin, I., B.E. Smith, I.M. Howat, T. Scambos and T. Moon. 2010. Greenland flow variability from ice-sheet-wide velocity mapping. *J. Glaciol.*, **56**(197), 415–430.

Lüthi, M., M. Funk, A. Iken, S. Gogineni and M. Truffer. 2002. Mechanisms of fast flow in Jakobshavn Isbrae, West Greenland. Part III. Measurements of ice deformation, temperature and cross-borehole conductivity in boreholes to the bedrock. *J. Glaciol.*, **48**(162), 369–385.

MacAyeal, D.R. 1993. A tutorial on the use of control methods in ice-sheet modeling. *J. Glaciol.*, **39**(131), 91–98.

Oswald, G.K.A. and S.P. Gogineni. 2008. Recovery of subglacial water extent from Greenland radar survey data. *J. Glaciol.*, **54**(184), 94–106.

Paterson, W.S.B. 1994. *The physics of glaciers. Third edition*. Oxford, etc., Elsevier.

Paterson, W.S.B. and W.F. Budd. 1982. Flow parameters for ice sheet modelling. *Cold Reg. Sci. Technol.*, **6**(2), 175–177.

Pattyn, F. 2003. A new three-dimensional higher-order thermomechanical ice-sheet model: basic sensitivity, ice stream development, and ice flow across subglacial lakes. *J. Geophys. Res.*, **108**(B8), 2382.

Price, S.F., A.J. Payne, G.A. Catania and T.A. Neumann. 2008. Seasonal acceleration of inland ice via longitudinal coupling to marginal ice. *J. Glaciol.*, **54**(185), 213–219.

Shapiro, N.M. and M.H. Ritzwoller. 2004. Inferring surface heat flux distribution guided by a global seismic model: particular application to Antarctica. *Earth Planet. Sci. Lett.*, **233**(1–2), 213–224.

Strang, G. 2007. *Computational science and engineering*. Wellesey, MA, Wellesey-Cambridge Press.

Van de Wal, R.S.W. *and 6 others*. 2008. Large and rapid melt-induced velocity changes in the ablation zone of the Greenland Ice Sheet. *Science*, **321**(5885), 111–113.

Weertman, J. 1968. Comparison between measured and theoretical temperature profiles of the Camp Century, Greenland, borehole. CRREL Research Report No. 246, Cold Regions Research and Engineering Laboratory, US Army Corps of Engineers, Hanover, NH.

Zwally, H.J., W. Abdalati, T. Herring, K. Larson, J. Saba and K. Steffen. 2002. Surface melt-induced acceleration of Greenland ice-sheet flow. *Science*, **297**(5579), 218–222.

igs.cls v2.01 February 23, 2011 Article ref t59A065 Typeset by Sukie Proof no 1

Appendix 2

Classification of GAP groundwater using DNA fingerprinting

Sara Jägevall
Microbial Analytics Sweden AB

A2.1 Objectives

The microbial part of the GAP experiment was performed to be able to track and classify groundwater DNA signatures from the borehole DH-GAP01 and a lake close to this borehole. Diversity was studied to confirm that the groundwater sampled from the borehole was not contaminated by lake water. Groundwater was sampled at two different dates, 2009-07-12 and 2010-09-05. The first groundwater sample was collected solely from the borehole as a result of difficulties associated with sampling the lake at these low temperatures. However, at the last sampling occasion groundwater was successfully collected from the borehole and lake. The methods used to study biomass were quantitative PCR (qPCR) (Jägevall et al. 2011) and total number of cells (TNC) (Hobbie et al. 1977). These methods can only be used for biomass estimations. Hence, cloning (Jägevall et al. 2011) was needed to study diversity and identify DNA signatures in the different groundwater samples.

A2.2 Microbial sampling and monitoring

A method to detect total number of cells (TNC) was used for the determination of biomass in a sample as described previously (Hobbie et al. 1977, Pedersen and Ekendahl 1990).

DNA extractions were performed as described earlier (Jägevall et al. 2011). Five 50 mL groundwater samples were extracted for DNA from the borehole groundwater and then pooled and five samples of 50, 40, 40, 20 and 20 mL were extracted for DNA from the lake water and then pooled. Numbers of Bacteria and Eukarya were determined based on known genetic information using quantitative PCR (qPCR) for 16S rRNA gene Bacteria, 16S rRNA gene Archaea, 18S rRNA gene Eukarya, a*psA*, *fthfs*, p*moA*, *mxaF*, p*vsA*, *narG1*, n*arG2*, *nirK* and ANME1, 2a, 2c, to detect Bacteria, Archaea, Eukarya, sulphate-reducing bacteria, acetogens, methanotrophs, methylotrophs, *Pseudomonas fluorescens*, nitrate-reducing bacteria and anaerobic methane oxidizers as described earlier (Jägevall et al. 2011, Ginzinger 2002, Pedersen et al. 2010, Inagaki et al. 2004).

Cloning and sequencing were used for the determination of the diversity, DNA signatures and species of microorganisms (Jägevall et al. 2011, Pedersen et al. 1997, 2010).

A2.3 Classification of groundwater

A2.3.1 Classification of groundwater by cloning

Cloning was used to classify DNA signatures in groundwater collected from the borehole and nearby lake at the second sampling occasion, 2010-09-05. The borehole groundwater possessed a low diversity of microorganisms while the lake water had a broader diversity. The diversities were completely different between the borehole groundwater and lake water as none of the DNA signatures (DNA sequences) found in the borehole were identical to the DNA signatures found in the lake water (Table A2-1, A2-2).

Borehole groundwater

DNA signatures obtained from the cloned borehole groundwater were dominated by Clostridia, mostly *Desulfosporosinus lacus* (14/47 clones), *Acetobacterium malicum* (6/47 clones) and *Bacteriodetes* (16/47 clones). Betaproteobacteria (6/47 clones), gammaproteobacteria (2/47 clones), *Acidobacteria* (1/47 clones) and deltaproteobacteria (1/47 clones) were less abundant compared to the dominating DNA signatures (Table A2-1).

Lake water

The lake water collected 2010-09-05 was cloned and the sequences consisted mostly of DNA signatures from betaproteobacteria (9/44 clones), Bacteriodetes (7/44 clones) and alphaproteobacteria (6/44 clones (Table A2-2). Cyanobacterial DNA signatures were common as well (5/44 clones). Less frequent DNA signatures belonged to Actinobacteria (2/44 clones), Bulkholderiales (1/44 clones), *Cytophaga* (1/44 clones), Deltaproteobacteria (2/44 clones), *Flavobacterium* (1/44 clones), Flexibacter (3/44 clones) and *Verrucomicrobia* (2/44 clones). No sequences were identical between the borehole and lake water. One of the clones (HQ625536) resembled a clone (GQ240219) previously found in the groundwater collected close to the borehole KA1362A06 in the Äspö tunnel in Oskarshamn, Sweden.

Accession numbers

The sequence data from this study have been submitted to the GenBank database and were given the accession numbers HQ625523–HQ625563.

A2.4 Evaluation of classification of data

Samples were collected at two different occasions over a one year period and qPCR data together with TNC revealed a resemblance in amount of biomass between groundwater samples from the borehole DH-GAP01 over this time. 16S rRNA gene qPCR for Bacteria and 18S rRNA gene qPCR for Eukarya as well as TNC were used to analyse biomass from the groundwater samples. qPCR performed on the borehole sample from the first sampling occasion 2009-07-12 revealed low total biomass and consequently low numbers of Bacteria, Archaea, Eukarya, sulfate-reducing bacteria, acetogens, methanotrophs, methylotrophs, ANME, nitrate-reducing bacteria and *Pseudomonas fluorescen*s analysed by qPCR. Cloning together with TNC were for this reason analysed on samples collected at the second sampling occasion (2010-09-05) instead of qPCR to study the diversity in the borehole DH-GAP01 and lake groundwater. DNA signatures revealed that the diversity was completely different in the borehole groundwater compared to lake water. Hence, there was no contamination of the borehole from the lake recently. These results are very encouraging and support further cloning analyses to classify groundwater DNA signatures from the borehole DH-GAP01.

A2.4.1 Classification by biomass

Biomass estimated by TNC from the second sampling occasion was somewhat higher in the borehole compared to the lake (Table A2-3). qPCR for the 16S rRNA gene for Bacteria quantifying biomass was only performed at the first borehole sample and showed similar results but the number of gene copies were about three times lower than the TNC measured at the second borehole sample. This may be due to filtration and RNA later storage solution problems or due to substances inhibiting the qPCR. Eukarya DNA signatures were only measured in the DH-GAP01 groundwater sampled 2009-07-12. Classification of groundwater from the DH-GAP01 borehole and nearby lake

DNA signatures detected by cloning analyses are discussed below as TNC and qPCR was used solely for biomass estimations. The chemistry analyses were considered as well and overall chemistry analyses complemented. The groundwater could be distinguished between the DH-GAP01borehole groundwater and the lake water as they differed completely in diversity. Hence the borehole groundwater was not contaminated by the lake water recently (Table A2-1, A2-2).

Clostridia (Gram-positive bacteria) indicate anaerobic environments (Madigan and Martinko 2006). These spore-forming bacteria demonstrated the largest differences between the borehole and the lake groundwater as they dominated the borehole groundwater but were absent in the lake.

Bacteriodetes DNA signatures include several different groups of bacteria (Madigan and Martinko 2006). They were common in the borehole groundwater but found in the lake water as well. However, none of the DNA signatures from the borehole respectively the lake water shared identical sequences.

Alphaproteabacterial DNA signatures are found under aerobic conditions (Madigan and Martinko 2006). Bacteria found in these DNA signatures photosynthese. These DNA signatures differed greatly between groundwater from the borehole and the lake water. Several alphaproteobacterial DNA signatures were frequently found in the lake water but not in the borehole groundwater.

Betaproteobacterial DNA signatures are found in aerobic or facultative aerobic environments and include several nitrogen fixing bacteria (Madigan and Martinko 2006). Betaproteobacterial DNA signatures were more abundant in the lake water than in the DH-GAP01 borehole groundwater.

Deltaproteobacterial DNA signatures are mostly sulphate-reducing bacteria using sulphate as electron acceptor to produce hydrogen sulphide under anaerobically conditions (Madigan and Martinko 2006). In groundwater where these signatures are found sulphate reduction can be an ongoing process. The lake water revealed two signatures and the DH-GAP borehole groundwater none.

Gammaproteobacterial DNA signatures are found in aerobic or anaerobic environments. They were widely distributed among groups of microbes (Madigan and Martinko 2006) and were found in the borehole DH-GAP01 but not in the lake.

Actinobacterial signatures are found mostly in aerobic environments (Ventura et al. 2007) and they were only found in the lake water.

Acidobacterial DNA signatures are found in acidic environments (Barns et al. 2007) but these DNA signatures were found as one clone in the borehole groundwater but not the lake.

Bulkholderiales DNA signatures are found in aerobic environments (Madigan and Martinko 2006) and were found solely in the lake water.

Cyanobacteria were found in the lake water but not at all in the borehole groundwater. They are generally photosynthetic and need light (Madigan and Martinko 2006).

Cytophaga and **Flexibacter** are found in aerobic environments. Flexibacter can additionally be found in anaerobic environments. These DNA signatures were found in the lake water but not in the borehole groundwater (Madigan and Martinko 2006).

Verrumicrobial DNA signatures were few but present in the lake water but not in the borehole groundwater. They are aerobic or facultatively anaerobic (Madigan and Martinko 2006).

All these observations pointed in the same direction. Some DNA signatures were similar but no sequences were identical between the borehole DH-GAP01 and the lake groundwater. Most DNA signatures indicated anaerobic conditions in the borehole and aerobic conditions in the lake. The borehole groundwater diversity was low compared to the lake water diversity.

A2.5 Conclusions

- DNA signatures obtained by cloning could successfully be used to classify the water samples.
- Biomass evaluated by TNC and 16S rRNA qPCR for Bacteria resulted in low, similar numbers of cells in DH-GAP01 borehole and in the lake. These results were supported by 16S rRNA gene qPCR for Bacteria.
- Some DNA signatures such as Bacteriodetes, beta- and deltaproteobacteria were found in the borehole DH-GAP01 as well as the lake groundwater. However, no DNA sequences were identical between the borehole groundwater and lake water samples.
- The diversity in DH-GAP01 borehole groundwater was lower and completely different compared to the lake water. 14 unique DNA sequences were found and submitted to the database GenBank from the borehole groundwater compared to the 30 unique DNA sequences obtained from the lake water. None of the DNA signatures found in the lake was found in the borehole. The borehole was, therefore, not recently contaminated by lake water.
- Clostridia dominated the borehole water and indicated anaerobic conditions. Bacteriodetes, alpha- and betaproteobacteria were frequently found in the lake water. Most of the lake water DNA signatures indicated aerobic conditions and photosynthesis requiring light as predicted in the lake water.

Table A2-1. DNA signatures found by cloning the borehole DH-GAP01 groundwater sampled 2010-09-05.

Phylum	Species	Id. Closest match GenBank (%)	Accession no GenBank	Number of clones
Bacteriodetes	Uncultured bacterium (HM141898)	97	HQ625528	16
Clostridia	*Desulfosporosinus lacus* (AJ582757)	96	HQ625530	14
Clostridia	*Acetobacterium malicum* (NR_026326)	98	HQ625524	6
Betaproteobacteria	*Herminiimonas fonticola* (AM989095)	99	HQ625525/27	2
Betaproteobacteria	*Polaromonas sp.* (EU106605/ FM955859)	93/99	HQ625531/32	2/1
Betaproteobacteria	*Polynucleobacter necessarius* (CP000655)	99	HQ625526	1
Gammaproteobacteria	*Pseudomonas peli* (HQ202835)	99	HQ625523	1
Acidobacteria	*Acidobacteria bacterium* (FR716684)	98	HQ625529	1
Gammaproteobacteria	*Pseudomonas anguilliseptica* (NR029319)	98	HQ625534	1
Unclassified	Uncultured bacterium (GU236035)	96	HQ625533	1
Unclassified	Uncultured bacterium (FM956230)	96	HQ625535	1

Table A2-2. DNA signatures obtained by cloning of the lake water sampled 2010-09-05.

Phylum	Species	Id. Closest match GenBank (%)	Accession no GenBank	Number of clones
Bacteriodetes	Uncultured *Flectobacillus sp.* (FN668109)	99	HQ625542	4
Alphaproteobacteria	Uncultured bacterium (HM483831/EF667921/ GU305752)	99/92/99*	HQ625556/ HQ625553	3/1/1*
Betaproteobacteria	Uncultured bacterium (AM849432/EU802045/ GQ240219/FJ916348)	99/99/99/97*	HQ625555/ HQ625536/ HQ625546	3/1/1/1*
Cyanobacteria	Uncultured *Synechococcus sp.* (EU703425)	99	HQ625557	3
Bacteriodetes	Uncultured bacterium (EU640023/ EU703442)	100/99*	HQ625550/ HQ625548	2/1*
Actinobacteria	Uncultured bacterium (EU117782/88)	99/97*	HQ625551/58/	1/1*
Alphaproteobacteria	*Sphingomonas sp.* (AY584572)	99	HQ625541	1
Betaproteobacteria	*Methylibium petroleiphilum* (CP000555)	97	HQ625544	1
Betaproteobacteria	*Polynucleobacter acidiphobus* (AJ876403)	100	HQ625547	1
Betaproteobacteria	*Rhodoferax ferrireducens* (CP000267)	98	*	1
Bulkholderiales	Uncultured bacterium (EU803423)	98	*	1
Cyanobacteria	*Cyanobium sp.* (AM710378)	99	HQ625554	1
Cyanobacteria	*Synechococcus rubescens* (AF317076)	99	HQ625563	1
Cytophaga	Uncultured bacterium (AF361200)	94	*	1
Deltaproteobacteria	*Spirobacillus cienkowskii* (EU220836)	99	HQ625552	1
Deltaproteobacteria	Uncultured bacterium (EU449596)	94	HQ625543	1
Flavobacterium	Uncultured bacterium (FJ694511)	97	HQ625538	1
Flexibacter	Uncultured *Flexibacter sp.* (FN668178)	99	HQ625549	1
Flexibacter	Uncultured bacterium (AY509281/ AY509320)	97/97*	HQ625540/ HQ625537	1/1*
Unclassified	Uncultured bacterium (EU234313/ FN297294/353/459/ GU305849)	100/99/99/96/99*	HQ625539/ HQ625559–HQ625562	1/1/1/1/1*
Verrucomicrobia	Uncultured bacterium (GQ347385/GU472738)	98/99*		1/1*

*Several similar clones were found and submitted and they are listed after each other and separated by /. Were no accession number is addressed the sequence failed our quality tests and were therefore not submitted.

Table A2-3. TNC and qPCR for 16S rRNA gene Bacteria and 18S rRNA Eukarya were detected for the DH-GAP01 borehole and lake water samples at the two different sampling dates 2009-12-07 and 2010-09-05.

Sample	TNC	Standard deviation	16S rRNA gene Bacteria qPCR		18S rRNA gene Eukarya qPCR		16S rRNA gene Archaea qPCR	
			Gene copy number (copies mL–1)	Standard deviation	Gene copy number (copies mL–1)	Standard deviation	Gene copy number (copies mL–1)	Standard deviation
DH-GAP01 borehole 2009-07-12	*	*	4.9×10^3	3.8×10^3	3.3×10^5	1.6×10^5	<100	<100
DH-GAP01 borehole 2010-09-05	1.4×10^4	4.9×10^3	*	*	*	*	*	*
DH-GAP01 lake 2010-09-05	8.8×10^3	1.6×10^3	*	*	*	*	*	*

Table A2-4. DNA signatures found in the groundwater samples collected at the DH-GAP01 borehole respectively the lake. The different signatures that were found by cloning and their modes of action were listed together with a reference.

DNA signature	Mode of action	Reference
Acidobacteria	Favour or demands acidic environments.	Barns et al. 2007
Actinobacteria	Mostly aerobic but anaerobic environments possible.	Ventura et al. 2007
Alphaproteobacteria	Aerobic environments. Photosynthesize commonly to acquire energy.	Madigan and Martinko 2006
Bacteriodetes		Madigan and Martinko 2006
Betaproteobacteria	Aerobic / facultatively aerobic. Nitrogen fixation in plants. May use photosynthesis.	Madigan and Martinko 2006
Chloroflexi	Facultatively anaerobic, produce energy from light, hence they are phototrophic.	Madigan and Martinko 2006
Clostridia	Sporeforming obligate anaerobic bacteria. May reduce sulfite.	Madigan and Martinko 2006
Cyanobacteria	Facultatively anaerobic. Obtain their energy through photosynthesis.	Madigan and Martinko 2006
Cytophaga	Aerobic, rod-shaped gliding bacteria.	Madigan and Martinko 2006
Gammaproteobacteria	Aerobic or anaerobic environments.	Madigan and Martinko 2006
Deltaproteobacteria	Anaerobic bacteria belong to these DNA signatures. Mostly sulfate reduction by SRB.	Madigan and Martinko 2006
Flexibacter		Madigan and Martinko 2006
Verrucomicrobia	Aerobic or facultatively anaerobic bacteria fermenting different sugars.	Madigan and Martinko 2006

Appendix 3

Evaluation of pressure responses in borehole DH-GAP01

Kent Werner, 2011-02-24

Background

This appendix describes evaluation of hydraulic properties (transmissivity and hydraulic conductivity) of the rock surrounding borehole DH-GAP01, based on pressure-response data associated with water withdrawal from the borehole. The borehole has a radius of 0.0284 m (borehole diameter 0.0568 m) and a total length of 221 m. The borehole is inclined and reaches a vertical depth of 191.5 m. There is a borehole packer at borehole length 150 m, at a true vertical depth of 130 m. The water withdrawal and pressure responses refer to the borehole section below the packer. This section has a length of 71 m and a vertical depth of 61.5 m. Hence, the evaluated hydraulic properties refer to the rock surrounding the borehole in the depth interval 130–191.5 m.

The pressure responses are due to water removal (up to 0.0118 m^3) for chemical sampling of the borehole section. Specifically, the pressure recovery following water removal is evaluated using methods developed for evaluation of so-called slug tests ("bailer tests"). It is therefore assumed that the pressure drawdown in the borehole section is instantaneous, i.e. that there is negligible inflow from the rock to the borehole section during water removal. The conducted tests have short durations and involve small volumes of water. This implies that evaluated parameters pertain to the rock immediately surrounding the borehole, which may be affected by the drilling of the borehole. Moreover, there is large uncertainty regarding storativity values (S) evaluated from single-hole tests.

As shown in the table below, data are evaluated from two tests, here denoted test #1 and test #2. Water was also removed from the borehole section on 2010-09-05. However, during that test, pressures were only registered every 30 minutes, which is not sufficient for evaluation. According to the field log book, some additional water sampling was done ca. 30 minutes after the initiation of the test #1 recovery. Therefore, the test #1 recovery is evaluated for a time period of 30 minutes. Moreover, at initiation of test #2, the pressure in the borehole section had not fully recovered subsequent to test #1. Therefore, for test #2, the pressure drawdown Δh_0 (m) refers to the pre-drawdown pressure of test #1, which hence is assumed to represent the undisturbed pressure.

The theoretical initial pressure drawdown can be estimated by the relation $\Delta h_0 = \frac{\Delta V}{\pi r_{bh}^2}$, where ΔV is the removed water volume and r_{bh} is the borehole radius. $\Delta V = 0.0118$ m^3 and $\Delta h_0 = 9.388$ m (test #1) yields $r_{bh} = 0.020$ m. This value is less than the actual borehole radius (0.0284 m) and indicates that the downhole equipment must be taken into account when assigning an effective borehole radius in the data evaluation. Therefore, in the data evaluation, an effective borehole radius of 0.020 m is used. This value is based on the measured Δh_0 and takes into account that there is borehole equipment only in part of the tested borehole section.

The recovery data are evaluated by three commonly employed methods: Cooper-Bredehoeft-Papadopulos (Cooper et al. 1967), Bouwer-Rice (Bouwer and Rice 1976) and Hvorslev (1951). The evaluation is done using the AQTESOLV software. Measured pressures p (bar) are converted to pressure heads h (m) by the relation $h = \frac{p \cdot 10^5}{\rho \cdot g}$, using ρ (density of water) = 1,000 kg/m^3 and g = 9.81 m/s^2.

Table A3-1.

Test #	Initiation of pressure drawdown (YYYY:MM:DD hh:mm:ss)	Initiation of pressure recovery (YYYY:MM:DD hh:mm:ss)	Pre-drawdown pressure head (m)	Pre-recovery pressure head (m)	Initial pressure drawdown, Δh_0 (m)	Comments
1	2010-09-04 17:19:00	2010-09-04 17:22:00	139.817	130.428	9.388	Additional water sampling 30 minutes after initiation of recovery.
2	2010-09-04 19:54:00	2010-09-04 19:58:00	139.552	128.400	11.417	Pressure not fully recovered from test #1.

Test #1

The three following figures show evaluation plots according to the Cooper, Bouwer-Rice and Hvorslev methods (the name of the evaluation method is stated under "Solution" to the right of each plot). The vertical axes show normalized head (h_n), i.e. the residual pressure-head drawdown divided by the undisturbed pressure head. There is a good fit of the test #1 recovery data to the Cooper type curve for transmissivity $T = 1.51 \cdot 10^{-6}$ m²/s. Dividing T by the vertical depth of the borehole section (61.5 m) yields $K = 2.46 \cdot 10^{-8}$ m/s. The Bouwer-Rice and Hvorslev methods are based on fitting the recovery data to straight lines using a log-scale on the vertical (h_n) axis, specifically in the ranges $h_n = 0.2–0.3$ and $h_n = 0.15–0.25$, respectively. These two methods provide $K = 4.62 \cdot 10^{-8}$ m/s and $K = 2.67 \cdot 10^{-8}$ m/s, respectively.

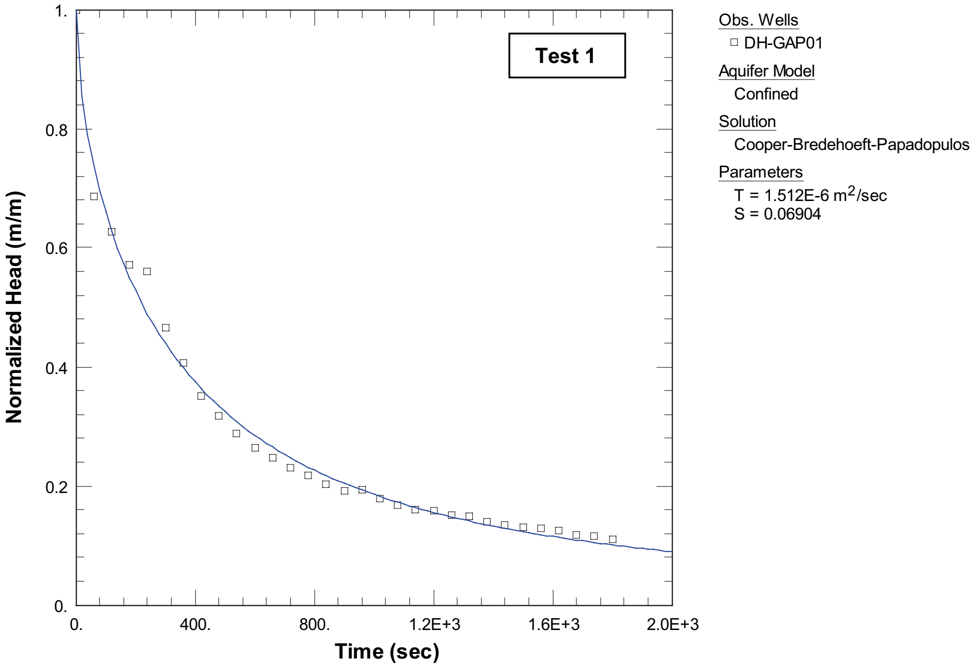

Figure A3-1.

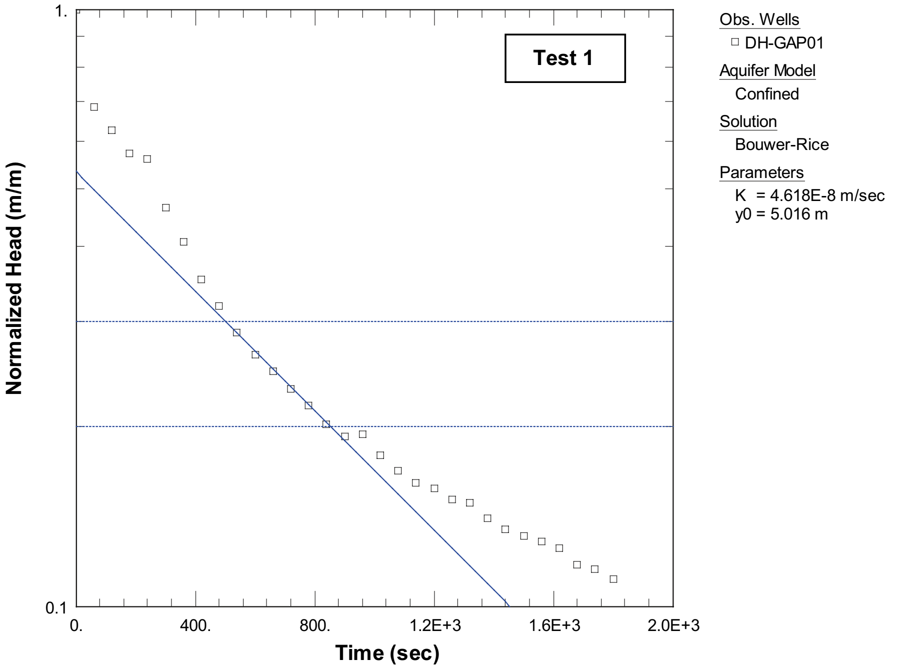

Figure A3-2.

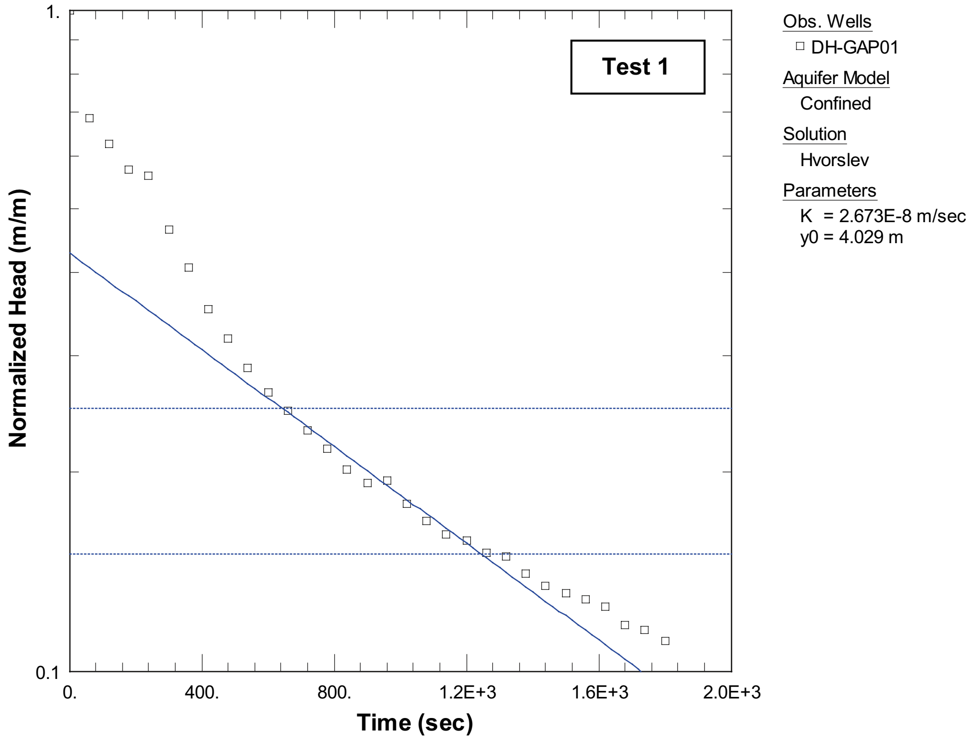

Figure A3-3.

Test #2

As can be seen in the figure below, it is not possible to obtain a good fit of the test #2 recovery data using the Cooper method. The data indicate that the recovery may be influenced by borehole skin, i.e. a zone immediately surrounding the borehole and with hydraulic properties that deviate from those of the rock. The deviation from the type curve is larger for lower values of h_n, i.e. for smaller hydraulic gradients between the borehole section and the rock.

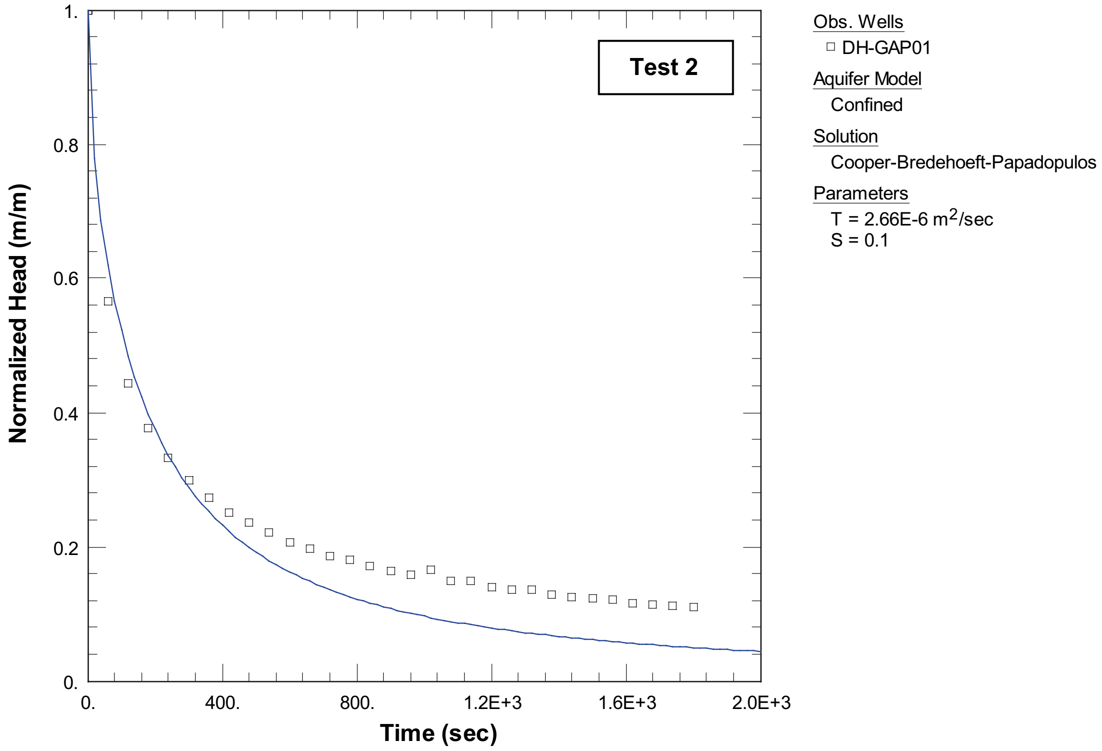

Figure A3-4.

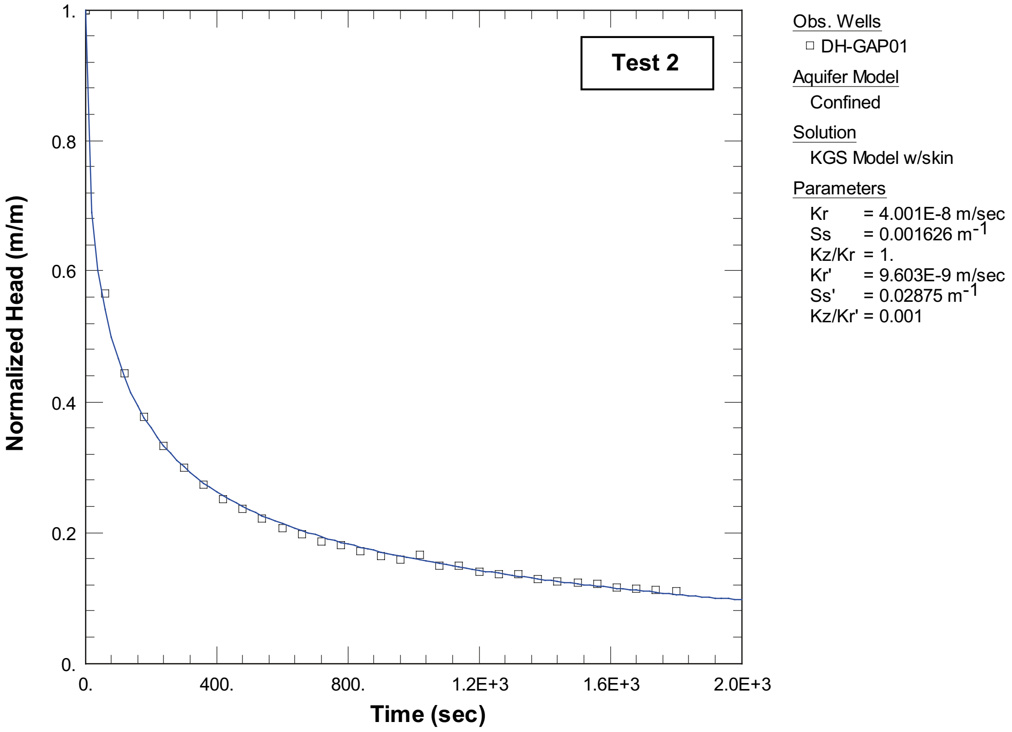

Figure A3-5.

The potential influence of borehole skin was tested using the so-called KGS method (Hyder et al. 1994), using a skin thickness of 0.02 m. As can be seen in the figure below, the recovery data can be well fitted to a KGS type curve for $K_r = 4.00 \cdot 10^{-8}$ m/s (hydraulic conductivity of the rock, assuming radial flow) and a skin with a somewhat lower hydraulic conductivity (K'_r) compared to the rock.

In order to check the consistency of the skin hypothesis, the test #1 recovery data were also evaluated using the KGS method. As shown in the figure below, it is possible to obtain a reasonable fit ($K_r = 2.74 \cdot 10^{-8}$ m/s) of the test #1 data also if a skin factor is considered.

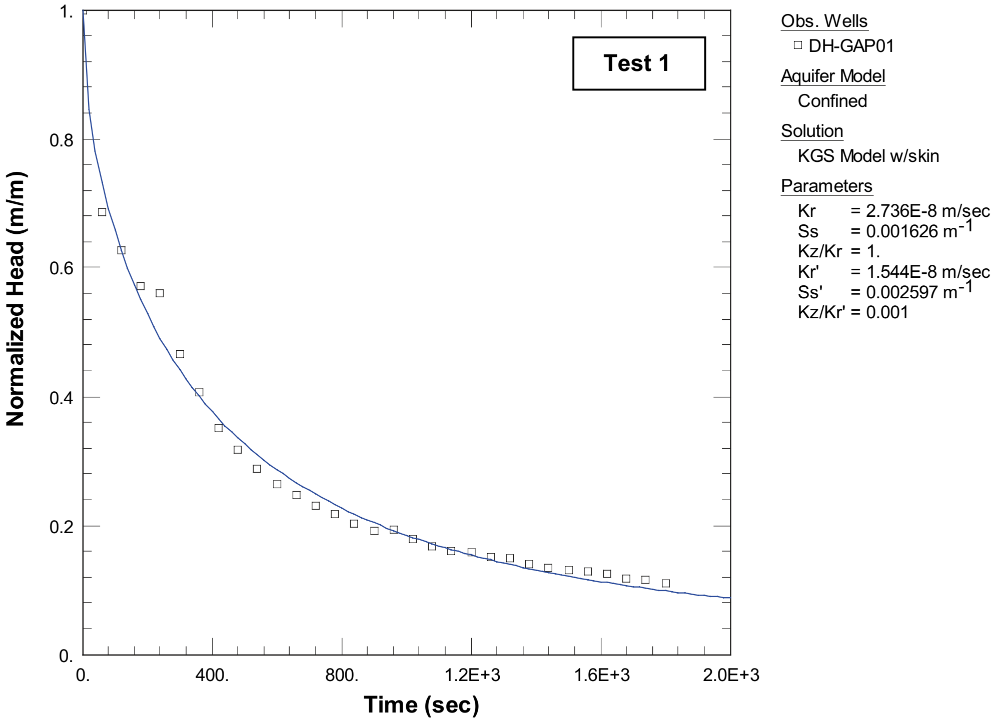

Figure A3-6.

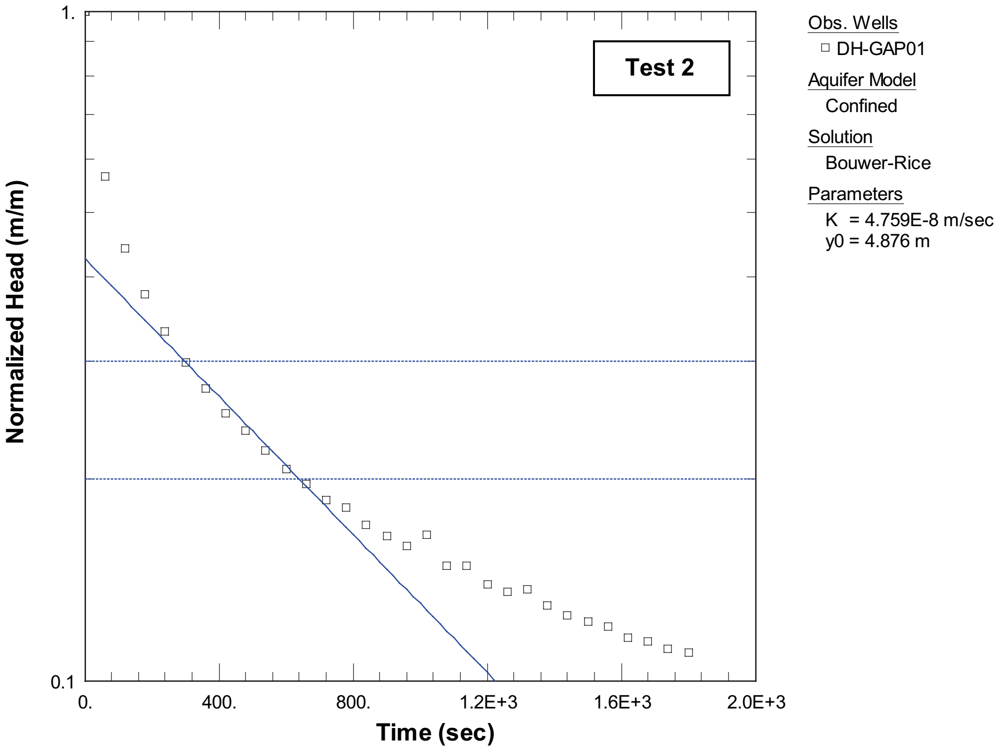

Figure A3-7.

The figures below show Bouwer-Rice and Hvorslev plots of the test #2 recovery data. Using the same approach as described above, the recovery data can be fitted for K = $4.76 \cdot 10^{-8}$ m/s and K = $2.48 \cdot 10^{-8}$ m/s, respectively.

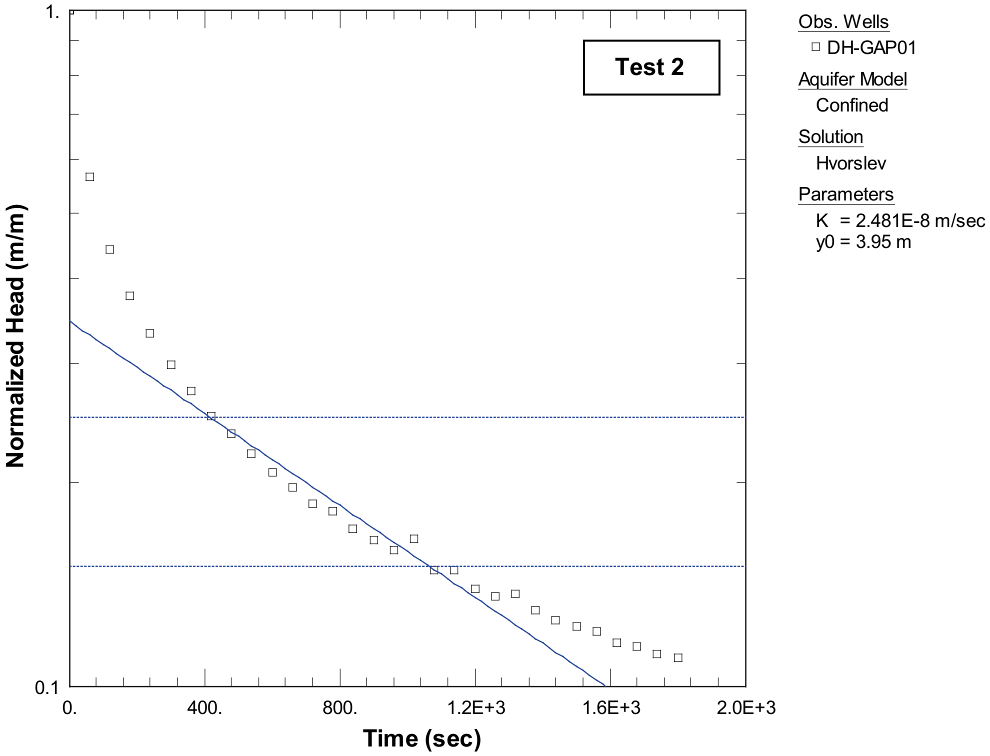

Figure A3-8.

Table A3-2.

	Cooper et al.	Bouwer-Rice	Hvorslev	KGS (w. skin)
T (m^2/s)	#1: $1.51\cdot10^{-6}$ $K = 2.46\cdot10^{-8}$ m/s	N.A.	N.A.	N.A.
	#2: –	N.A.	N.A.	N.A.
K (m/s)	#1: –	#1: $4.62\cdot10^{-8}$	#1: $2.67\cdot10^{-8}$	N.A.
	#2: –	#2: $4.76\cdot10^{-8}$	#2: $2.48\cdot10^{-8}$	N.A.
K_r (m/s)	N.A.	N.A.	N.A.	#1: $2.74\cdot10^{-8}$
	N.A.	N.A.	N.A.	#2: $4.00\cdot10^{-8}$
K'_r (m/s)	N.A.	N.A.	N.A.	#1: $1.54\cdot10^{-8}$
	N.A.	N.A.	N.A.	#2: $9.60\cdot10^{-9}$

Table A3-2 summarizes the results of the recovery-data evaluation. According to the table, the hydraulic conductivity of the rock in the depth interval 130–191.5 m at borehole DH-GAP01 is estimated to be on the order of $2–5\cdot10^{-8}$ m/s. The recovery data indicate the presence of borehole skin, with a somewhat lower hydraulic conductivity (ca. $1\cdot10^{-8}$ m/s) compared to the rock. It should be emphasized that the evaluated K-values are effective values for the tested borehole section. The main part of the inflow to the borehole section may occur through intersecting high-conductive fractures, whereas there may be little or no inflow along other parts. There are slug test- and other methods available for evaluation of the hydraulic conductivity of individual fractures. Such evaluations require information on fracture frequencies and widths, but such data were not available for the present evaluation.

Dual-porosity medium evaluation

General

The slug-test evaluation methods described above assume homogeneous conditions, i.e. they assume that the formation transmissivity (T) and storativity (S) are equal at every point along the tested borehole. Such methods are commonly used also for evaluation of slug tests in fractured rock. Available methods for evaluation of hydraulic properties of fractures and the rock mass between fractures, respectively, suffer from non-uniqueness (different combinations of parameter values and flow geometries may yield similar slug-test responses). However, Shapiro and Hsieh (1998) found that the transmissivity obtained using an evaluation method assuming homogenous conditions can be expected to be within an order of magnitude of the total fracture transmissivity of all fractures intersecting a slug-tested borehole (or borehole section) in fractured rock.

Moreover, Shapiro and Hsieh (1998) found that mismatch between an actual slug-test response and the response predicted using, for example, the Cooper et al. (1967) method; the deviation likely is due to non-radial flow in the vicinity of the borehole and/or interactions between fractures and the surrounding rock matrix. The latter case implies that groundwater flow takes place in a so called dual-porosity medium, i.e. in a fractured-rock formation consisting of permeable fractures that interact with a surrounding low-permeable rock matrix.

This section investigates whether the pressure-response data from borehole DH-GAP01 can be used to obtain reasonable estimates of the total fracture transmissivity and the hydraulic conductivity of the rock mass, respectively. The data are evaluated using the multi-parameter, dual-porosity method presented by Barker and Black (1983), assuming horizontal fractures (and hence radial flow) separated by regularly spaced "rock slabs". By means of borehole logging in DH-GAP01, a total of 137 fractures are observed in the depth interval 130–191.5 m (borehole length 150–221 m), corresponding to an approximate fracture frequency of 2 fractures m^{-1}. This yields an average inter-fracture distance of 0.3 m, which is equal to the "rock-slab size" that is required as input using the Barker and Black (1983) method.

Results

Figures A3-9 and A3-10 below show Barker-Black evaluation plots of test #1 and test#2, respectively. As in the previous evaluations, the vertical axes show normalized head (h_n), i.e. the residual pressure-head drawdown divided by the undisturbed pressure head. According to the first figure, the test #1 recovery data yields a reasonable fit to the Barker-Black type curve for a total fracture transmissivity (T) of approximately 10^{-6} m^2/s and a rock-mass hydraulic conductivity (K′) of approximately 10^{-8} m/s. The length of the tested borehole section, and an assumed total fracture width of ca. 1 m (for the 137 encountered fractures), yield a total transmissivity that is within an order of magnitude of the T value obtained using the Cooper method. This result is in accordance with the findings of Shapiro and Hsieh (1998).

As shown in the second figure, it is not possible to obtain a good fit of the test #2 recovery data. As mentioned previously, the recovery may be influenced by borehole skin and/or non-radial flow, the effects of which cannot be accounted for using the Barker-Black method, or any other slug-test evaluation method available. A better fit (not shown here) can in fact be obtained for a total fracture transmissivity that is ca. 1/3 of the value obtained from the test #1 data, but in that case for an unrealistically high rock-mass hydraulic conductivity.

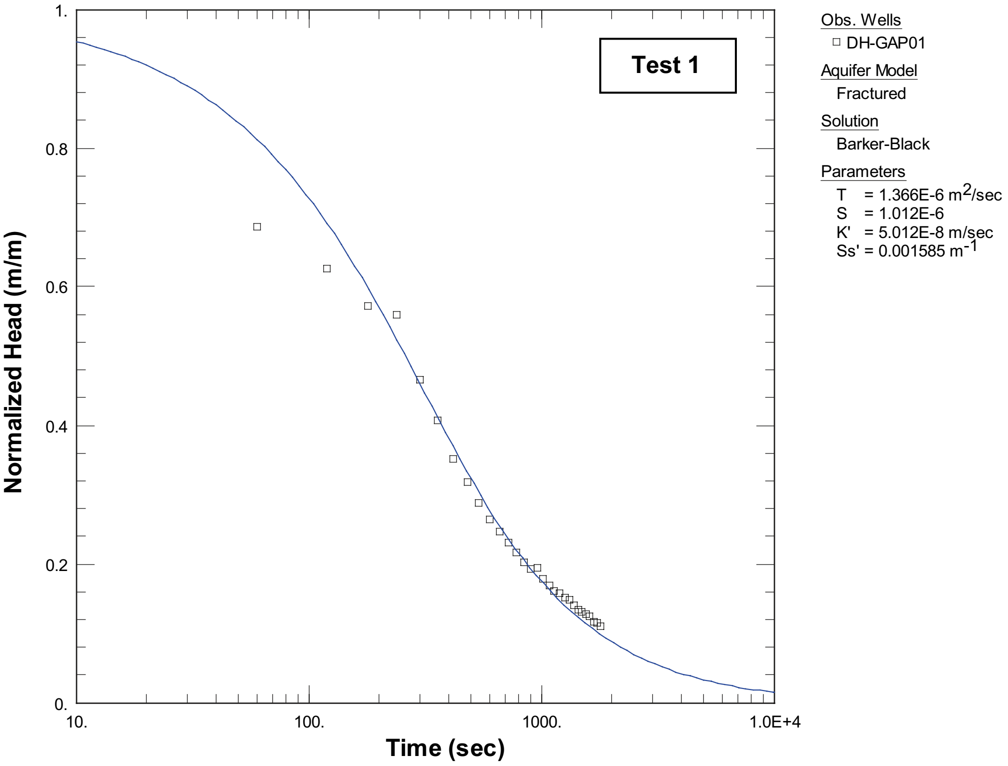

Figure A3-9.

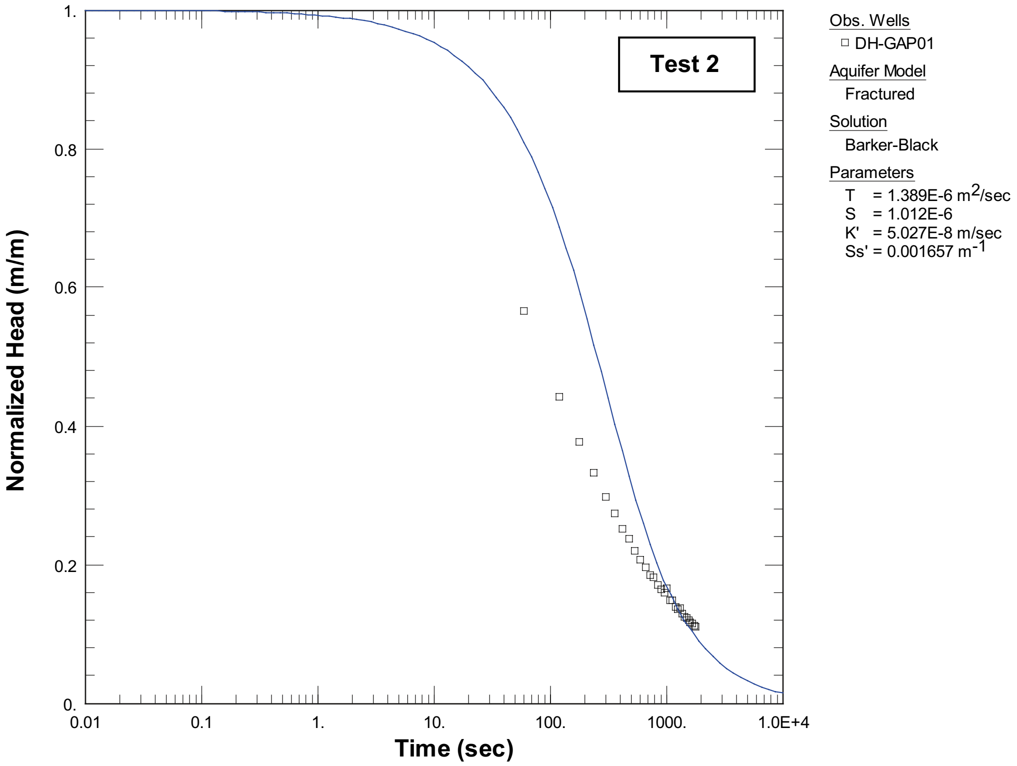
Test 2
Normalized Head (m/m)
1.
0.8
0.6
0.4
0.2
0.
0.01
0.1
1.
10.
100.
1000.
1.0E+4
Time (sec)
Obs. Wells
□ DH-GAP01
Aquifer Model
Fractured
Solution
Barker-Black
Parameters
T = 1.389E-6 m^2/sec
S = 1.012E-6
K' = 5.027E-8 m/sec
Ss' = 0.001657 m^{-1}

Figure A3-10.